Electron-Nuclear Quantum Fluxes in Adiabatic Chemical Processes

INAUGURAL DISSERTATION

zur Erlangung des Doktorgrades
der Freien Universität Berlin
Fachbereich Biologie, Chemie, Pharmazie

vorgelegt von

Timm Bredtmann

aus Essen

2013

Gutachter
Prof. Dr. Jörn Manz
Prof. Dr. Beate Paulus
Tag der mündlichen Prüfung: 16.09.2013

Abstract

In chemistry, the electronic rearrangement accompanying nuclear motion is typically sketched by curved arrows embedded in the Lewis structure of the reactant, indicating the net transfer of valence electrons associated with bond making, bond breaking and shifting of specific multiple bonds. In this thesis, molecular Quantum Dynamics is extended and related to such traditional, qualitative descriptions, yielding new insight into adiabatic chemical processes in terms of the underlying coupled electronic and nuclear quantum fluxes. Such processes involve the collective rearrangement of both electrons and nuclei in specific electronic states, and are exemplified in this thesis for a pericyclic reaction, the degenerate [3,3]-sigmatropic shift (degenerate Cope rearrangement) of semibullvalene occurring in the non-degenerate electronic ground state. In particular, it is shown that the directionality of the corresponding electronic bond-to-bond fluxes may be indicated by pincer-shaped curved arrows which may be complemented both by the number of electrons transferred from bond to bond from the reactant to the product and by labels indicating the respective time-sequences. These time-sequences of the electronic bond-to-bond fluxes associated with bond making and bond breaking are shown to depend on the preparation of the reactant. In particular, the corresponding electronic fluxes are synchronous when the reaction occurs at cryogenic temperatures corresponding to tunneling, whereas they are asynchronous when the reaction is induced by ultrashort laser pulses, both of which is simulated in this thesis. Analysis of the corresponding nuclear flux densities shows for instance for the tunneling scenario the phenomenon of increasing nuclear flux density with decreasing nuclear density, such that the nuclear flux density has its maximum at the potential barrier of the underlying symmetric double well potential energy surface. The error robustness of the results is tested and confirmed in detail, including the investigation of the effect of nuclear motion on the synchronicity of the electronic bond-to-bond fluxes. Motivated by the rich electron-nuclear flux phenomena in pericyclic reactions, discovered in the first part of the results of this thesis, the second part involves two further studies on experimentally readily accessible molecular systems: The first study involves a time-dependent analysis of electronic fluxes during large amplitude vibrations of single, double and triple bonds and is partly motivated by the objective to gain further insight into double-bond-shifting and bond making and bond breaking studied in the first part of this thesis. This time-dependent analysis reveals that in general, the number of electrons participating in the concerted electron-nuclear vibrations decreases from ethane via ethene to ethyne. These counter-intuitive results should stimulate the transfer of experiments from the domain of non-adiabatic attosecond electron dynamics to the domain of adiabatic single-state electron dynamics, ubiquitous in thermal chemistry. Such attosecond experiments have already been carried out for ethane and involve the preparation of the molecular system at sufficiently high energies allowing electronic transitions. Finally, interesting observations made in the detailed analysis of the nuclear flux densities in the degenerate Cope rearrangement of semibullvalene in the laser-induced scenario, lead to the extension of wave packet interferometry from nuclear densities, which was recently studied experimentally for the diatomic molecule I_2, to nuclear flux densities. Specifically, taking I_2 as particular example, it is shown that the interferences in the nuclear densities, manifested as a chain of lobe-shaped structures of these densities corresponding to a finite set of bond lengths of the molecule, also appear in the nuclear flux densities, with chains of lobes corresponding

to alternating bond stretches and bond compressions.

Kurzfassung

In der Chemie wird die mit der Bewegung der Atomkerne einhergehende Umlagerung der Elektronen typischerweise durch gebogene Pfeile skizziert, welche in die Lewis Strukturen der Reaktanten eingebettet sind, und die mit Bindungsbrüchen, Bindungsbildungen und Verschiebungen von spezifischen Doppelbindungen verbundene Verlagerung von Valenzelektronen anzeigen. In dieser Arbeit wird molekulare Quantendynamik erweitert und mit solchen traditionellen, qualitativen Beschreibungen in Beziehung gebracht, was zu neuen Erkenntnissen in adiabatische chemische Prozesse durch die zugrunde liegenden gekoppelten quantenmechanischen Flüsse der Kerne und Elektronen führt. Solche Prozesse umfassen die kollektive Umlagerung von Elektronen und Atomkernen in spezifischen elektronischen Zuständen und werden in dieser Arbeit für eine pericyclische Reaktion, die entartete [3,3]-sigmatrope Umlagerung (entartete Cope Umlagerung) von Semibullvalen im nicht entarteten elektronischen Grundzustand, beispielhaft dargestellt. Im Einzelnen wird gezeigt, dass die Direktionalität der Elektronenflüsse zwischen benachbarten Bindungen durch zangenförmige gebogene Pfeile beschrieben werden kann. Diese Pfeile können sowohl durch die Anzahl der zwischen den Bindungen vom Reaktanten zum Produkt übertragenen Elektronen als auch durch Symbole, welche die zeitliche Abfolge der entsprechenden Elektronenflüsse beschreiben, ergänzt werden. Es wird gezeigt, dass die zeitliche Abfolge der mit dem Bindungsbruch und der Bindungsbildung einhergehenden Elektronenflüsse von der Präparation des Reaktanten abhängt. Im Speziellen sind diese Elektronenflüsse synchron, wenn die Reaktion bei tiefen Temperaturen abläuft (Tunnelfall), wohingegen die Flüsse asynchron verlaufen, sofern die Reaktion durch ultrakurze Laserpulse initiiert wird. Beide Szenarien werden in dieser Arbeit simuliert. Die Analyse der zugehörigen Kernflussdichten zeigt unter anderem für den Tunnelfall das Auftreten von zunehmender Kernflussdichte mit abnehmender Kerndichte, so dass die Kernflussdichte das Maximum an der Potenzialbarriere des zugrunde liegenden symmetrischen Doppelmuldenpotenzials aufweist. Die Fehlerrobustheit dieser Ergebnisse wird im Detail getestet und bestätigt, was eine Untersuchung des Einflusses der Kernbewegung auf die Synchronizität der Elektronenflüsse zwischen benachbarten Bindungen beinhaltet. Motiviert durch die reichhaltigen Phänomene der Elektronen- und Kernflüsse in pericyclischen Reaktionen, welche im ersten Teil der Resultate dieser Arbeit entdeckt wurden, beinhaltet der zweite Teil dieser Arbeit zwei weitere Untersuchungen an experimentell leicht zugänglichen molekularen Systemen: Die erste Untersuchung umfasst die zeitabhängige Analyse von Elektronenflüssen bei großamplitudigen Schwingungen von Einfach-, Zweifach- und Dreifachbindungen und ist zum Teil durch das Ziel motiviert tieferen Einblick in den Ablauf der Verschiebung von Doppelbindungen, sowie in die Bildung und den Bruch von Bindungen, welche im ersten Teil dieser Arbeit untersucht wurden, zu erlangen. Diese zeitabhängige Analyse zeigt, dass die Anzahl der Elektronen, welche bei den gemeinsamen Kern- und Elektronenschwingungen beteiligt sind, von Ethan über Ethen zu Ethin abnimmt. Diese der Intuition widersprechenden Ergebnisse sollten den Transfer von Experimenten aus dem Bereich der nicht-adiabatischen Attosekunden-Elektronendynamik in den Bereich der in der thermischen Chemie allgegenwärtigen adiabatischen, einen elektronischen Zustand umfassenden, Elektronendynamik motivieren. Solche Attosekunden-Experimente, welche die Präparation des molekularen Systems bei genügend hohen Energien voraussetzt, so dass es zu elektronischen Übergängen kommt, wurden bereits für Ethan durchgeführt. Abschließend führten interessante Beobachtungen bei der de-

taillierten Analyse der Kernflussdichten während der entarteten Cope Umlagerung von Semibullvalen beim laserinduzierten Szenario zu der Erweiterung der Wellenpaket-Interferometrie von Kerndichten, welche kürzlich experimentell für das zweiatomige Molekül I_2 untersucht wurde, zu Kernflussdichten. Im Speziellen wird am Beispiel des I_2 Moleküls gezeigt, dass die Interferenzen in den Kerndichten, welche sich durch eine Kette von "lappenartigen" Strukturen der Kerndichten manifestieren, ebenfalls in den Kernflussdichten auftreten. Im ersten Fall entspricht die Kette von lappenartigen Strukturen einem begrenzten Satz an Bindungslängen des Moleküls, während diese Kette im zweiten Fall dem alternierenden Ausdehnen und Zusammenziehen der molekularen Bindung entspricht.

List of Publications[1,2]

First Part: Electron-Nuclear Quantum Fluxes in Pericyclic Reactions, Exemplified for the Cope Rearrangement of Semibullvalene

T1 D. Andrae, I. Barth, T. Bredtmann*, H.-C. Hege, J. Manz*, F. Marquardt, B. Paulus
Electronic Quantum Fluxes during Pericyclic Reactions Exemplified for the Cope Rearrangement of Semibullvalene
J. Phys. Chem. B, **115**, 5476-5483 (2011)
DOI: 10.1021/jp110365g
URL: http://dx.doi.org/10.1021/jp110365g

T2 T. Bredtmann*, J. Manz*
Quantum Control of the Initiation of a Pericyclic Reaction in the Electronic Ground State
J. Chem. Sci., **124**, 121-129 (2012)
DOI: 10.1007/s12039-011-0199-8
URL: http://dx.doi.org/10.1007/s12039-011-0199-8

T3 T. Bredtmann*, J. Manz*
Electronic Bond-to-Bond Fluxes in Pericyclic Reactions: Synchronous or Asynchronous?
Angew. Chem. Int. Ed., **50**, 12652-12654 (2011)
DOI: 10.1002/anie.201104465
URL: http://dx.doi.org/10.1002/anie.201104465

T4 T. Bredtmann*, H. Kono, J. Manz*, K. Nakamura*, C. Stemmle
Nuclear Flux Densities during a Model Pericyclic Reaction with Energies Well Above and Below the Potential Barrier
ChemPhysChem, **14**, 1397-1404 (2013)
DOI: 10.1002/cphc.201200943
URL: http://dx.doi.org/10.1002/cphc.201200943

T5 T. Bredtmann*, B. Paulus
Electron-Nuclear Motion in the Cope Rearrangement of Semibullvalene: Ever Synchronous?
J. Chem. Theor. Comput., **9**, 3026-3034 (2013)
DOI: 10.1021/ct400318z
URL: http://dx.doi.org/10.1021/ct400318z

[1]Refs. [T1] and [T3] highlighted as *publication of the month* at the Institute of Chemistry and Biochemistry, Free University Berlin, in June 2011 and December 2011, respectively.
[2]Publications with Prof. Dr. J. Manz in alphabetical order, corresponding author(s) marked by asterisk.

Second Part: Analysis of Electronic Fluxes and Nuclear Flux Densities in Experimentally Readily Accessible Molecular Systems

T6 T. Bredtmann*, E. Hupf, B. Paulus
Electronic Fluxes during Large Amplitude Vibrations of Single, Double and Triple Bonds
Phys. Chem. Chem. Phys., **14**, 15494-15501 (2012)
DOI: 10.1039/C2CP42494K
URL: http://dx.doi.org/10.1039/C2CP42494K

T7 T. Bredtmann, H. Katsuki, J. Manz*, K. Ohmori, C. Stemmle*
Wavepacket Interferometry for Nuclear Densities and Flux Densities
Mol. Phys., **111**, 1691-1696 (2013)
DOI: 10.1080/00268976.2013.780103
URL: http://dx.doi.org/10.1080/00268976.2013.780103

Additional Publications

B1 T. Bredtmann*, S. Chelkowski, A. D. Bandrauk, Monitoring attosecond dynamics of coherent electron-nuclear wave packets by molecular high-order-harmonic generation,
Phys. Rev. A **84**, 021401(R) (2011).

B2 S. Chelkowski*, T. Bredtmann, A. D. Bandrauk, High-order-harmonic generation from coherent electron wave packets in atoms and molecules as a tool for monitoring attosecond electrons,
Phys. Rev. A, **85**, 033404 (2012).

B3 T. Bredtmann*, S. Chelkowski, A. D. Bandrauk, Effect of Nuclear Motion on Molecular High Order Harmonic Pump Probe Spectroscopy,
J. Phys. Chem A, **116**, 11398 (2012).

B4 A. D. Bandrauk*, T. Bredtmann, S. Chelkowski, Attosecond Dynamics of Coherent Electron-Nuclear Wave Packets,
in Progress in Ultrafast Intense Laser Science, edited by K. Yamanouchi and K. Midorikawa, pages 33-54, Springer Tokyo, 2013.

Contents

1 Introduction

Chemical reactions and molecular vibrations involve the correlated motion of nuclei and electrons. The real-time observation and control of the nuclear dynamics using ultrashort laser sources with pulse durations on the order of 10-100 femtoseconds (fs, $1\mathrm{fs} = 10^{-15}\,\mathrm{s}$) constitutes the established field of *Femtochemistry*, pioneered by A. H. Zewail and co-workers [1], see also Refs. [2, 3]. More recently, new ultrashort pulse technologies, e.g. time-resolved photoelectron spectroscopy [4], time-resolved X-ray methods [5], high harmonic spectroscopy [6–10], also enabled monitoring changes of the electronic structure in real-time. These changes might roughly be divided into two regimes: On the one hand, non-adiabatic multi-state electron dynamics, i.e. preparation of the atomic or molecular systems at sufficiently high energies allowing electronic transitions, leads to electronic motion on the attosecond (as, $1\mathrm{as} = 10^{-18}\,\mathrm{s}$) timescale, which has recently been studied both experimentally and theoretically, see e.g. Refs. [11–13] and [11, 14–28]+[B1-B4], respectively. Such investigations provide mechanistic insight into photochemical processes. On the other hand, time-dependent adiabatic processes involve the collective rearrangement of both electrons and nuclei in specific electronic quantum states, most commonly the non-degenerate electronic ground state. The latter case, ubiquitous in organic, inorganic and biochemistry, see e.g. Refs. [29–35], corresponds to the thermal regime and is studied in this thesis. In particular, it is shown that the quantum dynamical evaluation and analysis of the corresponding electronic and nuclear quantum fluxes provides quantitative insight into these adiabatic processes. The reader is referred to Refs. [14, 15] and [16, 21, 25] for investigations of electronic quantum fluxes involving degenerate and quasi-degenerate excited electronic states, respectively, as well as to Refs. [18, 19] for analyses of multi-state non-adiabatic electron dynamics coupled to semiclassical Ehrenfest nuclear motion in terms of electronic quantum fluxes.

For several decades, calculations of nuclear quantum fluxes through a dividing surface which separates the domains associated with reactants and products are used for ab-initio calculations of chemical reaction rates [36–40]. Furthermore, analysis of the underlying nuclear current densities was shown to provide mechanistic insight into nuclear rearrangements, exemplified for a double proton transfer reaction [41]. The corresponding evaluation of electronic quantum fluxes in adiabatic processes involving non-degenerate electronic states routinely calculated within the Born-Oppenheimer (BO) approximation [42–44], however, is complicated by technical difficulties concerning their calculation in terms of BO wave functions, see Refs. [45–52], and section 2.1.1 in this thesis. Hence, most of the mechanistic insight into the electronic motion in such adiabatic chemical processes is based on qualitative rules predicting the net outcome of the reaction. Typically, electronic rearrangement accompanying nuclear motion is sketched by curved arrows embedded in the Lewis structure of the reactant, indicating the net transfer of valence electrons associated with bond making, bond breaking and shifting of specific multiple bonds, see e.g. Refs. [29–31, 34, 35]. Figure 1.1 underlines the ambiguity of such qualitative

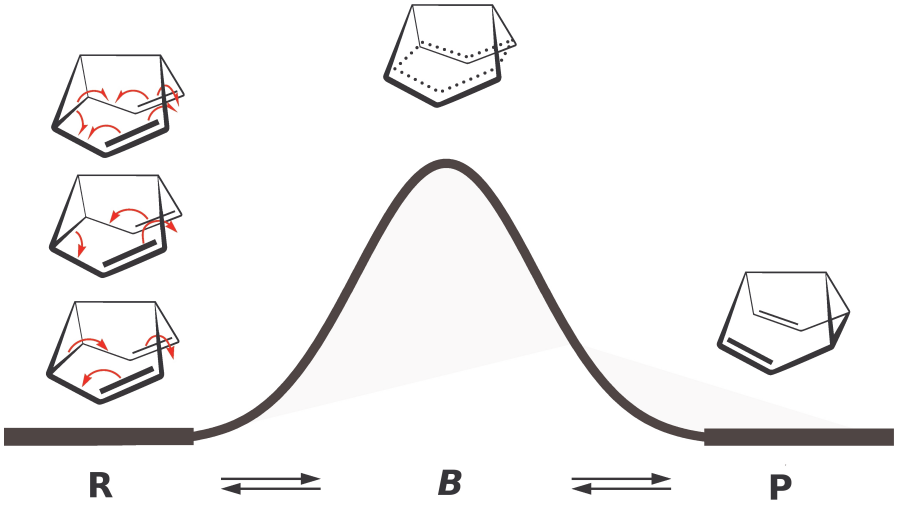

Figure 1.1: Lewis structures for the degenerate Cope rearrangement of semibullvalene from the reactant (R) over the potential barrier (B) to the product (P). In the reactant structure, the pincer-shaped (top), counter-clockwise (middle) and clockwise (bottom) curved arrows in red all symbolize the same net electron transfer.

representations exemplified for the degenerate Cope rearrangement (DCR) of semibullvalene (SBV). According to convention, single headed arrows indicate the rearrangement of single valence electrons (topmost depiction on the left), while double headed arrows indicate the rearrangement of valence electron pairs (middle and bottommost depiction on the left). Thus, one of the objectives of this thesis is to complement such traditional, well established depictions of chemical reactions, yielding deeper insight into such processes based on molecular quantum dynamics. For this purpose, the approach proposed in Ref. [53] and applied to the molecular ion H_2^+ for the calculation of electronic and nuclear quantum fluxes through dividing surfaces, also referred to as observer planes, situated within the molecule, see section 2.1.1 for details, is extended to larger systems, i.e. the DCR of SBV and to vibrating molecules representing single, double and triple bonds. In parallel to this thesis, the same method has also been applied to further studies of the single electron system H_2^+ and its heavier isotopes [54, 55], to probing electron correlation in the H_2 molecule [56], to tunneling in cyclo-octatetraene [57] and to the dynamics along the Kekulé mode of benzene [58]. The reader is also referred to Refs. [45–52] for the calculation of electronic current densities in adiabatic processes, which have, however, so far been limited to the single electron system H_2^+ [47–49, 51, 52] or to classical [50] or semiclassical [46] nuclear motion.

The first part of the results of this thesis deals with the mechanism of pericyclic reactions [29–31], exemplified for the DCR of SBV, Figure 1.1. This degenerate [3,3]-sigmatropic shift and its derivatives have been extensively studied both experimentally and theoretically since the first preparation of the parent compound in 1966 by Zimmerman et. al [59, 60], see e.g. Refs. [61–71] and [68–83], respectively. These investigations focused mainly on its thermochromicity [64, 66, 67, 70, 74], quantum dynamics simulation of its laser control [73–75], as well as on the

bishomoaromatic character of the transition state (TS) and its stabilization with respect to the reactant and product by appropriate substitution of the parent compound, see e.g. Refs. [68–70, 76, 78, 79, 81, 83] and Ref. [71] for a recent experimental realization of a bishomoaromatic ground state. The issues addressed here are for instance the quantification of the electron number participating in the electronic bond-to-bond-fluxes including their directionality, the time scales of the electronic rearrangement from reactants (R) to products (P) as well as the synchronicity of these fluxes [T1,T3,T5]. The latter issue, in particular the synchronicity of bond making and bond breaking in pericyclic reactions, has been debated for almost three decades in the literature with the sole focus on the nuclear rearrangement [84–88]. In this thesis, the analogous question of the synchronicity of the electronic bond-to-bond-fluxes associated with bond making and bond breaking is addressed, with special emphasis on concerted effects with nuclear motion. Different scenarios, i.e. preparation of the reactants with energies E well above and below the potential barrier B are compared [T1,T3], including a detailed discussion of the nuclear flux densities [T4]. The former scenario ($E > B$) may be initialized by ultrashort laserpulses as shown experimentally for the Claison rearrangement of allyl vinyl ether [89] and allyl phenyl ether [90] and applied in this thesis in the framework of Optimal Control Theory [T2]; see Refs. [91–99] and section 2.3.4. The latter scenario ($E < B$) corresponds to coherent tunneling which was previously shown to occur within 970 s [80]. The robustness of the discovered counter-intuitive results with respect to the employed quantum chemical method, to the observer planes used to monitor the electron-nuclear fluxes, and with respect to different paths along the potential energy surface (PES) for the reaction above the potential barrier, is tested and confirmed in detail [T5].

Motivated by the rich electron-nuclear flux phenomena discovered in pericyclic reactions, exemplified for the DCR of SBV, the second part of the results of this thesis involves two further studies on experimentally easier accessible systems. In particular, the study on electronic fluxes during large amplitude vibrations of single, double and triple bonds [T6] was partly motivated by the objective to gain further insight into the involved process of double-bond-shifting and bond making and bond breaking studied in the first part of this thesis [T1,T3,T5], c.f. Figure 1.1. This investigation extends well-established bond-analyses in the electronic ground state focusing primarily on stationary states on the PES [100–103] to the time-dependent domain including nuclear quantum motion. The reader is also referred to Refs. [104,105] for time-dependent bond-analysis involving non-adiabatic multi-state electron dynamics. Another motivation are recent experiments on one of the investigated compounds (ethane), which involve measurements of the multi-state electron dynamics on the attosecond time-scale using High Harmonic Spectroscopy [13]. The results presented here should stimulate corresponding experimental investigations in the regime of adiabatic single-state dynamics occurring in the non-degenerate electronic ground state.

The last study presented in this thesis [T7] deals with the extension of wave packet interferometry from nuclear densities [106–130] to nuclear flux densities, exemplified for the diatomic I_2. Again, these investigations are motivated by discoveries made in the analysis of nuclear fluxes in the DCR of SBV [T4], see also Ref [131]. In wave packet interferometry, starting from the vibrational ground state of the electronic ground state, typically two coherent, non-overlapping, time-delayed laser pulses excite successively two nuclear wave packets in a bound excited electronic state. These wave packets in the excited electronic state may overlap coherently, causing

quantum interferences. Optimization of specific laser parameters like the central laser frequency, the carrier envelope phase, or the time-delay between the two pulses, see section 2.3.3 for details, may result in quantum carpets [132,133] or quantum ripples [128,130]: In these structures, alternating constructive and destructive interferences enhance or extinguish the resulting nuclear densities of the total vibrational wave packet in the excited electronic state. These nuclear densities may thus appear as a set of lobes corresponding to a finite set of bond lengths of the molecule in the excited electronic state. The main goal of the study presented here is to show that an analogous chain of lobes with alternating signs equally exists in the nuclear flux densities, corresponding to alternating bond stretches and bond compressions.

This thesis is structured as follows: Chapter 2 describes the theoretical foundations, on which the numerical quantum dynamical simulations presented in this thesis are based. The separation of electronic and nuclear motion within the Born-Oppenheimer approximation is presented in section 2.1 including a discussion of its validity and extensions, which are important for investigations on electron-nuclear fluxes going beyond this thesis outlined in the outlook, Chapter 5. Technical aspects of the involved calculation of electron-nuclear fluxes from Born-Oppenheimer wave functions are discussed in section 2.1.1. Various approximate numerical solutions of the time-independent electronic Schrödinger equation used in this thesis are discussed in section 2.2. Although a full description of the technical details involved in the implementations of these quantum chemical methods into the employed program packages [134,135] is not possible in the framework of this *Theory Part*, in depth discussions of certain fundamental methods and concepts are given where it is deemed to be important by the author. Finally, section 2.3 deals with the numerical solution of the time-independent (section 2.3.1) and time-dependent (section 2.3.2) nuclear Schrödinger equation. The interaction of molecular systems with ultrashort laser-pulses is discussed in section 2.3.3 followed by a description of Optimal Control Theory, section 2.3.4, an algorithm to generate an optimal laser field to reach a given "target state" from a predefined initial state. Section 2.4 closes this *Theory Part* presenting the model for the simulation of the nuclear quantum dynamics used in Refs. [T1-T5] including extensions presented in Chapter 5.

Chapter 3 gives the results in the form of the published journal articles [T1-T7]. These results are summarized in a unifying framework in Chapter 4 and an outlook is given in Chapter 5. The Appendix, Chapter 6, gives additional details of functional derivatives (section 6.1) as well as of Hartree-Fock theory (section 6.2), including a comparison to Density Functional Theory.

2 Molecular Quantum Dynamics

The time-evolution of a molecular quantum system interacting with an external field is given in the non-relativistic case by the *time-dependent Schrödinger equation* (TDSE)[1] [138–142]

$$i\frac{\partial}{\partial t}\Psi(\mathbf{q},\mathbf{Q},t) = \hat{H}(\mathbf{r},\mathbf{R},t)\Psi(\mathbf{q},\mathbf{Q},t), \tag{2.1}$$

where $\mathbf{r}$ and $\mathbf{R}$ denote the set of electronic and nuclear spatial coordinates, respectively, and $\mathbf{q}$ and $\mathbf{Q}$ collectively denote the set of spatial and spin coordinates of the N electrons, $\mathbf{q} = \{\mathbf{r}, \boldsymbol{\sigma}\}$, and the M nuclei, $\mathbf{Q} = \{\mathbf{R}, \boldsymbol{\Sigma}\}$. The molecular wave function $\Psi(\mathbf{q},\mathbf{Q},t)$, which completely describes the molecular system, obeys the *antisymmetry principle*, i.e. it must be invariant to any permutation of identical bosons in the molecule and to any even permutation of identical fermions, but will be changed in sign by an odd permutation of identical fermions [143–145]. Hence, in the non-relativistic quantum mechanical treatment used throughout this thesis, the electronic and nuclear spin as well as the antisymmetry principle are accounted for as additional requirements on the molecular wave function, $\Psi(\mathbf{q},\mathbf{Q},t)$, whereas the Hamilton operator, $\hat{H}(\mathbf{r},\mathbf{R},t)$, makes no reference to spin, which is explicitly indicated by the notation used in eqn. (2.1) and in the following.

The Hamiltonian $\hat{H}(\mathbf{r},\mathbf{R},t)$ is the sum of the time-independent molecular Hamiltonian $\hat{H}_{\mathrm{mol}}(\mathbf{r},\mathbf{R})$ and the time-dependent interaction Hamiltonian $\hat{H}_{\mathrm{int}}(t)$:

$$\hat{H}(\mathbf{r},\mathbf{R},t) = \hat{H}_{\mathrm{mol}}(\mathbf{r},\mathbf{R}) + \hat{H}_{\mathrm{int}}(t). \tag{2.2}$$

The explicit form of the molecular Hamiltonian, $\hat{H}_{\mathrm{mol}}(\mathbf{r},\mathbf{R})$, for N electrons and M nuclei, is given by

$$\begin{aligned}\hat{H}_{\mathrm{mol}}(\mathbf{r},\mathbf{R}) = &\underbrace{-\sum_{i=1}^{N}\frac{1}{2}\boldsymbol{\nabla}_{\mathbf{r}_i}^2}_{\hat{T}_{\mathrm{el}}(\mathbf{r})} \underbrace{-\sum_{A=1}^{M}\frac{1}{2M_A}\boldsymbol{\nabla}_{\mathbf{R}_A}^2}_{\hat{T}_{\mathrm{nuc}}(\mathbf{R})} \underbrace{-\sum_{i=1}^{N}\sum_{A=1}^{M}\frac{Z_A}{|\mathbf{r}_i-\mathbf{R}_A|}}_{\hat{V}_{\mathrm{el-nuc}}(\mathbf{r},\mathbf{R})} \\ &\underbrace{+\sum_{i=1}^{N-1}\sum_{j>i}^{N}\frac{1}{|\mathbf{r}_i-\mathbf{r}_j|}}_{\hat{V}_{\mathrm{el-el}}(\mathbf{r})} \underbrace{+\sum_{A=1}^{M-1}\sum_{B>A}^{M}\frac{Z_A Z_B}{|\mathbf{R}_A-\mathbf{R}_B|}}_{\hat{V}_{\mathrm{nuc-nuc}}(\mathbf{R})},\end{aligned} \tag{2.3}$$

where Z_A is the atomic number of nucleus A, and M_A is the ratio of the mass of nucleus A to the mass of an electron. The Laplacian operators $\boldsymbol{\nabla}_{\mathbf{r}_i}^2$ and $\boldsymbol{\nabla}_{\mathbf{R}_A}^2$ involve differentiation with

[1] Atomic units [136,137] are used throughout this thesis.

respect to the spatial coordinates of the i-th electron and the A-th nucleus, respectively. The first term in eqn. (2.3), $\hat{T}_{\rm el}(\mathbf{r})$, is the operator for the kinetic energy of the electrons; the second term, $\hat{T}_{\rm nuc}(\mathbf{R})$, is the operator for the kinetic energy of the nuclei; the third term, $\hat{V}_{\rm el-nuc}(\mathbf{r},\mathbf{R})$, involves the Coulomb attraction between electrons and nuclei and the fourth and fifth terms, $\hat{V}_{\rm el-el}(\mathbf{r})$ and $\hat{V}_{\rm nuc-nuc}(\mathbf{R})$, represent the repulsion between electrons and nuclei, respectively, see e.g. Ref. [136,142]. For the explicit form of the interaction Hamiltonian, $\hat{H}_{\rm int}(t)$, eqn. (2.2), the reader is referred to section 2.3.3.

The time-dependent Schrödinger equation, eqn. (2.1), can only be solved in so-called *exact numerical calculations* for molecular systems containing up to two electrons, see for example Refs. [11, 53] and [B1-B4]. Consequently, for the numerical treatment of the molecular systems investigated in this thesis, numerous approximations have to be invoked, starting with the separation of the electronic and nuclear motion presented in the next section.

2.1 Separation of Electronic and Nuclear Motion: The Born-Oppenheimer Approximation

The separability of electronic and nuclear motion relies on the different masses of the underlying particles and hence on their different velocities. In this section it will be shown that in the case of electronic states which are well separated energetically from other electronic states to which they may couple, the electrons can instantly adjust to the slow nuclei and, consequently, their wave function depends parametrically on the nuclear coordinates. Thus in these special cases, the electronic and nuclear problem can be solved separately, which allows the solution of equation (2.1) for a broad range of molecules of chemical interest. The description given in this section follows Refs. [146] and [147]. For a historical approach, see the classical paper by Max Born and Julius Robert Oppenheimer, Ref. [42].

Setting the nuclear kinetic energy operator $\hat{T}_{\rm nuc}(\mathbf{R})$ in the molecular Hamiltonian, $\hat{H}_{\rm mol}(\mathbf{r},\mathbf{R})$, eqn. (2.3), equal to zero, and omitting additionally the repulsion between the nuclei $\hat{V}_{\rm nuc-nuc}(\mathbf{R})$, one obtains the *electronic Hamiltonian* [136,137]

$$\hat{H}_{\rm el}(\mathbf{r};\mathbf{R}) = \hat{T}_{\rm el}(\mathbf{r}) + \hat{V}_{\rm el-nuc}(\mathbf{r};\mathbf{R}) + \hat{V}_{\rm el-el}(\mathbf{r}), \tag{2.4}$$

which depends parametrically on the set of nuclear coordinates $\mathbf{R}$. This is expressed by usage of the semicolon. For each fixed nuclear conformation $\mathbf{R}$, the electronic wave functions $\Phi_{\rm i}(\mathbf{q};\mathbf{R})$ and electronic eigenvalues $E_{\rm i}(\mathbf{R})$ of electronic state i are found from the *time-independent electronic Schrödinger equation*[2]

$$\hat{H}_{\rm el}(\mathbf{r};\mathbf{R})\Phi_i(\mathbf{q};\mathbf{R}) = E_i(\mathbf{R})\Phi_i(\mathbf{q};\mathbf{R}). \tag{2.5}$$

The solution of eqn. (2.5) falls into the field of *Quantum Chemistry* or, more specifically, *Molecular Electronic Structure Theory* [136,137,148–151], for details see section 2.2. The electronic

[2]Note that the electronic wave functions $\Phi_i(\mathbf{q};\mathbf{R})$ and consequently the electronic eigenvalues $E_i(\mathbf{R})$ do not depend on nuclear spin, which may, however, been taken into account through the nuclear wave function, c.f. eqn. (2.10) below.

eigenvalues, $E_i(\mathbf{R})$, together with the nuclear-nuclear repulsion term, $\hat{V}_{\mathrm{nuc-nuc}}(\mathbf{R})$, form the adiabatic potential energy surface associated with electronic state i according to

$$V_i(\mathbf{R}) = E_i(\mathbf{R}) + \hat{V}_{\mathrm{nuc-nuc}}(\mathbf{R}). \tag{2.6}$$

As eigenfunctions of the Hermitian operator $\hat{H}_{\mathrm{el}}(\mathbf{r};\mathbf{R})$, the set of eigenfunctions $\{\Phi_i(\mathbf{q};\mathbf{R})\}$ forms a complete basis in the electronic space at every value of $\mathbf{R}$,

$$\sum_i \Phi_i^*(\mathbf{q}';\mathbf{R})\Phi_i(\mathbf{q};\mathbf{R}) = \delta(\mathbf{q}-\mathbf{q}') \tag{2.7}$$

with the orthonormality condition

$$\int \Phi_j^*(\mathbf{q};\mathbf{R})\Phi_i(\mathbf{q};\mathbf{R})\mathrm{d}\mathbf{q} \equiv \langle\Phi_j|\Phi_i\rangle = \delta_{ji}, \tag{2.8}$$

where the integration is over the whole set of electronic spatial and spin coordinates and the Dirac notation was introduced [142]. Accordingly, matrix elements of an operator $\hat{O}(\mathbf{r};\mathbf{R})$ in the basis of electronic wave functions are written as

$$\int \Phi_j^*(\mathbf{q};\mathbf{R})\hat{O}(\mathbf{r};\mathbf{R})\Phi_i(\mathbf{q};\mathbf{R})\mathrm{d}\mathbf{q} = \langle\Phi_j|\hat{O}|\Phi_i\rangle. \tag{2.9}$$

In order to solve the time-dependent Schrödinger equation describing electronic *and* nuclear movement, eqn. (2.1), the molecular wave function $\Psi(\mathbf{q},\mathbf{Q},t)$ is expanded in the complete set of electronic eigenfunctions $\{\Phi_i(\mathbf{q};\mathbf{R})\}$:

$$\Psi(\mathbf{q},\mathbf{Q},t) = \sum_i \chi_i(\mathbf{Q},t)\Phi_i(\mathbf{q};\mathbf{R}), \tag{2.10}$$

where the time-dependent nuclear wave functions, which act as the expansion coefficients, are denoted by $\chi_i(\mathbf{Q},t)$. This expansion is known as the *Born-representation* or *the Born-Oppenheimer expansion* [44] which is a formally exact ansatz when the molecular wave function describes a bound state solution of the Schrödinger equation, eqn. (2.1) [146]. Doubts have been expressed as to its validity for the description of continuum states, but it can be reasonably argued that even in these cases it is justified [146,147].

Inserting the Born-representation, eqn. (2.10), into the time-dependent Schrödinger equation, eqn. (2.1), multiplying from the left by $\Phi_j^*(\mathbf{q};\mathbf{R})$ and integrating over the set of electronic coordinates $\mathbf{q}$ and the set of nuclear spin-coordinates $\mathbf{\Sigma}$[3], leads to a set of coupled equations of motion for the nuclear wave functions

$$i\frac{\partial\chi_j(\mathbf{R},t)}{\partial t} = \left[\hat{T}_{\mathrm{nuc}}(\mathbf{R}) + V_j(\mathbf{R})\right]\chi_j(\mathbf{R},t) + \sum_i \hat{\Lambda}_{ji}(\mathbf{R})\chi_i(\mathbf{R},t). \tag{2.11}$$

[3] Quantum dynamical processes in symmetric molecules involving the exchange of identical nuclei, e.g. molecular rotation or molecular torsion, see e.g. Refs. [152,153] and references therein, is influenced by the nuclear spin. Since such processes are not considered in this thesis, the dependence of the nuclear wave function on nuclear spin will be omitted in the following.

Here, the non-adiabatic coupling operators $\hat{\Lambda}_{ji}(\mathbf{R})$ describe the dynamic interaction between the electronic and nuclear motion and are given by

$$\hat{\Lambda}_{ji}(\mathbf{R}) = \sum_A \frac{1}{2M_A}(2\underbrace{\langle\Phi_j|\boldsymbol{\nabla}_{\mathbf{R}_A}|\Phi_i\rangle}_{\hat{\mathbf{F}}^A_{ji}(\mathbf{R})}\boldsymbol{\nabla}_{\mathbf{R}_A} + \underbrace{\langle\Phi_j|\boldsymbol{\nabla}^2_{\mathbf{R}_A}|\Phi_i\rangle}_{\hat{G}^A_{ji}(\mathbf{R})}), \tag{2.12}$$

where the vectorial and scalar coupling operators were defined as $\hat{\mathbf{F}}^A_{ji}(\mathbf{R})$ and $\hat{G}^A_{ji}(\mathbf{R})$, respectively. Note that the scalar coupling operator $\hat{G}^A_{ji}$ can be expressed in terms of the vectorial coupling operators [146]

$$\hat{G}^A_{ji}(\mathbf{R}) = \langle\Phi_j|\boldsymbol{\nabla}^2_{\mathbf{R}_A}|\Phi_i\rangle = \boldsymbol{\nabla}_{\mathbf{R}_A}\hat{\mathbf{F}}^A_{ji}(\mathbf{R}) + \sum_k \hat{\mathbf{F}}^A_{ik}(\mathbf{R})\hat{\mathbf{F}}^A_{kj}(\mathbf{R}). \tag{2.13}$$

Since the non-adiabatic coupling operators $\hat{\Lambda}_{ji}(\mathbf{R})$ depend inversely on the quantities M_A, i.e. the ratio of the mass of nucleus A to the mass of an electron, one might expect their impact to be small. For a more involved analysis, the following expression for the vectorial coupling operators $\hat{\mathbf{F}}^A_{ji}$ may be obtained by applying first the gradient $\boldsymbol{\nabla}_{\mathbf{R}_A}$ with respect to nucleus A to the electronic Schrödinger equation, eqn. (2.5), followed by multiplication with $\Phi^*_j(\mathbf{q};\mathbf{R})$ from the left and integration over the set of electronic coordinates $\mathbf{q}$:

$$\hat{\mathbf{F}}^A_{ji}(\mathbf{R}) = \frac{\langle\Phi_j|(\boldsymbol{\nabla}_{\mathbf{R}_A}\hat{H}_{\text{el}}(\mathbf{r};\mathbf{R}))|\Phi_i\rangle}{\Delta V_{ij}(\mathbf{R})} \qquad \text{for} \qquad \text{i} \neq \text{j}, \tag{2.14}$$

where the denominator gives the energy gap between the electronic potential energy surfaces i and j, $\Delta V_{ij}(\mathbf{R}) = E_i(\mathbf{R}) - E_j(\mathbf{R}) = V_i(\mathbf{R}) - V_j(\mathbf{R})$, c.f. eqn. (2.6). Equation (2.14) is known as the off-diagonal form of the *Hellman-Feynman theorem* [146,147] which shows that the vectorial coupling operators $\hat{\mathbf{F}}^A_{ji}(\mathbf{R})$ - and hence the scalar coupling operators $\hat{G}^A_{ji}(\mathbf{R})$ and the non-adiabatic coupling terms $\hat{\Lambda}_{ji}(\mathbf{R})$, c.f. eqns. (2.13) and (2.12), respectively - depend inversely on the energy gap between the electronic states i and j. As the gap narrows, the coupling increases, outweighing the above mentioned mass factor, resulting in coupled nuclear motion on different electronic surfaces. Thus, a nuclear wave packet initially on one electronic surface will spread to another in a region where they are energetically close without losing energy, that is radiationless transitions can occur. In particular, in the presence of degeneracies of the potential energy surfaces $V_i(\mathbf{R})$ and $V_j(\mathbf{R})$ (conical intersections), the non-adiabatic derivative couplings $\hat{\mathbf{F}}^A_{ji}(\mathbf{R})$ diverge and the nuclear quantum dynamics is usually treated in the *diabatic representation*, for details see Refs. [147,154,155].

If, on the other hand, the considered electronic state is well separated energetically from other electronic states to which it may couple, eqn. (2.14) implies small non-diagonal derivative couplings $\hat{\mathbf{F}}_{ji}(\mathbf{R})$ and hence small non-diagonal non-adiabatic coupling operators $\hat{\Lambda}_{ji}(\mathbf{R})$, eqn. (2.12), and the coupled set of equations of motion, eqn. (2.11), reduces to

$$i\frac{\partial}{\partial t}\chi_i(\mathbf{R},t) = \left(\hat{T}_{\text{nuc}}(\mathbf{R}) + V_i(\mathbf{R}) - \hat{\Lambda}_{ii}(\mathbf{R})\right)\chi_i(\mathbf{R},t). \tag{2.15}$$

This equation is called the *Born-Oppenheimer approximation* [146,156]. It may also be obtained using the *adiabatic ansatz* [146,147] for the molecular wave function

$$\Psi_i^{\mathrm{BO}}(\mathbf{q},\mathbf{Q},t) = \chi_i(\mathbf{Q},t)\Phi_i(\mathbf{q};\mathbf{R}) \tag{2.16}$$

instead of the exact Born-representation, eqn. (2.10), by insertion of eqn. (2.16) into the time-dependent Schrödinger equation, eqn. (2.1), multiplying from the left by $\Phi_i^*(\mathbf{q};\mathbf{R})$ and integrating over the set of electronic coordinates $\mathbf{q}$ and the set of nuclear spin-coordinates $\mathbf{\Sigma}$. Hence, the adiabatic ansatz is valid if the electronic state i considered is energetically well separated from other electronic states. This implies a weak dependence of the electronic wave function $\Phi_i(\mathbf{q};\mathbf{R})$ on the nuclear coordinates $\mathbf{R}$, c.f. eqn. (2.12), which implies that the non-adiabatic term $\hat{\Lambda}_{ii}(\mathbf{R})$ is the smaller the better the adiabatic ansatz, eqn. (2.16), is [146]. Neglecting $\hat{\Lambda}_{ii}(\mathbf{R})$ in eqn. (2.15) leads to the *Born-Oppenheimer adiabatic approximation*, or briefly the *adiabatic approximation* [156]:

$$i\frac{\partial}{\partial t}\chi_i(\mathbf{R},t) = \underbrace{(\hat{T}_{\mathrm{nuc}}(\mathbf{R}) + V_i(\mathbf{R}))}_{\hat{H}_{\mathrm{nuc}}(\mathbf{R})}\chi_i(\mathbf{R},t). \tag{2.17}$$

The above discussion implies that as long as $\hat{\Lambda}_{ii}(\mathbf{R})$ is small, the usage of the Born-Oppenheimer approximation, eqn. (2.15), does provide an improvement to the adiabatic approximation, eqn. (2.17). However, once $\hat{\Lambda}_{ii}(\mathbf{R})$ becomes significant, the adiabatic ansatz, eqn. (2.16), and hence also the Born-Oppenheimer approximation, eqn. (2.15), breaks down [146,147].

In this thesis, molecular processes occurring on energetically isolated non-degenerate electronic states are considered. Hence, the adiabatic ansatz, eqn. (2.16), which will be referred to as Born-Oppenheimer (BO) wave function in the following, is used for the total wave function. Accordingly, the nuclear dynamics is evaluated within the Born-Oppenheimer adiabatic approximation, eqn. (2.17), since corrections associated with the diagonal coupling terms, eqns. (2.12) and (2.15), are expected to have a negligible impact on the corresponding electron-nuclear fluxes.

2.1.1 Electron-Nuclear fluxes from Born-Oppenheimer wave functions

The quantum mechanical evaluation of nuclear fluxes with dimension $1/time$ through *observer surfaces* separating the domains associated with the reactants and products, allow the ab-initio calculation of reaction rates [36–40]. The flux associated with nucleus k may be evaluated as surface integral over the vector field of the nuclear current density of nucleus k, $\mathbf{j}_k(\mathbf{R},t)$, with dimension $1/(time \times area)$, as

$$F_{\mathrm{nuc},k}(A_{\mathrm{obs}},t) = -\int_{A_{\mathrm{obs}}} \mathrm{d}\mathbf{A}\langle\mathbf{j}_{\mathrm{nuc},k}(\mathbf{R},t)\rangle. \tag{2.18}$$

Here, A_{obs} denotes the observer surface with unit normal vector $\mathbf{n}$, i.e. $\mathrm{d}\mathbf{A} = \mathbf{n}\mathrm{d}A$ [53]. Corresponding quantum mechanical analysis of the coupled electronic fluxes to obtain mechanistic details into chemical processes occurring in non-degenerate electronic states is, however, not straightforward due to technical problems concerning the extraction of electronic current densities and correspondingly electronic fluxes from BO wave functions, eqn. (2.16). Before describing

the approach developed in Ref. [53] and applied in this thesis to molecular processes of chemical interest, the problems associated with calculating electronic current densities from BO wave functions is illustrated using the example of the hydrogen atom in its electronic ground state moving through the laboratory. This illustration is adapted from Ref. [47], see also Refs. [50,157] for related investigations.

The vector field of the current density $\langle \mathbf{j}(\tilde{\mathbf{r}},t)\rangle$ for a *single particle system* with mass m is usually derived from the TDSE and the continuity equation,

$$\frac{\partial}{\partial t}|\psi(\tilde{\mathbf{r}},t)|^2 = -\boldsymbol{\nabla}_{\tilde{\mathbf{r}}}\langle \mathbf{j}(\tilde{\mathbf{r}},t)\rangle, \tag{2.19}$$

as

$$\langle \mathbf{j}(\tilde{\mathbf{r}},t)\rangle = \frac{1}{2im}\left[\psi^*(\tilde{\mathbf{r}},t)\boldsymbol{\nabla}_{\tilde{\mathbf{r}}}\psi(\tilde{\mathbf{r}},t) - \underbrace{\psi(\tilde{\mathbf{r}},t)\boldsymbol{\nabla}_{\tilde{\mathbf{r}}}\psi^*(\tilde{\mathbf{r}},t)}_{\text{c.c.}}\right], \tag{2.20}$$

where c.c. denotes the complex conjugate of the immediately preceding term, see for instance Refs. [141,142]. In analogy, for the *two particle system* hydrogen, the electronic and protonic probability current densities, $\langle \mathbf{j}_{\text{el}}(\mathbf{x},t)\rangle$ and $\langle \mathbf{j}_{\text{nuc}}(\mathbf{x},t)\rangle$, respectively, in the space-fixed coordinate frame, with $\mathbf{x}$ denoting the point of observation, are given by [47]

$$\langle \mathbf{j}_{\text{el}}(\mathbf{x},t)\rangle = \frac{1}{2i}\int \mathrm{d}\mathbf{r}_{\text{e}}\int \mathrm{d}\mathbf{R}_{\text{p}}\delta(\mathbf{x}-\mathbf{r}_{\text{e}})\left[\Psi^*(\mathbf{r}_{\text{e}},\mathbf{R}_{\text{p}},t)\boldsymbol{\nabla}_{\mathbf{r}_{\text{e}}}\Psi(\mathbf{r}_{\text{e}},\mathbf{R}_{\text{p}},t) - \text{c.c.}\right] \tag{2.21}$$

and

$$\langle \mathbf{j}_{\text{nuc}}(\mathbf{x},t)\rangle = \frac{1}{2iM_{\text{p}}}\int \mathrm{d}\mathbf{r}_{\text{e}}\int \mathrm{d}\mathbf{R}_{\text{p}}\delta(\mathbf{x}-\mathbf{R}_{\text{p}})\left[\Psi^*(\mathbf{r}_{\text{e}},\mathbf{R}_{\text{p}},t)\boldsymbol{\nabla}_{\mathbf{R}_{\text{p}}}\Psi(\mathbf{r}_{\text{e}},\mathbf{R}_{\text{p}},t) - \text{c.c.}\right]. \tag{2.22}$$

Here, $\mathbf{r}_{\text{e}}$ denotes the electronic position, $\mathbf{R}_{\text{p}}$ and M_{p} refer to the protonic position and mass, respectively, and δ designates the Dirac distribution [142].

The associated BO wave function for the H-atom in the electronic ground state is given by

$$\Psi_0^{\text{BO}}(\mathbf{r}_{\text{e}},\mathbf{R}_{\text{p}},t) = \Phi_0(\mathbf{r}_{\text{e}};\mathbf{R}_{\text{p}})\chi_0(\mathbf{R}_{\text{p}},t), \tag{2.23}$$

where $\Phi_0(\mathbf{r}_{\text{e}};\mathbf{R}_{\text{p}})$ is an eigenfunction of the associated electronic Hamiltonian, and $\chi(\mathbf{R}_{\text{p}},t)$ is a wave packet describing the motion of the proton, c.f. eqns. (2.5) and (2.16). Inserting eqn. (2.23) into eqn. (2.21) yields for non-degenerate electronic states

$$\langle \mathbf{j}_{\text{el}}(\mathbf{x},t)\rangle_{\text{BO}} = \frac{1}{2i}\int \mathrm{d}\mathbf{R}_{\text{p}}|\chi_0(\mathbf{R}_p,t)|^2\left[\Phi_0^*(\mathbf{r}_{\text{e}};\mathbf{R}_{\text{p}})\boldsymbol{\nabla}_{\mathbf{r}_{\text{e}}}\Phi_0(\mathbf{r}_{\text{e}};\mathbf{R}_{\text{p}}) - \text{c.c.}\right]_{\mathbf{r}_{\text{e}}=\mathbf{x}} = 0. \tag{2.24}$$

Hence, we obtain zero electronic current density within the Born-Oppenheimer approximation, because the BO electronic wave function, $\Phi_0^{\text{BO}}(\mathbf{r}_{\text{e}};\mathbf{R}_{\text{p}})$, is real for non-degenerate electronic states, which is the only situation regarded in this thesis. The reader is referred to Refs. [14,15] for the calculation of electronic current densities from BO wave functions in degenerate excited electronic states. For the nuclear current density, we obtain after insertion of eqn. (2.23) into eqn. (2.22)

$$\langle \mathbf{j}_{\text{nuc}}(\mathbf{x},t)\rangle_{\text{BO}} = \frac{1}{2iM_{\text{p}}}\left[\chi_0^*(\mathbf{R}_{\text{p}},t)\boldsymbol{\nabla}_{\boldsymbol{R}_{\text{p}}}\chi_0(\mathbf{R}_{\text{p}},t) - \text{c.c.}\right]_{\mathbf{R}_{\text{p}}=\mathbf{x}}, \tag{2.25}$$

which is the expected result, c.f. eqn. (2.20).

Since the electron is dragged along by the proton, eqn. (2.24) clearly is unphysical. In order to analyze this problem of missing electronic currents from BO wave functions, the exact treatment for the H-atom is given in the following: In the two-body Jacobi coordinates

$$\mathbf{R}_{\mathrm{com}} = \frac{(\mathbf{R}_{\mathrm{p}} M_{\mathrm{p}} + \mathbf{r}_{\mathrm{e}})}{M} \tag{2.26}$$

and

$$\mathbf{r}_{12} = \mathbf{r}_{\mathrm{e}} - \mathbf{R}_{\mathrm{p}}, \tag{2.27}$$

where $\mathbf{R}_{\mathrm{com}}$ denotes the center of mass (com) and $M = 1 + M_{\mathrm{p}}$ the total mass, the total wave function separates into

$$\Psi(\mathbf{r}_{\mathrm{e}}, \mathbf{R}_{\mathrm{p}}) = \tilde{\chi}_0(\mathbf{R}_{\mathrm{com}}, t)\tilde{\Phi}_0(\mathbf{r}_{12}). \tag{2.28}$$

Using eqn. (2.28), and the relations

$$\boldsymbol{\nabla}_{\mathbf{r}_{\mathrm{e}}} = \frac{1}{M}\boldsymbol{\nabla}_{\mathbf{R}_{\mathrm{com}}} + \boldsymbol{\nabla}_{\mathbf{r}_{12}} \tag{2.29}$$

and

$$\boldsymbol{\nabla}_{\mathbf{R}_{\mathrm{p}}} = \frac{M_{\mathrm{p}}}{M}\boldsymbol{\nabla}_{\mathbf{R}_{\mathrm{com}}} - \boldsymbol{\nabla}_{\mathbf{r}_{\mathrm{e}}}, \tag{2.30}$$

eqns. (2.21) and (2.22) become

$$\langle \mathbf{j}_{\mathrm{el}}(\mathbf{x}, t)\rangle = \frac{M^2}{2iM_{\mathrm{p}}^3}\int \mathrm{d}\mathbf{R}_{\mathrm{p}} |\tilde{\Phi}_0(\frac{M}{M_{\mathrm{p}}}(\mathbf{x} - \mathbf{R}_{\mathrm{com}}))|^2 \left[\tilde{\chi}_0^*(\mathbf{R}_{\mathrm{com}}, t)\boldsymbol{\nabla}_{\mathbf{R}_{\mathrm{com}}}\tilde{\chi}_0(\mathbf{R}_{\mathrm{com}}, t) - \mathrm{c.c.}\right] \tag{2.31}$$

and

$$\langle \mathbf{j}_{\mathrm{nuc}}(\mathbf{x}, t)\rangle = \frac{1}{2iM}\int \mathrm{d}\mathbf{r}_{12} |\tilde{\Phi}_0(\mathbf{r}_{12})|^2 \left[\tilde{\chi}_0^*(\mathbf{R}_{\mathrm{com}}, t)\boldsymbol{\nabla}_{\mathbf{R}_{\mathrm{com}}}\tilde{\chi}_0(\mathbf{R}_{\mathrm{com}}, t) - \mathrm{c.c.}\right]_{\mathbf{R}_{\mathrm{com}} = \mathbf{x} + m_{\mathrm{e}}\mathbf{r}_{12}/M}, \tag{2.32}$$

see Ref. [47] for details and further simplifications. Going back to the expression for the electronic gradient in Jacobi coordinates, eqn. (2.29), we see that the center of mass component, $(1/M)\boldsymbol{\nabla}_{\mathbf{R}_{\mathrm{com}}}$, yields non-vanishing contributions to the electronic current density while the relative component, $\boldsymbol{\nabla}_{\mathbf{r}_{12}}$, yields vanishing contributions due to the real electronic stationary wave function. Hence, the electronic current is generated from the center of mass motion, while the electron is in a stationary state with respect to the proton [47, 50].

In analogy to the usual definition of the one-electron density, see eqn. (2.35) below, the one-electron current density for a molecular system containing N electrons and M nuclei is given by

$$\langle \mathbf{j}_{\mathrm{el}}(\mathbf{r}_1, t)\rangle = \frac{N}{2\mathrm{i}}\int\cdots\int \left[\Psi^*(\mathbf{q}, \mathbf{Q}, t)\boldsymbol{\nabla}_{\mathbf{r}_1}\Psi(\mathbf{q}, \mathbf{Q}, t) - \mathrm{c.c.}\right] d\sigma_1 d\mathbf{q}_2 \cdots d\mathbf{q}_N d\mathbf{Q}_1 \cdots d\mathbf{Q}_M, \tag{2.33}$$

where the wave function $\Psi(\mathbf{q}, \mathbf{Q}, t)$ is a solution of the TDSE, eqn. (2.1), and the origin of the coordinate system is usually taken as the nuclear center of mass [134, 135]. The explicit reference to electron 1 is usually dropped since electrons are indistinguishable [136, 137] and

the one-electron current density is denoted as $\langle \boldsymbol{j}_{\mathrm{el}}(\boldsymbol{r},t)\rangle$. There exist a few approaches for the calculation of such electronic current densities induced by nuclear motion on single BO potential energy surfaces [45–51]. However, so far these investigations have been limited either to the single electron system H_2^+ in order to test and validate the approach against exact, non Born-Oppenheimer numerical results [47–49, 51] or to classical [50] or semiclassical [46] nuclear motion.

In this thesis, following the scheme proposed in Ref. [53], the problem of the evaluation of the electronic current density from BO wave functions is circumvented by calculating the electronic fluxes in terms of the one-electron density. For its definition, consider the wave function $\Psi(\mathbf{q},\mathbf{Q},t)$ accounting for N electrons and M nuclei. The probability of finding electron 1 with spin σ_1 in the volume element $\mathrm{d}\mathbf{r}_1$, electron 2 with spin σ_2 in $\mathrm{d}\mathbf{r}_2$ etc. is given by

$$\left(\int\cdots\int |\Psi(\mathbf{q},\mathbf{Q},t)|^2 \mathrm{d}\mathbf{Q}_1\ldots\mathrm{d}\mathbf{Q}_M\right)\mathrm{d}\mathbf{r}_1\mathrm{d}\mathbf{r}_2\ldots\mathrm{d}\mathbf{r}_N = |\Psi_{\mathrm{el}}(\mathbf{q},t)|^2\mathrm{d}\mathbf{r}_1\mathrm{d}\mathbf{r}_2\ldots\mathrm{d}\mathbf{r}_N, \quad (2.34)$$

where the nuclear coordinates have been taken into account in an average way. Integrating additionally over the space-spin coordinates of electrons $2,3,\ldots,N$ and over the spin-coordinate of electron 1 gives the probability of finding electron 1 in the volume element $\mathrm{d}\mathbf{r}_1$, while the other electrons are anywhere in space. Since electrons are indistinguishable, this corresponds to the probability of finding *any* one particular electron in this volume element. Since there are N electrons in the molecular system, the probability of finding an electron in the volume element $\mathrm{d}\mathbf{r}_1$ is given by

$$\left(N\int\cdots\int |\Psi_{\mathrm{el}}(\mathbf{q},t)|^2 \mathrm{d}\boldsymbol{\sigma}_1\mathrm{d}\mathbf{q}_2\ldots\mathrm{d}\mathbf{q}_N\right)\mathrm{d}\mathbf{r}_1 = \rho_{\mathrm{el}}(\mathbf{r}_1,t)\mathrm{d}\mathbf{r}_1, \quad (2.35)$$

where the time-dependent one-electron density, $\rho_{\mathrm{el}}(\mathbf{r}_1,t)$, was defined, see e.g. Refs. [137,159]. In the following, the explicit reference to electron 1 will be dropped and the one-electron density will be denoted as $\rho_{\mathrm{el}}(\mathbf{r},t)$.[4]

[4] Alternatively, the time-dependent one-electron density may be expressed as

$$\rho_{\mathrm{el}}(\mathbf{r},t) = \int\cdots\int \Psi^*_{\mathrm{el}}(\mathbf{q},t)\underbrace{\left(\sum_{i=1}^{N}\delta(\mathbf{r}-\mathbf{r}_i)\right)}_{\hat{\rho}_{\mathrm{el}}(\mathbf{r})}\Psi_{\mathrm{el}}(\mathbf{q},t)\mathrm{d}\mathbf{q}_1\cdots\mathrm{d}\mathbf{q}_N, \quad (2.36)$$

where the density operator $\hat{\rho}_{\mathrm{el}}(\mathbf{r})$ was defined [136]. This form is useful for simplifications of the respective formulas, for instance using the Condon-Slater rules [136,148] in the case that the electronic wave function is expressed in terms of Slater-Determinants, section 2.2.1. Analogous considerations also hold for the evaluation of the one-electron flux density, eqn. (2.33), that is

$$\langle \mathbf{j}_{\mathrm{el}}(\mathbf{r},t)\rangle = \frac{1}{2i}\int\cdots\int\left[\Psi^*(\mathbf{q},\mathbf{Q},t)\left(\sum_{i=1}^{N}\delta(\mathbf{r}-\mathbf{r}_i)\boldsymbol{\nabla}_{\mathbf{r}_i}\right)\Psi(\mathbf{q},\mathbf{Q},t) - \mathrm{c.c.}\right] d\mathbf{q}_1\cdots d\mathbf{q}_N d\mathbf{Q}_1\cdots d\mathbf{Q}_M. \quad (2.37)$$

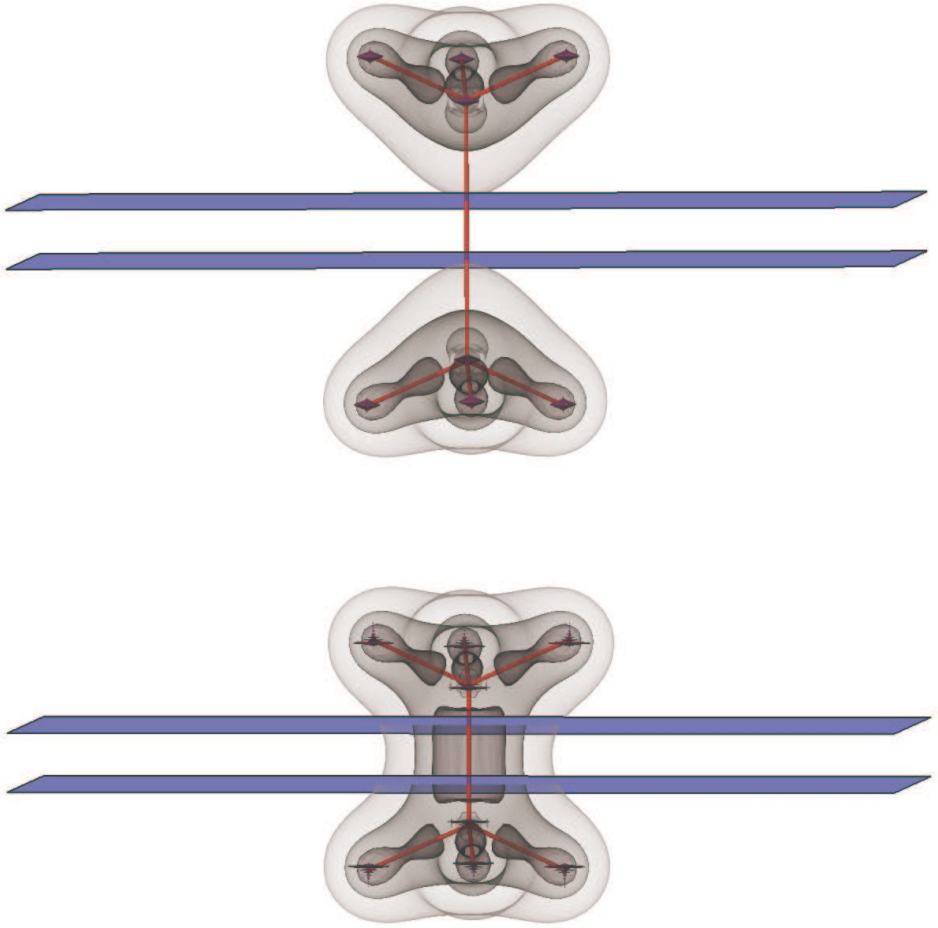

Figure 2.1: Illustration of two electronic observer planes A_{obs}, c.f. eqn. (2.38), shown in blue at symmetric positions above and below the center of mass for vibrating ethane at the outer turning point (upper panel) and at the inner turning point (lower panel), adapted from Ref. [T6]. The time-dependent valence Born-Oppenheimer one-electron density, $\rho^{\mathrm{BO}}_{\mathrm{el,val}}(\mathbf{r},t) = \rho^{\mathrm{BO}}_{\mathrm{el}}(\mathbf{r},t) - \rho^{\mathrm{BO}}_{\mathrm{el,core}}(\mathbf{r},t)$, where $\rho^{\mathrm{BO}}_{\mathrm{el,core}}(\mathbf{r},t)$ accounts for the four core electrons of the carbon atoms, is shown as three nested equidensity contours with values 0.34 $\mathrm{Å}^{-3}$ (light grey), 0.51 $\mathrm{Å}^{-3}$ (grey) and 1.01 $\mathrm{Å}^{-3}$ (dark grey). The program Amira [158] was used for data visualization.

According to Ref. [53]

The electronic flux, $F_{\mathrm{obs,el}}(t)$, out of or into a domain S_{obs} with volume V_{obs} through its boundary surface A_{obs} is given by

$$\begin{aligned} F_{\mathrm{el,obs}}(t) &= -\int_{A_{\mathrm{obs}}} \mathrm{d}\mathbf{A}\cdot\langle\mathbf{j}_{\mathrm{el}}(\mathbf{r},t)\rangle \\ &\overset{(a)}{=} -\int_{V_{\mathrm{obs}}} \boldsymbol{\nabla}_{\mathbf{r}}\langle\mathbf{j}_{\mathrm{el}}(\mathbf{r},t)\rangle\mathrm{d}V \\ &\overset{(b)}{=} \frac{\mathrm{d}}{\mathrm{d}t}\int_{V_{\mathrm{obs}}} \rho_{\mathrm{el}}(\mathbf{r},t)\mathrm{d}V. \end{aligned} \tag{2.38}$$

In step (a) in eqn. (2.38), the surface integral was transformed into a volume integral using Gauss's Theorem [160] and in step (b) the electronic continuity equation

$$\frac{\partial}{\partial t}\rho_{\mathrm{el}}(\mathbf{r},t) = -\boldsymbol{\nabla}_{\mathbf{r}}\langle\mathbf{j}_{\mathrm{el}}(\mathbf{r},t)\rangle \tag{2.39}$$

was used. Two examples of such boundary surfaces A_{obs} used in Ref. [T6], which are also referred to as electronic observer planes, are shown in Figure 2.1 in blue in the case of the vibrating ethane molecule. The molecule is shown at the outer turning point (upper panel) and at the inner turning point (lower panel). Time-integration of the electronic flux in terms of the one-electron density, last line in eqn. (2.38), gives the electronic yield

$$Y_{\mathrm{el,obs}}(t) = \int_{V_{\mathrm{obs}}} \rho_{\mathrm{el}}(\mathbf{r},t)\mathrm{d}V - \int_{V_{\mathrm{obs}}} \rho_{\mathrm{el}}(\mathbf{r},t=0)\mathrm{d}V, \tag{2.40}$$

that is the number of electrons that have flown out of (negative sign) or into (positive sign) the observer Volume V_{obs} bounded by the observer surface A_{obs} in the time-intervall [0,t]. Note that eqn. (2.38) is an *exact* expression. The approximation introduced in Ref. [53] and used in this thesis, Refs. [T1,T3,T6], is to express the time-dependent one-electron density, eqn. (2.35), by the Born-Oppenheimer electron density associated with the electronic ground state

$$\begin{aligned} \rho_{\mathrm{el}}(\mathbf{r},t) \approx & \rho_{\mathrm{el}}^{\mathrm{BO}}(\mathbf{r},t) = \\ & N\int\cdots\int |\chi_0(\mathbf{Q},t)|^2 \times |\Phi_0(\mathbf{q};\mathbf{R})|^2 \mathrm{d}\sigma_1\mathrm{d}\mathbf{q}_2\cdots\mathrm{d}\mathbf{q}_N\mathrm{d}\mathbf{Q}_1\cdots\mathrm{d}\mathbf{Q}_M, \end{aligned} \tag{2.41}$$

c.f. eqn. (2.16). Here, the subscript for the electronic ground state 0 was dropped in the expression for the BO one-electron density since all investigations in this thesis involving electronic fluxes refer to the electronic ground state. Hence, imposing the continuity equation on the

time-dependent Born-Oppenheimer electron density, eqns. (2.39) and (2.41), respectively, allows the calculation of electronic fluxes through specific electronic observer planes, eqn. (2.38) and Figure 2.1, thereby extending the BO approximation to time-dependent processes. This approach yields excellent results for the electronic fluxes as shown by comparison to accurate numerical solutions of the TDSE without invoking the Born-Oppenheimer approximation for the molecular ion H_2^+ [53].

Numerically, it is convenient to calculate at first the volume integral over the time-independent one-electron BO density

$$\rho_{\mathrm{el}}^{\mathrm{BO}}(\mathbf{r};\mathbf{R}) = N \int \cdots \int |\Phi_0(\mathbf{q};\mathbf{R})|^2 \mathrm{d}\sigma_1 \mathrm{d}\mathbf{q}_2 \cdots \mathrm{d}\mathbf{q}_N \tag{2.42}$$

according to

$$N_{\mathrm{obs}}^{\mathrm{BO}}(\mathbf{R}) = \int_{V_{\mathrm{obs}}} \rho_{\mathrm{el}}^{\mathrm{BO}}(\mathbf{r};\mathbf{R}) \mathrm{d}V. \tag{2.43}$$

This procedure is recommended to reduce the number of volume integrals to be evaluated since these "static" electron numbers, $N^{\mathrm{BO}}(\mathbf{R})$, may be evaluated for a limited number of nuclear structures $\mathbf{R}$ and then be interpolated for the subsequent calculation of the time-dependent electronic yield as

$$Y_{\mathrm{el,obs}}^{\mathrm{BO}}(t) = \underbrace{\int \cdots \int N_{\mathrm{obs}}^{\mathrm{BO}}(\mathbf{R}) |\chi_0(\mathbf{R},t)|^2 \mathrm{d}\mathbf{R}_1 \ldots \mathrm{d}\mathbf{R}_M}_{\bar{N}_{\mathrm{obs}}^{\mathrm{BO}}(t)} - \underbrace{\int \cdots \int N_{\mathrm{obs}}^{\mathrm{BO}}(\mathbf{R}) |\chi_0(\mathbf{R},t=0)|^2 \mathrm{d}\mathbf{R}_1 \ldots \mathrm{d}\mathbf{R}_M}_{\bar{N}_{\mathrm{obs}}^{\mathrm{BO}}(t=0)}, \tag{2.44}$$

where $\bar{N}_{\mathrm{obs}}^{\mathrm{BO}}(t)$ denotes the mean number of electrons in the Volume V_{obs} at time t [Tl]. Finally, the electronic flux is calculated as

$$F_{\mathrm{el,obs}}^{\mathrm{BO}}(t) = \frac{\mathrm{d}}{\mathrm{d}t} Y_{\mathrm{el,obs}}^{\mathrm{BO}}(t), \tag{2.45}$$

with corresponding expressions for the nuclear fluxes and yields.

In Ref. [Tl], the hitherto static electronic observer planes A_{obs}, associated with the fixed domain S_{obs} with constant volume V_{obs}, which were introduced in Ref. [53], c.f. Figure 2.1 and eqns. (2.40) and (2.43), are generalized to include a dependence on the nuclear configuration, $A_{\mathrm{obs}}(\mathbf{R})$, with corresponding variable domains and volumes, $S_{\mathrm{obs}}(\mathbf{R})$ and $V_{\mathrm{obs}}(\mathbf{R})$, respectively. Figure 2.2 shows the six particular electronic observer planes that are used to monitor the electronic bond-to-bond fluxes associated with bond breaking (bb), $A_{\mathrm{bb}}(\mathbf{R})$ and $A'_{\mathrm{bb}}(\mathbf{R})$, bond making (bm), $A_{\mathrm{bm}}(\mathbf{R})$ and $A'_{\mathrm{bm}}(\mathbf{R})$, and double-bond-shifting (dbs), $A_{\mathrm{dbs}}(\mathbf{R})$ and $A'_{\mathrm{dbs}}(\mathbf{R})$, in the degenerate Cope rearrangement of semibullvalene, c.f. Refs [Tl] and [T3] and Chapter 4. These observer planes are shown for the reactant and product structures and their dependence on the nuclear configuration is denoted by the respective superscripts. In particular, these electronic observers are half-planes, originating in the molecular center-of-mass and intersecting the respective carbon atoms of the six membered ring. Each adjacent pair of observer planes, e.g. $A'_{\mathrm{bb}}(\mathbf{R})/A_{\mathrm{bb}}(\mathbf{R})$, $A_{\mathrm{bb}}(\mathbf{R})/A_{\mathrm{dbs}}(\mathbf{R})$ etc., forms the boundary of the respective observer domains, $S_{\mathrm{obs}}(\mathbf{R})$ with volume $V_{\mathrm{obs}}(\mathbf{R})$. The resulting six domains are also indicated in Figure 2.2. Hence, at each instant of time during the reaction, each observer plane follows the mean position of the associated carbon atom of the six-membered ring, c.f.

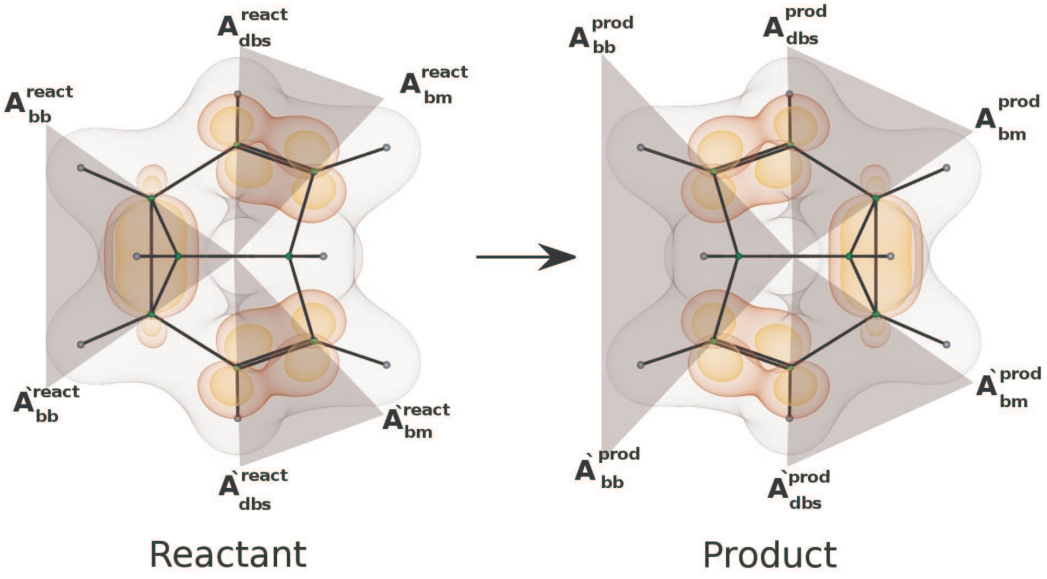

Figure 2.2: Bird's eye view of semibullvalene for the reactant and the product structures showing two equidensity contours of the pericyclic electron density (red and orange), accounting for the rearranging electrons according to the Lewis structure (see section 2.2.3 and Chapter 4 for details), and one equidensity contour of the total electron density (grey). Also shown are the electronic observer planes monitoring bond breaking (bb), $A_{\mathrm{bb}}(\mathbf{R})$ and $A'_{\mathrm{bb}}(\mathbf{R})$, bond making (bm), $A_{\mathrm{bm}}(\mathbf{R})$ and $A'_{\mathrm{bm}}(\mathbf{R})$, and double-bond-shifting (dbs), $A_{\mathrm{dbs}}(\mathbf{R})$ and $A'_{\mathrm{dbs}}(\mathbf{R})$. These observer planes depend on the nuclear configuration $\mathbf{R}$ as denoted by the respective superscripts "react" and "prod". More specifically, they are half-planes, originating in the molecular center-of-mass and intersecting the respective carbon atoms of the six membered ring. Also highlighted are the respective observer domains $S_{\mathrm{obs}}(\mathbf{R})$, whose boundaries are formed by the respective electronic observer planes. Taking into account the quantum distribution of the nuclear wave function at each instant of time, c.f. eqn. (2.44), the resulting time-dependent electronic observer planes have corresponding quantum distributions and may thus be regarded as *quantum walls*. The program Amira [158] was used for data visualization. Adapted from Ref. [T1].

eqns. (2.44) and (2.43), adapted for variable observer volumes, $V_{\mathrm{obs}}(\mathbf{R})$. Accordingly, due to the quantum distribution of the nuclear wave function, $\chi_0(\mathbf{r},t)$, these time-dependent electronic observer planes have corresponding quantum distributions and may thus be regarded as *quantum walls*.

Finally, the two following issues should be noted: Firstly, due to the underlying symmetry of the reaction, equal electronic bond-to-bond fluxes through the respective observer planes associated with bb, bm and dbs, and situated above and below the symmetry plane including the two carbon bridge atoms, Figure 2.2, are observed, c.f. Refs. [161] and [T1,T3] as well as Chapter 4. Hence, for example the electronic flux associated with bb through either of the observer planes $A_{\mathrm{bb}}(\mathbf{R})$ and $A'_{\mathrm{bb}}(\mathbf{R})$ equals half the flux out of the the corresponding domain bounded by these observer planes, which is readily calculated using eqns. (2.42)-(2.45), adapted for variable observer volumes, $V_{\mathrm{obs}}(\mathbf{R})$. The same strategy is, however, not applicable for systems that do not exhibit this symmetry, e.g. for the hydrogen transfer in malonaldehyde or the double proton transfer in the formic acid dimer, see e.g. Ref. [161] for details on these reactions. Secondly, for the numerical evaluation of the volume integral, eqn. (2.43), in the case that the respective boundaries intersect carbon-atoms, Figure 2.2, it is numerically efficient to adapt the step sizes of the underlying three dimensional spatial grid such that for the individual domains, the nuclei of the respective carbon atoms are centered in one of the cells of the grids.

2.2 Molecular Electronic Structure Theory

The main interest in *Quantum Chemistry*, or more specifically *Molecular Electronic Structure Theory*, is finding approximate solutions of the non-relativistic time-independent electronic Schrödinger equation, eqn. (2.5). The most popular approaches may be divided into two classes: *Wave Function Based Methods* [136,137,148–151] and *Density Functional Theory* [137,150,162,163], which are presented in sections 2.2.1 and 2.2.2, respectively. For notational convenience, the parametric dependence of the electronic wave functions, $\Phi_i(\mathbf{q};\mathbf{R})$, and of the one-electron densities, $\rho_{\mathrm{el}}^{\mathrm{BO}}(\mathbf{r};\mathbf{R})$, on the set of nuclear coordinates $\mathbf{R}$ as well as the dependence of the respective operators on the set of electronic and nuclear coordinates $(\mathbf{q},\mathbf{R})$ is not explicitly indicated throughout this section.

2.2.1 Wave Function Based Methods

For the complete description of electrons, it is necessary to specify both their spatial distribution and their spin. The spatial distribution of a single electron is described by the wave function $\psi_m(\mathbf{r})$, usually referred to as *spatial-orbital*, such that $|\psi_m(\mathbf{r})|^2\mathrm{d}\mathbf{r}$ is the probability of finding the electron in the volume element $\mathrm{d}\mathbf{r}$ surrounding $\mathbf{r}$ [136]. For the description of electron spin within the non-relativistic treatment used in this thesis, the spin angular-momentum operators $\left(\hat{S}^2,\,\hat{S}_x,\,\hat{S}_y,\,\hat{S}_z\right)$ are defined in analogy to the orbital angular-momentum operators $\left(\hat{L}^2,\,\hat{L}_x,\,\hat{L}_y,\,\hat{L}_z\right)$ [137,142]. They are postulated to be linear, Hermitian operators and to obey the same commutation relations as the orbital angular-momentum operators. Hence, the eigenvalues of $\hat{S}^2$ are $s(s+1)$ with $s = 0,\,\frac{1}{2},\,1,\,\frac{3}{2},\ldots$ and the eigenvalues of $\hat{S}_z$ are $\sigma = -s,\,-s+1,\ldots,s-1,\,s$. Additionally, experiment shows that electrons are spin-$\frac{1}{2}$ particles, such that they are restricted to have a single value for s, namely $s = \frac{1}{2}$ [137]. Consequently, the two possible eigenvalues of $\hat{S}_z$ are $\sigma = \frac{1}{2}$ and $\sigma = -\frac{1}{2}$, with the corresponding eigenfunctions denoted by α and β

$$\hat{S}_z\alpha = \frac{1}{2}\alpha \qquad \hat{S}_z\beta = -\frac{1}{2}\beta. \tag{2.46}$$

These spin-functions are orthogonal, since they are eigenfunctions of the Hermitian operator $\hat{S}_z$ corresponding to different eigenvalues, and are taken to be normalized. Usually, their eigenvalues σ are taken as the variable on which these eigenfunctions depend. Denoting the spin-functions by μ and ν [148], see also section 2.2.1.5, the corresponding orthonormality relation reads

$$\sum_{\sigma}\mu^*(\sigma)\nu(\sigma) = \delta_{\mu\nu} = \int\mu^*(\sigma)\nu(\sigma)\mathrm{d}\sigma, \tag{2.47}$$

which is satisfied if $\alpha(\sigma) = \delta_{\sigma,\frac{1}{2}}$ and $\beta(\sigma) = \delta_{\sigma,-\frac{1}{2}}$. The last equality in eqn. (2.47) was introduced for notational convenience, such that for the discrete spin-functions the same notation as for continuous spatial-functions can be used, interpreting integration in spin-space as summation over the two discrete values of σ [148], c.f. section 2.1. In non-relativistic theory, it is common to describe both the spatial distribution and the electron spin using so-called *spin-orbitals* of the form

$$\phi_{2m-1}(\mathbf{q}) = \psi_m(\mathbf{r})\alpha(\sigma) \qquad \phi_{2m}(\mathbf{q}) = \psi_m(\mathbf{r})\beta(\sigma). \tag{2.48}$$

Turning to N-electron wave functions in the molecular case, consider at first the electronic Schrödinger equation, eqn. (2.5), without the electron-electron repulsion term, $\hat{V}_{\mathrm{el-el}}(\mathbf{r})$. The corresponding Hamilton operator is given by

$$\hat{H}^0 = \sum_i \left(\underbrace{-\frac{1}{2}\boldsymbol{\nabla}^2_{\mathbf{r}_i} - \sum_A \frac{Z_A}{|\mathbf{r}_i - \mathbf{R}_A|}}_{\hat{f}(\mathbf{r}_i)} \right), \tag{2.49}$$

and the spatial-orbitals are eigenfunctions of the Hermitian one-electron operator $\hat{f}(\mathbf{r}_i)$ according to

$$\hat{f}(\mathbf{r}_i)\psi_m(\mathbf{r}_i) = \epsilon_m \psi_m(\mathbf{r}_i). \tag{2.50}$$

Taking into account electron-spin as well as the antisymmetry principle, the corresponding N-electron eigenfunctions are found to be so-called *Slater determinants* (SDs) [136, 137, 148–151], which are antisymmetrized products of the corresponding spin-orbitals, eqn. (2.48):

$$\Phi_i^{\mathrm{SD}}(\mathbf{q}) = \frac{1}{\sqrt{N!}} \begin{vmatrix} \phi_1(\mathbf{q}_1) & \phi_2(\mathbf{q}_1) & \dots & \phi_N(\mathbf{q}_1) \\ \phi_1(\mathbf{q}_2) & \phi_2(\mathbf{q}_2) & \dots & \phi_N(\mathbf{q}_2) \\ \vdots & \vdots & \ddots & \vdots \\ \phi_1(\mathbf{q}_N) & \phi_2(\mathbf{q}_N) & \dots & \phi_N(\mathbf{q}_N) \end{vmatrix}. \tag{2.51}$$

Eqn. (2.48) gives rise to so-called restricted SDs, eqn. (2.51), since the spatial-parts of the respective spin-orbitals are restricted to be the same for α and β spin-functions. This is the only case considered in this thesis; the reader is referred to Refs. [136, 148] for the usage of so-called unrestricted SDs, which are formed from spin-orbitals that have different spatial-parts for different spin-functions.

Usually, the spin-orbitals are ordered according to increasing energy, such that eqn. (2.51) with $\Phi_0^{\mathrm{SD}}(\mathbf{q})$ is a crude approximation to the electronic ground state. In principle, there is of course an infinite number of spin-orbitals and consequently an infinite number of SDs, each of which is an antisymmetrized product of N spin-orbitals. These SDs, being eigenfunctions of a Hermitian operator, eqn. (2.49), constitute a complete set of N-electron basis-functions. Hence, formally the exact solution of the time-independent electronic Schrödinger equation may be expressed as a linear combination of antisymmetrized products of one-electron functions according to

$$\Phi_i(\mathbf{q}) = \sum_j C_{ij} \Phi_j^{\mathrm{SD}}(\mathbf{q}). \tag{2.52}$$

In numerical calculations, the spatial-orbitals $\psi_m(\mathbf{r}_i)$, also referred to as molecular-orbitals (MOs) in the following, are usually expanded in a finite set of K real-valued one-electron basis-functions, also referred to as atomic orbitals (AOs), $\{\lambda_\mu(\mathbf{r}_i)\}$, according to

$$\psi_m(\mathbf{r}_i) = \sum_\mu^K c_{m\mu} \lambda_\mu(\mathbf{r}_i), \tag{2.53}$$

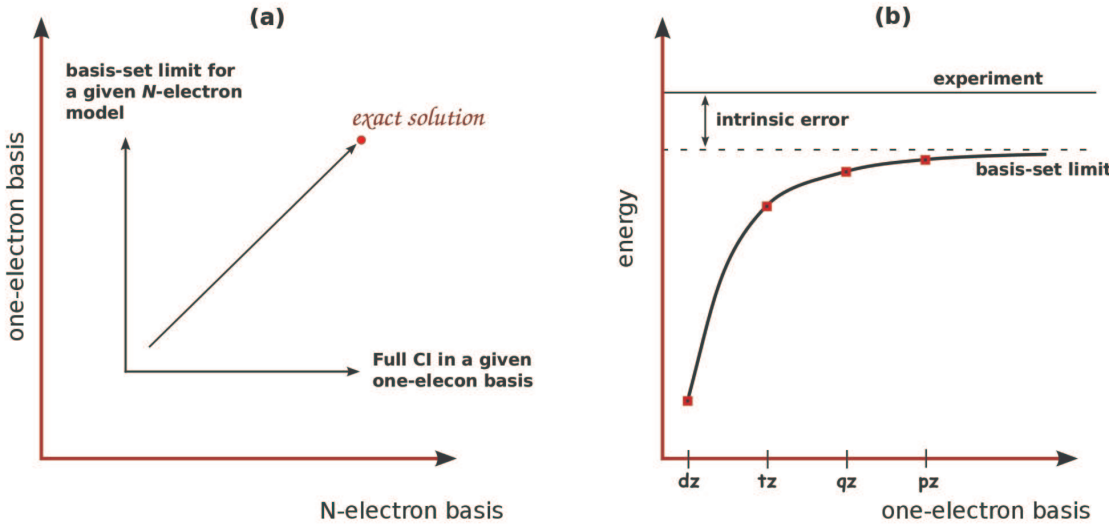

Figure 2.3: (a) The dependence of calculations on the size of the one-electron and N-electron basis-sets. (b) Dependence of the energy on the quality of the one-electron basis-set. Adapted from Ref. [148], see also Refs. [136,149].

resulting in $2K$ spin-orbitals [136]. The AOs are usually simple analytical functions centered on the atomic nuclei, see section 2.2.4 for details.

Consequently, to arrive at an exact solution of the electronic Schrödinger equation, both the AOs, in terms of which the MOs and finally the SDs are constructed, must form a complete set in the one-electron space and all SDs that can be generated from the corresponding spin-orbitals must be included in the expansion of the N-electron wave function, eqn. (2.52). In practice, however, both spaces need to be truncated at some point and Figure 2.3(a) illustrates how the exact solution to the electronic Schrödinger equation may be approached by systematic improvements in the one-electron and N-electron spaces. As indicated by the horizontal arrow in Figure 2.3(a), calculations using all SDs that can be generated from the spin-orbitals obtained in a given one-electron basis are denoted as *Full Configuration Interaction* (FCI) calculations in the specific one-electron basis. The term *configuration* refers to a single SD or to a linear combination of a small number of SDs, see section 2.2.1.3. The vertical arrow indicates the approach of a calculation to the (one-electron) *basis-set limit*, i.e. usage of a complete one-electron basis for a given number of N-electron basis-functions.

The errors introduced by truncating the one-electron space are qualitatively different from those that arise from approximations made in the N-electron space and a poor description in either of the two spaces cannot be compensated for by an improved description in the other [148]. Consider for instance the calculation depicted in Figure 2.3(b), which shows the approach to the one-electron basis-set limit in a given N-electron basis (for a description of the acronyms, see section 2.2.4). Going from the dz to the tz one-electron basis, a significant improvement in the calculated energy is observed compared with the intrinsic error of the N-electron model, whereas beyond the qz basis, the basis-set change is small compared to the

intrinsic error. Thus, the qz basis is said to represent a balanced level of description in this case. Sometimes, calculations in the qz basis and beyond may be computationally too expensive in a desired N-electron model. In those cases, approximate extrapolations to the basis-set limit, using the results in the dz and tz basis, may be used [148].

Moreover, the errors made in the one-electron and N-electron treatment are not entirely independent of each other. For example, the basis-set requirements for a single determinant wave function are rather different from those for a wave function containing a large number of SDs [148]. It may also be noted that the exact solution to the electronic Schrödinger equation can be approached in a manner different from that illustrated in Figure 2.3(a), for example by employing explicitly correlated wave functions, using for example the *R12 method* [164–166].

2.2.1.1 Variation Method

The variation method is - besides perturbation theory (section 2.2.1.2) - the standard method in Molecular Electronic Structure Theory to design approximate electronic wave functions. It is based on a general variation principle [148]: Consider the expectation value of the electronic Hamiltonian, eqn. (2.4),

$$E[\Phi(\mathbf{q})] = \langle \Phi(\mathbf{q}) | \hat{H}_{\mathrm{el}} | \Phi(\mathbf{q}) \rangle, \tag{2.54}$$

where $\Phi(\mathbf{q})$ is some electronic wave function that satisfies the appropriate boundary conditions, e.g. it has to tend to zero at infinite values of any of the coordinates $\mathbf{r}_i$, it cannot be zero everywhere etc., see Ref. [167] for an extensive list. The stationary points of this functional subject to the constraint that the electronic wave function is normalized, i.e. $\langle \Phi(\mathbf{q}) | \Phi(\mathbf{q}) \rangle = 1$, are found by defining the auxiliary functional

$$G[\Phi(\mathbf{q})] = E[\Phi(\mathbf{q})] - \mathcal{V}(\langle \Phi(\mathbf{q}) | \Phi(\mathbf{q}) \rangle - 1), \tag{2.55}$$

where $\mathcal{V}$ is a *Lagrange multiplier* [136], and then setting the functional derivative[5] of $G[\Phi(\mathbf{q})]$ with respect to $\Phi^*(\mathbf{q})$ equal to zero:

$$\frac{\delta G[\Phi(\mathbf{q})]}{\delta \Phi^*(\mathbf{q})} = \hat{H}_{\mathrm{el}} \Phi(\mathbf{q}) - \mathcal{V} \Phi(\mathbf{q}) \stackrel{!}{=} 0. \tag{2.56}$$

Note that it is sufficient to take the functional derivative with respect to either $\Phi(\mathbf{q})$ or the complex conjugate $\Phi^*(\mathbf{q})$, the result being independent of this choice [167][6]. Hence,

> Those wave functions $\Phi_i(\mathbf{q})$, for which the auxiliary functional, eqn. (2.55), becomes stationary,
>
> $$\delta G[\Phi_i(\mathbf{q})] = 0, \tag{2.57}$$
>
> are solutions of the electronic Schrödinger equation, eqn. (2.5), and the values of $G[\Phi_i(\mathbf{q})]$ at the stationary points are the corresponding eigenvalues [148,168].

[5] The reader is referred to Appendix 6.1 for details on functionals and functional derivatives.

[6] Equivalently, the stationary points of the Rayleigh quotient, $\frac{\langle \Phi(\mathbf{q}) | \hat{H}_{\mathrm{el}} | \Phi(\mathbf{q}) \rangle}{\langle \Phi(\mathbf{q}) | \Phi(\mathbf{q}) \rangle}$, may be calculated [148,167,168].

Since the reverse relation is also true, that is the eigenstates of the time-independent electronic Schrödinger equation represent stationary points of the auxiliary functional, eqn. (2.55), the variational optimization of this energy functional is equivalent to the solution of the time-independent electronic Schrödinger equation [148]. This variation principle is the basis for the *variation method* or *Ritz method* used to generate approximate wave functions, which, assuming a discrete set of L variational parameters, $\{\alpha_j\}$, works as follows [148,168]:

- Choose a *trial function*

$$\Phi(\mathbf{q}) = f(\Xi_1(\mathbf{q}), \ldots, \Xi_{\tilde{L}}(\mathbf{q}); \alpha_1, \ldots, \alpha_L) \tag{2.58}$$

  as function of predefined basis states, $\Xi_1(\mathbf{q}), \ldots, \Xi_{\tilde{L}}(\mathbf{q})$, which are mathematically easy to handle, see also section 2.2.4. Additionally, the trial function contains a finite set of parameters, $\alpha_1, \ldots, \alpha_L$.

- Use the ansatz (2.58) for the calculation of the auxiliary functional $G[\Phi(\mathbf{q})]$, eqn. (2.55), which then becomes a function of the parameters $\alpha_1, \ldots, \alpha_L$

$$G[\Phi(\mathbf{q})] \equiv g(\alpha_1, \ldots, \alpha_L). \tag{2.59}$$

- Demanding that

$$\frac{\partial}{\partial \alpha_j} G[\Phi(\mathbf{q})] \equiv \frac{\partial}{\partial \alpha_j} g(\alpha_1, \ldots, \alpha_L) \stackrel{!}{=} 0 \qquad \text{with} \qquad \mathrm{j} = 1, \ldots, \mathrm{L} \tag{2.60}$$

  yields a set of equations for the optimal set of parameters, $\tilde{\alpha}_1, \ldots, \tilde{\alpha}_L$, for which the auxiliary function becomes stationary.

- The approximation for the ground state wave function is then given by

$$\tilde{\Phi}_0(\mathbf{q}) = f(\Xi_1(\mathbf{q}), \ldots, \Xi_{\tilde{L}}(\mathbf{q}); \tilde{\alpha}_1, \ldots, \tilde{\alpha}_L), \tag{2.61}$$

  with $G[\tilde{\Phi}_0(\mathbf{q})]$ being the approximation for the ground state energy.

linear variational expansion

For a linear ansatz, expanding the trial function in an L-dimensional set of fixed, orthonormal and antisymmetric N-electron functions, that is in the case of a configuration interaction (CI) calculation, c.f. eqs. (2.52), the set of expansion coefficients $\{C_{ij}\}$ corresponds to the discrete set of variational parameters and the set of SDs $\left\{\Phi_j^{\mathrm{SD}}(\mathbf{q})\right\}$ to the predefined fixed basis states, c.f. eqn. 2.58. In this case, the above procedure leads to a standard L-dimensional eigenvalue problem of linear algebra

$$\mathbf{HC} = E\mathbf{C}, \tag{2.62}$$

where $\mathbf{C}$ is a column vector containing the linear expansion coefficients, c.f. eqn. (2.52), E is the approximate eigenvalue equal to the Lagrange multiplier $\mathcal{V}$, c.f. eqn. (2.55), and $\mathbf{H}$ is the Hamiltonian matrix with elements

$$H_{jk} = \langle \Phi_j^{\mathrm{SD}}(\mathbf{q}) | \hat{H}_{\mathrm{el}}(\mathbf{r}) | \Phi_k^{\mathrm{SD}}(\mathbf{q}) \rangle. \tag{2.63}$$

Since $\mathbf{H}$ is Hermitian, eqn. (2.62) has L orthonormal solutions

$$\mathbf{C}_i = \begin{pmatrix} C_{i1} \\ C_{i2} \\ \vdots \\ C_{iL} \end{pmatrix} \qquad \text{with} \qquad \mathbf{C}_{\mathrm{i}}^{\mathrm{T}}\mathbf{C}_{\mathrm{j}} = \delta_{\mathrm{ij}} \tag{2.64}$$

with the associated eigenenergies

$$\tilde{E}_1 \leq \tilde{E}_2 \leq \ldots \leq \tilde{E}_L, \tag{2.65}$$

which may or may not be distinct. The eigenvectors $\mathbf{C}_i$ in eqn. (2.64) represent the approximate wave function

$$\tilde{\Phi}_i(\mathbf{q}) = \sum_j^L C_{ij}\Phi_j^{\mathrm{SD}}(\mathbf{q}) \tag{2.66}$$

and the associated eigenvalues $\tilde{E}_i$ in eqn. (2.65) represent the approximate energies [136, 137, 148, 150].

The linear variational expansion provides a high degree of control over the calculation: Consider two orthonormal sets of N-electron basis-functions (SDs) $S' = \left\{\Phi_j'^{\mathrm{SD}}(\mathbf{q})\right\}$ and $S'' = \left\{\Phi_j''^{\mathrm{SD}}(\mathbf{q})\right\}$, where S' is a subset of S'', $S' \subset S''$. The corresponding eigenvalue equations in the two N-electron basis-sets are given by

$$\mathbf{H}'\mathbf{C}_i' = E_i'\mathbf{C}_i' \quad \text{and} \quad \mathbf{H}''\mathbf{C}_i'' = E_i''\mathbf{C}_i''. \tag{2.67}$$

According to *Cauchy's interlace theorem*

> The eigenvalues of two linear variational spaces S' and S'' with $S' \subset S''$ are related to one another and to the exact electronic energy E_i, eqn. (2.5), by
>
> $$E_i \leq E_i'' \leq E_i' \leq E_{i+\delta}'', \tag{2.68}$$
>
> where δ is the difference in the dimensions of the two spaces:
>
> $$\delta = \mathrm{dim}S'' - \mathrm{dim}S'. \tag{2.69}$$

For a derivation see e.g. Ref. [148]. Hence, the ith eigenvalue of the extended space S'' is always less than or equal to the ith eigenvalue of the smaller linear variational space S', so that the exact eigenvalue E_i, eqn. (2.5), is approached from above and is only obtained in the case of a complete set of N-electron functions. As special case of *Cauchy's interlace theorem*, one obtains for $\delta = 1$ the *Hylleraas-Undheim Theorem*

$$E_1'' \leq E_1' \leq E_2'' \leq E_2' \leq \ldots E_j'' \leq E_j' \leq E_{j+1}'', \tag{2.70}$$

which relates the eigenvalues of two variational spaces $S' \subset S''$, one of which contains one more N-electron basis-function than the other [148]. It should be noted that in actual quantum chemical calculations, the dimension of the variational space usually increases by more than one when the accuracy of a calculation is enhanced and hence the *Hyleraas-Undheim Theorem*, eqn. (2.70) - contrary to *Cauchy's interlace theorem*, eqns. (2.68) and (2.69) - does not apply: The energy E'_j obtained in one space is therefore in general not a lower bound to the energy E''_{j+1} obtained in the next space.

The *variation method* is of course not limited to linear expansions: Any normalized *trial function*, eqn. (2.58), that satisfies the appropriate boundary conditions, see above, fulfills

$$\langle \Phi(\mathbf{q}) | \hat{H}_{\mathrm{el}} | \Phi(\mathbf{q}) \rangle \geq E_0, \tag{2.71}$$

where E_0 is the exact ground state energy. Furthermore, in the case of non-linear optimizations, the L optimized states must be orthogonal to each other in order to ensure that their eigenvalues, $\tilde{E}_j$, are upper bounds to the respective exact energies, E_j [136,137].

2.2.1.2 Perturbation Theory

A different approximate approach is perturbation theory [136,137,148,150], in which the Hamilton operator, that is the electronic Hamilton operator $\hat{H}_{\mathrm{el}}$ in the present context, eqn. (2.4), is partitioned into two terms: a zeroth-order part $\hat{H}^{(0)}$, which has known eigenfunctions and eigenvalues, and a perturbation described by $\hat{H}'$ according to

$$\hat{H}_{\mathrm{el}} = \hat{H}^{(0)} + \hat{H}' \tag{2.72}$$

with

$$\hat{H}^{(0)} \Phi_i^{(0)}(\mathbf{q}) = E_i^{(0)} \Phi_i^{(0)}(\mathbf{q}). \tag{2.73}$$

In perturbation theory, the known eigenfunction and eigenvalue for electronic state i are used as first approximation to the exact state i, which are systematically improved using the remaining unperturbed eigenfunctions and eigenvalues, $\Phi_j^{(0)}(\mathbf{q})$ and $E_j^{(0)}$ with $i \neq j$. Special precaution has to be taken if the state of interest i is degenerate [136,137,148,150], which is, however, not the case in this thesis. Additionally, it is assumed in the following that the perturbed form of the ground state $\Phi_0^{(0)}(\mathbf{q})$ of energy $E_0^{(0)}(\mathbf{q})$ is calculated. This is also the case in section 2.2.1.3.

At first, an ordering parameter λ, which is set to unity at the end of the calculation, is introduced according to

$$\hat{H}_{\mathrm{el}} = \hat{H}^{(0)} + \lambda \hat{H}'. \tag{2.74}$$

Next, the exact eigenfunctions and eigenvalues of the state of interest are expanded in a power series in λ

$$\Phi_0(\mathbf{q}) = \Phi_0^{(0)}(\mathbf{q}) + \lambda \Phi_0^{(1)}(\mathbf{q}) + \lambda^2 \Phi_0^{(2)}(\mathbf{q}) + \ldots \tag{2.75}$$

and

$$E_0 = E_0^{(0)} + \lambda E_0^{(1)} + \lambda^2 E_0^{(2)} + \ldots . \tag{2.76}$$

$\Phi_0^{(n)}(\mathbf{q})$ and $E_0^{(n)}$ are called the nth order corrections to the wave function and energy, respectively. For a detailed discussion concerning the convergence of this perturbation expansion, the

reader is referred to Ref. [169]. Inserting eqns. (2.74), (2.75) and (2.76) into the time-independent electronic Schrödinger equation, eqn. (2.5), followed by collection of terms that have the same power of λ results in

$$\begin{aligned}
\lambda\left(\hat{H}^{(0)}\Phi_0^{(0)}(\mathbf{q}) - E_0^{(0)}\Phi_0^{(0)}(\mathbf{q})\right) \\
+\lambda^1\left(\hat{H}^{(0)}\Phi_0^{(1)}(\mathbf{q}) + \hat{H}'\Phi_0^{(0)}(\mathbf{q}) - E_0^{(0)}\Phi_0^{(1)}(\mathbf{q}) - E_0^{(1)}\Phi_0^{(0)}(\mathbf{q})\right) \\
+\lambda^2\left(\hat{H}^{(0)}\Phi_0^{(2)}(\mathbf{q}) + \hat{H}'\Phi_0^{(1)}(\mathbf{q}) - E_0^{(0)}\Phi_0^{(2)}(\mathbf{q}) - E_0^{(1)}\Phi_0^{(1)}(\mathbf{q}) - E_0^{(2)}\Phi_0^{(0)}(\mathbf{q})\right) + \ldots \;=\; 0.
\end{aligned}$$

Because λ is an arbitrary parameter, the coefficients of each power of λ must equal zero separately, yielding the following set of equations up to second order

$$\hat{H}^{(0)}\Phi_0^{(0)}(\mathbf{q}) - E_0^{(0)}\Phi_0^{(0)}(\mathbf{q}) = 0, \tag{2.77}$$

$$\left(\hat{H}^{(0)} - E_0^{(0)}\right)\Phi_0^{(1)}(\mathbf{q}) + \left(\hat{H}' - E_0^{(1)}\right)\Phi_0^{(0)}(\mathbf{q}) = 0, \tag{2.78}$$

$$\left(\hat{H}^{(0)} - E_0^{(0)}\right)\Phi_0^{(2)}(\mathbf{q}) + \left(\hat{H}' - E_0^{(1)}\right)\Phi_0^{(1)}(\mathbf{q}) - E_0^{(2)}\Phi_0^{(0)}(\mathbf{q}) = 0. \tag{2.79}$$

The first-order correction to the energy and wave function, $E_0^{(1)}$ and $\Phi_0^{(1)}(\mathbf{q})$, respectively, are obtained by inserting the expansion of $\Phi_0^{(1)}(\mathbf{q})$ in terms of the known unperturbed eigenstates,

$$\Phi_0^{(1)}(\mathbf{q}) = \sum_j c_j \Phi_j^{(0)}(\mathbf{q}), \tag{2.80}$$

into eqn. (2.78) yielding

$$\sum_j c_j\left(\hat{H}^{(0)} - E_0^{(0)}\right)\Phi_j^{(0)}(\mathbf{q}) + \left(\hat{H}' - E_0^{(1)}\right)\Phi_0^{(0)}(\mathbf{q}) = 0. \tag{2.81}$$

Multiplying eqn. (2.81) from the left by $\Phi_0^{(0)*}(\mathbf{q})$ and integrating over the set of electronic spatial and spin coordinates yields

$$E_0^{(1)} = \langle\Phi_0^{(0)}(\mathbf{q})|\hat{H}'|\Phi_0^{(0)}(\mathbf{q})\rangle, \tag{2.82}$$

whereas multiplying eqn. (2.81) from the left by $\Phi_j^{(0)*}(\mathbf{q})$ with $j \neq 0$ and integration over the set of electronic spatial and spin coordinates yields for the expansion coefficients in eqn. (2.80) the relation

$$c_j = \frac{\langle\Phi_j^{(0)}(\mathbf{q})|\hat{H}'|\Phi_0^{(0)}(\mathbf{q})\rangle}{E_0^{(0)} - E_j^{(0)}} = \frac{H'_{j0}}{E_0^{(0)} - E_j^{(0)}}, \tag{2.83}$$

resulting in

$$\Phi_0^{(1)}(\mathbf{q}) = \sum_{j\neq 0}\left(\frac{H'_{j0}}{E_0^{(0)} - E_j^{(0)}}\right)\Phi_j^{(0)}(\mathbf{q}). \tag{2.84}$$

Hence, the distortion of the state of interest by the perturbation is modeled by mixing into it the other states of the system. This mixing is often described by stating that the perturbation induces virtual transitions to the other unperturbed states [150].

The second-order correction to the energy is obtained by the same technique, that is inserting the expansion of the second-order correction to the wave function,

$$\Phi_0^{(2)}(\mathbf{q}) = \sum_j b_j \Phi_j^{(0)}(\mathbf{q}), \tag{2.85}$$

into eqn. (2.79), followed by multiplication from the left by $\Phi_0^{(0)*}(\mathbf{q})$ and integration over the set of electronic spatial and spin coordinates yielding

$$E_0^{(2)} = \sum_{j\neq 0} c_j \langle \Phi_0^{(0)}(\mathbf{q}) | \hat{H}' | \Phi_j^{(0)}(\mathbf{q}) \rangle = \sum_{j\neq 0} \frac{H'_{0j} H'_{j0}}{E_0^{(0)} - E_j^{(0)}}, \tag{2.86}$$

where the expression for the expansion coefficients c_j and the notation for the matrix elements from eqn. (2.83) was used and $H'_{0j}H'_{j0} = |H'_{0j}|^2$. The algebra involved becomes more and more complicated at higher orders of perturbation theory and it is common to use diagrammatic techniques to classify and represent the various terms that appear in the perturbation theories expressions [136,150]. However, note that to obtain the energy correct to order $2n+1$ in the perturbation, it is sufficient to know the wave functions only to nth order in the perturbation [136,150]. In this thesis, energy corrections up to third-order are employed, see section (2.2.1.3) and Ref. [T5].

2.2.1.3 Standard Models

As described in section 2.2.1, the exact electronic wave function may formally be expressed as an (infinite) linear combination of SDs, eqn. (2.52), which are - as one possibility - obtained as eigenfunctions of the electronic Hamiltonian neglecting electron-electron interactions, c.f. eqn. (2.49). Unfortunately, even for medium sized one-electron expansions, eqn. (2.53), the number of SDs becomes too large to handle computationally for all but the smallest molecular systems: More precisely, expanding all MOs in K AOs, one gets $2K$ spin-orbitals that can be used to construct $\binom{2K}{N}$ SDs, where N is the number of electrons. Consequently, quantum chemical wave function based methods aim to achieve high accuracy using approximate N-electron expansions as short as possible, see also Figure 2.3.

Generally, these approximations seek to retain as many symmetries and properties of the exact wave function as possible. The antisymmetry requirement of the electronic wave function was already discussed and is taken into account using SDs. Furthermore [145,148,151]:

- In non-relativistic theory, the exact electronic wave functions are eigenfunctions of the total and projected spin-operators $\hat{S}^2$ and $\hat{S}_z$, respectively. The correct spin behavior may be enforced by expanding the approximate wave function in symmetry-adapted linear combinations of SDs, so-called configuration-state-functions (CSFs) or simply configurations. In the case of closed-shell singlet states the CSF corresponds to a single SD.
- Within the Born-Oppenheimer approximation, the exact electronic wave functions form a basis for an irreducible representation of the molecular point group. The same spatial symmetry may be enforced by expanding the approximate wave function in SDs

constructed from a set of symmetry-adapted orbitals. Consequently, the approximate wave functions of nonlinear molecules become eigenfunctions of the discrete symmetry operations $\hat{R}$ of the molecular point group and linear molecules additionally become eigenfunctions of the projected orbital angular momentum operator $\hat{L}_{\mathrm{z}}$.

- Approximate methods should scale correctly - that is, should scale as the exact energy does - with the number of particles in the systems [170,171]. This property is referred to as size-extensitivity, see section (2.2.1.4) for further details and empirical corrections for approximate methods that are not size-extensive.

- The variational optimization of the energy expectation value $E[\Phi(\mathbf{q})] = \langle\Phi(\mathbf{q})|\hat{H}_{\mathrm{el}}|\Phi(\mathbf{q})\rangle$ subject to the constraint of normalized electronic wave functions, $\langle\Phi(\mathbf{q})|\Phi(\mathbf{q})\rangle = 1$, is equivalent to the solution of the time-independent electronic Schrödinger equation (section 2.2.1.1). It is desirable to optimize approximate wave functions variationally, resulting in a high degree of control over the calculations, such as the systematic approach to the exact ground state energy from above upon increase of the variational parameters in the approximate electronic wave function.

The reader is referred to Ref. [148] for an elaborate list of requirements on the electronic wave function. Here, it shall be added that the enforcement of spin and point-group symmetries on approximate wave functions constitutes a restriction on the wave function, which in variational calculations may raise the electronic energy above what would be obtained in an unrestricted treatment. Furthermore, it turns out to be difficult to reconcile the requirements of variational optimizations and of size-extensitivity [148].

Hartree-Fock (HF) Method

Electronic ground state wave functions are often dominated by a single CSF, which corresponds to a single SD in the case of closed-shell molecular systems, which is the only case considered in this section. This SD is obtained by choosing a SD, $\Phi^{\mathrm{SD}}(\mathbf{q})$, as trial function in the variation method (section 2.2.1.1) and finding those spin-orbitals, for which the auxiliary functional, $G[\Phi^{\mathrm{SD}}(\mathbf{q})] = G[\{\phi_m(\mathbf{q}_i)\}]$, c.f. eqn. (2.55), becomes stationary according to

$$\frac{\delta G[\{\phi_m(\mathbf{q}_i)\}]}{\delta\phi_m^*(\mathbf{q}_i)} \stackrel{!}{=} 0, \tag{2.87}$$

c.f. eqns. (2.56) and (2.60)[7]. This procedure, which is referred to as the Hartree-Fock (HF) method, leads, after some minor modifications, see Appendix 6.2, to the canonical HF equations, determining the set of optimal HF spin-orbitals $\left\{\phi_m^{\mathrm{HF}}(\mathbf{q}_i)\right\}$ as eigenfunctions of the one-electron HF operator $\hat{f}^{\mathrm{HF}}(\mathbf{q}_i)$ according to

$$\underbrace{\left(-\frac{1}{2}\boldsymbol{\nabla}_{\mathbf{r}_i}^2 - \sum_{A=1}^{M}\frac{Z_A}{|\mathbf{r}_i-\mathbf{R}_A|} + v^{\mathrm{HF}}(\mathbf{q}_i)\right)}_{\hat{f}^{\mathrm{HF}}(\mathbf{q}_i)}\phi_m^{\mathrm{HF}}(\mathbf{q}_i) = \epsilon_m^{\mathrm{HF}}\phi_m^{\mathrm{HF}}(\mathbf{q}_i). \tag{2.88}$$

[7] In section 2.2.1.1, the trial function, eqn. (2.58), was optimized in terms of a set of parameters $\{\alpha_j\}$ by means of partial derivatives. Here, the trial function $\Phi^{\mathrm{SD}}(\mathbf{q})$ is optimized in terms of a set of functions $\{\phi_m(\mathbf{q}_i)\}$ by means of functional derivatives; see also Appendix 6.1 and 6.2.

Here, $\vartheta^{\mathrm{HF}}(\mathbf{q}_i)$ is an average potential experienced by one electron due to the presence of the other electrons in the molecular system; for further details see Appendix 6.2. Hence, the essence of the HF approximation is to replace the complicated many-electron problem by a one-electron problem, in which the electron-electron repulsion is treated in an average way. Moreover, since the HF potential $\vartheta^{\mathrm{HF}}(\mathbf{q}_i)$ for electron i depends on the spin-orbitals of all other electrons, the Fock operator $\hat{f}^{\mathrm{HF}}(\mathbf{q}_i)$ depends on its eigenfunctions. Hence, the HF equations are non-linear and must be solved iteratively[8].

In the restricted HF method (RHF), the set of HF spin-orbitals is expressed according to eqn. (2.48) and the spin-orbital HF equations (2.88) are converted to spatial eigenvalue equations by integrating out the spin-functions [136]. Moreover, since the numerical solution of the resulting equations is feasible only for systems containing a few electrons, the set of spatial molecular-orbitals $\left\{\psi_m^{\mathrm{HF}}(\mathbf{r}_i)\right\}$ is usually expanded in an auxiliary set of K real-valued one-electron basis-functions, c.f. eqn. (2.53) and section (2.2.4). Such a treatment yields K HF MOs, $\psi_m^{\mathrm{HF}}(\mathbf{r}_i)$, and $2K$ HF spin-orbitals, $\phi_m^{\mathrm{HF}}(\mathbf{q}_i)$. The HF wave function $\Phi^{\mathrm{HF}}(\mathbf{q})$ is constructed using the N HF spin-orbitals with the lowest associated eigenvalues, ϵ_m^{HF} with $i = 1, \ldots, N$, where N is the number of electrons and the associated energy is given by $E^{\mathrm{HF}} = \langle \Phi^{\mathrm{HF}}(\mathbf{q}) | \hat{H}_{\mathrm{el}} | \Phi^{\mathrm{HF}}(\mathbf{q}) \rangle$, which is readily calculated in terms of the HF spin-orbitals using the Condon-Slater rules [136], see also Appendix 6.2. These spin-orbitals are referred to as the occupied HF spin-orbitals, whereas the remaining $2K - N$ spin-orbitals are the virtual spin-orbitals. The HF wave function yields quite good equilibrium structures and reasonable molecular properties such as dipole moments, electric polarizabilities, force constants [148].

Post HF Methods

Even more importantly, the HF method serves as the starting point for more accurate methods. The most straightforward extension is to perform a CI calculation using the HF wave function as reference. Hence, the CI wave function is written as a linear combination of L CSFs

Single Reference Methods

$$\Phi^{\mathrm{CI}}(\mathbf{q}) = \underbrace{\underbrace{C^{\mathrm{HF}}\Phi^{\mathrm{HF}}(\mathbf{q}) + \sum_{ar} C_{a\to r}\Phi^{\mathrm{HF}}_{a\to r}(\mathbf{q}) + +}_{\mathrm{CIS}} \sum_{\substack{a<b \\ r<s}} C_{\substack{a\to r \\ b\to s}} \Phi^{\mathrm{HF}}_{\substack{a\to r \\ b\to s}}(\mathbf{q}) + \ldots .}_{\mathrm{CISD}} \tag{2.89}$$

Here, $\Phi^{\mathrm{HF}}_{a\to r}(\mathbf{q})$ is a so-called singly excited CSF, resulting from the replacement of the occupied HF spin-orbital $\phi_a^{\mathrm{HF}}(\mathbf{q}_i)$ by the unoccupied HF spin-orbital $\phi_r^{\mathrm{HF}}(\mathbf{q}_i)$ in the HF wave function including spin-adaptation [136], $\Phi^{\mathrm{HF}}_{\substack{a\to r \\ b\to s}}(\mathbf{q})$ is a doubly excited CSF in which the occupied spin-orbitals $\phi_a^{\mathrm{HF}}(\mathbf{q}_i)$ and $\phi_b^{\mathrm{HF}}(\mathbf{q}_i)$ have been replaced by the unoccupied spin-orbitals $\phi_r^{\mathrm{HF}}(\mathbf{q}_i)$ and $\phi_s^{\mathrm{HF}}(\mathbf{q}_i)$ including spin-adaptation and so on. Usually, the core-orbitals, that is the spin-orbitals associated with the 1s shell in the case of carbon-atoms, remain doubly occupied, resulting in so-called valence CI calculations. The same approximation is usually used in all post HF methods discussed in the following.

Truncation of the CI expansion including only singly excited CSFs is termed a CI calculation with singles (CIS), whereas calculations including also the double excitations are referred to as CI

[8] Note that crude approximations of the respective lowest lying electronic states, which have different symmetries than the electronic ground state, may be calculated by imposing the respective symmetry on the trial function $\Phi^{\mathrm{SD}}(\mathbf{q})$. However, usually - as well as in this thesis - the HF method is applied solely to the electronic ground state.

calculations with singles and doubles (CISD) and so on, c.f. eqn. (2.89). Hence, the HF method serves as a so-called spin-orbital generator [148] for the CI method, which yields reasonable results for the electronic ground state when the exact electronic wave function is dominated by the HF wave function. Such methods are referred to as single reference methods. Note that, although the CI method allows the straightforward calculation of excited electronic states (section 2.2.1.1), usually more sophisticated, so-called multi-reference methods are used, see below, since the HF method is no appropriate orbital-generator for the quantitative description of excited electronic states.

A Full CI calculation based on the HF reference function using a complete one-electron basis-set is of course formally exact since the HF operator is Hermitian such that eqns. (2.52) and (2.89) yield the same result in the Full CI limit. In practical calculations, the one-electron basis has to be truncated at some point and Full CI calculations in a reasonably large one-electron basis serve as benchmark calculations for small molecular systems against which different post HF methods, which may on their term be applied to bigger systems, can be tested and calibrated. The non-variational but size-extensive [136, 148, 171] Møller-Plesset and Coupled-Cluster approaches are two prominent examples: They are also single reference methods and as such based on the requirement that the HF wave function represents a reasonable zeroth-order approximation to the true wave function.

In the Møller-Plesset (MP) method, the HF method is improved by means of perturbation theory (section 2.2.1.2). The MP unperturbed Hamiltonian is taken as the sum of the one-electron Fock operators, eqn. (2.88), according to

$$\hat{H}^{(0)} = \sum_{i}^{N} \hat{f}^{\mathrm{HF}}(\mathbf{q}_i), \tag{2.90}$$

such that the zeroth-order wave functions are all possible SDs formed using any N of the HF spin-orbitals, $\Phi_j^{(0)}(\mathbf{q}) = \Phi_j^{\mathrm{HF}}(\mathbf{q})$, c.f. eqn. (2.73), with corresponding energies $E_j^{(0)} = E_j^{\mathrm{HF}}$. Furthermore, the perturbation $\hat{H}'$ is the difference between the exact inter-electronic repulsions and the average HF potentials $\vartheta^{\mathrm{HF}}(\mathbf{r}_i)$, c.f. eqns. (2.72) and (2.88). Consequently, the MP energy correct to first order is just the HF energy, $E_0^{(0)} + E_0^{(1)} = E^{\mathrm{HF}}$, c.f. eqn. (2.82). The second order correction to the energy is given by

$$E_0^{(2)} = \sum_{j} \frac{|\langle \Phi_j^{\mathrm{HF}}(\mathbf{q}) | \hat{H}' | \Phi^{\mathrm{HF}}(\mathbf{q}) \rangle|^2}{E^{\mathrm{HF}} - E_j^{\mathrm{HF}}}, \tag{2.91}$$

c.f. eqn. (2.86). Since, according to Brillouin's theorem (see e.g. Ref. [136]), singly excited SDs do not interact directly with a reference HF determinant, $\langle \Phi_{a\to r}^{\mathrm{HF}}(\mathbf{q}) | \hat{H}' | \Phi^{\mathrm{HF}}(\mathbf{q}) \rangle = 0$, and, according to the Condon-Slater rules, matrix elements of two-electron operators involving SDs differing by more than two spin-orbitals vanish, only doubly excited SDs appear in eqn. (2.91).

The inclusion of the second-order energy correction in MP perturbation theory is designated MP2, the inclusion of the third order energy correction MP3 and so on, with MP2 being the most popular correction.

In the Coupled-Cluster (CC) method, the exact electronic ground state wave function is related to the Hartree-Fock wave function by [137,148,150]

$$\Phi_0(\mathbf{q}) = e^{\hat{C}}\Phi^{\mathrm{HF}}(\mathbf{q}). \tag{2.92}$$

The exponential operator $e^{\hat{C}}$ is defined by the series expansion

$$e^{\hat{C}} = \sum_{n}^{\infty} \frac{1}{n!}\hat{C}^n. \tag{2.93}$$

The cluster operator $\hat{C}$ is the sum of a one-electron excitation operator $\hat{C}_1$, two-electron excitation operator $\hat{C}_2$, ..., N-electron excitation operator $\hat{C}_N$ according to

$$\hat{C} = \hat{C}_1 + \hat{C}_2 + \ldots + \hat{C}_N \tag{2.94}$$

with

$$\hat{C}_1\Phi^{\mathrm{HF}}(\mathbf{q}) = \sum_{ar} t_{a\to r}\Phi^{\mathrm{HF}}_{a\to r}(\mathbf{q}), \qquad \hat{C}_2\Phi^{\mathrm{HF}}(\mathbf{q}) = \sum_{\substack{a<b\\ r<s}} t^{\,a\to r}_{\,b\to s}\,\Phi^{\mathrm{HF}}_{\substack{a\to r\\ b\to s}}(\mathbf{q}), \tag{2.95}$$

c.f. eqn. (2.89). The coefficients $t_{a\to r}$ are called single excitation amplitudes, the coefficients $t^{\,a\to b}_{\,r\to s}$ double excitation amplitudes and so on. Since no more than N electrons can be excited from the N-electron wave function $\Phi^{\mathrm{HF}}(\mathbf{q})$, no operators beyond $\hat{C}_N$ appear in eqn. (2.94). By definition, when any of the excitation operators in eqn. (2.94) acts on a SD containing both occupied and virtual spin-orbitals, the resulting sum contains only determinants with excitations from those spin-orbitals that are occupied in $\Phi^{\mathrm{HF}}(\mathbf{q})$ and not from virtual spin-orbitals.

The CI and CC wave functions, eqns. (2.89) and (2.92), respectively, are entirely equivalent provided all excitations are included in the expressions [148]. Their non-equivalence becomes apparent only when the respective expressions are truncated: In the approach referred to as "Coupled Cluster singles and doubles" (CCSD), the cluster operator, eqn. (2.94), is approximated as $\hat{C} \approx \hat{C}_1 + \hat{C}_2$. Furthermore, in CCD, only $\hat{C}_2$ is employed, whereas in CCSDT, $\hat{C}$ is given by $\hat{C}_1 + \hat{C}_2 + \hat{C}_3$. It is important to realize that any approximate CC wave function contains contributions from all SDs that may be generated within a given one-electron basis-set of Hartree-Fock orbitals [148]. Thus, for example the CCSD wave function may be regarded as a particular approximation to the Full CI wave function, where the coefficients of the higher than doubly excited determinants are generated from those associated with the single and double excitations so as to ensure size-extensitivity. Thus, in CC theory one usually works with individual SDs rather than with configuration state functions [137].

In the variational CI method, direct optimization of the corresponding energy function in terms of the variational parameters, c.f. eqn. (2.60), leads to a standard eigenvalue problem of linear algebra, eqn. (2.62). The analogous variational minimization of the CC energy, on the other hand, is far more complicated and is of practically no use in molecular calculations [148]. In practice, CC wave functions may be optimized by the solution of the projected electronic Schrödinger equation [148]

$$\langle\Phi^{\mathrm{HF}}_j(\mathbf{q})|\hat{H}_{\mathrm{el}}|e^{\hat{C}}\Phi^{\mathrm{HF}}(\mathbf{q})\rangle = E_0\langle\Phi^{\mathrm{HF}}_j(\mathbf{q})|e^{\hat{C}}\Phi^{\mathrm{HF}}(\mathbf{q})\rangle, \tag{2.96}$$

where $\Phi_j^{\mathrm{HF}}(\mathbf{q})$ is any excited HF wave function that appears in the expansion of the wave function according to eqn. (2.92) at the given level of approximation of the Cluster operator $\hat{C}$, resulting in m equations for m unknown connected amplitudes[9].

Moreover, the CC energy is obtained by projection against the Hartree-Fock state

$$E_0 = \langle \Phi^{\mathrm{HF}}(\mathbf{q}) | \hat{H}_{\mathrm{el}} | e^{\hat{C}} \Phi^{\mathrm{HF}}(\mathbf{q}) \rangle. \tag{2.97}$$

In CC theory, contrary to CI theory, the solution of the projected electronic Schrödinger equation is not equivalent to the variational optimization of the energy, such that CC theory is not variational [136,148].

In the case of the CCD approximation with $\hat{C} \approx \hat{C}_2$, this procedure leads to [150]

$$\begin{aligned} \langle \Phi^{\mathrm{HF}}_{\substack{a\to b \\ r\to s}}(\mathbf{q}) | \hat{H}_{\mathrm{el}} | \Phi^{\mathrm{HF}}(\mathbf{q}) \rangle + \langle \Phi^{\mathrm{HF}}_{\substack{a\to b \\ r\to s}}(\mathbf{q}) | \hat{H}_{\mathrm{el}} \hat{C}_2 | \Phi^{\mathrm{HF}}(\mathbf{q}) \rangle + \tfrac{1}{2} \langle \Phi^{\mathrm{HF}}_{\substack{a\to b \\ r\to s}}(\mathbf{q}) | \hat{H}_{\mathrm{el}} \hat{C}_2^2 | \Phi^{\mathrm{HF}}(\mathbf{q}) \rangle \\ = \left(E^{\mathrm{HF}} + \langle \Phi^{\mathrm{HF}}(\mathbf{q}) | \hat{H}_{\mathrm{el}} \hat{C}_2 | \Phi^{\mathrm{HF}}(\mathbf{q}) \rangle \right) \langle \Phi^{\mathrm{HF}}_{\substack{a\to b \\ r\to s}}(\mathbf{q}) | \hat{C}_2 | \Phi^{\mathrm{HF}}(\mathbf{q}) \rangle \end{aligned} \tag{2.98}$$

and

$$E^{\mathrm{HF}} + \langle \Phi^{\mathrm{HF}}(\mathbf{q}) | \hat{H}_{\mathrm{el}} \hat{C}_2 | \Phi^{\mathrm{HF}}(\mathbf{q}) \rangle = E_{\mathrm{CC}}, \tag{2.99}$$

where the Coupled-Cluster energy E_{CC} was introduced. In the derivation, the orthonormality of SDs as well as the the Condon-Slater rules [137,150] were used. These non-linear equations must be solved iteratively.

Finally, it is convenient for various applications of CC theory to express the projected CC equations, eqns. (2.96) and (2.97), in the equivalent forms

$$\langle \Phi_j^{\mathrm{HF}}(\mathbf{q}) | e^{-\hat{C}} \hat{H}_{\mathrm{el}} e^{\hat{C}} | \Phi^{\mathrm{HF}}(\mathbf{q}) \rangle = 0 \tag{2.100}$$

and

$$E_0 = \langle \Phi^{\mathrm{HF}}(\mathbf{q}) | e^{-\hat{C}} \hat{H}_{\mathrm{el}} e^{\hat{C}} | \Phi^{\mathrm{HF}}(\mathbf{q}) \rangle, \tag{2.101}$$

which is, among other technical advantages, a useful starting point for improvements of the respective CC approximations based on perturbation theory [148]. Such an improvement is realized in the so-called CCSD(T) method, in which, on top of the CCSD approximation, the contributions from the triple excitation amplitudes are estimated by perturbation theory [148].

Multi Reference Methods

In the case that different CSFs are (near) degenerate, strong mixing might occur, resulting in electronic wave functions which are dominated by more than one electronic configuration. Such situations occur for example in the process of the dissociation of chemical bonds or at certain points on the potential energy surface with competing valence structures [172], see also Ref. [T5] for details. The single reference post Hartree-Fock methods described above are incapable to give a reasonable description of the electronic structure in such situations, since the HF method is inappropriate as an orbital-generator for these multiconfigurational wave functions: The HF orbitals optimized for a single CSF may have little or no relevance to the

[9] In Coupled-Cluster Theory, the effect of $e^{\hat{C}}$ on $\Phi^{\mathrm{HF}}(\mathbf{q})$ results, among many other excitations, in double excitations of the form $\hat{C}_2 \Phi^{\mathrm{HF}}(\mathbf{q})$ and $\hat{C}_1 \hat{C}_1 \Phi^{\mathrm{HF}}(\mathbf{q})$. The former double excitations are referred to as "connected" double excitation, whereas the latter are referred to as "disconnected" double excitation.

optimal MOs for the multiconfigurational wave function [148]. A straightforward solution to this multiconfigurational problem is to carry out a CI calculation, in which the MOs are variationally optimized simultaneously with the coefficients of the CSFs, thereby ensuring that the orbitals employed in the wave function are optimal for the problem at hand and do not introduce a bias towards a particular configuration in the calculation. This approach is referred to as the multiconfigurational self-consistent field (MCSCF) method [172–174]. The most commonly used form of MCSCF calculations are complete active space (CAS) calculations, in which the total MO space, obtained by a preceding HF calculation, is partitioned into a set of inactive orbitals, a set of active orbitals and a set of secondary (virtual) orbitals: The CASSCF wave function is then constructed as a linear combination of CSFs in which the inactive orbitals are restricted to be doubly occupied, the active orbitals are subject to no restrictions, and the secondary orbitals are not occupied in all the configurations, and the MOs as well the CI expansion coefficients are variationally optimized. The CASSCF method is used either to provide reasonable qualitative descriptions of multiconfigurational electronic wave functions or as an orbital-generator for more elaborate treatments of the electronic structure. The choice of an active space may be rationalized by certain criteria, for instance the proper description of molecular dissociation or the inclusion of all CSFs, which describe competing valence structures of molecular systems. The reader is referred to the Appendix in Ref. [T5] for the motivation of a minimal active space in the latter case, exemplified for the DCR of SBV. The simultaneous variational optimization of both the orbitals and the CI expansion coefficients is technically demanding and is described in more detail in section 2.2.1.5.

MCSCF wave functions, especially in their CASSCF version, often serve as the starting point for successive CI or perturbational calculations. Hence, in the same spirit as HF wave functions serve as the starting point, that is as reference, for successive CI calculations, eqn. (2.89), MCSCF wave functions may be used as the reference in multi-reference CI calculations referred to as MRCI calculations [175, 176]. A popular version is MRCISD, in which single and double excitations in the reference CSFs are taken into account. This method is also widely used for the calculation of excited electronic states. In this context, different optimization schemes for the underlying MCSCF, or more typically, CASSCF wave function may be used. One possibility is the simultaneous optimization of the respective electronic states in so-called state-averaged calculations [148], leading to a common set of MOs for the respective electronic states or separate optimizations of the respective states, which are refined afterwards; see also section 2.2.1.5 for further details.

Analogously, instead of improving a HF wave function as zeroth-order wave function using perturbation theory as in the Møller-Plesset method, a CASSCF wave function may be used as zeroth-order order wave function, leading to the CASPT2 method [172, 177] when energy corrections up to second order are included, and to the CASPT3 method [178] when energy corrections up to third order are included.

static and dynamic electron correlation

The difference between the lowest, exact non-relativistic eigenvalue of the time-independent electronic Schrödinger equation, E_0, and the HF energy, E^{HF}, at the basis-set limit, is defined as the correlation energy E_{corr} [136]

$$E_{\mathrm{corr}} = E_0 - E^{\mathrm{HF}}. \tag{2.102}$$

Hence in Quantum Chemistry, the term electron correlation is reserved for the correlation that

occurs upon superposition of CSFs, and the description provided by a single CSF is consequently referred to as uncorrelated. In this context, it is interesting to note that in general, a truly uncorrelated many-electron state is always represented by a product of one-particle functions, or more specifically by a product of MOs [148]. Using this definition, electronic states represented by a single SD may be either correlated or uncorrelated, depending on the spatial- and spin-parts of the electronic wave function: For example, the antisymmetry principle may be fulfilled by an antisymmetric spin-part, leaving the spatial-part in the product form, hence leading to a truly uncorrelated electronic wave function. On the other hand, a symmetric spin-part leads to an antisymmetric spatial-part, hence introducing so-called Fermi correlation, also referred to as exchange correlation, into the electronic wave function [148]. However, as stated above, correlated wave functions in Quantum Chemistry arise as superpositions of CSFs.

Correlation effects in molecules are normally partitioned into near-degeneracy effects (static correlation) and dynamic correlation. Inclusion of dynamic correlation arises from a desire to describe the detailed correlated motion of the electrons as induced by their instantaneous mutual repulsion. In the case of near-degeneracy effects, on the contrary, going beyond the HF method is unrelated to the repulsion of the electrons but necessary to describe e.g. molecular dissociation, see above. Summarizing, in the case of degeneracy effects, MCSCF methods are employed to deal primarily with the associated static electron correlation and serve in these cases as an orbital-generator for methods which account for dynamic electron correlation, e.g. the MRCI or CASPT2 methods. In the absence of degeneracy effects, the HF method constitutes a valid orbital-generator and single-reference correlation methods such as Møller-Plesset perturbation theory or single reference Coupled-Cluster methods may be used for the description of dynamic electron correlation.

2.2.1.4 Size-Extensitivity and the Davidson Correction

An approximate method for the solution of the time-independent electronic Schrödinger equation, eqn. (2.5), that scales correctly - that is, scales as the exact energy does - with the number of particles in the systems is termed size-extensive [170]. This is to be contrasted to size-consistency. According to Ref. [179], a size-consistent approximate method is one for which

$$E_{\mathrm{AB}}(d \to \infty) = E_{\mathrm{A}} + E_{\mathrm{B}}, \tag{2.103}$$

that is the energy of a dimer AB, consisting of the two monomers A and B, computed at infinite separation between the dimers ($d \to \infty$) equals the sum of the monomer energies, see also Ref. [171]. According to this definition, various single reference methods such as HF, MP2 or CCSD in their restricted versions are size-consistent for some fragmentation processes, e.g. dissociation of the H_2 dimer from the electronic ground state, while they are not size-consistent for others, e.g. dissociation of the H_2 molecule from the electronic ground state. These methods, however, are always size-extensive [171].

Truncated CI wave functions, including multireference CI, on the other hand, are neither size-consistent nor size-extensive. As an illustration, consider the CID method applied to a system containing two non-interacting fragments A and B with associated Hamilton operators $\hat{H}_{\mathrm{A}}$ and $\hat{H}_{\mathrm{B}}$, eigenfunctions $\Phi_{\mathrm{A}}^{\mathrm{CID}}(\mathbf{q})$ and $\Phi_{\mathrm{B}}^{\mathrm{CID}}(\mathbf{q})$, and associated composite CID wave function $\Phi_{\mathrm{AB}}^{\mathrm{CID}}(\mathbf{q})$. The associated total energy may be partitioned into a HF contribution $E_{\mathrm{AB}}^{\mathrm{HF}} =$

$E_A^{\mathrm{HF}} + E_B^{\mathrm{HF}}$ and a correlation contribution $E^{\mathrm{c}}_{\mathrm{AB}}$ due to the double excitations according to [148]

$$\begin{aligned} E^{\mathrm{c}}_{\mathrm{AB}} &= \frac{\langle \Phi^{\mathrm{CID}}_{\mathrm{AB}}(\mathbf{q}) | \hat{H}_{\mathrm{A}} + \hat{H}_{\mathrm{B}} - E^{\mathrm{HF}}_{\mathrm{A}} - E^{\mathrm{HF}}_{\mathrm{B}} | \Phi^{\mathrm{CID}}_{\mathrm{AB}}(\mathbf{q}) \rangle}{\langle \Phi^{\mathrm{CID}}_{\mathrm{AB}}(\mathbf{q}) | \Phi^{\mathrm{CID}}_{\mathrm{AB}}(\mathbf{q}) \rangle} \\ &= \frac{\langle \Phi^{\mathrm{CID}}_{\mathrm{A}}(\mathbf{q}) | \hat{H}_{\mathrm{A}} - E^{\mathrm{HF}}_{\mathrm{A}} | \Phi^{\mathrm{CID}}_{\mathrm{A}}(\mathbf{q}) \rangle + \langle \Phi^{\mathrm{CID}}_{\mathrm{B}}(\mathbf{q}) | \hat{H}_{\mathrm{B}} - E^{\mathrm{HF}}_{\mathrm{B}} | \Phi^{\mathrm{CID}}_{\mathrm{B}}(\mathbf{q}) \rangle}{\langle \Phi^{\mathrm{CID}}_{\mathrm{A}}(\mathbf{q}) | \Phi^{\mathrm{CID}}_{\mathrm{A}}(\mathbf{q}) \rangle + \langle \Phi^{\mathrm{CID}}_{\mathrm{B}}(\mathbf{q}) | \Phi^{\mathrm{CID}}_{\mathrm{B}}(\mathbf{q}) \rangle - 1}. \end{aligned} \tag{2.104}$$

Here, intermediate normalization of the CI wave function was used, that is the coefficient of the HF wave function is set to one, $C^{\mathrm{HF}} = 1$, c.f. eqn. (2.89), yielding $\langle \Phi^{\mathrm{HF}}(\mathbf{q}) | \Phi^{\mathrm{CID}}(\mathbf{q}) \rangle = 1$ [136, 148]. Hence, the correlation contributions $E^{\mathrm{c}}_{\mathrm{AB}}$, eqn. (2.104), of the truncated CID wave function is not size-extensive, since it does not separate into contribution of the individual fragments [148]. The use of truncated CI wave functions introduces an unphysical coupling of the non-interacting fragments, since, for a given CSF, the excitations allowed in one fragment depend on the excitations present in the other fragment [148].

Realizing that the numerator in eqn. (2.104) is size-extensive, approximately size-extensive schemes may be motivated [148]: Assuming that the correlation contribution to the wave function is small, the denominator in eqn. (2.104) may be replaced by 1, yielding the size-extensive expression

$$\tilde{E}^{\mathrm{c}}_{\mathrm{AB}} = \langle \Phi^{\mathrm{CID}}_{\mathrm{AB}}(\mathbf{q}) | \hat{H}_{\mathrm{A}} + \hat{H}_{\mathrm{B}} - E^{\mathrm{HF}}_{\mathrm{A}} - E^{\mathrm{HF}}_{\mathrm{B}} | \Phi^{\mathrm{CID}}_{\mathrm{AB}}(\mathbf{q}) \rangle. \tag{2.105}$$

Furthermore, the difference between the variational correlation contribution, eqn. (2.104), and the size-extensive expression, eqn. (2.105), for fragment A yields [148]

$$\begin{aligned} \tilde{E}^{\mathrm{c}}_{\mathrm{A}} - E^{\mathrm{c}}_{\mathrm{A}} &= \frac{\langle \Phi^{\mathrm{CID}}_{\mathrm{A}}(\mathbf{q}) | \hat{H}_{\mathrm{A}} - E^{\mathrm{HF}}_{\mathrm{A}} | \Phi^{\mathrm{CID}}_{\mathrm{A}}(\mathbf{q}) \rangle}{1 + \langle \Phi^{\mathrm{c}}_{\mathrm{A}}(\mathbf{q}) | \Phi^{\mathrm{c}}_{\mathrm{A}}(\mathbf{q}) \rangle} \langle \Phi^{\mathrm{c}}_{\mathrm{A}}(\mathbf{q}) | \Phi^{\mathrm{c}}_{\mathrm{A}}(\mathbf{q}) \rangle \\ &= E^{\mathrm{c}}_{\mathrm{A}} \frac{1 - C_0^2}{C_0^2}, \end{aligned} \tag{2.106}$$

where $\Phi^{\mathrm{c}}_{\mathrm{A}}(\mathbf{q}) = \Phi^{\mathrm{CID}}_{\mathrm{A}}(\mathbf{q}) - \Phi^{\mathrm{HF}}_{\mathrm{A}}(\mathbf{q})$ and C_0 is the normalization constant for the intermediately normalized CID wave function. Hence, the normalized CID wave function is given by

$$\Phi^{\mathrm{CID}}_{\mathrm{A,norm}}(\mathbf{q}) = C_0 \left(\Phi^{\mathrm{HF}}_{\mathrm{A}}(\mathbf{q}) + \Phi^{\mathrm{c}}_{\mathrm{A}}(\mathbf{q}) \right), \tag{2.107}$$

such that C_0 corresponds to the expansion coefficient of the Hartree-Fock wave function $\Phi^{\mathrm{HF}}_{\mathrm{A}}(\mathbf{q})$. Since C_0^2 is assumed to be close to one, the term $\frac{1-C_0^2}{C_0^2}$ may be replaced by $1 - C_0^2$ such that eqn. (2.106) reduces to

$$E^{\mathrm{Dav}}_{\mathrm{A}} = E^{\mathrm{corr}}_{\mathrm{A}} \left(1 - C_0^2 \right), \tag{2.108}$$

which is the Davidson correction [180]. This expression is often used to correct for the lack of size-extensitivity or, equivalently, for the lack of quadruple excitations in small molecular systems [148]. This is due to the fact that, for molecules containing roughly 50 electrons, CI calculations including quadruple excitations are effectively size-extensive [136]. It should be emphasized, however, that the Davidson correction does not provide a rigorous size-extensive

energy, since for example the term $\Phi_{\mathrm{A}}^{\mathrm{c}}(\mathbf{q})$, which represents the set of doubly excited CSFs, is obtained from the non-interacting composite system and differs from the one obtained in calculations on the individual system [148]. The Davidson correction, however, was shown by a large number of calculations to yield reasonable results [148], see also Ref. [T5]. The reader is also referred to Refs. [171,181] for alternative approximate corrections for size-extensitivity.

2.2.1.5 Technical aspects of MCSCF Theory

The MCSCF treatment in its CAS version, section 2.2.1.3, and subsequent MRCISD calculations including the Davidson correction (MRCISD+Dav, section 2.2.1.4) accounting for dynamic electron correlation, constitute the benchmark methods used in this thesis for the approximate solution of the time-independent electronic Schrödinger equation. In Refs. [T5] and [T6], these calculations focus on the electronic ground state, whereas Chapter 5 presents additionally results for the first excited electronic state in the case of the degenerate Cope rearrangement of semibullvalene as well as results of the potential energy curves of the two lowest lying electronic states for the diatomic molecule NaCl. Although the very involved numerical calculation of these MCSCF wave functions is readily implemented in most Quantum Chemistry ab-initio packages, see e.g. Refs. [134,135], these methods are not deemed to be black-box methods [148,172]. Consequently, in the following, some technical details of the optimization of MCSCF wave functions are given, with special emphasize on the simultaneous optimization of several electronic states in so-called state-averaged MCSCF calculations [182] as employed in Chapter 5.

In MCSCF calculations, both the set of CI coefficients $\{C_{ij}\}$, eqn. (2.52), and the set of molecular orbitals $\{\psi_m(\mathbf{r}_i)\}$, eqn. (2.53), are simultaneously optimized using the variation method, section 2.2.1.1. An important area of application of MCSCF Theory is the simultaneous study of several electronic states. Such studies may be carried out in different ways with the most common approaches being the separate optimization of the individual states [183] and the state averaged MCSCF approach [182], see also Refs. [148,172]: As usual, the n electronic states to be optimized are expressed as linear combinations of L N-electron basis functions according to

$$\Phi_i^{\mathrm{MCSCF}}(\mathbf{q}) = \sum_j^L C_{ij}\Phi'_j(\mathbf{q}) \quad \text{with} \quad i = 1, 2, \ldots, n, \tag{2.109}$$

where the N-electron basis functions $\Phi'_j(\mathbf{q})$ are usually taken to be CSFs, c.f. section 2.2.1.3, but may also be taken to be single SDs [148,172]. In the separate optimization of the individual states, the corresponding MCSCF energy for electronic state i,

$$E_i^{\mathrm{MCSCF}} = \langle\Phi_i^{\mathrm{MCSCF}}(\mathbf{q})|\hat{H}_{\mathrm{el}}|\Phi_i^{\mathrm{MCSCF}}(\mathbf{q})\rangle, \tag{2.110}$$

is variationally optimized. The n wave functions obtained in this way are not orthogonal since they have been calculated independently in separate calculations. However, to obtain a set of orthogonal and non-interacting states, $\langle\Phi_i^{\mathrm{MCSCF}}(\mathbf{q})|\Phi_j^{\mathrm{MCSCF}}(\mathbf{q})\rangle = \delta_{ij}$ and $\langle\Phi_i^{\mathrm{MCSCF}}(\mathbf{q})|\hat{H}_{\mathrm{el}}|\Phi_j^{\mathrm{MCSCF}}(\mathbf{q})\rangle = E_i^{\mathrm{MCSCF}}\delta_{ij}$, respectively, one may subsequently carry out an additional CI calculation in the basis of the n previously optimized MCSCF wave functions [183].

In the state averaged MCSCF approach, on the other hand, the n electronic states are simultaneously optimized in a common basis of MOs. In this approach, the MOs are not optimized separately for each electronic state, but are instead determined to minimize an average MCSCF energy according to [182]

$$E_{\mathrm{av}}^{\mathrm{MCSCF}} = \sum_{i}^{n} w_i E_i^{\mathrm{MCSCF}}, \tag{2.111}$$

where a weight factor w_i was introduced for each electronic state i. These weight factors are fixed numerical parameters, which may be chosen on some physical considerations [148]. In this state-averaged approach, the description of each electronic state suffers from the fact that the MOs are not optimal for each state separately. On the other hand, this method provides directly a set of orthonormal, non-interacting electronic states and is well suited as an orbital-generator for subsequent CI calculations.

Depending on the chosen optimization scheme, one of the expressions, eqns. (2.110) or (2.111), must be made stationary with respect to changes in the set of CI coefficients $\{C_{ij}\}$ and the set of MOs $\{\psi_m(\mathbf{r}_i)\}$, subject to the normalization and orbital orthogonality constraints,

$$\sum_{j}^{L} |C_{ij}|^2 = 1 \qquad \text{and} \qquad \langle \psi_i(\mathbf{r}_i) | \psi_j(\mathbf{r}_i) \rangle = \delta_{ij}, \tag{2.112}$$

respectively. These constraints might be taken into account using Lagrange multipliers, see section 2.2.1.1 and Appendix 6.2, but such optimization schemes converge slowly or not at all in the case of MCSCF wave functions [148,172,182]. Hence, for such optimizations, it is usually necessary to use a so-called exponential parametrization of the MCSCF wave function leading to a set of independent variational parameters instead of the set of CI coefficients $\{C_{ij}\}$ and the set of MOs $\{\psi_m(\mathbf{r}_i)\}$. There is then no need for Lagrange multipliers, and numerical methods for unconstrained optimizations may be used [148,172,182]; further details of the exponential parametrization of the MCSCF wave function are given below[10]. Additionally, the straightforward variational optimization of the respective MCSCF energy functions as described in section 2.2.1.1, see also Appendix 6.2, with respect to these independent variational parameters, do usually not converge either [148,172,182]. Instead, so-called second-order methods, involving the expansion of the respective MCSCF energy function up to second-order in the variational parameters must be used. These second-order methods will also be sketched below. Before discussing the exponential parametrization of the MCSCF wave function and the second-order optimization scheme, the "second quantization" formalism is introduced. This is the standard formalism for practically all post HF methods, since it reduces much of the formal manipulations to algebra, allowing the emerging relations to be developed in an elegant manner [148].

[10] Note that, concerning the variational optimization of the set of CI expansion coefficients $\{C_{ij}\}$, so-called redundant optimizations might be used in the case of single state optimizations using the energy function given in eqn. (2.110), which avoid the more involved exponential parametrization, for details see e.g. Ref. [148]. In multi-state optimizations, using the MCSCF energy function given in eqn. (2.111), however, an exponential parametrization of the configuration space must usually be used [148,172,182]. The exponential parametrization of the orbital space, on the other hand, allowing for unconstrained optimizations, is necessary both in single state and state-averaged MCSCF calculations [148,172,182].

Second Quantization

In the second quantization formalism [148, 172], both the electronic wave function and the quantum mechanical operators, e.g. the electronic Hamiltonian, are expressed in terms of elementary creation and annihilation operators. In second quantization, a linear vector space, the Fock space, is introduced, where each SD, eqn. (2.51), is represented by an occupation number (ON) vector

$$|\mathbf{k}\rangle = |k_1 k_2, \ldots, k_l\rangle, \qquad \text{with} \qquad \mathrm{k_P} = \begin{cases} 1 & \phi_P \text{ occupied} \\ 0 & \phi_P \text{ unoccupied} \end{cases}, \tag{2.113}$$

where l is the number of spin-orbitals. Thus, the occupation number k_P is 1 if the spin-orbital ϕ_P is present in the SD and 0 if it is absent. The ON vector which contains no electrons is referred to as the vacuum state

$$|\mathrm{vac}\rangle = |0_1, 0_2, \ldots, 0_l\rangle. \tag{2.114}$$

The N elementary creation operators, $\hat{a}_P^\dagger$, which add an electron in spin-orbital P, are defined by

$$\begin{aligned} \hat{a}_P^\dagger |k_1, k_2, \ldots, 0_P, \ldots, k_l\rangle &= \Gamma_P^{\mathbf{k}} |k_1, k_2, \ldots, 1_P, \ldots, k_l\rangle \\ \hat{a}_P^\dagger |k_1, k_2, \ldots, 1_P, \ldots, k_l\rangle &= 0, \end{aligned} \tag{2.115}$$

where

$$\Gamma_P^{\mathbf{k}} = \prod_{Q=1}^{p-1} (-1)^{k_Q}. \tag{2.116}$$

The phase factor $\Gamma_P^{\mathbf{k}}$ is equal to $+1$ if there are an even number of electrons in the spin-orbitals $Q < P$ and -1 if there are an odd number of electrons in these spin-orbitals. The corresponding annihilation operator, $\hat{a}_P$, is defined as

$$\hat{a}_P |\mathbf{k}\rangle = \delta_{k_P 1} \Gamma_P^{\mathbf{k}} |k_1, \ldots, 0_P, \ldots, k_l\rangle, \tag{2.117}$$

i.e. it reduces k_P from 1 to 0 if spin-orbital P is occupied and it gives 0 if the spin-orbital is unoccupied. The creation and annihilation operators are the adjoint of each other and the latter gives zero when acting on the vacuum state

$$a_P |\mathrm{vac}\rangle = 0, \tag{2.118}$$

for more details see e.g. Refs. [148, 172].

Electronic Hamiltonian in Second Quantization

A second quantization operator is constructed by requiring its matrix elements between two ON vectors to be equal to the matrix elements of the corresponding first quantization operators between the corresponding SDs. Consequently, the second quantization analog of the electronic

Hamiltonian $\hat{H}_{\mathrm{el}}$, eqn. (2.4), is given in the spin-orbital basis by [148,172]

$$\begin{aligned}\hat{H}_{\mathrm{el}}^{\mathrm{2nd}} = &\sum_{PQ} \underbrace{\int \phi_P^*(\mathbf{q}_i) \left(-\frac{1}{2}\nabla^2 - \sum_A \frac{Z_A}{|\mathbf{r}_i - \mathbf{R}_A|} \right) \phi_Q(\mathbf{q}_i) \mathrm{d}\mathbf{q}_i}_{h_{PQ}} \hat{a}_P^\dagger \hat{a}_Q \\ &+ \frac{1}{2} \sum_{PQRS} \underbrace{\int\int \frac{\phi_P^*(\mathbf{q}_i)\phi_R^*(\mathbf{q}_j)\phi_Q(\mathbf{q}_i)\phi_S(\mathbf{q}_j)}{|\mathbf{r}_i - \mathbf{r}_j|} \mathrm{d}\mathbf{q}_i \mathrm{d}\mathbf{q}_j}_{g_{PQRS}} a_P^\dagger a_R^\dagger a_S a_Q,\end{aligned} \tag{2.119}$$

where the molecular one- and two-electron integrals, h_{PQ} and g_{PQRS}, respectively, were introduced with the respective summations running over all spin-orbitals. In the case of spin-free operators as the electronic Hamiltonian and using spin-orbitals of the form $\phi_{p\mu}(\mathbf{q}_i) = \psi_p(\mathbf{r}_i)\mu(\sigma)$, c.f. eqn. (2.48), integration over the spin-variables, c.f. eqn. (2.47), leads to the second quantization representation of the electronic Hamiltonian in the MO basis [148,172]:

$$\hat{\tilde{H}}_{\mathrm{el}}^{\mathrm{2nd}} = \sum_{pq} h_{pq} \underbrace{\sum_{\mu} \hat{a}_{p\mu}^\dagger \hat{a}_{q\mu}}_{\hat{E}_{pq}} + \frac{1}{2} \sum_{pqrs} g_{pqrs} \underbrace{\left(\sum_{\mu\nu} a_{p\mu}^\dagger a_{r\nu}^\dagger a_{s\nu} a_{q\mu} \right)}_{\hat{e}_{pqrs}}. \tag{2.120}$$

Here, the summation is over the MOs and the one- and two-electron integrals are defined in the MO basis, with analogous expressions as in the spin-orbital basis, eqn. (2.119), except that the integrations are over the spatial coordinates only. Note that upper case letters are used when referring to spin-orbitals and lower case letters are used for MOs. Furthermore, the singlet excitation operator and the two-electron excitation operator, $\hat{E}_{pq}$ and $\hat{e}_{pqrs}$, respectively, were introduced. These operators contain the elementary operators, e.g. the annihilation operator $\hat{a}_{p\mu}$, with composite indices, where the first index p refers to the orbital part and the second index μ to the spin-part of the spin-orbital $\phi_{p\mu}(\mathbf{q}_i) = \psi_p(\mathbf{r}_i)\mu(\sigma)$. Accordingly, the second quantization expression for the MCSCF energy for electronic state i, c.f. eqn. (2.110), is given by

$$E_i^{\mathrm{MCSCF}} = \langle I | \hat{\tilde{H}}_{\mathrm{el}}^{\mathrm{2nd}} | I \rangle = \sum_{pq} \underbrace{\langle I | \hat{E}_{pq} | I \rangle}_{D_{pq}} h_{pq} + \frac{1}{2} \sum_{pqrs} \underbrace{\sum_{\mu\nu} \langle I | a_{p\mu}^\dagger a_{r\nu}^\dagger a_{s\nu} a_{q\mu} | I \rangle}_{d_{pqrs}}, \tag{2.121}$$

where the MCSCF wave function $\Phi_i^{\mathrm{MCSCF}}(\mathbf{q})$ for state i, c.f. eqn. (2.109), is represented by the ON vector $|I\rangle$. Additionally, in eqn. (2.121), the one- and two-electron orbital density matrix elements, D_{pq} and d_{pqrs}, respectively, were introduced.

Exponential Parametrization

For the exponential parametrization of the orbital space, consider an ON vector $|\tilde{I}\rangle$, where the occupation numbers $\tilde{k}_1, \tilde{k}_2, \ldots, \tilde{k}_l$, c.f. eqn. (2.113), refer to a set of orthonormal spin-orbitals $\left\{ \tilde{\phi}_{p\mu}(\mathbf{q}_i) \right\}$. These spin-orbitals are obtained from another set $\{\phi_{p\mu}(\mathbf{q}_i)\}$, belonging to an ON vector $|I\rangle$, by a unitary transformation among the underlying MOs according to [172]

$$\tilde{\psi}_p(\mathbf{r}_i) = \sum_q \psi_q(\mathbf{r}_i) U_{qp}. \tag{2.122}$$

The corresponding transformation of the set of spin-orbitals $\{\phi_{p\mu}(\mathbf{q}_i)\}$ is obtained by multiplying eqn. (2.122) with an α or β spin-function. The elements of the unitary matrix $\mathbf{U}$ are not independent, since they are coupled by the unitary relation $\mathbf{U}^\dagger\mathbf{U} = \mathbf{U}\mathbf{U}^\dagger = \mathbf{1}$ and hence cannot be used as the independent variational parameters. It can be shown, however, that any unitary matrix $\mathbf{U}$ can be written as the matrix exponential of an anti-Hermitian matrix $\boldsymbol{\kappa}$ [148]

$$\mathbf{U} = \exp(-\boldsymbol{\kappa}) \qquad \text{with} \qquad \boldsymbol{\kappa}^\dagger = -\boldsymbol{\kappa}. \tag{2.123}$$

The matrix elements of $\boldsymbol{\kappa}$ at the diagonal and below the diagonal may now be taken as the independent elements and the remaining elements may be generated by the anti-Hermitian condition $\kappa_{pq}^* = -\kappa_{qp}$. Keeping this restriction in mind, the elements of anti-Hermitian matrices like $\boldsymbol{\kappa}$ will be referred to as independent in the following. Assuming real MOs as usual, a transformation that preserves both the orthonormality of the MOs and the spin of the wave function may be written as [148,172]

$$|\tilde{I}(\boldsymbol{\kappa})\rangle = \exp(-\hat{\kappa})|I\rangle, \tag{2.124}$$

where the anti-Hermitian one-electron operator $\hat{\kappa}$ is given by

$$\hat{\kappa} = \sum_{p>q} \kappa_{pq}(\hat{E}_{pq} - \hat{E}_{qp}) = \sum_{p>q} \kappa_{pq}\hat{E}^-_{pq}. \tag{2.125}$$

The elements κ_{pq} with $p > q$ constitute the set of (real-valued) variational parameters for the optimization of the MOs and the singlet-excitation operators, $\hat{E}_{pq}$ and $\hat{E}_{qp}$, were defined in eqn. (2.120). Note that with the particular definition of the anti-Hermitian operator in eqn. (2.125), only spin-adapted unitary transformations among the MOs are carried out. Such kinds of restricted unitary transformations are usually referred to as spin-adapted rotations among the MOs [148]. Accordingly, further restrictions might be introduced via the anti-Hermitian operator $\hat{\kappa}$, i.e. preservation of the spatial symmetry of the associated wavefuncion in terms of so-called point-group symmetry-adapted rotations among the MOs [148].

The exponential parametrization of the configuration space works in much the same way as in the orbital space: Consider a set of L orthonormal states $|I\rangle$ which form a basis in the L dimensional configuration space. From the L states $|I\rangle$, a new set of orthonormal states $|\tilde{I}\rangle$ may be generated by a unitary transformation according to [148,172]

$$\begin{aligned} |\tilde{I}(\mathbf{S})\rangle &= \sum_Q |Q\rangle U_{QI} = \sum_Q |Q\rangle [\exp(-\mathbf{S})]_{QI} \\ &= \exp(-\hat{S})|I\rangle = \exp\left[-\sum_{QR} S_{QR}|Q\rangle\langle R|\right]|I\rangle, \end{aligned} \tag{2.126}$$

where S_{QR} are the independent elements of the anti-Hermitian matrix $\mathbf{S}$. The equivalence of the matrix and operator representation in eqn. (2.126) is established by expanding the exponential operator $\exp(-\hat{S})$, for further details see Refs. [148,172]. Hence, $\exp(-\hat{\mathrm{S}})|\mathrm{I}\rangle$, eqn. (2.126), represents a unitarily transformed configuration state, whereas $\exp(-\hat{\kappa})|\mathrm{I}\rangle$, eqns. (2.124) and (2.125), represents a state where the set of MOs $\{\psi_p(\mathbf{r}_i)\}$ has been unitarily transformed.

In the configuration space, however, one is mostly interested in transformations of a single electronic state or of a small number of such states. Specifically, in the case of state-averaged MCSCF calculations involving n real-valued electronic states to be optimized, c.f. eqn. (2.109), the corresponding unitary transformation is given by [148]

$$\begin{aligned} |\tilde{I}(\mathbf{R})\rangle &= \exp(-\hat{R})|I\rangle \\ &= \exp\left[-\sum_{\substack{K>J \\ J\leq n}} R_{KJ}(|K\rangle\langle J| - |J\rangle\langle K|)\right]|I\rangle, \end{aligned} \tag{2.127}$$

where the summation is over pairs of states $|K\rangle$ and $|J\rangle$ and the parameters R_{KJ} constitute the independent variational parameters. Here, the index J refers to any of the n reference states and the index K refers to these states and also to the orthogonal complement, that is to the $L-n$ remaining states that are not explicitly optimized. Furthermore, the states $|K\rangle$ are ordered such that the n states $|J\rangle$ precede the $L-n$ states of the orthonormal complement; the reader is referred to Refs. [148,172] for further details including efficient methods for the generation of a basis for the orthogonal complement to the reference states. Finally, note that the parametrization of the MCSCF wave function should, besides being independent, also exclude those variational parameters that are not needed for a general transformation of the wave function, that is the parametrization should also be non-redundant; see Ref. [148] for a detailed discussions of the associated additional restrictions.

Newton-Raphson Method

After having discussed the parametrization of the MCSCF wave function, we now turn to the actual optimization of the MCSCF energy function, c.f. eqns. (2.111) and (2.121). As already mentioned above, the straightforward variational optimization with respect to the independent variational parameters, does usually not converge. Hence, so-called second-order methods for the variational optimization are employed. The most prominent of these methods is the second-order Newton-Raphson approach, where the energy is expanded as a Taylor series in the variational parameters: Assume that the variational parameters are arranged as a column vector, $\mathbf{p}$. Expansion of the energy function $E(\mathbf{p})$ in these variational parameters $\mathbf{p}$ around $\mathbf{p}=0$ gives in matrix notation [148,172]

$$E(\mathbf{p}) = E^{(0)} + \mathbf{g}^T\mathbf{E}^{(1)} + \frac{1}{2}\mathbf{p}^T\mathbf{E}^{(2)}\mathbf{p} + \ldots. \tag{2.128}$$

Here, $E^{(0)}$ is the energy at the expansion point, $\mathbf{E}^{(1)}$ is a column vector representing the electronic gradient at the expansion point and $\mathbf{E}^{(2)}$ is a matrix representing the electronic Hessian with elements

$$E_i^{(1)} = \left.\frac{\partial E(\mathbf{p})}{\partial p_i}\right|_{\mathbf{p}=0} \qquad \text{and} \qquad E_{ij}^{(2)} = \left.\frac{\partial^2 E}{\partial p_i \partial p_j}\right|_{\mathbf{p}=0}. \tag{2.129}$$

The stationary points on the energy surface, eqn. (2.128), or equivalently the (approximate) solutions of the time-independent Schrödinger equation, c.f. section 2.2.1.1, are obtained as solutions to the equations $\partial E(\mathbf{p})/\partial p_i = 0$. They can be found iteratively by truncating the Taylor expansion of the energy function $E(\mathbf{p})$, eqn. (2.128), at second order, and setting the

derivatives of this truncated energy expression equal to zero. This leads to the following system of linear equations

$$\mathbf{E}^{(1)} + \mathbf{E}^{(2)}\mathbf{p} = 0 \qquad \text{or} \qquad \mathbf{p} = -\mathbf{E}^{(2)^{-1}}\mathbf{E}^{(1)}. \tag{2.130}$$

A sequence of Newton-Raphson iterations is obtained by generating an initial guess for the set of variational parameters $\mathbf{p}$, solving eqn. (2.130), redefining the solution as the new zero point, recalculating the vector $\mathbf{E}^{(1)}$ and the Hessian matrix $\mathbf{E}^{(2)}$ and returning to eqn. (2.130). Sufficiently close to the stationary point, the Newton-Raphson method converges quadratically [148,172].

State-Averaged MCSCF Theory

To arrive at explicit expressions for the electronic gradient and the Hessian in the Taylor series, eqn. (2.128), in the case of state-averaged MCSCF wave functions, consider the transformed MCSCF wave function using the exponential parametrization of both the orbital and the configuration space

$$|\tilde{I}(\boldsymbol{\kappa}, \mathbf{R})\rangle = \exp(-\hat{\kappa})\exp(-\hat{R})|I\rangle. \tag{2.131}$$

The state-averaged energy of the transformed MCSCF states $|\tilde{I}(\boldsymbol{\kappa}, \mathbf{R})\rangle$, c.f. eqn. (2.111), which depends on the set of independent variational parameters $\{\boldsymbol{\kappa}, \mathbf{R}\}$, may now be written as

$$E^{\mathrm{av}}(\boldsymbol{\kappa}, \mathbf{R}) = \sum_I w_I \langle \tilde{I}|\hat{\tilde{H}}^{\mathrm{2nd}}_{\mathrm{el}}|\tilde{I}\rangle = \sum_I w_I \langle I|\exp(\hat{R})\exp(\hat{\kappa})\hat{\tilde{H}}^{\mathrm{2nd}}_{\mathrm{el}}\exp(-\hat{\kappa})\exp(-\hat{R})|I\rangle. \tag{2.132}$$

This state-averaged energy expression may be expanded in a Baker-Campbell-Hausdorff (BCH) expansion[11] yielding [172]

$$\begin{aligned} E^{\mathrm{av}}(\boldsymbol{\kappa}, \mathbf{R}) = \sum_I w_I \langle I|\hat{\tilde{H}}^{\mathrm{2nd}}_{\mathrm{el}} \\ + [\hat{\kappa}, \hat{\tilde{H}}^{\mathrm{2nd}}_{\mathrm{el}}] + [\hat{R}, \hat{\tilde{H}}^{\mathrm{2nd}}_{\mathrm{el}}] \\ + \frac{1}{2}[\hat{\kappa}, [\hat{\kappa}, \hat{\tilde{H}}^{\mathrm{2nd}}_{\mathrm{el}}]] + \frac{1}{2}[\hat{R}, [\hat{R}, \hat{\tilde{H}}^{\mathrm{2nd}}_{\mathrm{el}}]] + [\hat{R}, [\hat{\kappa}, \hat{\tilde{H}}^{\mathrm{2nd}}_{\mathrm{el}}]] + \ldots |I\rangle. \end{aligned} \tag{2.133}$$

The first term in this expression is the zeroth order energy $E^{\mathrm{av}}(\boldsymbol{\kappa} = 0, \mathbf{R} = 0)$. Taking the derivatives of eqn. (2.133) with respect to the variational parameters κ_{pq}, eqn. (2.125), one obtains the following expression for the electronic gradient at $\boldsymbol{\kappa} = 0$ [148]

$${}^{\mathrm{o}}E^{\mathrm{av}(1)}_{pq} = \left.\frac{\partial E^{\mathrm{av}}(\boldsymbol{\kappa}, \mathbf{R})}{\partial \kappa_{pq}}\right|_{\boldsymbol{\kappa}=0} = \sum_I w_I \langle I|[\hat{E}^-_{pq}, \hat{\tilde{H}}^{\mathrm{2nd}}_{\mathrm{el}}]|I\rangle, \tag{2.134}$$

where the operator $\hat{E}^-_{pq}$ was defined in eqn. (2.125) and the superscript o refers to variations in the orbital space. Accordingly, for the configuration space (c) one obtains

$${}^{\mathrm{c}}E^{\mathrm{av}(1)}_{KJ} = \left.\frac{\partial E^{\mathrm{av}}(\boldsymbol{\kappa}, \mathbf{R})}{\partial R_{KJ}}\right|_{\mathbf{R}=0} = \sum_I w_I \langle I|[|K\rangle\langle J| - |J\rangle\langle K|, \hat{\tilde{H}}^{\mathrm{2nd}}_{\mathrm{el}}]|I\rangle, \tag{2.135}$$

[11] In general, a BCH expansion is defined as $\exp(\mathbf{A})\mathbf{B}\exp(-\mathbf{A}) = \mathbf{B} + [\mathbf{A}, \mathbf{B}] + \frac{1}{2}[\mathbf{A}, [\mathbf{A}, \mathbf{B}]] + \ldots$, where $\mathbf{A}$ and $\mathbf{B}$ might be operators or matrices, for a derivation see [148].

where the variational parameters were defined in eqn. (2.127). For the elements of the Hessian matrix one obtains

$$ {}^{\mathrm{oo}}E^{\mathrm{av}(2)}_{pq,rs} = \left.\frac{\partial^2 E^{\mathrm{av}}(\boldsymbol{\kappa},\mathbf{R})}{\partial\kappa_{pq}\partial\kappa_{rs}}\right|_{\boldsymbol{\kappa}=0} = \frac{1}{2}(1+\hat{P}_{pq,rs})\sum_I w_I\langle I|[\hat{E}^-_{pq},[\hat{E}^-_{rs},\hat{\tilde{H}}^{\mathrm{2nd}}_{\mathrm{el}}]]|I\rangle, \tag{2.136} $$

where the operator $\hat{P}_{pq,rs}$ permutes the pair indices pq and rs,

$$ {}^{\mathrm{cc}}E^{\mathrm{av}(2)}_{KJ,K'J'} = \left.\frac{\partial^2 E^{\mathrm{av}}(\boldsymbol{\kappa},\mathbf{R})}{\partial R_{KJ}\partial R_{K'J'}}\right|_{\mathbf{R}=0} = \sum_I w_I\langle I|[|K\rangle\langle J|-|J\rangle\langle K|,[|K'\rangle\langle J'|-|J'\rangle\langle K'|,\hat{\tilde{H}}^{\mathrm{2nd}}_{\mathrm{el}}]]|I\rangle \tag{2.137} $$

and

$$ {}^{\mathrm{co}}E^{\mathrm{av}(2)}_{KJ,pq} = \left.\frac{\partial^2 E^{\mathrm{av}}(\boldsymbol{\kappa},\mathbf{R})}{\partial R_{KJ}\partial\kappa_{rs}}\right|_{\substack{\mathbf{R}=0\\ \boldsymbol{\kappa}=0}} = \sum_I w_I\langle I|[|K\rangle\langle J|-|J\rangle\langle K|,[E^-_{pq},\hat{\tilde{H}}^{\mathrm{2nd}}_{\mathrm{el}}]]|I\rangle. \tag{2.138} $$

For further details for the evaluation of eqs. (2.134)-(2.138), see e.g. Refs. [148,172,182].

As already mentioned, the Newton-Raphson procedure is iterative, each iteration consisting of the construction of the respective gradients and Hessian matrices, eqns. (2.134)-(2.138), followed by the solutions of the Newton-Raphson linear equations, eqn. (2.130). Due to the size of the problem, usually each of these Newton-Raphson steps need to be solved iteratively as well. These iterations within each Newton-Raphson step are usually referred to as microiterations to distinguish them from the enclosing so-called macroiterations [148,172,182].

2.2.2 Density Functional Theory

The correlated methods discussed so far based on the $4N$ dimensional many-electron wave function scale poorly with the system size and they require the usage of extensive one-electron expansions to describe the electron-electron cusp [148]. *Density Functional Theory* (DFT), on the other hand, is based on the one-electron density $\rho_{\rm el}^{\rm BO}(\mathbf{r})$, c.f. eqn. (2.42), which depends on just three spatial coordinates. Hence, DFT is computationally much less demanding and, since the wave function is not explicitly modeled, much smaller one-electron basis-sets are needed. DFT based methods are very popular for the calculation of large molecular systems. It should be noted that, although there exists a certain hierarchy of approximations (section 2.2.2.3), the different approximations discussed later are not variational, i.e. no systematic improvements are possible and they usually need to be tested against correlated wave function based methods, e.g. CCSD(T), MRCISD, CASPT2, or against experimental data.

In section 2.2.2.1 the fundamental Hohenberg-Kohn Theorems [184] are presented, while section 2.2.2.2 deals with the Kohn-Sham method [185], the standard scheme employed nowadays for DFT calculations. Finally, section 2.2.2.3 describes various approximations to the exchange-correlation functional (section 2.2.2.2), which constitutes the "holy grail" of Density Functional Theory [163].

2.2.2.1 The Hohenberg-Kohn Theorems

The **first Hohenberg - Kohn Theorem** proves that the electron density of the non-degenerate electronic ground state, $\rho_{\rm el}^{\rm BO}(\mathbf{r})$, determines the electronic Hamiltonian $\hat{H}_{\rm el}$ and hence all properties associated with the electronic Schrödinger equation, eqn. (2.5): Consider the electronic Hamiltonian

$$\hat{H}_{\rm el} = \hat{T}_{\rm el} + \hat{V}_{\rm el-nuc} + \hat{V}_{\rm el-el}, \tag{2.139}$$

which was already given in eqn. (2.4), see also eqn. (2.3) for explicit expressions of the respective terms. The mean electron-nuclear attraction energy is given by [137]

$$\begin{aligned} \bar{V}_{\rm el-nuc} = \langle\Phi_0(\mathbf{q})|\hat{V}_{\rm el-nuc}|\Phi_0(\mathbf{q})\rangle &= \langle\Phi_0(\mathbf{q})|\sum_i \underbrace{\left(\sum_A \frac{Z_A}{|\mathbf{r}_i - \mathbf{R}_A|}\right)}_{v(\mathbf{r}_i)}|\Phi_0(\mathbf{q})\rangle \\ &= \int \rho_{\rm el}^{\rm BO}(\mathbf{r}) \underbrace{\left(-\sum_A \frac{Z_A}{|\mathbf{r}_i - \mathbf{R}_A|}\right)}_{v(\mathbf{r})} \mathrm{d}\mathbf{r}, \end{aligned} \tag{2.140}$$

where $v(\mathbf{r})$ is usually referred to as the *external potential* in DFT.

Hohenberg and Kohn proved in 1964 that for systems with a non-degenerate electronic ground state

> The electron density, $\rho_{\rm el}^{\rm BO}(\mathbf{r})$, eqn. (2.42), *determines* uniquely the external potential, $v(\mathbf{r})$, up to an additive constant [184],

by showing that there do not exist two external potentials, $v(\mathbf{r})$ and $v'(\mathbf{r})$, associated with the same ground state electron density $\rho_{\mathrm{el}}^{\mathrm{BO}}(\mathbf{r})$ (other than the trivial case of the potentials differing by an additive constant). Additionally, the electron density determines the number of electrons N,

$$\int \rho_{\mathrm{el}}^{\mathrm{BO}}(\mathbf{r})\mathrm{d}\mathbf{r} = N, \tag{2.141}$$

c.f. eqn. (2.42). Hence, it determines *all* components of the electronic Hamiltonian, $\hat{H}_{\mathrm{el}}$, and thereby the electronic wave function $\Phi_0(\mathbf{q})$[12]. The electronic energy, c.f. eqn. (2.5), may thus be expressed as a *functional*[13] of the electron density

$$E_0[\rho_{\mathrm{el}}^{\mathrm{BO}}(\mathbf{r})] = \bar{V}_{\mathrm{el-nuc}}[\rho_{\mathrm{el}}^{\mathrm{BO}}(\mathbf{r})] + \bar{T}_{\mathrm{el}}[\rho_{\mathrm{el}}^{\mathrm{BO}}(\mathbf{r})] + \bar{V}_{\mathrm{el-el}}[\rho_{\mathrm{el}}^{\mathrm{BO}}(\mathbf{r})], \tag{2.142}$$

with $\bar{V}_{\mathrm{el-nuc}}[\rho_{\mathrm{el}}^{\mathrm{BO}}(\mathbf{r})]$ given by eqn. (2.140). The mean kinetic energy and the mean electron-electron interaction energy functionals, $\bar{T}_{\mathrm{el}}[\rho_{\mathrm{el}}^{\mathrm{BO}}(\mathbf{r})]$ and $\bar{V}_{\mathrm{el-el}}[\rho_{\mathrm{el}}^{\mathrm{BO}}(\mathbf{r})]$, respectively, are often grouped together in the *Hohenberg-Kohn Functional* $F_{\mathrm{HK}}[\rho_{\mathrm{el}}^{\mathrm{BO}}(\mathbf{r})]$ [163],

$$F_{\mathrm{HK}}[\rho_{\mathrm{el}}^{\mathrm{BO}}(\mathbf{r})] = \bar{T}_{\mathrm{el}}[\rho_{\mathrm{el}}^{\mathrm{BO}}(\mathbf{r})] + \bar{V}_{\mathrm{el-el}}[\rho_{\mathrm{el}}^{\mathrm{BO}}(\mathbf{r})] = \langle\Phi_0(\mathbf{q})|\hat{T}_{\mathrm{el}} + \hat{V}_{\mathrm{el-el}}|\Phi_0(\mathbf{q})\rangle, \tag{2.143}$$

for which as yet no exact expression is known and which is thus the holy grail of density functional theory [163]. It is interesting to note that formally, since $\rho_{\mathrm{el}}^{\mathrm{BO}}(\mathbf{r})$ uniquely determines the electronic Hamiltonian $\hat{H}_{\mathrm{el}}$, all properties of all excited electronic states are determined by the ground state density [163]. For excited states, however, other functionals than $\bar{V}_{\mathrm{el-nuc}}[\rho_{\mathrm{el}}^{\mathrm{BO}}(\mathbf{r})] + F_{\mathrm{HK}}[\rho_0(\mathbf{r})]$ are needed. Hence, in practice, DFT is mostly applied to the electronic ground state with extensions to excited electronic states in the framework of linear response theory (TDDFT) [187]. Furthermore note that it is only the ground state density, $\rho_{\mathrm{el}}^{\mathrm{BO}}(\mathbf{r})$, that contains the information about positions and charges of the nuclei allowing the mapping from density to external potential; the density of an excited electronic state cannot be used [163].

The second Hohenberg-Kohn Theorem gives a formal prescription of how the ground state electron density might be found: Consider a trial density $\rho'_{\mathrm{el}}(\mathbf{r})$ that satisfies the boundary conditions $\rho'_{\mathrm{el}}(\mathbf{r}) \geq 0$ and $\int \mathrm{d}\mathbf{r}\rho'_{\mathrm{el}}(\mathbf{r}) = N$ for all $\mathbf{r}$ and that defines the external potential $v'(\mathbf{r})$ and hence the electronic Hamiltonian $\hat{H}'_{\mathrm{el}}$ and the associated trial wave function $\Phi'(\mathbf{q})$[14]. Invoking the relation for *variationally optimized* wave functions, eqn. (2.71), yields

$$\begin{aligned}\langle\Phi'(\mathbf{q})|\hat{H}_{\mathrm{el}}|\Phi'(\mathbf{q})\rangle = \bar{T}_{\mathrm{el}}[\rho'_{\mathrm{el}}(\mathbf{r})] + \bar{V}_{\mathrm{el-el}}[\rho'_{\mathrm{el}}(\mathbf{r})] + \int d\mathbf{r}\rho'_{\mathrm{el}}(\mathbf{r})v(\mathbf{r}) = E[\rho'_{\mathrm{el}}(\mathbf{r})] \\ \geq E_0[\rho_{\mathrm{el}}^{\mathrm{BO}}(\mathbf{r})] = \langle\Phi_0(\mathbf{q})|\hat{H}_{\mathrm{el}}|\Phi_0(\mathbf{q})\rangle.\end{aligned} \tag{2.144}$$

[12] The limitation to non-degenerate electronic ground states was lifted in Ref. [186].

[13] For details on functionals and functional derivatives, see Appendix 6.1

[14] This proof relies on the prerequisite that $\rho'_{\mathrm{el}}(\mathbf{r})$ is associated with some external potential $v'(\mathbf{r})$, i.e. that it is v-representable. This requirement can be replaced by the weaker condition that $\rho'_{\mathrm{el}}(\mathbf{r})$ must be associated with an antisymmetric wave function without being necessarily $v(\mathbf{r})$-representable [186]. Such densities are referred to as being N-representable, which is fulfilled in practically all implementations of DFT in use, see sections 2.2.2.2 and 2.2.2.3.

Note that the expectation value of the exact electronic Hamiltonian $\hat{H}_{\mathrm{el}}$ is considered and consequently the external potential $v(\mathbf{r})$ and not $v'(\mathbf{r})$ must be used. Hence, the ground state density is formally found as the density which makes the energy functional $E[\rho_{\mathrm{el}}^{\mathrm{BO}}(\mathbf{r})]$, subject to the constraint that the number of electrons is conserved, eqn. (2.141), stationary, c.f. eqn. (2.57). Specifically, this is achieved by setting the functional derivative of the auxiliary functional $G[\rho_{\mathrm{el}}^{\mathrm{BO}}(\mathbf{r})] = E[\rho_{\mathrm{el}}^{\mathrm{BO}}(\mathbf{r})] - \mu\left(\int \rho_{\mathrm{el}}^{\mathrm{BO}}(\mathbf{r})\mathrm{d}\mathbf{r} - N\right)$, containing the constraint $\int \rho_{\mathrm{el}}^{\mathrm{BO}}(\mathbf{r})\mathrm{d}\mathbf{r} = N$ and associated Lagrange multiplier μ, equal to zero according to

$$\frac{\delta}{\delta\rho_{\mathrm{el}}^{\mathrm{BO}}(\mathbf{r})}\left(E[\rho_{\mathrm{el}}^{\mathrm{BO}}(\mathbf{r})] - \mu\left(\int \rho_{\mathrm{el}}^{\mathrm{BO}}(\mathbf{r})\mathrm{d}\mathbf{r} - N\right)\right) = 0, \tag{2.145}$$

yielding

$$\mu = v(\mathbf{r}) + \frac{\delta\bar{T}_{\mathrm{el}}[\rho_{\mathrm{el}}^{\mathrm{BO}}(\mathbf{r})]}{\delta\rho_{\mathrm{el}}^{\mathrm{BO}}(\mathbf{r})} + \frac{\delta\bar{V}_{\mathrm{el-el}}[\rho_{\mathrm{el}}^{\mathrm{BO}}(\mathbf{r})]}{\delta\rho_{\mathrm{el}}^{\mathrm{BO}}(\mathbf{r})}. \tag{2.146}$$

Eqn. (2.146) is the Euler-Lagrange equation with the chemical potential μ [159,162].

2.2.2.2 The Kohn-Sham method

Eqn. (2.146) is only of practical use if reasonable approximations of the functionals $\bar{T}_{\mathrm{el}}[\rho_{\mathrm{el}}^{\mathrm{BO}}(\mathbf{r})]$ and $\bar{V}_{\mathrm{el-el}}[\rho_{\mathrm{el}}^{\mathrm{BO}}(\mathbf{r})]$ are available. Especially the contribution of the kinetic energy is expected to be large according to the virial theorem [137,159] such that early attempts by Thomas, Fermi, Dirac and others to model $\bar{T}_{\mathrm{el}}[\rho_{\mathrm{el}}^{\mathrm{BO}}(\mathbf{r})]$ as rather simple function did not even predict chemical bonding [159, 162]. The major breakthrough is due to Kohn and Sham [185] who introduced orbitals into the problem, which allows the kinetic energy to be evaluated reasonably accurately, leaving just a "small" residual correction.

To derive the Kohn-Sham equations, the total energy functional is rewritten as

$$\begin{aligned} E[\rho_{\mathrm{el}}^{\mathrm{BO}}(\mathbf{r})] &= \bar{T}_{\mathrm{el}}[\rho_{\mathrm{el}}^{\mathrm{BO}}(\mathbf{r})] + \bar{V}_{\mathrm{el-el}}[\rho_{\mathrm{el}}^{\mathrm{BO}}(\mathbf{r})] + \int \rho_{\mathrm{el}}^{\mathrm{BO}}(\mathbf{r})v(\mathbf{r})\mathrm{d}\mathbf{r} \\ &= \bar{T}_{\mathrm{s}}[\rho_{\mathrm{el}}^{\mathrm{BO}}(\mathbf{r})] + \bar{J}[\rho_{\mathrm{el}}^{\mathrm{BO}}(\mathbf{r})] + \int \rho_{\mathrm{el}}^{\mathrm{BO}}(\mathbf{r})v(\mathbf{r})\mathrm{d}\mathbf{r} \\ &\quad + \underbrace{\bar{T}_{\mathrm{el}}[\rho_{\mathrm{el}}^{\mathrm{BO}}(\mathbf{r})] - \bar{T}_{\mathrm{s}}[\rho_{\mathrm{el}}^{\mathrm{BO}}(\mathbf{r})]}_{\Delta\bar{T}_{\mathrm{el}}[\rho_{\mathrm{el}}^{\mathrm{BO}}(\mathbf{r})]} + \underbrace{\bar{V}_{\mathrm{el-el}}[\rho_{\mathrm{el}}^{\mathrm{BO}}(\mathbf{r})] - \bar{J}[\rho_{\mathrm{el}}^{\mathrm{BO}}(\mathbf{r})]}_{\Delta\bar{V}_{\mathrm{el-el}}[\rho_{\mathrm{el}}^{\mathrm{BO}}(\mathbf{r})]}, \end{aligned} \tag{2.147}$$

where the first line is just eqn. (2.142). In the second line, the term $\bar{T}_{\mathrm{s}}[\rho_{\mathrm{el}}^{\mathrm{BO}}(\mathbf{r})] - \bar{T}_{\mathrm{s}}[\rho_{\mathrm{el}}^{\mathrm{BO}}(\mathbf{r})] + \bar{J}[\rho_{\mathrm{el}}^{\mathrm{BO}}(\mathbf{r})] - \bar{J}[\rho_{\mathrm{el}}^{\mathrm{BO}}(\mathbf{r})] = 0$ was added and the terms entering the exchange correlation functional $E_{\mathrm{XC}}[\rho_{\mathrm{el}}^{\mathrm{BO}}(\mathbf{r})] = \Delta\bar{T}_{\mathrm{el}}[\rho_{\mathrm{el}}^{\mathrm{BO}}(\mathbf{r})] + \Delta\bar{V}_{\mathrm{el-el}}[\rho_{\mathrm{el}}^{\mathrm{BO}}(\mathbf{r})]$ were defined. $\bar{J}[\rho_{\mathrm{el}}^{\mathrm{BO}}(\mathbf{r})]$ is the classical (Hartree) Coulomb repulsion of the density with itself

$$\bar{J}[\rho_{\mathrm{el}}^{\mathrm{BO}}(\mathbf{r})] = \frac{1}{2}\int\int \frac{\rho_{\mathrm{el}}^{\mathrm{BO}}(\mathbf{r})\rho_{\mathrm{el}}^{\mathrm{BO}}(\mathbf{r}')}{|\mathbf{r}-\mathbf{r}'|}\mathrm{d}\mathbf{r}\mathrm{d}\mathbf{r}'. \tag{2.148}$$

In this way, part of the unknown functional $\bar{V}_{\mathrm{el-el}}[\rho_{\mathrm{el}}^{\mathrm{BO}}(\mathbf{r})]$ may be evaluated by the known functional $\bar{J}[\rho_{\mathrm{el}}^{\mathrm{BO}}(\mathbf{r})]$ with the residual part shifted to the unknown exchange-correlation functional $E_{\mathrm{XC}}[\rho_{\mathrm{el}}^{\mathrm{BO}}(\mathbf{r})]$, i.e. $\bar{V}_{\mathrm{el-el}}[\rho_{\mathrm{el}}^{\mathrm{BO}}(\mathbf{r})] = \bar{J}[\rho_{\mathrm{el}}^{\mathrm{BO}}(\mathbf{r})] + \Delta\bar{V}_{\mathrm{el-el}}[\rho_{\mathrm{el}}^{\mathrm{BO}}(\mathbf{r})]$. In the same spirit, the

unknown kinetic energy functional is evaluated as $\bar{T}_{\mathrm{el}}[\rho_{\mathrm{el}}^{\mathrm{BO}}(\mathbf{r})] = \bar{T}_{\mathrm{s}}[\rho_{\mathrm{el}}^{\mathrm{BO}}(\mathbf{r})] + \Delta\bar{T}_{\mathrm{el}}[\rho_{\mathrm{el}}^{\mathrm{BO}}(\mathbf{r})]$, where $\bar{T}_{\mathrm{s}}[\rho_{\mathrm{el}}^{\mathrm{BO}}(\mathbf{r})]$ is taken to be the mean kinetic energy of a hypothetical reference system of N non-interacting electrons in an external potential $v_{\mathrm{s}}(\mathbf{r})$, selected so that the electron density of the reference system, $\rho_{\mathrm{s}}(\mathbf{r})$, is identical to the true electron density, $\rho_{\mathrm{s}}(\mathbf{r}) = \rho_{\mathrm{el}}^{\mathrm{BO}}(\mathbf{r})$[15]. A similar system has already been encountered in this thesis in the context of Hartree-Fock Theory, see section 2.2.1.3 and Appendix 6.2, with the external potential given by $v^{\mathrm{HF}}(\mathbf{q}_i) = v(\mathbf{r}_i) + \vartheta^{\mathrm{HF}}(\mathbf{q}_i)$, where $\vartheta^{\mathrm{HF}}(\mathbf{q}_i)$ is the average Hartree-Fock potential experienced by one electron due to the presence of the $N-1$ remaining electrons, eqn. (2.88). The Hamiltonian of this hypothetical non-interacting reference system is given by

$$\hat{H}_{\mathrm{s}}^{\mathrm{KS}} = \sum_{i}^{N}\left(-\frac{1}{2}\boldsymbol{\nabla}_{\mathbf{r}_i}^2 + v_{\mathrm{s}}(\mathbf{r}_i)\right) = \sum_{i}^{N}\hat{h}^{\mathrm{KS}}(\mathbf{r}_i). \tag{2.149}$$

The Kohn-Sham (KS) spin-orbitals $\phi_m^{\mathrm{KS}}(\mathbf{q}_i)$ are eigenfunctions of the one-electron KS Hamiltonian $\hat{h}^{\mathrm{KS}}(\mathbf{r}_i)$ according to

$$\hat{h}^{\mathrm{KS}}(\mathbf{r}_i)\phi_m^{\mathrm{KS}}(\mathbf{q}_i) = \epsilon_m^{\mathrm{KS}}\phi_m^{\mathrm{KS}}(\mathbf{q}_i) \tag{2.150}$$

and the wave function representing the ground state of this non-interacting system is given by the Slater determinant

$$\Phi_{\mathrm{s}}^{\mathrm{SD}}(\mathbf{q}) = \frac{1}{\sqrt{N!}}\begin{vmatrix} \phi_1^{\mathrm{KS}}(\mathbf{q}_1) & \phi_2^{\mathrm{KS}}(\mathbf{q}_1) & \dots & \phi_N^{\mathrm{KS}}(\mathbf{q}_1) \\ \phi_1^{\mathrm{KS}}(\mathbf{q}_2) & \phi_2^{\mathrm{KS}}(\mathbf{q}_2) & \dots & \phi_N^{\mathrm{KS}}(\mathbf{q}_2) \\ \vdots & \vdots & \ddots & \vdots \\ \phi_1^{\mathrm{KS}}(\mathbf{q}_N) & \phi_2^{\mathrm{KS}}(\mathbf{q}_N) & \dots & \phi_N^{\mathrm{KS}}(\mathbf{q}_N) \end{vmatrix}. \tag{2.151}$$

Since in this formulation, the external potential $v_{\mathrm{s}}(\mathbf{r})$ does not contain electron-spin, the solutions of eqn. (2.150) are doubly degenerate: For each eigenvalue ϵ_m^{KS}, there are two independent solutions that can be chosen according to eqn. (2.48) [162]. Hence, the underlying KS spatial-orbitals $\psi_m^{\mathrm{KS}}(\mathbf{r}_i)$ are defined in analogy to the spatial-orbitals $\psi_m^{\mathrm{HF}}(\mathbf{r}_i)$ in restricted HF theory, c.f. section 2.2.1.3 and Appendix 6.2. Note however, that the restriction on the spatial KS orbitals is the natural consequence of the theory, whereas the restriction in the restricted HF method is a further qualification on the determinantal-wave-function approximation [162][16]. Hence, for closed shell-systems, the electron-density may be expressed in terms of the corresponding spatial KS MOs, $\psi_m^{\mathrm{KS}}(\mathbf{r}_i)$, according to

$$\rho_{\mathrm{el}}^{\mathrm{BO}}(\mathbf{r}) = \rho_{\mathrm{s}}(\mathbf{r}) = \langle\Phi_{\mathrm{s}}^{\mathrm{SD}}(\mathbf{q})|\sum_i \delta(\mathbf{r}-\mathbf{r}_i)|\Phi_{\mathrm{s}}^{\mathrm{SD}}(\mathbf{q})\rangle = 2\sum_{m}^{N/2}|\psi_m^{\mathrm{KS}}(\mathbf{r}_i)|^2, \tag{2.152}$$

c.f. eqn. (2.36). The corresponding energy of the hypothetical reference system is given by

$$E_{\mathrm{s}}[\rho_{\mathrm{el}}^{\mathrm{BO}}(\mathbf{r})] = \langle\Phi_{\mathrm{s}}^{\mathrm{SD}}(\mathbf{q})|\hat{H}_{\mathrm{s}}^{\mathrm{KS}}|\Phi_{\mathrm{s}}^{\mathrm{KS}}(\mathbf{q})\rangle = \bar{T}_{\mathrm{s}}[\rho_{\mathrm{el}}^{\mathrm{BO}}(\mathbf{r})] + \int v_{\mathrm{s}}(\mathbf{r})\rho_{\mathrm{el}}^{\mathrm{BO}}(\mathbf{r})\mathrm{d}\mathbf{r}, \tag{2.153}$$

[15] Here, it was assumed that $\rho_{\mathrm{el}}^{\mathrm{BO}}(\mathbf{r})$ is non-interacting v-representable, that is there must exist a non-interacting ground state associated with $\rho_{\mathrm{el}}^{\mathrm{BO}}(\mathbf{r})$, for details see Ref. [162].

[16] In spin-density-functional theory, which is analogous to the unrestricted HF method, a spin-dependence is introduced in the external potential, leading to differing α-spin and β-spin electron densities, for details see Ref. [162]

with

$$\bar{T}_{\mathrm{s}}[\rho_{\mathrm{el}}^{\mathrm{BO}}(\mathbf{r})] = \langle \Phi_{\mathrm{s}}^{\mathrm{SD}}(\mathbf{q}) | \sum_i -\frac{1}{2}\boldsymbol{\nabla}_{\mathbf{r}_i}^2 | \Phi_{\mathrm{s}}^{\mathrm{KS}}(\mathbf{q}) \rangle = 2\sum_m^{N/2} \langle \psi_m^{\mathrm{KS}}(\mathbf{r}_i) | -\frac{1}{2}\boldsymbol{\nabla}_{\mathbf{r}_i}^2 | \psi_m^{\mathrm{KS}}(\mathbf{r}_i) \rangle, \quad (2.154)$$

where the last equation follows from the Condon-Slater rules [136]. Finally, the Euler-Lagrange equation of the reference system is

$$\mu_{\mathrm{s}} = \frac{\delta \bar{T}_{\mathrm{s}}[\rho_{\mathrm{el}}^{\mathrm{BO}}(\mathbf{r})]}{\delta \rho_{\mathrm{el}}^{\mathrm{BO}}(\mathbf{r})} + v_{\mathrm{s}}(\mathbf{r}), \quad (2.155)$$

c.f. eqns. (2.145) and (2.146).

Now, an expression for $v_{\mathrm{s}}(\mathbf{r})$ is obtained by rewriting eqn. (2.146) using eqn. (2.147) as

$$\mu = \frac{\delta \bar{T}_{\mathrm{s}}[\rho_{\mathrm{el}}^{\mathrm{BO}}(\mathbf{r})]}{\delta \rho_{\mathrm{el}}^{\mathrm{BO}}(\mathbf{r})} + \underbrace{\frac{\delta \bar{J}[\rho_{\mathrm{el}}^{\mathrm{BO}}(\mathbf{r})]}{\delta \rho_{\mathrm{el}}^{\mathrm{BO}}(\mathbf{r})} + v(\mathbf{r}) + \frac{\delta E_{\mathrm{XC}}[\rho_{\mathrm{el}}^{\mathrm{BO}}(\mathbf{r})]}{\delta \rho_{\mathrm{el}}^{\mathrm{BO}}(\mathbf{r})}}_{v_{\mathrm{eff}}(\mathbf{r})}, \quad (2.156)$$

where the effective potential $v_{\mathrm{eff}}(\mathbf{r})$ was defined. Using

$$\frac{\delta \bar{J}[\rho_{\mathrm{el}}^{\mathrm{BO}}(\mathbf{r})]}{\delta \rho_{\mathrm{el}}^{\mathrm{BO}}(\mathbf{r})} = \frac{1}{2}\int \frac{\rho_{\mathrm{el}}^{\mathrm{BO}}(\mathbf{r}')}{|\mathbf{r}-\mathbf{r}'|}\mathrm{d}\mathbf{r}' \quad (2.157)$$

and defining the exchange-correlation potential

$$v_{\mathrm{XC}}(\mathbf{r}) = \frac{\delta E_{\mathrm{XC}}[\rho_{\mathrm{el}}^{\mathrm{BO}}(\mathbf{r})]}{\delta \rho_{\mathrm{el}}^{\mathrm{BO}}(\mathbf{r})}, \quad (2.158)$$

the effective potential reads

$$v_{\mathrm{eff}}(\mathbf{r}) = \frac{1}{2}\int \mathrm{d}\mathbf{r}' \frac{\rho_{\mathrm{el}}^{\mathrm{BO}}(\mathbf{r}')}{|\mathbf{r}-\mathbf{r}'|} + v(\mathbf{r}) + v_{\mathrm{XC}}(\mathbf{r}). \quad (2.159)$$

Comparison of eqns. (2.155) and (2.156) shows that they are equal with $\mu = \mu_{\mathrm{s}}$ if $v_{\mathrm{s}}(\mathbf{r}) = v_{\mathrm{eff}}(\mathbf{r})$. Therefore, for a given effective potential $v_{\mathrm{eff}}(\mathbf{r})$, one obtains $\rho_{\mathrm{el}}^{\mathrm{BO}}(\mathbf{r})$ that satisfies eqn. (2.156) by solving the Kohn-Sham equations

$$\begin{aligned}\left(-\frac{1}{2}\boldsymbol{\nabla}_{\mathbf{r}_i}^2 + v_{\mathrm{eff}}(\mathbf{r}_i)\right)\phi_m^{\mathrm{KS}}(\mathbf{q}_i) &= \left(-\frac{1}{2}\boldsymbol{\nabla}_{\mathbf{r}_i}^2 + v(\mathbf{r}_i) + \frac{1}{2}\int \mathrm{d}\mathbf{r}' \frac{\rho_{\mathrm{el}}^{\mathrm{BO}}(\mathbf{r}')}{|\mathbf{r}_i-\mathbf{r}'|} + v_{\mathrm{XC}}(\mathbf{r}_i)\right)\phi_m^{\mathrm{KS}}(\mathbf{q}_i) \\ &= \epsilon_{\mathrm{m}}^{\mathrm{KS}}\phi_m^{\mathrm{KS}}(\mathbf{q}_i), \end{aligned} \quad (2.160)$$

and using eqn. (2.152) with the underlying KS spatial orbitals. The corresponding energy of the interacting systems is obtained using eqn. (2.147), which contains the unknown exchange-correlation functional $E_{\mathrm{XC}}[\rho_{\mathrm{el}}^{\mathrm{BO}}(\mathbf{r})]$. Since according to eqn. (2.159) $v_{\mathrm{eff}}(\mathbf{r})$ depends on $\rho_{\mathrm{el}}^{\mathrm{BO}}(\mathbf{r})$, the Kohn-Sham equations need to be solved iteratively. Furthermore, as in the HF method, the underlying KS spatial-orbitals $\psi_m^{\mathrm{KS}}(\mathbf{r}_i)$ are usually expanded in an auxiliary set of one-electron basis-functions (AOs, section 2.2.4), see Appendix 6.2 for further details.

2.2.2.3 The exchange correlation energy

In principle, the Kohn-Sham equations, eqn. (2.160), would yield the exact ground state density $\rho_{\mathrm{el}}^{\mathrm{BO}}(\mathbf{r})$ using eqn. (2.152) if the exchange-correlation functional $E_{\mathrm{XC}}[\rho_{\mathrm{el}}^{\mathrm{BO}}(\mathbf{r})]$, eqn. (2.158), containing the kinetic correlation energy $\Delta\bar{T}_{\mathrm{el}}[\rho_{\mathrm{el}}^{\mathrm{BO}}(\mathbf{r})]$ and the non-classical part of the average electron-electron repulsion energy $\Delta\bar{V}_{\mathrm{el}-el}[\rho_{\mathrm{el}}^{\mathrm{BO}}(\mathbf{r})]$, were known exactly. Hartree-Fock theory, by contrast, is approximate by definition and electron correlation effects need to be included a posteriori, see section 2.2.1.3.

There exists a hierarchy of approximations to $E_{\mathrm{XC}}[\rho_{\mathrm{el}}^{\mathrm{BO}}(\mathbf{r})]$, termed Jacob's ladder [159], which is, however, not variational:

- In the local density approximation (LDA), the exchange correlation energy is expressed as the integral of a function of just the density according to

$$E_{\mathrm{XC}}[\rho_{\mathrm{el}}^{\mathrm{BO}}(\mathbf{r})] \approx E_{\mathrm{XC}}^{\mathrm{LDA}}[\rho_{\mathrm{el}}^{\mathrm{BO}}(\mathbf{r})] = \int F\left(\rho_{\mathrm{el}}^{\mathrm{BO}}(\mathbf{r})\right) \mathrm{d}\mathbf{r} = \int \rho_{\mathrm{el}}^{\mathrm{BO}}(\mathbf{r}) \epsilon_{\mathrm{XC}}[\rho_{\mathrm{el}}^{\mathrm{BO}}(\mathbf{r})] \mathrm{d}\mathbf{r}. \tag{2.161}$$

  Here, $\epsilon_{\mathrm{XC}}(\rho_{\mathrm{el}}^{\mathrm{BO}}(\mathbf{r}))$ is the exchange correlation energy per particle taken from the uniform electron gas. This is a hypothetical electrically neutral infinite volume system consisting of an infinite number of interacting electrons moving in a space throughout which positive charge is continously and uniformly distributed [137, 159, 162, 163]. The quantity $\epsilon_{\mathrm{XC}}[\rho_{\mathrm{el}}^{\mathrm{BO}}(\mathbf{r})]$ can be further split into exchange and correlation contributions

$$\epsilon_{\mathrm{XC}}[\rho_{\mathrm{el}}^{\mathrm{BO}}(\mathbf{r})] = \epsilon_{\mathrm{X}}[\rho_{\mathrm{el}}^{\mathrm{BO}}(\mathbf{r})] + \epsilon_{\mathrm{C}}[\rho_{\mathrm{el}}^{\mathrm{BO}}(\mathbf{r})]. \tag{2.162}$$

  For the exchange part, analytical expressions were first derived by Bloch and Dirac, see Ref. [163] and Refs. therein, whereas for the correlation part no explicit analytical expressions are known. There exist, however, highly accurate quantum Monte-Carlo simulations [188], on the basis of which analytical expressions have been obtained by interpolation schemes [189]. The uniform electron gas is the model system on which most approximate exchange correlation functionals are based.

- In the generalized gradient approximation (GGA), $E_{\mathrm{XC}}[\rho_{\mathrm{el}}^{\mathrm{BO}}(\mathbf{r})]$ is expressed as an integral of a function of the density and its gradient

$$E_{\mathrm{XC}}[\rho_{\mathrm{el}}^{\mathrm{BO}}(\mathbf{r})] \approx E_{\mathrm{XC}}^{\mathrm{GGA}}[\rho_{\mathrm{el}}^{\mathrm{BO}}(\mathbf{r})] = \int F\left(\rho_{\mathrm{el}}^{\mathrm{BO}}(\mathbf{r}), \boldsymbol{\nabla}_{\mathbf{r}} \rho_{\mathrm{el}}^{\mathrm{BO}}(\mathbf{r})\right) \mathrm{d}\mathbf{r}, \tag{2.163}$$

  such that the LDA is corrected for the variation of the electron density with position. $E_{\mathrm{XC}}^{\mathrm{GGA}}[\rho_{\mathrm{el}}^{\mathrm{BO}}(\mathbf{r})]$ is usually split into exchange and correlation parts, which are modeled separately

$$E_{\mathrm{XC}}^{\mathrm{GGA}}[\rho_{\mathrm{el}}^{\mathrm{BO}}(\mathbf{r})] = E_{\mathrm{X}}^{\mathrm{GGA}}[\rho_{\mathrm{el}}^{\mathrm{BO}}(\mathbf{r})] + E_{\mathrm{C}}^{\mathrm{GGA}}[\rho_{\mathrm{el}}^{\mathrm{BO}}(\mathbf{r})]. \tag{2.164}$$

  These approximate functionals are developed using theoretical considerations such as the known behavior of the exact (but unknown) functionals $E_{\mathrm{X}}[\rho_{\mathrm{el}}^{\mathrm{BO}}(\mathbf{r})]$ and $E_{\mathrm{C}}[\rho_{\mathrm{el}}^{\mathrm{BO}}(\mathbf{r})]$ in various limiting situations as a guidance [162,163]. Quite often, also additional parameters

are included, which are fitted to available experimental data. Usually, the exchange part is written as

$$E_{\mathrm{X}}^{\mathrm{GGA}}[\rho_{\mathrm{el}}^{\mathrm{BO}}(\mathbf{r})] = E_{\mathrm{x}}^{\mathrm{LDA}}[\rho_{\mathrm{el}}^{\mathrm{BO}}(\mathbf{r})] - \int \tilde{F}\left(\frac{|\boldsymbol{\nabla}_{\mathbf{r}}\rho_{\mathrm{el}}^{\mathrm{BO}}(\mathbf{r})|}{\left(\rho_{\mathrm{el}}^{\mathrm{BO}}(\mathbf{r})\right)^{4/3}}\right)\left(\rho_{\mathrm{el}}^{\mathrm{BO}}(\mathbf{r})\right)^{4/3}\mathrm{d}\mathbf{r}, \quad (2.165)$$

where the argument of the function $\tilde{F}$ is the dimensionless reduced density gradient. For the function $\tilde{F}$, two main classes of approximations have been established [163]: The first class is based on a GGA exchange functional developed by Becke [190] and is usually abbreviated as B or B88. It contains one empirical parameter optimized by a least squares fit to the exchange energies of the rare gas atoms He through Rn. Often used GGA exchange correlation functionals of the second class are for example the functionals developed by Perdew (P) [191] and the one developed by Perdew, Burke and Ernzerhof (PBE) [192]. These functionals are free of empirical parameters fitted to experimental data [163]. Among the most popular GGA correlation functionals are the functional by Perdew and Wang (PW91) [193], which contains no empirical parameters [163], and the correlation functional due to Lee, Yang and Parr (LYP) [194]. The latter functional is not based on the uniform electron gas but on the correlation energy of the He atom calculated using wave function based methods [195]. It contains one empirical parameter. In principle, any GGA exchange functional might be combined with any GGA correlation functional. However, only a few combinations are currently in use, since the respective results rely on error compensations. Popular combinations are for example BLYP and BPW91.

- In meta-GGAs, higher order derivatives are introduced, e.g.

$$E_{\mathrm{XC}}[\rho_{\mathrm{el}}^{\mathrm{BO}}(\mathbf{r})] \approx E_{\mathrm{XC}}^{\mathrm{mGGA}}[\rho_{\mathrm{el}}^{\mathrm{BO}}(\mathbf{r})] = \int F\left(\rho_{\mathrm{el}}^{\mathrm{BO}}(\mathbf{r}), \boldsymbol{\nabla}_{\mathbf{r}}\rho_{\mathrm{el}}^{\mathrm{BO}}(\mathbf{r}), \boldsymbol{\nabla}_{\mathbf{r}}^{2}\rho_{\mathrm{el}}^{\mathrm{BO}}(\mathbf{r})\right)\mathrm{d}\mathbf{r}. \quad (2.166)$$

  For details, the reader is referred to Ref. [159] and Refs. therein, since the meta-GGAs have not been employed in this thesis.

- In hybrid-functionals, $E_{\mathrm{XC}}[\rho_{\mathrm{el}}^{\mathrm{BO}}(\mathbf{r})]$ is approximated as

$$E_{\mathrm{XC}}[\rho_{\mathrm{el}}^{\mathrm{BO}}(\mathbf{r})] \approx E_{\mathrm{XC}}^{\mathrm{hyb}}[\rho_{\mathrm{el}}^{\mathrm{BO}}(\mathbf{r})] = \int F\left(\rho_{\mathrm{el}}^{\mathrm{BO}}(\mathbf{r}), \boldsymbol{\nabla}_{\mathbf{r}}\rho_{\mathrm{el}}^{\mathrm{BO}}(\mathbf{r})\right) + \beta E_{\mathrm{X}}^{0}[\rho_{\mathrm{el}}^{\mathrm{BO}}(\mathbf{r})], \quad (2.167)$$

  that is a GGA functional is combined with a fraction of exactly computed exchange, $E_{\mathrm{X}}^{0}[\rho_{\mathrm{el}}^{\mathrm{BO}}(\mathbf{r})]$, defined by the same formula obtained within Hartree-Fock theory for the exchange energy integrals, see Appendix 6.2, eqn. (6.6), except for the replacement of the Hartree-Fock orbitals by the Kohn-Sham orbitals. It may be interesting to note that the sole combination of $E_{\mathrm{X}}^{0}[\rho_{\mathrm{el}}^{\mathrm{BO}}(\mathbf{r})]$ with approximate expressions for the exchange correlation functional leads to poor results for molecular properties [137,159,163]. Modeling both the exchange and the correlation functionals as in the GGA, by contrast, leads to cancellation of errors and better results. Hence, in hybrid functionals, both the advantages of exact exchange and the cancellation of errors in the GGA are combined, and commonly

additional parameters are introduced, which are fitted to experimental data.
Specifically, Becke's B3PW91 exchange correlation hybrid functional [196] is given by

$$\begin{aligned} E_{\rm XC}^{\rm B3PW91}[\rho_{\rm el}^{\rm BO}(\mathbf{r})] &= (1-a)E_{\rm X}^{\rm LDA}[\rho_{\rm el}^{\rm BO}(\mathbf{r})] + aE_{\rm X}^{0}[\rho_{\rm el}^{\rm BO}(\mathbf{r})] + bE_{\rm X}^{\rm B88}[\rho_{\rm el}^{\rm BO}(\mathbf{r})] \\ &\quad + cE_{\rm C}^{\rm PW91}[\rho_{\rm el}^{\rm BO}(\mathbf{r})] + E_{\rm C}^{\rm LDA}[\rho_{\rm el}^{\rm BO}(\mathbf{r})]. \end{aligned} \tag{2.168}$$

The three empirical parameters $a = 0.20$, $b = 0.72$, $\mathrm{and\,c} = 0.81$ were chosen such that the atomization energies and ionization energies as well as the proton affinities included in the G2 data base [197] were optimally reproduced, see Refs. [159,163] for further details. Minor modifications introduced in Ref. [198] lead to the ubiquitous B3LYP functional

$$\begin{aligned} E_{\rm XC}^{\rm B3LYP}[\rho_{\rm el}^{\rm BO}(\mathbf{r})] &= (1-a)E_{\rm X}^{\rm LDA}[\rho_{\rm el}^{\rm BO}(\mathbf{r})] + aE_{\rm X}^{0}[\rho_{\rm el}^{\rm BO}(\mathbf{r})] + bE_{\rm x}^{\rm B88}[\rho_{\rm el}^{\rm BO}(\mathbf{r})] \\ &= +(1-c)E_{\rm C}^{\rm LDA}[\rho_{\rm el}^{\rm BO}(\mathbf{r})] + cE_{\rm C}^{\rm LYP}[\rho_{\rm el}^{\rm BO}(\mathbf{r})]. \end{aligned} \tag{2.169}$$

2.2.3 Localized Molecular-Orbitals

Hartree-Fock and Kohn-Sham wave functions consisting of a single SD, c.f. sections 2.2.1.3 and 2.2.2, respectively, are invariant to any unitary transformation of the occupied spin-orbitals according to

$$\phi'_m(\mathbf{q}_i) = \sum_n^N U_{nm}\phi_n(\mathbf{q}_i) \quad \text{with} \quad \mathbf{U}\mathbf{U}^\dagger = 1, \tag{2.170}$$

see for example Ref. [136]. This constitutes the basis of orbital localization procedures, which aim at finding a unitarily transformed set of spin-orbitals $\{\phi'_m(\mathbf{q}_i)\}$, which satisfies a given optimal localization criterion. One of the goals of these procedures is to derive localized spin-orbitals which are approximately constant between structurally similar units in different molecules [199], see also Ref. [200]. In this thesis, the set of localized spin-orbitals is used in order to decompose electronic quantum fluxes into contributions from different sets of localized orbitals, corresponding e.g. to contributions from CH-bonds and so-called pericyclic orbitals, which correspond to the rearranging bonds in a pericyclic reaction according to the Lewis-structure, see Chapter 3 and Refs. [T1,T2,T5] for details.

Pipek and Mezey showed that for the underlying molecular-orbitals, c.f. eqn. (2.48), a localization quantity can be defined that measures the number of atoms over which the MO extends, see Ref. [201] and Refs. therein. This measure of localization for the particular MO $\psi_m(\mathbf{r}_i)$ is defined according to

$$d_m = \left\{ \sum_{A=1}^{M} \left(Q_A^m\right)^2 \right\}^{-1}, \tag{2.171}$$

where

$$Q_A^m = \sum_{\mu\in A} \sum_{\nu} c_{\mu m} c_{\nu m} S_{\mu\nu} \quad \text{with} \quad S_{\mu\nu} = \int \mathrm{d}\mathbf{r}_i \lambda_u(\mathbf{r}_i)\lambda_\nu(\mathbf{r}_i) \tag{2.172}$$

are the gross atomic Mullikan populations [202] for the MO m, with $S_{\mu\nu}$ being an element of the overlap matrix of AOs, c.f. eqn. (2.53). Hence, in the Pipek-Mezey localization scheme [201], they proposed to maximize the sum of the gross atomic Mullikan populations by maximizing the function

$$\Omega_{\mathrm{PM}} = 2\sum_{m}^{N/2} \sum_{A}^{M} \left(Q_A^m\right)^2, \tag{2.173}$$

where the sum over m runs over the $N/2$ occupied MOs. In these kind of optimizations, it is common to determine the optimal unitary transformations among the MOs and consequently among the spin-orbitals, c.f. eqn. (2.170), by consecutive two by two rotations according to

$$\begin{aligned} \psi'_s(\mathbf{r}_i) &= \cos(\gamma)\psi_{\mathrm{s}}(\mathbf{r}_i) + \sin(\gamma)\psi_t(\mathbf{r}_i) \\ \psi'_t(\mathbf{r}_i) &= -\sin(\gamma)\psi_{\mathrm{s}}(\mathbf{r}_i) + \cos(\gamma)\psi_t(\mathbf{r}_i), \end{aligned} \tag{2.174}$$

see Ref. [201] and Refs. therein for more details.

Alternative localization schemes are for example the Boys localization [199], in which the expectation value

$$\langle\Omega\rangle_{\text{Boys}} = 2\sum_{m}^{N/2} \underbrace{\int\int \mathrm{d}\mathbf{r}_i \mathrm{d}\mathbf{r}_j \psi_m^*(\mathbf{r}_i)\psi_m^*(\mathbf{r}_j)(\mathbf{r}-\mathbf{r}')^2\psi_m(\mathbf{r}_i)\psi_m(\mathbf{r}_j)}_{\langle\psi_m\psi_m|(\mathbf{r}_i-\mathbf{r}_j)^2|\psi_m\psi_m\rangle} \tag{2.175}$$

is minimized[17]. This corresponds to determining a set of localized MOs which minimize the spatial extent, that is they are as compact as possible.

Another approach is the Edmiston-Ruedenberg localization [203], in which the expectation value

$$\langle\Omega\rangle_{\text{ER}} = 2\sum_{m}^{N/2}\langle\psi_m\psi_m|\frac{1}{|\mathbf{r}_i-\mathbf{r}_j|}|\psi_m\psi_m\rangle \tag{2.176}$$

is minimized. Equation (2.176), in which the notation for the two-electron integrals introduced in eqn. (2.175) was used, corresponds to minimizing the self-repulsion energy, see also Ref. [200].

For most molecules, these localization schemes give very similar results [200]. The main exception is that the Pipek-Mezey method, eqn. (2.173), preserves the σ/π-separation, whereas the Boys and Edmiston-Ruedenberg schemes usually produce "banana" bonds in systems containing π-bonds. In this thesis, solely the Pipek-Mezey localization method [201] is used.

2.2.4 Atomic Orbitals (AOs)

All electronic structure calculations presented in this thesis use real-valued *Gaussian-type orbitals* (GTOs) as one-electron basis-functions, c.f. eqn. (2.53), which are given by

$$\lambda_{\zeta lm}^{\text{GTO}}(\mathbf{r}) = N_{\zeta lm}^{\text{GTO}} S_{lm}(\mathbf{r})\exp(-\zeta r^2), \tag{2.177}$$

with $\mathbf{r} = (r,\theta,\phi)$. $N_{\zeta lm}^{\text{GTO}}$ is a normalization constant, ζ is the orbital exponent and $S_{lm}(\mathbf{r})$ is one of the *real-values solid harmonics* [148]. The real-values solid harmonics are related to the complex valued spherical harmonics $Y_{lm}(\theta,\phi)$ [142] by

$$S_{l0}(\mathbf{r}) = N_l r^l Y_{l0}(\theta,\phi) \qquad \text{for} \qquad m = 0 \tag{2.178}$$

and

$$\begin{pmatrix} S_{lm}(\mathbf{r}) \\ S_{l,-m}(\mathbf{r}) \end{pmatrix} = \frac{1}{\sqrt{2}}\begin{pmatrix} (-1)^m & 1 \\ -(-1)^m i & i \end{pmatrix}\begin{pmatrix} N_l r^l Y_{lm}(\theta,\phi) \\ N_l r^l Y_{l,-m}(\theta,\phi) \end{pmatrix} \qquad \text{for} \qquad m > 0, \tag{2.179}$$

where N_l is a normalization constant [148], see also section 6.4.4 in Ref. [148] for explicit Cartesian expressions for the real-valued solid harmonics. Note that in electronic structure calculations for atoms and diatomics, *Slater-type orbitals* (STOs) [148] are often used. These STOs are in principle better suited for the description of atomic or molecular-orbitals leading to shorter expansion lengths for given accuracies. The longer expansion lengths for GTOs are,

[17] The MOs are usually real-valued functions, such that $\psi_m(\mathbf{r}_i) = \psi_m^*(\mathbf{r}_i)$.

however, computationally largely compensated by the faster evaluation of multi-center two-electron integrals, see Appendix 6.2, eqns. (6.6) and (6.15), employing the Gaussian product rule. Additionally, the integrals over the solid harmonic GTOs, eqn. (2.177), may be generated as linear combinations of integrals over Cartesian GTOs which are, on their turn, separable in the three Cartesian directions, making them the standard approach in molecular applications.

It turns out that a large number of GTOs is needed to give an accurate description of the electronic structure. Realizing, however, that this large number of GTOs is primarily needed to describe the unperturbed atomic electron distributions, modern basis-sets are constructed from so-called contracted GTOs, $\lambda_{\zeta lm}^{\mathrm{cGTO}}(\mathbf{r})$, which are fixed linear combinations of primitive GTOs, c.f. eqn. (2.177), according to [148, 204–208]:

$$\lambda_{\zeta lm}^{\mathrm{cGTO}}(\mathbf{r}) = \sum_i d_{ia} \lambda_{\zeta_i lm}^{\mathrm{GTO}}(\mathbf{r}). \tag{2.180}$$

There is a large variety of Gaussian basis-sets, which differ in the strategy used in the determination of the *orbital exponents* ζ_i and the *contraction coefficients* d_{ia} as well as in the actual contraction scheme, eqn. (2.180), see Refs. [148, 204–208] for various approaches. In this work, Dunning's *correlation-consistent* (cc) basis-sets [206] are used, which are designed for electronic structure calculations including a high degree of electron correlation. For this purpose, the contracted GTOs must represent both the occupied Hartree-Fock orbitals of the atomic systems and the virtual correlating orbitals into which the correlated electrons can be excited. Since the lowest lying virtual atomic Hartree-Fock orbitals are quite diffuse and hence ill suited for correlating the ground state electrons, the following strategy is used for the first group elements boron to neon:

- At first, a set of primitive GTOs, consisting typically of at least 9 primitive GTOs with $l = 0$ (s-functions) and 4 sets of primitive GTOs with $l = 1$ (p-functions) and $m = -1, 0, 1$, is chosen. This particular set of primitive GTOs is abbreviated by (9s4p). Next, the orbital exponents ζ_i and contraction coefficients d_{ia} of these primitive GTOs are variationally optimized in atomic Hartree-Fock calculations in order to obtain an accurate representation of the atomic ground-state Hartree-Fock orbitals. In these optimizations, all primitive GTOs of a given angular momentum are allowed to mix freely (*general contraction scheme*), giving rise to two optimized contracted GTOs with $l = 0$ and one optimized set with $l = 1$ and $m = -1, 0, 1$, with short-hand notation [2s1p]. Hence, in this short-hand notation, brackets refer to contracted GTOs and parentheses to primitive GTOs.

- Next, correlating orbitals, being represented by a single primitive GTO, are added in a step-wise fashion and their orbital exponents are determined by maximizing their contribution to the correlation energy in an atomic valence CISD calculation. All of those thus obtained correlating orbitals, giving similar contributions to the correlation energy, are then grouped together. Hence, a hierarchy of basis-sets is set up that is *correlation-consistent* in the sense that each basis-set contains all correlating orbitals that lower the CISD correlation energy by comparable amounts as well as all orbitals that lower the energy by larger amounts [206]. In this scheme, the s- and p-functions are added jointly

	Ground State HF Orbitals		Correlating Orbitals	Total
	Primitive	Contracted		
cc-pVDZ	(9s4p)	[2s1p]	(1s1p1d)	[3s2p1d]
cc-pVTZ	(10s5p)	[2s1p]	(2s2p2d1f)	[4s3p2d1f]
cc-pVQZ	(12s6p)	[2s1p]	(3s3p2d2f1g)	[5s4p2d2f1g]

Table 2.1: The structure of the correlation-consistent polarized split-valence basis-sets for atoms boron through neon [206]. Parentheses refer to primitive sets of GTOs, whereas brackets refer to contracted sets of GTOs.

giving rise to (sp)-sets, whereas the correlating orbitals with $l > 1$ are added separately to the respective (sp)-sets, for further details see Ref. [206].

It turns out that the first (sp)-set lowers the correlation energy by approximately the same amount as the first d-set (1d) with the contributions of the remaining sets being considerably lower, giving rise to the [3s2p1d] basis-set. Since one contracted GTO is used per core orbital while two contracted GTOs are used per valence orbital and since the correlation functions with $l > 1$ also serve as *polarization functions* upon molecule formation, this basis-set is referred to as *correlation-consistent - polarized split-valence double-zeta* (cc-pVDZ) basis-set, c.f. Table 2.1. Extension of this basis-set by another (sp)- and (d)-set and by a (f)-set, that all provide smaller but similar contributions to the correlation energy, yields the cc-pVTZ basis-set. Hence the notation of this hierarchical correlation-consistent basis-set is cc-pVXZ, where the cardinal number $X = D, T, Q, 5, 6, \ldots$ denotes the number of contracted GTOs describing each valence orbital. In practice, firstly the size of the primitive Gaussian basis used in the general contraction to obtain the atomic ground-state Hartree-Fock orbitals increases with the cardinal number X, e.g. for the cc-pVDZ set, a (9s4p)-set is contracted to [2s1p] and for the cc-pVTZ set a (10s5p)-set is contracted to [2s1p], see Table 2.1. Secondly, to save computational time, the exponents in the (sp)-correlating sets are usually not optimized variationally, but are taken as the most diffuse primitive functions from the preceding general contractions, which was shown to yield excellent results [206].

These basis-sets give excellent results for highly correlated calculations on molecules and are therefore adopted in molecular calculations without further scaling [148, 206]. The only exception is the hydrogen-atom for which the cc-basis-sets to be used in molecular calculations are obtained from optimizations on the hydrogen molecule, for details see Refs. [148, 206].

2.3 Nuclear Quantum Dynamics

Having discussed the numerical solution of the time-independent electronic Schrödinger equation, eqn. (2.5), we now turn to the solution of the time-dependent nuclear Schrödinger equation (TDNSE) in the adiabatic approximation, eqn. (2.17). At first, the numerical calculation of stationary nuclear states associated with electronic state i, $\zeta_j^{(i)}(\mathbf{R})$, is discussed in section 2.3.1. These stationary states, in particular the state associated with the lowest energy, $\zeta_0^{(i)}(\mathbf{R})$, often serves as the initial state for quantum dynamical simulations. They are obtained by applying the method of *separation of variables* to the TDNSE, i.e. solutions that can be written in the product form

$$\chi_i(\mathbf{R},t) = \chi_{i,j}(\mathbf{R},t) = f_j^{(i)}(t)\zeta_j^{(i)}(\mathbf{R}) \tag{2.181}$$

are sought. We obtain

$$i\frac{\mathrm{d}}{\mathrm{d}t}f_j^{(i)}(t) = \tilde{E}_j^{(i)}f_j^{(i)}(t) \qquad \text{with} \qquad f_j^{(i)}(t) = f_0 e^{-i\tilde{E}_j^{(i)}t} \tag{2.182}$$

and

$$\hat{H}_{\mathrm{nuc}}(\mathbf{R})\zeta_j^{(i)}(\mathbf{R}) = \left(\hat{T}_{\mathrm{nuc}}(\mathbf{R}) + V_i(\mathbf{R})\right)\zeta_j^{(i)}(\mathbf{R}) = \tilde{E}_j^{(i)}\zeta_j^{(i)}(\mathbf{R}), \tag{2.183}$$

where $\tilde{E}_j^{(i)}$ corresponds to the energy of the j-th stationary state associated with electronic state i and eqn. (2.183) is the time-independent nuclear Schrödinger equation (TINSE), see e.g. Refs. [137, 209]. The associated nuclear probability density

$$|\chi_i(\mathbf{R},t)|^2 = \left(\zeta_j^{(i)}(\mathbf{R})e^{-i\tilde{E}_j^{(i)}t}\right)^* \left(\zeta_j^{(i)}(\mathbf{R})e^{-i\tilde{E}_j^{(i)}t}\right) = |\zeta_j^{(i)}(\mathbf{R})|^2 \tag{2.184}$$

is of course time-independent and the multiplicative prefactor f_0 in eqn. (2.182) is usually absorbed into the orthonormal stationary states $\zeta_j^{(i)}(\mathbf{R})$.

The time-dependence of the nuclear density and other observables is regained by forming nuclear wave packets, i.e. linear combinations of non-degenerate stationary states, which are of course also solutions of the TDNSE. Consider for example a symmetric double well (DW) potential, $V_i^{\mathrm{DW}}(\mathbf{R})$, and the initial state

$$\chi_i(\mathbf{R},t=0) = \frac{1}{\sqrt{2}}\left(\zeta_0^{(i)}(\mathbf{R}) + \zeta_1^{(i)}(\mathbf{R})\right), \tag{2.185}$$

where $\zeta_0^{(i)}(\mathbf{R})$ and $\zeta_1^{(i)}(\mathbf{R})$ correspond to the lowest stationary nuclear states of *gerade* and *ungerade* symmetry, respectively. Then, the time-dependent nuclear wave function is given by

$$\chi_i(\mathbf{R},t) = \frac{1}{\sqrt{2}}\zeta_0^{(i)}(\mathbf{R})e^{-i\tilde{E}_0^{(i)}t} + \frac{1}{\sqrt{2}}\zeta_1^{(i)}(\mathbf{R})e^{-i\tilde{E}_1^{(i)}t} \tag{2.186}$$

with associated probability density

$$|\chi_i(\mathbf{R},t)|^2 = \frac{1}{2}|\zeta_0^{(i)}(\mathbf{R})|^2 + \frac{1}{2}|\zeta_1^{(i)}(\mathbf{R})|^2 + \zeta_0^{(i)}(\mathbf{R})\zeta_1^{(i)}(\mathbf{R})\cos\left(\left(\tilde{E}_1^{(i)} - \tilde{E}_0^{(i)}\right)t\right). \tag{2.187}$$

Hence, the time evolution is periodic and inversely proportional to the energy gap between the two states under consideration with period $\tilde{T} = \frac{2\pi}{\Delta\tilde{E}}$, where $\Delta\tilde{E} = \tilde{E}_1^{(i)} - \tilde{E}_0^{(i)}$. This example corresponds to coherent tunneling, with tunneling time $\tilde{T}$ and tunneling splitting $\Delta\tilde{E}$, see also Ref. [T4]. Section 2.3.2 describes the solution of the TDNSE in the case of more complicated initial states, including the case of time-dependent Hamilton-operators for nuclear movement. Finally, section 2.3.3 gives the explicit form of the interaction Hamiltonian used in this thesis and section 2.3.4 describes Optimal Control Theory (OCT), an algorithm for shaping the external laser field to reach a predefined quantum state from a given initial state.

2.3.1 Stationary nuclear states

We wish to solve the TINSE numerically using the *Fourier grid Hamiltonian method* (FGH) [210] in the one-dimensional case along some coordinate ξ describing a collective nuclear rearrangement with associated reduced mass m_ξ, which is the only case considered in this thesis, see section 2.4. The FGH method exploits the fact that the matrix representation of the potential energy operator is diagonal in the coordinate representation, whereas the representation of the kinetic energy operator is diagonal in the momentum representation. Hence, we first introduce the basis vectors of the coordinate representation $|\xi\rangle$ which are eigenvectors of the position operator

$$\hat{\xi}|\xi\rangle = \xi|\xi\rangle \tag{2.188}$$

with orthogonality and completeness relations

$$\langle\xi|\xi'\rangle = \delta(\xi - \xi') \qquad \text{and} \qquad \hat{I}_\xi = \int |\xi\rangle\langle\xi| \mathrm{d}\xi, \tag{2.189}$$

respectively. The eigenfunctions of the momentum operator are given by

$$\hat{p}|k\rangle = k|k\rangle \tag{2.190}$$

with analogous relations

$$\langle k|k'\rangle = \delta(k - k') \qquad \text{and} \qquad \hat{I}_k = \int |k\rangle\langle k| \mathrm{d}k. \tag{2.191}$$

Finally, the transformation matrix elements between the coordinate and momentum representation are given by

$$\langle k|\xi\rangle = \frac{1}{\sqrt{2\pi}} e^{-ik\xi}. \tag{2.192}$$

Hence, the matrix representation of the nuclear Hamilton operator in the coordinate representation is given by

$$\begin{aligned} \langle\xi|\hat{H}_{\mathrm{nuc}}(\xi)|\xi'\rangle &= \langle\xi|\hat{T}_{\mathrm{nuc}}(\xi) + V_i(\xi)|\xi'\rangle \\ &= \langle\xi|\frac{\hat{p}(\xi)^2}{2m_\xi} + V_i(\xi)|\xi'\rangle = \langle\xi|\frac{\hat{p}(\xi)^2}{2m_\xi}|\xi'\rangle + V_i(\xi)\delta(\xi - \xi'). \end{aligned} \tag{2.193}$$

Inserting the identity operator $\hat{I}_k$, eqn. (2.191), to the right of the kinetic energy operator, we obtain

$$\langle\xi|\hat{H}_{\rm nuc}(\xi)|\xi'\rangle = \langle\xi|\frac{\hat{p}(\xi)^2}{2m_\xi}\hat{I}_k|\xi'\rangle + V_i(\xi)\delta(\xi-\xi') \tag{2.194}$$

$$= \frac{1}{2\pi}\int e^{ik(\xi-\xi')}\frac{k^2}{2m_\xi}\mathrm{d}k + V_i(\xi)\delta(\xi-\xi'). \tag{2.195}$$

Next, the continous range of the coordinate values ξ is replaced by a grid of discrete values

$$\xi_l = l\Delta\xi \qquad \text{with} \qquad l = 1,2,\ldots,\tilde{N}, \tag{2.196}$$

where $\Delta\xi$ is the uniform spacing between the $\tilde{N}$ grid points. The grid size and spacing chosen in the coordinate space determines the reciprocal grid size in the momentum space

$$\Delta k = \frac{2\pi}{\tilde{N}\Delta\xi}. \tag{2.197}$$

The eigenvectors in this discrete basis satisfy

$$\Delta\xi\langle\xi_m|\xi_n\rangle = \delta_{mn} \qquad \text{and} \qquad \hat{I}'_\xi = \sum_l^{\tilde{N}}\Delta\xi|\xi_l\rangle\langle\xi_l|, \tag{2.198}$$

c.f. eqn. (2.189). The discretized analog to eqn. (2.195) hence becomes for odd numbers of grid points

$$\langle\xi_m|\hat{H}_{\rm nuc}(\xi)|\xi_n\rangle = H^{(i)}_{mn} = \frac{1}{\Delta\xi}\left(\frac{\Delta k^2}{2m_\xi\tilde{N}}\sum_{l=-\frac{\tilde{N}-1}{2}}^{\frac{\tilde{N}-1}{2}} l^2 e^{il2\pi(m-n)/\tilde{N}} + V_i(\xi_m)\delta_{mn}\right). \tag{2.199}$$

The summation in eqn. (2.199) may be performed analytically yielding [209]

$$H^{(i)}_{mn} = \frac{1}{2m_\xi\Delta\xi}\begin{cases}\frac{\pi^2}{3\Delta\xi^2}\left(1+\frac{1}{\tilde{N}^2}\right)+V_i(\xi_m) & (m=n)\\ \frac{2\pi^2}{\Delta\xi^2\tilde{N}^2}\frac{\cos\left(\pi\frac{n-m}{\tilde{N}}\right)(-1)^{n-m}}{\sin^2(\pi\frac{m-n}{\tilde{N}})} & (m\neq n).\end{cases} \tag{2.200}$$

Any state function $|\zeta^{(i)}_j\rangle$ corresponding to the stationary state $\zeta^{(i)}_j(\xi)$ may be expressed as a linear combination of the basis functions $|\xi_l\rangle$

$$|\zeta^{(i)}_j\rangle = \hat{I}'_\xi|\zeta_j\rangle = \sum_l^{\tilde{N}}|\xi_l\rangle\Delta\xi\zeta^{(i)}_j(\xi_l), \tag{2.201}$$

c.f. eqn. (2.198). The corresponding energy is given by

$$\tilde{E}^{(i)}_j = \frac{\langle\zeta^{(i)}_j|\hat{H}_{\rm nuc}(\xi)|\zeta^{(i)}_j\rangle}{\langle\zeta^{(i)}_j|\zeta^{(i)}_j\rangle} = \frac{\sum_{mn}\zeta^{(i)*}_j(\xi_m)\Delta\xi H^{(i)}_{mn}\zeta^{(i)}_j(\xi_n)\Delta\xi}{\Delta\xi\sum_m|\zeta^{(i)}_j(\xi_m)|^2} \tag{2.202}$$

$$= \frac{\sum_{mn}\zeta^{(i)*}_j(\xi_m)\tilde{H}^{(i)}_{mn}\zeta^{(i)}_j(\xi_n)}{\sum_m|\zeta^{(i)}_j(\xi_m)|^2},$$

where the renormalized Hamiltonian matrix $\tilde{\mathbf{H}}^{(i)}$ with elements $\tilde{H}^{(i)}_{mn} = \Delta\xi H^{(i)}_{mn}$ was defined. Hence the nuclear eigenfunctions $\zeta^{(i)}_j(\xi)$ with corresponding eigenvalues $\tilde{E}^{(i)}_j$, eqn. (2.183), are obtained by diagonalization of $\tilde{\mathbf{H}}^{(i)}$ [210].

2.3.2 Propagating nuclear wave packets

We now turn to the time-propagation of nuclear wave packets. Starting from the TDNSE, eqn. (2.17), we get for time-independent nuclear Hamilton operators $\hat{H}_{\mathrm{nuc}}(\xi)$

$$\begin{aligned} \int_{\chi_i(\xi,0)}^{\chi_i(\xi,t)} \frac{1}{\chi_i(\xi,t)} \mathrm{d}\chi_i(\xi,t) = \hat{H}_{\mathrm{nuc}}(\xi) \int_0^t \frac{1}{i} \mathrm{d}t' \quad &\Longrightarrow \quad \ln\frac{\chi_i(\xi,t)}{\chi_i(\xi,0)} = -i\hat{H}_{\mathrm{nuc}}(\xi)t \\ &\Longrightarrow \quad \chi_i(\xi,t) = e^{-i\hat{H}_{\mathrm{nuc}}(\xi)t}\chi(\xi,0). \end{aligned} \tag{2.203}$$

In the split operator method [211], see also Ref. [209], the propagator $\hat{U}(t,0) = e^{-i\hat{H}_{\mathrm{nuc}}(\xi)t}$ over the global time interval [0,t] is at first expressed as a product of propagators over $\tilde{M}$ short time intervals Δt, with $\tilde{M}\Delta t = t$, yielding

$$\hat{U}(t,0) = e^{-i\hat{H}_{\mathrm{nuc}}(\xi)t} = \underbrace{e^{-i\hat{H}_{\mathrm{nuc}}(\xi)\Delta t} e^{-i\hat{H}_{\mathrm{nuc}}(\xi)\Delta t} \ldots e^{-i\hat{H}_{\mathrm{nuc}}(\xi)\Delta t}}_{\tilde{M}\,\mathrm{times}}. \tag{2.204}$$

Each short time propagator is then expressed as a symmetrized product of a kinetic and a potential factor

$$\begin{aligned} e^{-i\hat{H}_{\mathrm{nuc}}(\xi)\Delta t} &= e^{-i(\hat{T}_{\mathrm{nuc}}(\xi)+V_i(\xi))\Delta t} \\ &\approx e^{-iV_i(\xi)\Delta t/2} e^{-i\hat{T}_{\mathrm{nuc}}(\xi)\Delta t} e^{-iV_i(\xi)\Delta t/2} + O(\Delta t^3), \end{aligned} \tag{2.205}$$

yielding an error of third order in Δt which is proportional to the commutator $[\hat{T}_{\mathrm{nuc}}(\xi), V_i(\xi)]$ [209]. Linking multiple time steps, we finally get

$$e^{-i\hat{H}_{\mathrm{nuc}}(\xi)t} = e^{-iV_i(\xi)\Delta t/2} \underbrace{e^{-i\hat{T}_{\mathrm{nuc}}(\xi)\Delta t} e^{-iV_i(\xi)\Delta t}}_{\tilde{M}-1\,\mathrm{times}} e^{-i\hat{T}_{\mathrm{nuc}}(\xi)\Delta t} e^{-iV_i(\xi)\Delta t/2}. \tag{2.206}$$

Since the matrix representation of the potential energy operator in the coordinate representation is diagonal, $\langle\xi_m|V_i(\xi)|\xi_n\rangle = V_i(\xi_n)\delta_{mn}/\Delta\xi$, eqn. (2.199), the operation $e^{-iV_i(\xi)\Delta t}\chi_i(\xi)$ is readily obtained on a grid with $\tilde{N}$ grid points by matrix vector multiplication according to

$$\begin{pmatrix} e^{-iV_i(\xi_1)\Delta t} & 0 & \ldots & 0 \\ 0 & e^{-iV_i(\xi_2)\Delta t} & \ldots & 0 \\ \vdots & \vdots & \ddots & 0 \\ 0 & 0 & \ldots & e^{-iV_i(\xi_{\tilde{N}})\Delta t} \end{pmatrix} \begin{pmatrix} \chi_i(\xi_1,t) \\ \chi_i(\xi_2,t) \\ \vdots \\ \chi_i(\xi_{\tilde{N}},t) \end{pmatrix}. \tag{2.207}$$

The operation involving the exponential of the kinetic energy operator $e^{-i\hat{T}_{\mathrm{nuc}}(\xi)\Delta t}$ is evaluated by the analogous expression in momentum space, since firstly the matrix representation of the kinetic energy operator is diagonal in this representation, $\langle k_m|\hat{T}_{\mathrm{nuc}}|k_n\rangle = \frac{k_n^2}{2m_\xi}\delta_{mn}/\Delta k$, and

secondly the effect of the kinetic energy operator on the wave function in this representation corresponds to a simple multiplication. The corresponding transformation $Ze^{-i\hat{T}_{\mathrm{nuc}}(\xi)\Delta t/\hbar}Z^{\dagger}\chi_i(\xi)$, where $Z^{\dagger}$ is the transformation between the coordinate and momentum representation, is readily implemented using Fast Fourier Transformation, for details see e.g. Ref. [209]. For the propagation of nuclear wave packets on multiple electronic states see end of section 2.3.3.

2.3.3 Interaction with external laser fields

In order to set up the theoretical framework for the treatment of the dynamics of molecules in the presence of external ultra-short laser pulses, at first the dynamics of a single particle in an electromagnetic field is considered. Hence, this particle with charge q and mass m located at position $\tilde{\mathbf{r}}$ is subjected to the Lorentz force

$$\mathbf{F}(\tilde{\mathbf{r}},\dot{\tilde{\mathbf{r}}},t) = q\left[\boldsymbol{\mathcal{E}}(\tilde{\mathbf{r}},t) + \dot{\tilde{\mathbf{r}}}\times\mathbf{B}(\tilde{\mathbf{r}},t)\right], \tag{2.208}$$

with $\mathbf{E}(\tilde{\mathbf{r}},t)$ and $\mathbf{B}(\tilde{\mathbf{r}},t)$ denoting the classical electric and magnetic fields, respectively [142]. The corresponding classical Hamilton function is given by

$$H^{\mathrm{cl}}(\tilde{\mathbf{r}},\tilde{\mathbf{p}},t) = \frac{[\tilde{\mathbf{p}} - q\mathbf{A}(\tilde{\mathbf{r}},t)]^2}{2m} + qU(\tilde{\mathbf{r}},t), \tag{2.209}$$

where $\tilde{\mathbf{p}} = m\dot{\tilde{\mathbf{r}}} + q\boldsymbol{A}(\tilde{\mathbf{r}},t)$ is the conjugate momentum. Obviously, in the Hamilton formalism, the vector and scalar potentials, $\mathbf{A}(\tilde{\mathbf{r}},t)$ and $U(\tilde{\mathbf{r}},t)$, respectively, are used instead of the electric and magnetic fields with relations

$$\mathbf{B}(\tilde{\mathbf{r}},t) = \boldsymbol{\nabla}_{\tilde{\mathbf{r}}}\times\mathbf{A}(\tilde{\mathbf{r}},t) \tag{2.210}$$

and

$$\boldsymbol{\mathcal{E}}(\tilde{\mathbf{r}},t) = -\boldsymbol{\nabla}_{\tilde{\mathbf{r}}}U(\tilde{\mathbf{r}},t) - \frac{\partial}{\partial t}\mathbf{A}(\tilde{\mathbf{r}},t). \tag{2.211}$$

This reformulation is possible due to the structure of the Maxwell equations and is standard both in the Lagrangian and Hamilton formalisms, for details see Refs. [142, 212]. Furthermore, the potentials $\mathbf{A}(\tilde{\mathbf{r}},t)$ and $U(\tilde{\mathbf{r}},t)$ are mathematical quantities which may be adjusted as long as the fields $\boldsymbol{\mathcal{E}}(\tilde{\mathbf{r}},t)$ and $\mathbf{B}(\tilde{\mathbf{r}},t)$ are unchanged. Such adjustments are referred to as *gauge transformations* [142].

To proceed, several approximations are invoked: *Firstly*, the electromagnetic radiation is treated classically such that the corresponding quantum mechanical Hamilton operator in the position representation is obtained by replacing in the corresponding classical expression, eqn. (2.209), the conjugate momentum $\tilde{\mathbf{p}}$ by the generator of translations in position space, $\hat{\boldsymbol{p}}(\tilde{\mathbf{r}}) = -i\boldsymbol{\nabla}_{\tilde{\mathbf{r}}}$, and the position $\tilde{\mathbf{r}}$ by the multiplication operator $\tilde{\mathbf{r}}\cdot$, yielding

$$\hat{H}(\tilde{\mathbf{r}},t) = \frac{[-i\boldsymbol{\nabla}_{\tilde{\mathbf{r}}} - q\mathbf{A}(\tilde{\mathbf{r}},t)]^2}{2m} + qU(\tilde{\mathbf{r}},t). \tag{2.212}$$

For the external radiation consider at first a plane electromagnetic wave of wave vector $\mathbf{k}$ parallel to the y-axis, with angular frequency $\omega = kc$, where c denotes the speed of light. For

such a wave, the gauge, that is the set of potentials ($\mathbf{A}(\tilde{\mathbf{r}},t)$, $U(\tilde{\mathbf{r}},t)$) may be chosen according to

$$U^{\mathrm{VG}}=0 \qquad \text{and} \qquad \mathbf{A}^{\mathrm{VG}}(\tilde{\mathbf{r}},t)=-\int_{-\infty}^{t}\boldsymbol{\mathcal{E}}(\tilde{\mathbf{r}},t')\mathrm{d}t'=\frac{\mathcal{E}_0}{\omega}\mathbf{e}_{\mathrm{z}}\sin(k\tilde{y}-\omega t), \tag{2.213}$$

where $\mathcal{E}_0$ denotes the amplitude of the electric field and the superscript stands for velocity gauge [142]. Hence, the vector potential $\mathbf{A}^{\mathrm{VG}}(\tilde{\mathbf{r}},t)$ and the electric field are parallel to the z-axis and the magnetic field is parallel to the x-axis, eqn. (2.210).

The *second approximation* involves the neglect of the spatial variations of the vector potential,

$$\mathbf{A}^{\mathrm{VG}}(\tilde{\mathbf{r}},t)\approx\mathbf{A}^{\mathrm{VG}}(t)=-\frac{\mathcal{E}_0}{\omega}\mathbf{e}_{\mathrm{z}}\sin(\omega t). \tag{2.214}$$

The validity of this approximation can be seen by a comparison of the atomic radii or molecular diameters to the spatial variations of the field, which are on the order of the wavelength at each instant of time. This approximation also implies the neglect of the magnetic field, c.f. eqn. (2.210), including the interaction of the spin magnetic moment of the electron with the magnetic field [142]. These approximations, usually referred to as the *semiclassical dipole approximation*, yield the Hamiltonian in velocity gauge

$$\hat{H}^{\mathrm{VG}}(t)=\frac{\hat{\mathbf{p}}(\tilde{\mathbf{r}})^2}{2m}+\frac{q}{m}\mathbf{A}^{\mathrm{VG}}(t)\hat{\mathbf{p}}(\tilde{\mathbf{r}})+\frac{q^2}{2m}\mathbf{A}^{\mathrm{VG}}(t)^2. \tag{2.215}$$

The space independent term proportional to $\mathbf{A}^{\mathrm{VG}}(t)^2$ is usually dropped since it merely leads to a global phase term [213].

Expressing the Hamiltonian in another gauge is achieved by the gauge transformation

$$\tilde{\boldsymbol{A}}(\tilde{\mathbf{r}},t)=\mathbf{A}^{\mathrm{VG}}(\tilde{\mathbf{r}},t)+\boldsymbol{\nabla}_{\tilde{\mathbf{r}}}\theta(\tilde{\mathbf{r}},t) \tag{2.216}$$

and

$$\tilde{U}(\tilde{\mathbf{r}},t)=U^{\mathrm{VG}}(\tilde{\mathbf{r}},t)-\frac{\partial}{\partial t}\theta(\tilde{\mathbf{r}},t), \tag{2.217}$$

where $\theta(\tilde{\mathbf{r}},t)$ is the so-called gauge function, an arbitrary function of $\tilde{\mathbf{r}}$ and t [142]. The Hamiltonian in the so-called length gauge (LG) is obtained by the Göppert-Mayer transformation [214] with

$$\theta(\tilde{\mathbf{r}},t)=-\tilde{\mathbf{r}}\mathbf{A}^{\mathrm{VG}}(0,t), \tag{2.218}$$

yielding

$$U^{\mathrm{LG}}(\tilde{\mathbf{r}},t)=-\tilde{z}\mathcal{E}_0\cos(\omega t)=-\tilde{z}\mathcal{E}_z(t) \quad \text{and} \quad \mathbf{A}^{\mathrm{LG}}(\tilde{\mathbf{r}},t)=\mathbf{e}_z\frac{\mathcal{E}_0}{\omega}\left(\sin(k\tilde{y}-\omega t)+\sin(\omega t)\right), \tag{2.219}$$

where $\mathcal{E}_z(t)$ denotes the z-component of the space independent electric field and $\mathbf{A}^{\mathrm{LG}}(\tilde{\mathbf{r}},t)=0$ upon neglect of the spatial variations according to the dipole approximation [142, 213, 214]. Hence, the Hamiltonian in length gauge takes on the form

$$\hat{H}^{\mathrm{LG}}(t)=\frac{\hat{\mathbf{p}}(\tilde{\mathbf{r}})^2}{2m}-q\tilde{z}\mathcal{E}_z(t). \tag{2.220}$$

Although in principle the results of a given calculation should be gauge invariant, different results are often obtained in numerical calculations, mostly due to basis-set truncations, see e.g. Refs. [213, 215]. These problems, however, are mostly encountered in strong-field physics [8], and do not play a role in the rather straightforward quantum dynamical calculations presented in this thesis, in which the length gauge is chosen.

The plane waves discussed so far have infinite temporal extensions and are appropriate to describe continuous wave lasers. Ultrashort laser pulses, on the other hand, may be described by superpositions of plane waves with different frequencies and well defined phase relationships between the frequency components, see for instance Ref. [216] for an illustrative description. In this thesis, only linearly polarized ultrashort laser pulses with polarization along the z-axis with $\boldsymbol{\mathcal{E}}(t) = (0, 0, \mathcal{E}_z(t))$, are considered. For quantum dynamical simulations employing circularly polarized laser pulses, see e.g. Refs. [14, 15]. In order to assure that the electric field $\mathcal{E}_z(t)$ is a solution of the Maxwell equations in the propagation region [217], satisfying $-\int_{-\infty}^{t_\mathrm{f}} \mathcal{E}_z(t)\mathrm{d}t = \mathbf{A}^{\mathrm{VG}}(t_\mathrm{f}) = 0$, where t_f denotes the end of the laser pulse, the electric field is often derived from the vector potential in velocity gauge $\mathbf{A}^{\mathrm{VG}}(t) = (0, 0, A^{\mathrm{VG}}(t))$, according to [218–221]

$$\mathcal{E}_z(t) = -\frac{\mathrm{d}}{\mathrm{d}t} A^{\mathrm{VG}}(t), \tag{2.221}$$

c.f. eqn. (2.213).

The vector potential, resulting from the superposition of plane waves with different frequencies and well defined phase relationships, may be described by

$$A^{\mathrm{VG}}(t) = -\frac{\mathcal{E}_0}{\omega_0} s(t) \sin(\omega t + \eta), \tag{2.222}$$

where ω_0 is the laser carrier frequency and η is the carrier envelope phase [218–221]. For the shape function $s(t)$, two different expressions are used in this thesis: $\sin^2$-functions [222, 223]

$$s(t) = \begin{cases} \sin^2(\frac{\pi t}{t_\mathrm{p}}) & \text{for} \quad 0 \leq t \leq t_\mathrm{p} \\ 0 & \text{else,} \end{cases} \tag{2.223}$$

with total pulse duration t_p are used in Ref. [T2], whereas Gaussian shape functions

$$s(t) = \exp\left(-\frac{t^2}{2\tau_\mathrm{p}^2}\right) \tag{2.224}$$

with duration τ_p are used in Ref. [T7], see also Ref. [218] for a test of different shape functions. For the z-component of the electric field, we get

$$\mathcal{E}_z(t) = \mathcal{E}_0 s(t) \cos(\omega_0 t + \eta) + \frac{\mathcal{E}_0}{\omega_0} \left[\frac{\mathrm{d}}{\mathrm{d}t} s(t)\right] \sin(\omega_0 t + \eta). \tag{2.225}$$

The first term corresponds to a pulse with a cosine-oscillating carrier field, while the second term (switching term) arises because of the finite pulse duration. Since this switching term is only important in simulations with electric fields containing few optical cycles, see for instance Refs. [219, 220]+[B1-B4], it is neglected in this thesis because only analytical pulses containing a

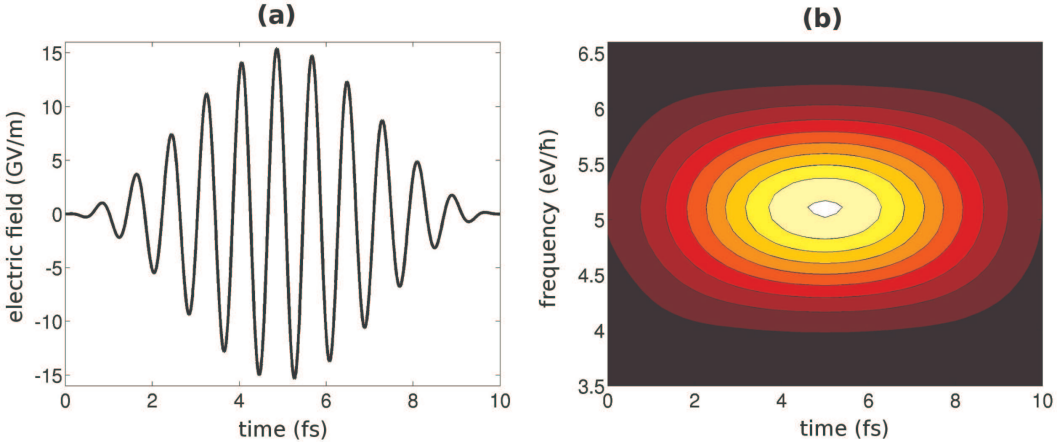

Figure 2.4: (a) Electric field of the initial laser pulse from Ref. [T2], containing solely one sub-pulse, $q = 1$, eqn. (2.226), with $\mathcal{E}_{0,1} = 15.4\,\mathrm{GV/m}$ and corresponding maximal transient intensity $I_{\max} = 4.1 \times 10^{12}\,\mathrm{W/cm^2}$, eqn. (2.227), using a $\sin^2$-shape function with $\tau_{\mathrm{d},1} = 0$, $t_p = 10\,\mathrm{fs}$ and central frequency $\omega_{0,1} = 5.1\,\mathrm{eV}/\hbar$. (b) Time-frequency profile of the electric field shown in (a), obtained by a Gabor transform using a Gaussian time-window, eqn. (2.228), with $\sigma = 1.5\,\mathrm{fs}$.

large number of optical cycles are used in Refs. [T2,T7]. Accordingly, the z-component of the electric field of a laser pulse containing q sub-pulses with equal shape functions $s(t)$ as used in Ref. [T7] is given by

$$\mathcal{E}_z(t) = \sum_{i=1}^{q} \mathcal{E}_{0,i}\, s(t - \tau_{\mathrm{d},i}) \cos(\omega_{0,i}(t - \tau_{\mathrm{d},i}) + \eta_i), \tag{2.226}$$

where $\tau_{\mathrm{d},i}$ denotes, for sub-pulse i, the temporal center in the case of Gaussian shape functions, eqn. (2.224), and the starting time in the case of $\sin^2$-shape functions, eqn. (2.223).

Figure 2.4(a) shows the electric field for $q = 1$ using a $\sin^2$-shape function with amplitude $\mathcal{E}_{0,1} = 15.4\,\mathrm{GV/m}$, starting time $\tau_{\mathrm{d},1} = 0$, pulse duration $t_{\mathrm{p},1} = 10\,\mathrm{fs}$ and central frequency $\omega_{0,1} = 5.1\,\mathrm{eV}/\hbar$. The corresponding maximal transient intensity

$$I_{\max} = c\epsilon_0 \mathcal{E}_{0,1}^2 = 4.1 \times 10^{12}\,\mathrm{W/cm^2}, \tag{2.227}$$

where c is the speed of light and ϵ_0 the vacuum permittivity. Note that this is the laser pulse used in Ref. [T2] as initial guess for the Optimal Control Theory algorithm, for details see section 2.3.4.

For the analysis of electric fields in Ref. [T2], time-frequency profiles of the form

$$F(t', \omega) = \left| \int_{-\infty}^{\infty} \mathcal{E}_z(t)\, g(t - t')\, e^{-i\omega t} \mathrm{d}t \right| \tag{2.228}$$

are calculated, where $g(t - t')$ is a gate function that selects a small part of the signal around time t' which is then Fourier transformed, see e.g. Refs. [98,99,224]+[B1,B3]. A Gaussian window

function is used for this gate in Ref. [T2] with the form $g(u) = (\sigma^2\pi)^{-1/4}\exp(-u^2/2\sigma^2)$ corresponding to a Gabor transform [224]. Figure 2.4(b) shows the time-frequency profile $F(t',\omega)$ of the $\sin^2$-pulse from Figure 2.4(a) with $\sigma = 1.5\,\mathrm{fs}$.

Extending the example of a single particle of charge q and mass m interacting with an ultrashort laser pulse described in length gauge, eqn. (2.220), the corresponding total Hamiltonian in the molecular case is given by

$$\hat{H}(\mathbf{r},\mathbf{R},t) = \hat{H}_{\mathrm{mol}}(\mathbf{r},\mathbf{R}) + H_{\mathrm{int}}^{\mathrm{LG}}(t) = \hat{H}_{\mathrm{mol}}(\mathbf{r},\mathbf{R}) - \boldsymbol{\mathcal{E}}(t)\underbrace{\left(\sum_i (-1)\mathbf{r}_i + \sum_A Z_A\mathbf{R}_A\right)}_{\hat{\boldsymbol{\mu}}(\mathbf{r},\mathbf{R})}, \tag{2.229}$$

where the molecular Hamiltonian was given in eqn. (2.3). $\boldsymbol{\mathcal{E}}(t)$ and $\hat{\boldsymbol{\mu}}(\mathbf{R},\mathbf{r})$ are the time-dependent external electric laser field, taken to be linearly polarized in this thesis, and the molecular dipole operator, respectively, with components $\boldsymbol{\mathcal{E}}(t) = (0,0,\mathcal{E}_z(t))$ and $\hat{\boldsymbol{\mu}}(\mathbf{R},\mathbf{r}) = (\hat{\mu}_x(\mathbf{R},\mathbf{r}),\hat{\mu}_y(\mathbf{R},\mathbf{r}),\hat{\mu}_z(\mathbf{R},\mathbf{r}))$. Considering a two state system, the Born-representation, eqn. (2.10), becomes

$$\Psi(\mathbf{q},\mathbf{Q},t) = \chi_{\mathrm{g}}(\mathbf{Q},t)\Phi_{\mathrm{g}}(\mathbf{q};\mathbf{R}) + \chi_{\mathrm{e}}(\mathbf{Q},t)\Phi_{\mathrm{e}}(\mathbf{q};\mathbf{R}), \tag{2.230}$$

where g denotes the electronic ground state and e denotes the first excited electronic state, c.f. Ref. [T2]. Employing the same procedure described in section 2.1, i.e. insertion of eqn. (2.230) into the TDSE, eqn. (2.1), followed by multiplication from the left by $\Phi_j(\mathbf{q};\mathbf{R})$ and integration over the set of electronic coordinates $\mathbf{q}$ and the set of nuclear spin coordinates $\boldsymbol{\Sigma}$, leads to the following TDNSE after neglecting non-adiabatic couplings, eqn. (2.12),

$$i\frac{\partial}{\partial t}\begin{pmatrix}\chi_g(\mathbf{R},t)\\ \chi_e(\mathbf{R},t)\end{pmatrix} = \begin{pmatrix}\hat{T}_{\mathrm{nuc}}(\mathbf{R}) + V_g(\mathbf{R}) - \mathcal{E}_z(t)\mu_{z,gg}(\mathbf{R}) & -\mathcal{E}_z(t)\mu_{z,ge}(\mathbf{R})\\ -\mathcal{E}_z(t)\mu_{z,eg}(\mathbf{R}) & \hat{T}_{\mathrm{nuc}}(\mathbf{R}) + V_e(\mathbf{R}) - \mathcal{E}_z(t)\mu_{z,ee}(\mathbf{R})\end{pmatrix}\begin{pmatrix}\chi_g(\mathbf{R},t)\\ \chi_e(\mathbf{R},t)\end{pmatrix}. \tag{2.231}$$

Here, $\mu_{z,gg}(\mathbf{R}) = \langle\Phi_g|\hat{\mu}_z|\Phi_g\rangle$ and $\mu_{z,ee}(\mathbf{R}) = \langle\Phi_e|\hat{\mu}_z|\Phi_e\rangle$ are the z-components of the permanent dipole moments associated with the electronic ground and excited state, respectively, which are important for transitions between (stationary) nuclear states within a given electronic state. These terms are usually neglected when the respective electronic states are energetically well separated and electric fields with carrier frequencies ω_0, which are near resonant to the transition between these electronic states, are used. This approximation was also used in Refs. [T2] and [T7]. The z-components of the transition dipole moments, $\mu_{z,ij}(\mathbf{R}) = \langle\Phi_i|\hat{\mu}_z|\Phi_j\rangle$ with $i \neq j$, on the other hand, mediate transitions between the electronic states.

The interaction with the external laser field couples the two electronic states such that the propagation scheme described in section 2.3.2 needs to be slightly modified since the matrix representation of the potential energy operators including the interaction with the external laser field is not diagonal [225]: For this two state system, the symmetrized short time evolution operator, eqn. (2.205), is given by

$$\begin{aligned}\exp\left[-i\begin{pmatrix}\hat{T}_{\mathrm{nuc}}+V_g & W\\ W & \hat{T}_{\mathrm{nuc}}+V_e\end{pmatrix}\Delta t\right] &= \exp\left[-i\begin{pmatrix}\hat{T}_{\mathrm{nuc}} & 0\\ 0 & \hat{T}_{\mathrm{nuc}}\end{pmatrix}\frac{\Delta t}{2}\right]\exp\left[-i\begin{pmatrix}V_g & W\\ W & V_e\end{pmatrix}\Delta t\right]\\ &\quad\times\exp\left[-i\begin{pmatrix}\hat{T}_{\mathrm{nuc}} & 0\\ 0 & \hat{T}_{\mathrm{nuc}}\end{pmatrix}\frac{\Delta t}{2}\right] + O(\Delta t^3),\end{aligned} \tag{2.232}$$

where for notational convenience the dependence of the respective terms on the nuclear coordinate ξ was dropped and $W = -\mathcal{E}_z(t)\mu_{z,eg} = -\mathcal{E}_z(t)\mu_{z,ge}$. The last equality holds for real electronic wave functions, which is the case in this thesis. In addition to the transformation between the coordinate and momentum representation for the evaluation of the kinetic energy part described in section 2.3.2, the potential energy matrix including the interaction with the external laser field needs to be diagonalized at every time step. This is achieved by the unitary transformation matrix

$$\mathbf{U} = \begin{pmatrix} -\frac{V_e - V_g + \sqrt{D}}{W\sqrt{4 + (V_e - V_g + \sqrt{D})^2/W^2}} & -\frac{V_e - V_g - \sqrt{D}}{W\sqrt{4 + (V_e - V_g - \sqrt{D})^2/W^2}} \\ -\frac{2}{\sqrt{4 + (V_e - V_g + \sqrt{D})^2/W^2}} & -\frac{2}{\sqrt{4 + (V_e - V_g - \sqrt{D})^2/W^2}} \end{pmatrix} \tag{2.233}$$

with $D = (V_e - V_g)^2 + 4W^2$ according to

$$\begin{aligned} \exp\left[-i \begin{pmatrix} V_g & W \\ W & V_e \end{pmatrix} \Delta t\right] &= \mathbf{U} \exp\left[-i\mathbf{U}^T \begin{pmatrix} V_g & W \\ W & V_e \end{pmatrix} \mathbf{U} \Delta t\right] \mathbf{U}^T \\ &= \mathbf{U}\left[\begin{pmatrix} \exp(-i\lambda_+ \Delta t) & 0 \\ 0 & \exp(-i\lambda_- \Delta t) \end{pmatrix}\right] \mathbf{U}^T \\ &= \exp\left[-i(V_g + V_e)\frac{\Delta t}{2}\right] \times \\ &\quad \left[\cos\left(\sqrt{D}\frac{\Delta t}{2}\right) \begin{pmatrix} 1 & 0 \\ 0 & 1 \end{pmatrix} + i\frac{\sin\left(\sqrt{D}\frac{\Delta t}{2}\right)}{\sqrt{D}} \begin{pmatrix} V_e - V_g & -2W \\ -2W & V_g - V_e \end{pmatrix}\right]. \end{aligned} \tag{2.234}$$

Here, the superscript T indicates the transpose of the matrix and the eigenvalues $\lambda_\pm$ are given by $\lambda_\pm = \frac{1}{2}\left(V_\mathrm{g} + V_\mathrm{e} \pm \sqrt{D}\right)$. Hence, for two state systems, the application of non-diagonal potential energy matrices reduces to matrix multiplications without any numerical diagonalization [225].

2.3.4 Optimal Control Theory

The aim of Optimal Control Theory (OCT) [91–99] is to find an optimal electric field $\boldsymbol{\mathcal{E}}(t)$ that drives the system from a predefined initial state at time $t = 0$, $\Psi(\mathbf{q}, \mathbf{Q}, t = 0) = \Psi_\mathrm{init}$, to a predefined target. In this section, again only linearly polarized laser pulses are discussed.

Specifically, in the OCT-algorithm implemented in the MCDTH-program package [226], which is based on Ref. [97] and was used in this thesis, Ref. [T2], the expectation value of a given positive definite target operator $\hat{O}$ at a predefined time, $t = t_\mathrm{tar}$, the so-called *control yield*,

$$O[t_\mathrm{tar;}\mathcal{E}_z(t)] = \langle \Psi(t_\mathrm{tar}) | \hat{O} | \Psi(t_\mathrm{tar}) \rangle, \tag{2.235}$$

is maximized while minimizing the intensity of the optimized laser field. In eqn. (2.235) involving the total wave function $\Psi(\mathbf{q}, \mathbf{Q}, t)$, the integration is over both the set of electronic and nuclear coordinates, c.f. eqn. (2.9). Such target operators may, for instance, be projections on specific stationary nuclear states in the electronic ground state [96,98,99], as well as projections on an excited electronic state without specification of the nuclear wave function [227] or the projection on a given product channel of a chemical reaction [228].

This optimization is achieved by first constructing the *control functional*

$$J[t_{\rm tar};\mathcal{E}_z(t)] = O[t_{\rm tar};\mathcal{E}_z(t)] - \lambda_0 \int_0^{t_{\rm tar}} {\rm d}t \frac{\mathcal{E}_z^2(t)}{\sin^2(\pi t/t_{\rm tar})} - 2{\rm Re}\left[\int_0^{t_{\rm tar}} {\rm d}t \langle\Theta(t)| \frac{\partial}{\partial t} + i\left(\hat{H}_{\rm mol} - \hat{\mu}_z \mathcal{E}_z(t)\right)|\Psi(t)\rangle\right]. \quad (2.236)$$

The second and third term on the right hand side of this functional are constraints introduced to minimize the intensity of the optimized laser field $\mathcal{E}_z(t)$ and to ensure that the wave function $\Psi(\mathbf{q},\mathbf{Q},t)$ evolves according to the TDSE, respectively. The second term contains a time-dependent shape function, $\sin^2(\pi t/t_{\rm tar})$, which guarantees smooth pulse envelopes [229]. In order to keep the OCT functional, eqn. (2.236), dimensionless, the associated parameter λ_0 must have dimensions $\left[\frac{e^2 a_0^2}{E_h \hbar}\right]$, where m_e and e are the mass and minus the charge of an electron, respectively, a_0 is the Bohr radius and $E_h = \frac{\hbar^2}{m_e a_0^2}$ is the atomic unit of energy, the Hartree; see e.g. Refs. [136,150] for details on atomic units. This parameter λ_0, which is also referred to as *penalty factor*, needs to be optimized for the specific problem at hand to yield reasonable ratios between the control yield, eqn. (2.235), and the laser intensity. Note that according to the third term with the Lagrange multiplier $\Theta(\mathbf{q},\mathbf{Q},t)$, the interaction with the external laser field $\mathcal{E}_z(t)$ to be optimized is described in length gauge, c.f. eqn. (2.229).

Requiring $\delta J[t_{\rm tar};\mathcal{E}_z(t)] = 0$ yields the following equations for the wave function $\Psi(\mathbf{q},\mathbf{Q},t)$, the Lagrange multiplier $\Theta(\mathbf{q},\mathbf{Q},t)$, and the optimized laser field $\mathcal{E}_z(t)$, respectively [97]:

$$i\frac{\partial}{\partial t}\Psi(\mathbf{q},\mathbf{Q},t) = \left(\hat{H}_{\rm mol}(\mathbf{r},\mathbf{R}) - \hat{\mu}_z(\mathbf{r},\mathbf{R})\mathcal{E}_z(t)\right)\Psi(\mathbf{q},\mathbf{Q},t), \quad \Psi(t=0) = \Psi_{\rm init}, \quad (2.237)$$

$$i\frac{\partial}{\partial t}\Theta(\mathbf{q},\mathbf{Q},t) = \left(\hat{H}_{\rm mol}(\mathbf{r},\mathbf{R}) - \hat{\mu}_z(\mathbf{r},\mathbf{R})\mathcal{E}_z(t)\right)\Theta(\mathbf{q},\mathbf{Q},t), \quad \Theta(t_{\rm tar}) = \hat{O}\Psi(t_{\rm tar}) \quad (2.238)$$

and

$$\mathcal{E}_z(t) = -\frac{\sin^2(\pi t/t_{\rm tar})}{\lambda_0}{\rm Im}\langle\Theta(t)|\hat{\mu}_z|\Psi(t)\rangle. \quad (2.239)$$

Hence, $\Theta(\mathbf{q},\mathbf{Q},t)$ is calculated similarly to $\Psi(\mathbf{q},\mathbf{Q},t)$ but progagated backward in time starting at $t = t_{\rm tar}$ and ending at $t = 0$. The corresponding initial condition is given in eqn. (2.238), and couples eqns. (2.238) and (2.237). Obviously, in order to solve these equations, iterative methods need to be used, c.f. Appendix 6.2. Straightforward iterative methods, i.e. solving the coupled equations by guessing an initial field to obtain $\Psi(\mathbf{q},\mathbf{Q},t)$ and then $\Theta(\mathbf{q},\mathbf{Q},t)$ according to eqns. (2.237) and (2.238), respectively, and using these wave functions to calculate a new field according to eqn. (2.239) for the next iteration, usually do not converge [96,97].

In Ref. [96], the following iteration scheme was established, which was shown to have quadratic monotonic convergence behavior for positive definite target operators $\hat{O}$: In this scheme, the electric field in eqns. (2.237) and (2.238) is replaced by the right hand side of eqn. (2.239), resulting in coupled non-linear TDSEs for forward and backward propagations. In the

iterative scheme to solve these equations, at first (step (0)) an initial field $\bar{\mathcal{E}}_z(t)$ is guessed to compute the zeroth order wave function $\Psi^{(0)}(\mathbf{q},\mathbf{Q},t)$ according to

$$i\frac{\partial}{\partial t}\Psi^{(0)}(\mathbf{q},\mathbf{Q},t) = \left(\hat{H}_{\rm mol}(\mathbf{r},\mathbf{R}) - \hat{\mu}_z(\mathbf{r},\mathbf{R})\bar{\mathcal{E}}_z(t)\right)\Psi^{(0)}(\mathbf{q},\mathbf{Q},t). \tag{2.240}$$

Step (1) starts with the first backward propagation to obtain $\Theta^{(1)}(\mathbf{q},\mathbf{Q},t)$, followed by the first forward propagation to obtain $\Psi^{(1)}(\mathbf{q},\mathbf{Q},t)$ and ends with the calculation of an improved electric field $\mathcal{E}^{(1)}(t)$ according to

$$\text{Step (1)} \begin{cases} i\frac{\partial}{\partial t}\Theta^{(1)}(\mathbf{q},\mathbf{Q},t) = \left(\hat{H}_{\rm mol}(\mathbf{r},\mathbf{R}) + \frac{\hat{\mu}_z(\mathbf{r},\mathbf{R})\sin^2(\pi t/t_{\rm tar})}{\lambda_0}{\rm Im}\langle\Theta^{(1)}(t)|\hat{\mu}_z|\Psi^{(0)}(t)\rangle\right)\Theta^{(1)}(\mathbf{q},\mathbf{Q},t), \\ i\frac{\partial}{\partial t}\Psi^{(1)}(\mathbf{q},\mathbf{Q},t) = \left(\hat{H}_{\rm mol}(\mathbf{r},\mathbf{R}) + \frac{\hat{\mu}_z(\mathbf{r},\mathbf{R})\sin^2(\pi t/t_{\rm tar})}{\lambda_0}{\rm Im}\langle\Theta^{(1)}(t)|\hat{\mu}_z|\Psi^{(1)}(t)\rangle\right)\Psi^{(1)}(\mathbf{q},\mathbf{Q},t), \\ \mathcal{E}^{(1)}(t) = -\frac{\sin^2(\pi t/t_{\rm tar})}{\lambda_0}{\rm Im}\langle\Theta^{(1)}(t)|\hat{\mu}_z|\Psi^{(1)}(t)\rangle. \end{cases} \tag{2.241}$$

Here, the initial condition for the backward propagation is given as $\Theta^{(1)}(t_{\rm tar}) = \hat{O}\Psi^{(0)}(t_{\rm tar})$. Hence, the n-th backward iteration uses the result of the $(n-1)$-th forward propagation and the n-th forward iteration the result of the n-th backward iteration and these steps are repeated until convergence is achieved. The reader is referred to Refs. [98,99,227] for further technical aspects concerning the implementation of this iteration scheme in the MCTDH-program package.

Finally, notice that in Ref. [T2], the expectation value to be optimized, eqn. (2.235), is given by $O[t_{\rm tar};\mathcal{E}_z(t)] = |\langle\chi_{\rm g}(\xi,t_{\rm tar})|\chi_{\rm target}(\xi)\rangle|^2$, where ξ denotes the one-dimensional reaction coordinate, see also section 2.4, and $\chi_{\rm g}(t_{\rm tar})$ denotes the laser driven nuclear wave packet in the electronic ground state (g) at time $t = t_{\rm tar}$, c.f. eqn. (2.231). The target state is given by $\chi_{\rm target}(\xi) = \chi_{g,\nu=0}(\xi - \Delta\tilde{\xi}) \times e^{ik\xi}$, where $\chi_{g,\nu=0}(\xi - \Delta\tilde{\xi})$ denotes a nuclear wave function in the electronic ground state obtained by replacing the initial state, $\chi_{g,\nu=0}(\xi, t=0)$, by $\Delta\tilde{\xi}$ along the reaction coordinate ξ. Additionally, the term $e^{ik\xi}$ describes nuclear motion along ξ with momentum k. See also Figure 4.2(b) in Chapter 4 for a depiction of $\chi_{g,\nu=0}(\xi - \Delta\tilde{\xi})$, marked by "**a**", and a depiction of $\xi_{\rm target}(\xi)$, marked by "**target**" and shown as dashed line.

2.4 Design of models in reduced dimensionality

A major challenge in the quantum mechanical description of the nuclear motion is the number of nuclear degrees of freedom (dof) that are taken into account explicitly. The straightforward quantum dynamical methods described in section 2.3 allow the treatment of 4-6 dof but studies of systems with more than 6 dof, e.g. semibullvalene with its 42 internal dof, are not feasible using these approaches. One way of treating such large systems, which was chosen in this thesis, is to reduce the dimensionality of the problem by constructing collective coordinates which are linear combinations of the $3M$ Cartesian coordinates, where M is the number of atoms. These collective coordinates are then separated into "active" modes which undergo large amplitude motions and "passive" or so-called "spectator" modes with small amplitudes. In the simulation, only the former active modes are treated, whereas the "spectator" modes remain frozen. Alternative approaches for solving the time-dependent nuclear Schrödinger equation is for example the Multi Configuration Time Dependent Hartree (MCTDH) method [230], a numerically efficient propagation method for nuclear wave packets. The straightforward

application of this MCTDH scheme allows the correlated treatment of up to 14 dof, see e.g. Refs. [231,232]. For the treatment of still larger systems, the multilayer MCTDH scheme [233] has been introduced. This scheme was applied to the quantum dynamical treatment of 100-1000 correlated dof employing model Hamilton operators, see e.g. Refs. [233–235] and Refs. [235–239] for further extensions including applications to realistic molecular systems. Another alternative albeit intrinsically approximate approach is ab-initio molecular dynamics [240], in which the nuclear motion is treated classically.

When constructing models in reduced dimensionality, the emergence of nondiagonal kinetic energy operators as a result of the transformation from Cartesian coordinates to a new set of collective coordinates complicates the numerical simulation of the nuclear quantum dynamics. In section 2.4.1 at first an introductory example of such nondiagonal kinetic energy operators is given and then it is shown how these nondiagonal terms can be eliminated by special construction of the collective coordinates involving Jacobi coordinates [209,241], which are also referred to as Mobile coordinates [242, 243]. In section 2.4.2, the afore developed ideas are applied to the degenerate Cope rearrangement (DCR) of semibullvalene (SBV), and a set of Jacobi/Mobile coordinates is derived which guarantees the diagonal form of the kinetic energy operator, c.f. Refs. [242,243]. Analysis of the DCR of SBV in terms of these Jacobi/Mobile coordinates, describing relative separations between the atoms, allows the identification of three large amplitude vibrations, while the remaining dof show considerably smaller contributions. This analysis provides a connection to previous studies on the DCR of SBV in reduced dimensionality [72], which motivated the present analysis. Additionally, the set of Jacobi/Mobile coordinates is transformed into a new set of coordinates, preserving the diagonal form of the kinetic energy operator, employing a sequence of unitary transformations (section 2.4.2.1), thereby going beyond the original definition of Jacobi/Mobile coordinates, c.f. Ref. [244]. This strategy leads to the one-dimensional reaction coordinate ξ used in Refs. [T1-T4]. This one-dimensional reaction coordinate describes the DCR of SBV from the reactant to the product reasonably well as shown by comparison to ab-initio molecular dynamics calculations [240] in full dimensionality in Ref. [T4].

It is worth noting that, although providing a useful physical picture of the underlying reaction, the transformation to Jacobi/Mobile coordinates is not necessary for the derivation of the employed reaction coordinate ξ, which can also be constructed in terms of the original Cartesian coordinates, section 2.4.2.1. Finally, in section 2.4.2.2, the one-dimensional model is extended in analogy to the *Cartesian reaction plane Hamiltonian* [245,246], see also Refs. [244,247,248]. The corresponding results of the two-dimensional potential energy surface are presented in Chapter 5.

2.4.1 The problem of nondiagonal kinetic energy

In the following the nuclear kinetic energy operator of a triatomic collinear molecule ABC is derived for two different sets of coordinates according to Ref. [241], see also Ref. [209]. At first bond coordinates (Figure 2.5(a)) are considered which leads to nondiagonal terms in $\hat{T}_{\mathrm{nuc}}(\mathbf{R})$. Thereafter the kinetic energy operator is derived in Jacobi coordinates, also referred to as Mobile coordinates [242, 243] (Figure 2.5(b)), which leads to a diagonal kinetic energy operator. These well-known examples serve as motivation for the usage of Jacobi/Mobile coordinates for the quantum dynamical description of the degenerate Cope rearrangement of semibullvalene,

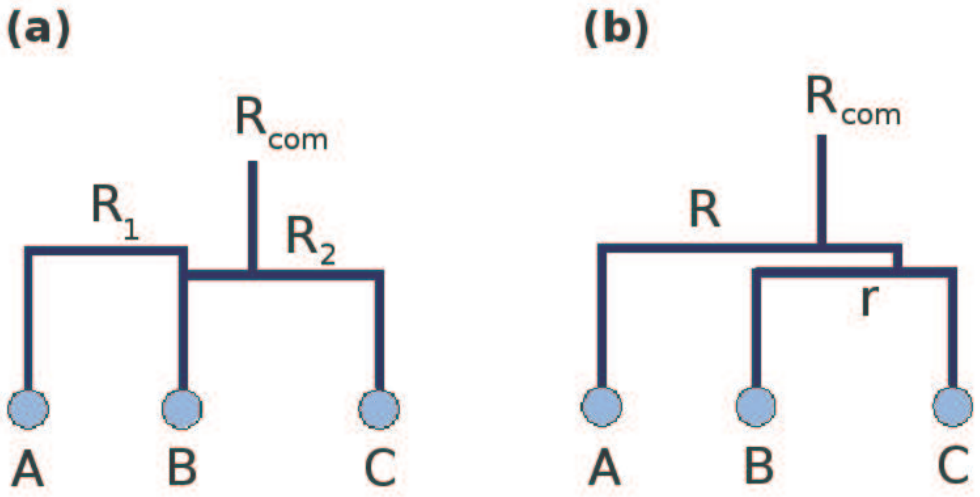

Figure 2.5: Definition of Bond coordinates (a) and Jacobi/Mobile coordinates (b).

section 2.4.2.

2.4.1.1 Bond coordinates

The starting point are the Cartesian coordinates at the atomic centers, x_A, x_B, x_C, aligned along the $\underline{x}$-axis, which are expressed in bond coordinates $R_1 = x_\mathrm{B} - x_\mathrm{A}$, $R_2 = x_\mathrm{C} - x_\mathrm{B}$ and $R_\mathrm{com} = (m_\mathrm{A}x_\mathrm{A} + m_\mathrm{B}x_\mathrm{B} + m_\mathrm{C}x_\mathrm{C})/m_\mathrm{ABC}$, where R_com is the center of mass coordinate and $m_\mathrm{ABC} = m_\mathrm{A} + m_\mathrm{B} + m_\mathrm{C}$ the total mass with m_A, m_B, m_C being the masses of atoms A, B and C. This coordinate transformation can be written in matrix notation as

$$\underbrace{\begin{pmatrix} R_1 \\ R_2 \\ R_\mathrm{com} \end{pmatrix}}_{\mathbf{R}} = \underbrace{\begin{pmatrix} -1 & 1 & 0 \\ 0 & -1 & 1 \\ \frac{m_\mathrm{A}}{m_\mathrm{ABC}} & \frac{m_\mathrm{B}}{m_\mathrm{ABC}} & \frac{m_\mathrm{C}}{m_\mathrm{ABC}} \end{pmatrix}}_{\boldsymbol{B}} \underbrace{\begin{pmatrix} x_\mathrm{A} \\ x_\mathrm{B} \\ x_\mathrm{C} \end{pmatrix}}_{\mathbf{x}}. \tag{2.242}$$

The "old" Cartesian momenta $\mathbf{p}$ are obtained from the new momenta $\mathbf{P}$ and the transformation matrix $\boldsymbol{B}$ via canonical transformation by

$$\mathbf{p}^T = \mathbf{P}^T\boldsymbol{B} \qquad \text{or} \qquad \mathbf{p} = \boldsymbol{B}^T\mathbf{P}. \tag{2.243}$$

The classical kinetic energy can now be written as

$$\begin{aligned} T_\mathrm{nuc}^\mathrm{cl} &= \frac{p_\mathrm{A}^2}{2m_\mathrm{A}} + \frac{p_\mathrm{B}^2}{2m_\mathrm{B}} + \frac{p_\mathrm{C}^2}{2m_\mathrm{C}} \\ &= \frac{1}{2}\mathbf{p}^T\boldsymbol{g}\mathbf{p} \\ &= \frac{1}{2}\mathbf{P}^T\boldsymbol{B}\boldsymbol{g}\boldsymbol{B}^T\mathbf{P} \\ &= \frac{1}{2}\mathbf{P}^T\boldsymbol{G}\mathbf{P}, \end{aligned} \tag{2.244}$$

where

$$\boldsymbol{g} = \begin{pmatrix} \frac{1}{m_\mathrm{A}} & 0 & 0 \\ 0 & \frac{1}{m_\mathrm{B}} & 0 \\ 0 & 0 & \frac{1}{m_\mathrm{C}} \end{pmatrix} \tag{2.245}$$

is the diagonal matrix with the inverse masses of the Cartesian coordinates $\mathbf{x}$ on its diagonal and

$$\boldsymbol{G} = \boldsymbol{B}\boldsymbol{g}\boldsymbol{B}^T = \begin{pmatrix} \frac{1}{m_\mathrm{A}} + \frac{1}{m_\mathrm{B}} & -\frac{1}{m_\mathrm{B}} & 0 \\ -\frac{1}{m_\mathrm{B}} & \frac{1}{m_\mathrm{B}} + \frac{1}{m_\mathrm{C}} & 0 \\ 0 & 0 & \frac{1}{m_\mathrm{ABC}} \end{pmatrix}. \tag{2.246}$$

Replacing the classical variable P_i in the classical expression for the kinetic energy operator by the operator $-i\frac{\partial}{\partial R_i}$ gives

$$\hat{T}_\mathrm{nuc}(\mathbf{R}) = -\frac{1}{2\mu_1}\frac{\partial^2}{\partial R_1^2} - \frac{1}{2\mu_2}\frac{\partial^2}{\partial R_2^2} - \frac{1}{2\mu_4}\frac{\partial^2}{\partial R_\mathrm{com}^2} + \frac{1}{2\mu_3}\frac{\partial^2}{\partial R_1 \partial R_2}, \tag{2.247}$$

where

$$\begin{aligned} \mu_1 &= (m_\mathrm{A}^{-1} + m_\mathrm{B}^{-1})^{-1}, & \mu_2 &= (m_\mathrm{B}^{-1} + m_\mathrm{C}^{-1})^{-1} \\ \mu_3 &= m_B, & \mu_4 &= m_\mathrm{ABC}, \end{aligned} \tag{2.248}$$

c.f. Refs. [249–251].

Hence, a nondiagonal matrix $\boldsymbol{G}$ leads to nondiagonal terms in the kinetic energy operator. Furthermore, diagonal elements of the $\boldsymbol{G}$-matrix correspond to the masses of the new coordinates and off-diagonal elements correspond to masses of the coupled degrees of freedom.

2.4.1.2 Jacobi/Mobile Coordinates

Using Jacobi/Mobile coordinates (Figure 2.5(b)), the new coordinate R is defined as the distance from atom A to the center of mass of atoms B and C, r is the distance between B and C and the center of mass coordinate is again R_com. For this coordinate transformation the transformation matrix takes on the form

$$\boldsymbol{B} = \begin{pmatrix} -1 & \frac{m_\mathrm{B}}{m_\mathrm{BC}} & \frac{m_\mathrm{C}}{m_\mathrm{BC}} \\ 0 & -1 & 1 \\ \frac{m_\mathrm{A}}{m_\mathrm{ABC}} & \frac{m_\mathrm{B}}{m_\mathrm{ABC}} & \frac{m_\mathrm{C}}{m_\mathrm{ABC}} \end{pmatrix} \tag{2.249}$$

with $m_\mathrm{BC} = m_\mathrm{B} + m_\mathrm{C}$. For the $\boldsymbol{G}$-matrix we get

$$\boldsymbol{G} = \begin{pmatrix} \frac{m_\mathrm{ABC}}{m_\mathrm{A} m_\mathrm{BC}} & 0 & 0 \\ 0 & \frac{m_\mathrm{BC}}{m_\mathrm{B} m_\mathrm{C}} & 0 \\ 0 & 0 & \frac{1}{m_\mathrm{ABC}} \end{pmatrix}. \tag{2.250}$$

Hence, the kinetic energy operator in Jacobi/Mobile coordinates is diagonal and we get

$$\hat{T}_\mathrm{nuc}(\mathbf{R}) = -\frac{1}{2\mu_1}\frac{\partial^2}{\partial R^2} - \frac{1}{2\mu_2}\frac{\partial^2}{\partial r^2} - \frac{1}{2\mu_3}\frac{\partial^2}{\partial R_\mathrm{com}^2}, \tag{2.251}$$

where

$$\mu_1 = \frac{m_\mathrm{A} m_\mathrm{BC}}{m_\mathrm{ABC}}, \qquad \mu_2 = m_\mathrm{B} m_\mathrm{C}/m_\mathrm{BC}, \qquad \mu_3 = m_\mathrm{ABC}. \tag{2.252}$$

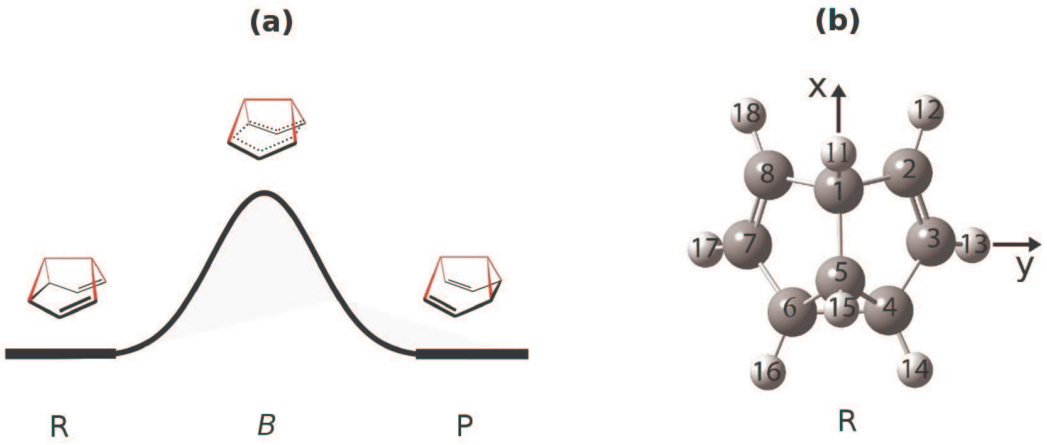

Figure 2.6: (a) Degenerate Cope rearrangement of semibullvalene (side view) from the reactant (R) over the potential barrier (B) to the product (P). (b) Top view of the reactant with numbering of atoms and orientation in space.

2.4.2 Kinetic energy operator for semibullvalene

After having shown how a diagonal kinetic energy operator is obtained using Jacobi/Mobile coordinates for a collinear triatomic molecule, in this section an analog procedure is applied in order to describe the degenerate Cope rearrangement of semibullvalene (Figure 2.6(a)). One starts by considering the eight CH bonds and takes the difference between the position vectors of carbon- and hydrogen-atoms for the eight pairs:

$$\mathbf{Q}_i = \mathbf{C}_i - \mathbf{H}_{1i}, \qquad i = 1 - 8 \tag{2.253}$$

with $\mathbf{C}_i$ and $\mathbf{H}_{1i}$ being the position vectors of carbon C_i and hydrogen H_{1i}, respectively (Figure 2.6(b)), and $\mathbf{Q}_i$ being the i-th new coordinate with x- , y- and z-components X_i, Y_i and Z_i. This is illustrated in the bottom line of Figure 2.7, where the numbers over the connecting lines refer to the index i. Next we calculate the position vector of the center of mass of the eight CH bonds and construct coordinates $\mathbf{Q}_9$ to $\mathbf{Q}_{13}$ by calculating the difference between these center of mass vectors as indicated in Figure 2.7. For example the coordinate $\mathbf{Q}_9$ is constructed by

$$\mathbf{Q}_9 = \frac{m_\mathrm{C}\mathbf{C}_2 + m_\mathrm{H}\mathbf{H}_{12}}{m_\mathrm{C} + m_\mathrm{H}} - \frac{m_\mathrm{C}\mathbf{C}_8 + m_\mathrm{H}\mathbf{H}_{18}}{m_\mathrm{C} + m_\mathrm{H}} \tag{2.254}$$

with m_C and m_H being the mass of a carbon- and a hydrogen-atom, respectively. We successively apply this strategy according to Figure 2.7 until we reach the top of the associated "Mobile tree" with coordinate $\mathbf{Q}_{16}$ corresponding to the center of mass coordinate. Hence, the additional designation of these coordinates $\mathbf{Q}_j$ with j=1-16 as Mobile coordinates is due to their mode of construction, giving rise to the "Mobile tree" shown in Figure 2.7. Note that the strategy for the construction of this "Mobile tree" was to connect the center of masses of fragments $\mathrm{C_2H_{12}}$ and $\mathrm{C_8H_{18}}$ as well as of fragments $\mathrm{C_4H_{14}}$ and $\mathrm{C_6H_{16}}$ because those are the atoms which are supposed to perform the largest amplitude motions according to Figure 2.6, see also Ref. [72].

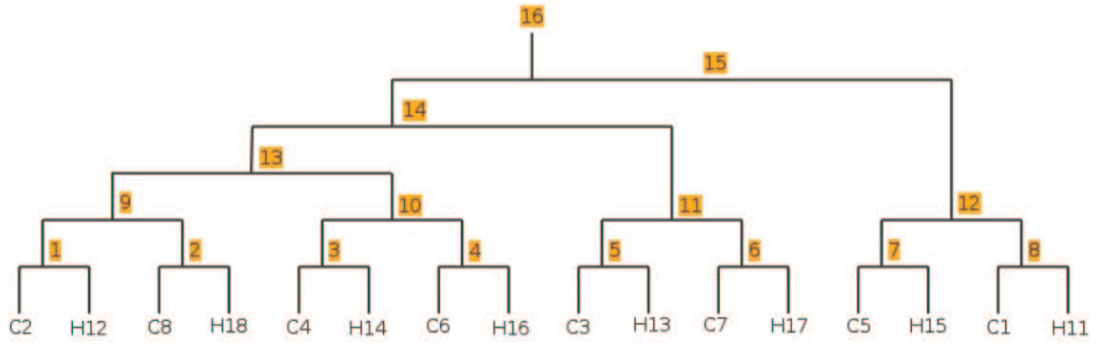

Figure 2.7: Jabobi/Mobile coordinates $\mathbf{Q}_j$=(X_j, Y_j, Z_j) labeled by numbers j=1-16, for SBV with carbon atoms C_i, i=1-8, and hydrogen atoms H_{1i} as defined in Figure 2.6.

The new Jabobi/Mobile coordinates are obtained from the old Cartesian coordinates by

$$\mathbf{Q} = \boldsymbol{B}\mathbf{x}, \tag{2.255}$$

where $\mathbf{Q}$ denotes the vector of the Jabobi/Mobile coordinates, $\boldsymbol{B}$ is the transformation matrix and $\mathbf{x}$ denotes the vector of the Cartesian coordinates. See equation (2.256) for the detailed form of $\mathbf{Q}$, $\boldsymbol{B}$ and $\mathbf{x}$:

$$
\underbrace{\begin{pmatrix} \mathbf{Q}_1 \\ \mathbf{Q}_2 \\ \mathbf{Q}_3 \\ \mathbf{Q}_4 \\ \mathbf{Q}_5 \\ \mathbf{Q}_6 \\ \mathbf{Q}_7 \\ \mathbf{Q}_8 \\ \mathbf{Q}_9 \\ \mathbf{Q}_{10} \\ \mathbf{Q}_{11} \\ \mathbf{Q}_{12} \\ \mathbf{Q}_{13} \\ \mathbf{Q}_{14} \\ \mathbf{Q}_{15} \\ \mathbf{Q}_{\mathrm{com}} \end{pmatrix}}_{\mathbf{Q}} = \underbrace{\begin{pmatrix}
-1 & 1 & 0 & 0 & 0 & 0 & 0 & 0 & 0 & 0 & 0 & 0 & 0 & 0 & 0 & 0 \\
0 & 0 & -1 & 1 & 0 & 0 & 0 & 0 & 0 & 0 & 0 & 0 & 0 & 0 & 0 & 0 \\
0 & 0 & 0 & 0 & -1 & 1 & 0 & 0 & 0 & 0 & 0 & 0 & 0 & 0 & 0 & 0 \\
0 & 0 & 0 & 0 & 0 & 0 & -1 & 1 & 0 & 0 & 0 & 0 & 0 & 0 & 0 & 0 \\
0 & 0 & 0 & 0 & 0 & 0 & 0 & 0 & -1 & 1 & 0 & 0 & 0 & 0 & 0 & 0 \\
0 & 0 & 0 & 0 & 0 & 0 & 0 & 0 & 0 & 0 & -1 & 1 & 0 & 0 & 0 & 0 \\
0 & 0 & 0 & 0 & 0 & 0 & 0 & 0 & 0 & 0 & 0 & 0 & -1 & 1 & 0 & 0 \\
0 & 0 & 0 & 0 & 0 & 0 & 0 & 0 & 0 & 0 & 0 & 0 & 0 & 0 & -1 & 1 \\
a & b & -a & -b & 0 & 0 & 0 & 0 & 0 & 0 & 0 & 0 & 0 & 0 & 0 & 0 \\
0 & 0 & 0 & 0 & a & b & -a & -b & 0 & 0 & 0 & 0 & 0 & 0 & 0 & 0 \\
0 & 0 & 0 & 0 & 0 & 0 & 0 & 0 & a & b & -a & -b & 0 & 0 & 0 & 0 \\
0 & 0 & 0 & 0 & 0 & 0 & 0 & 0 & 0 & 0 & 0 & 0 & a & b & -a & -b \\
\frac{a}{2} & \frac{b}{2} & \frac{a}{2} & \frac{b}{2} & -\frac{a}{2} & -\frac{b}{2} & -\frac{a}{2} & -\frac{b}{2} & 0 & 0 & 0 & 0 & 0 & 0 & 0 & 0 \\
-\frac{a}{4} & -\frac{b}{4} & -\frac{a}{4} & -\frac{b}{4} & -\frac{a}{4} & -\frac{b}{4} & -\frac{a}{4} & -\frac{b}{4} & \frac{a}{2} & \frac{b}{2} & \frac{a}{2} & \frac{b}{2} & 0 & 0 & 0 & 0 \\
-\frac{a}{6} & -\frac{b}{6} & -\frac{a}{6} & -\frac{b}{6} & -\frac{a}{6} & -\frac{b}{6} & -\frac{a}{6} & -\frac{b}{6} & -\frac{a}{6} & -\frac{b}{6} & -\frac{a}{6} & -\frac{b}{6} & \frac{a}{2} & \frac{b}{2} & \frac{a}{2} & \frac{b}{2} \\
\frac{a}{8} & \frac{b}{8} & \frac{a}{8} & \frac{b}{8} & \frac{a}{8} & \frac{b}{8} & \frac{a}{8} & \frac{b}{8} & \frac{a}{8} & \frac{b}{8} & \frac{a}{8} & \frac{b}{8} & \frac{a}{8} & \frac{b}{8} & \frac{a}{8} & \frac{b}{8}
\end{pmatrix}}_{\boldsymbol{B}} \underbrace{\begin{pmatrix} \mathbf{C}_2 \\ \mathbf{H}_{12} \\ \mathbf{C}_8 \\ \mathbf{H}_{18} \\ \mathbf{C}_4 \\ \mathbf{H}_{14} \\ \mathbf{C}_6 \\ \mathbf{H}_{16} \\ \mathbf{C}_3 \\ \mathbf{H}_{13} \\ \mathbf{C}_7 \\ \mathbf{H}_{17} \\ \mathbf{C}_5 \\ \mathbf{H}_{15} \\ \mathbf{C}_1 \\ \mathbf{H}_{11} \end{pmatrix}}_{\mathbf{x}} \tag{2.256}
$$

with

$$
a = \frac{m_{\mathrm{C}}}{m_{\mathrm{C}} + m_{\mathrm{H}}} \qquad \text{and} \qquad b = \frac{m_{\mathrm{H}}}{m_{\mathrm{C}} + m_{\mathrm{H}}}. \tag{2.257}
$$

Here, it is important to note that such constructions of new collective coordinates yield the desired diagonal form of the kinetic energy operator. For a proof see Refs. [242, 243].

For SBV, the $\boldsymbol{G}$-matrix (section 2.4.1.1) takes on the form:

$$\boldsymbol{G} = \begin{pmatrix} \mu_1 & 0 & 0 & 0 & 0 & 0 & 0 & 0 & 0 & 0 & 0 & 0 & 0 & 0 & 0 & 0 \\ 0 & \mu_2 & 0 & 0 & 0 & 0 & 0 & 0 & 0 & 0 & 0 & 0 & 0 & 0 & 0 & 0 \\ 0 & 0 & \mu_3 & 0 & 0 & 0 & 0 & 0 & 0 & 0 & 0 & 0 & 0 & 0 & 0 & 0 \\ 0 & 0 & 0 & \mu_4 & 0 & 0 & 0 & 0 & 0 & 0 & 0 & 0 & 0 & 0 & 0 & 0 \\ 0 & 0 & 0 & 0 & \mu_5 & 0 & 0 & 0 & 0 & 0 & 0 & 0 & 0 & 0 & 0 & 0 \\ 0 & 0 & 0 & 0 & 0 & \mu_6 & 0 & 0 & 0 & 0 & 0 & 0 & 0 & 0 & 0 & 0 \\ 0 & 0 & 0 & 0 & 0 & 0 & \mu_7 & 0 & 0 & 0 & 0 & 0 & 0 & 0 & 0 & 0 \\ 0 & 0 & 0 & 0 & 0 & 0 & 0 & \mu_8 & 0 & 0 & 0 & 0 & 0 & 0 & 0 & 0 \\ 0 & 0 & 0 & 0 & 0 & 0 & 0 & 0 & \mu_9 & 0 & 0 & 0 & 0 & 0 & 0 & 0 \\ 0 & 0 & 0 & 0 & 0 & 0 & 0 & 0 & 0 & \mu_{10} & 0 & 0 & 0 & 0 & 0 & 0 \\ 0 & 0 & 0 & 0 & 0 & 0 & 0 & 0 & 0 & 0 & \mu_{11} & 0 & 0 & 0 & 0 & 0 \\ 0 & 0 & 0 & 0 & 0 & 0 & 0 & 0 & 0 & 0 & 0 & \mu_{12} & 0 & 0 & 0 & 0 \\ 0 & 0 & 0 & 0 & 0 & 0 & 0 & 0 & 0 & 0 & 0 & 0 & \mu_{13} & 0 & 0 & 0 \\ 0 & 0 & 0 & 0 & 0 & 0 & 0 & 0 & 0 & 0 & 0 & 0 & 0 & \mu_{14} & 0 & 0 \\ 0 & 0 & 0 & 0 & 0 & 0 & 0 & 0 & 0 & 0 & 0 & 0 & 0 & 0 & \mu_{15} & 0 \\ 0 & 0 & 0 & 0 & 0 & 0 & 0 & 0 & 0 & 0 & 0 & 0 & 0 & 0 & 0 & \mu_{\mathrm{com}} \end{pmatrix} \tag{2.258}$$

with

$$\mu_1 = \mu_2 = \mu_3 = \mu_4 = \mu_5 = \mu_6 = \mu_7 = \mu_8 = \frac{m_{\mathrm{C}} m_{\mathrm{H}}}{m_{\mathrm{C}} + m_{\mathrm{H}}}$$

$$\mu_9 = \mu_{10} = \mu_{11} = \mu_{12} = \frac{1}{2}(m_{\mathrm{C}} + m_{\mathrm{H}})$$

$$\mu_{13} = m_{\mathrm{C}} + m_{\mathrm{H}} \quad \mu_{14} = \frac{4}{3}(m_{\mathrm{C}} + m_{\mathrm{H}}) \quad \mu_{15} = \frac{3}{2}(m_{\mathrm{C}} + m_{\mathrm{H}}) \quad \mu_{\mathrm{com}} = 8(m_{\mathrm{C}} + m_{\mathrm{H}}).$$

Hence, the kinetic energy operator is diagonal in the new coordinates $\mathbf{Q}$ and the reduced masses for the corresponding fragments are given on the diagonal of the $\boldsymbol{G}$-matrix. Table 2.2 shows the displacement of the x-, y- and z-components of the Jabobi/Mobile coordinates during the Cope rearrangement of semibullvalene when going from the reactant to the product. The structures of the reactant and product are obtained by B3LYP/cc-pVTZ calculations (see section 2.2.2 for details). Note that the origin of the coordinate system is chosen as the respective center of mass such that $\mathbf{Q}_{\mathrm{com}} = 0$ (Table 2.2) and that the carbon bridge C_1/C_5 is fixed perpendicular to the x-axis, c.f. Figure 2.6(b). There are only three large amplitude displacements (highlighted in blue).

2.4.2.1 One-dimensional reaction coordinate ξ

In order to reduce further the dimensionality of the problem, we first combine coordinates $\bar{Q}_9$ and $\bar{Q}_{10}$ (step (i)) and then combine one of the thus obtained dof with all remaining Jabobi/Mobile coordinates (step (ii)).

(i) The new coordinates $\tilde{\mathbf{Q}}_9$ and $\tilde{\mathbf{Q}}_{10}$ are formed by

$$\tilde{\mathbf{Q}}_9 = \mathbf{Q}_9 - \mathbf{Q}_{10} \qquad \text{and} \qquad \tilde{\mathbf{Q}}_{10} = \frac{1}{2}(\mathbf{Q}_9 + \mathbf{Q}_{10}). \tag{2.259}$$

The corresponding reduced masses for the new coordinates $\tilde{\mathbf{Q}}_9$ and $\tilde{\mathbf{Q}}_{10}$ are

$$\tilde{\mu}_9 = \frac{\mu_9 \mu_{10}}{\mu_9 + \mu_{10}} = \frac{1}{4}(m_{\mathrm{C}} + m_{\mathrm{H}}) \qquad \text{and} \qquad \tilde{\mu}_{10} = m_{\mathrm{C}} + m_{\mathrm{H}}. \tag{2.260}$$

Table 2.2: Displacement of Jabobi/Mobile coordinates during the Cope rearrangement of semibullvalene in Å from the reactant to the product. Structures refer to B3LYP/cc-pVTZ calculations.

	Jabobi/Mobile coordinate	ΔX	ΔY	ΔZ
$\mathbf{Q}_1$:	C_2H_{12}	0.0285	-0.0901	0.0478
$\mathbf{Q}_2$:	C_8H_{18}	0.0285	0.0901	0.0478
$\mathbf{Q}_3$:	C_4H_{14}	0.0285	0.0901	-0.0478
$\mathbf{Q}_4$:	C_6H_{16}	0.0285	-0.0901	-0.0478
$\mathbf{Q}_5$:	C_3H_{13}	0.0183	0.0000	0.0000
$\mathbf{Q}_6$:	C_7H_{17}	0.0183	0.0000	0.0000
$\mathbf{Q}_7$:	C_5H_{15}	-0.0958	0.0000	0.0615
$\mathbf{Q}_8$:	C_1H_{11}	-0.0958	0.0000	-0.0615
$\mathbf{Q}_9$:	C_2H_{12}, C_8H_{18}	0.0000	0.7338	0.0000
$\mathbf{Q}_{10}$:	C_4H_{14}, C_6H_{16}	0.0000	-0.7338	0.0000
$\mathbf{Q}_{11}$:	C_3H_{13}, C_7H_{17}	0.0000	0.0000	0.0000
$\mathbf{Q}_{12}$:	C_1H_{11}, C_5H_{15}	0.0000	0.0000	0.0095
$\mathbf{Q}_{13}$:	$C_2H_{12}C_8H_{18}, C_4H_{14}C_6H_{16}$	0.0000	0.0000	-0.5926
$\mathbf{Q}_{14}$:	$C_3H_{13}C_7H_{17}, C_6H_{16}C_4H_{14}C_8H_{18}C_2H_{12}$	0.1256	0.0000	0.0000
$\mathbf{Q}_{15}$:	$C_1H_{11}C_5H_{15}, C_2H_{12}C_8H_{18}C_4H_{14}C_6H_{16}C_3H_{13}C_7H_{17}$	-0.0265	0.0000	0.0000
$\mathbf{Q}_{\mathrm{com}}$:		0.0000	0.0000	0.0000

This transformation is achieved by

$$\mathbf{Q}' = \boldsymbol{U}\boldsymbol{B}\mathbf{x} = \boldsymbol{U}\mathbf{Q}, \tag{2.261}$$

where $\boldsymbol{U}$ is a unitary matrix which differs from the unity matrix only in the elements

$$U_{9,10} = -1 \qquad U_{10,9} = \frac{1}{2} \qquad U_{10,10} = \frac{1}{2}. \tag{2.262}$$

The displacement from the reactant to the product of the coordinate $\tilde{Q}_{9y}$ is 1.468 Å and the displacements of the remaining components of $\tilde{\mathbf{Q}}_9$ and $\tilde{\mathbf{Q}}_{10}$ are zero! Note that $\tilde{Q}_{9\mathrm{y}}$ with associated mass $\tilde{\mu}_9 = (m_C + m_{\mathrm{H}})/4$ was used as one-dimensional reaction coordinate in previous studies on the degenerate Cope rearrangement of semibullvalene [72]. Now, the kinetic energy operator has the following diagonal form

$$\hat{T}_{\mathrm{nuc}}(\mathbf{R}) = -\frac{1}{2\tilde{\mu}_9}\frac{\partial^2}{\partial \tilde{Q}_{9y}^2} - \frac{1}{2\mu_{13}}\frac{\partial^2}{\partial Q_{13z}^2} - \sum_i \ldots, \tag{2.263}$$

where Q_{13z} denotes the third most important Jabobi/Mobile coordinate (Table 2.2) and the sum runs over all remaining small amplitude motions.

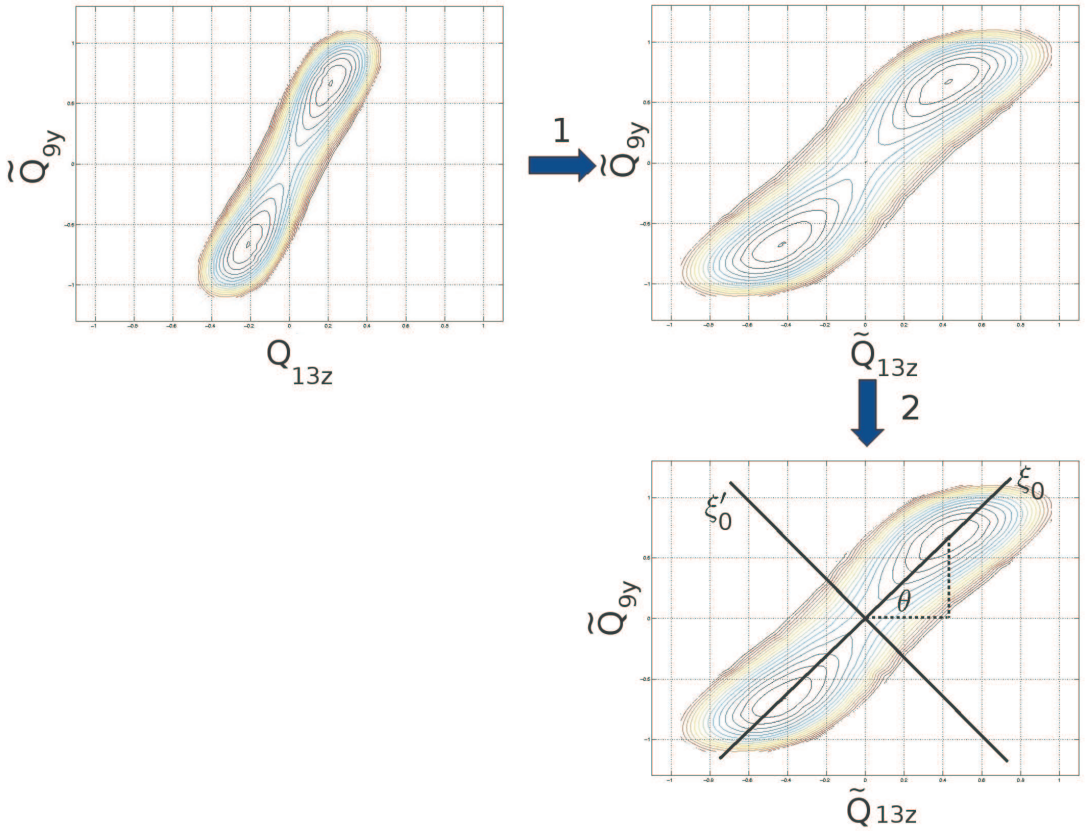

Figure 2.8: Combination of Jacobi/Mobile coordinates $\tilde{Q}_{9y}$ and Q_{13z}

(ii) In the following, at first coordinates $\tilde{Q}_{9y}$ and Q_{13z} will be combined and two new coordinates will be obtained, one of which will become the new large amplitude coordinate, whereas the other coordinate will show a negligible amplitude. The same scheme is then successively applied to incorporate the remaining Jabobi/Mobile coordinates and to define a one dimensional reaction coordinate ξ, retaining the associated mass $\tilde{\mu}_9 = (m_{\mathrm{C}} + m_{\mathrm{H}})/4$.

At first coordinate Q_{13z} is mass-weighted (step 1 in Figure 2.8) which gives for the kinetic energy operator:

$$\hat{T}_{\mathrm{nuc}}(\mathbf{R}) = -\frac{1}{2\tilde{\mu}_9}\left(\frac{\partial^2}{\partial \tilde{Q}_{9y}^2} + \frac{\partial^2}{\partial \tilde{Q}_{13z}^2}\right) - \sum_i \ldots \tag{2.264}$$

with

$$\tilde{Q}_{13z} = \sqrt{\frac{\mu_{13}}{\tilde{\mu}_9}} Q_{13z} = \sqrt{\frac{m_C + m_{\mathrm{H}}}{\frac{1}{4}(m_C + m_{\mathrm{H}})}} = 2Q_{13z}.$$

Then a unitary transformation is performed (step 2 in Figure 2.8) such that two new

coordinates (ξ_0 and ξ_0') are obtained. One of those coordinates (ξ_0) connects the two potential minima with the other one (ξ_0') running orthogonal to it. The rotation angle θ is

$$\tan(\theta) = \frac{\Delta\tilde{Q}_{9y}}{\Delta\tilde{Q}_{13z}} = \frac{\Delta\tilde{Q}_{9y}}{2\Delta Q_{13z}} = \frac{0.734\,\text{Å}}{2 \times 0.2965\,\text{Å}} \qquad \rightarrow \qquad \theta = 51.07^\circ, \tag{2.265}$$

where $\Delta\tilde{Q}_{9y}$ and ΔQ_{13z} are the displacements of coordinates $\tilde{Q}_{9y}$ and Q_{13z} from the associated potential barrier to one of the minimima (Figure 2.8 and Table 2.2).

The displacement $\Delta\xi_0$ when going from this barrier to one of the minima is

$$\begin{aligned} &\Delta\xi_0^2 = \Delta\tilde{Q}_{13z}^2 + \Delta\tilde{Q}_{9y}^2 = \Delta\tilde{Q}_{13z}^2 + 2\Delta Q_{9y}^2 = 0.890\,\text{Å}^2 \\ &\rightarrow \Delta\xi_0 = 0.943\,\text{Å}. \end{aligned} \tag{2.266}$$

Using the same strategy to combine ξ_0 with Q_{14x} (next most important Jabobi/Mobile coordinate, see Table 2.2) gives for the displacement when going from the (new) associated potential barrier to one of the minima:

$$\Delta\xi_1 = \sqrt{\Delta\tilde{Q}_{9y}^2 + \Delta\tilde{Q}_{13z}^2 + \Delta\tilde{Q}_{14x}^2} = 0.954\,\text{Å}. \tag{2.267}$$

Inclusion of ALL Jabobi/Mobile coordinates finally gives

$$\Delta\xi = \sqrt{\sum_k \Delta\tilde{Q}_k^2} = 0.958\,\text{Å}, \tag{2.268}$$

where the sum runs over the x, y and z-components of *all* Jabobi/Mobile coordinates.

Hence, the set of Jacobi/Mobile coordinates, Table 2.2, was condensed into one coordinate ξ performing a large amplitude motion, while the remaining resulting coordinates exhibit considerably smaller contributions to the DCR of SBV. The new coordinates were obtained by a sequence of unitary transformations, thereby extending the original definition of Jacobi/Mobile coordinates [242, 243], while preserving the diagonal form of the kinetic energy operator, c.f. Ref. [244].

Note that these results were obtained subject to the constraint that the molecule's center of mass should not move and that the orientation of the C1-C5 carbon bridge is fixed along the x-axis, see above as well as Figure 2.6(b) and Table 2.2. The first constraint leads to a separation of the translational motion associated with the center of mass coordinates $\mathbf{Q}_{\text{com}}$ from the remaining dof. The second constraint, however, was chosen for practical reasons, such that the vibrational and rotational dof are not separated, leading to a total angular-momentum associated with the nuclear rearrangement unequal to zero from the reactant to the product, that is angular-momentum is not conserved in this particular model. Note, however, that similar results are obtained for an alternative scenario, where the total angular-momentum for

the degenerate Cope rearrangement of SBV from the reactant to the product is conserved [T4]. This might be achieved by first aligning the reactant R and the product P again in the center of mass frame. Then, P is rotated, at first arbitrarily, with respect to the reactant, yielding the particular structure P' and the total angular momentum associated with the reaction from R to P' is calculated. This procedure is repeated until a rotated product structure $\tilde{P}$ has been found, such that the reaction from R to $\tilde{P}$ proceeds with zero total angular-momentum [252]. Such a procedure yields $\Delta\xi = 0.82\,\text{Å}$, see Ref. [T4].

In our one dimensional model the kinetic energy operator takes on the form

$$\hat{T}_{\text{nuc}}(\xi) = -\frac{1}{2m_\xi}\frac{\partial^2}{\partial\xi} \qquad \text{with} \qquad m_\xi = \tilde{\mu}_9 = \frac{1}{4}(m_{\text{C}} + m_{\text{H}}). \tag{2.269}$$

The reaction coordinate ξ leads straight from the minimum of the symmetric double well potential energy surface representing the reactant (R) to the other potential minimum representing the product (P). It accounts for synchronous motions of all the nuclei from the reactant to the product. The potential barrier associated with this direct one-dimensional path will be denoted as B_{d} in the following.

The displacement $\Delta\xi$, eqn. (2.268), from R to the barrier B_{d} can of course also be calculated in terms of the original Cartesian coordinates, c.f. eqns. (2.255) and (2.256). For this purpose, at first the Cartesian displacement coordinates from R to P, Δx_k, are calculated in analogy to the Jabobi/Mobile displacement coordinates, c.f. Table 2.2. Next, the displacement coordinates associated with the carbon atoms, Δx_k^C with $k = 1, \ldots, 3M/2$, where M is the number of atoms in the molecular system, c.f. eqn. (2.3), are weighted by the factor $\sqrt{\frac{m_{\text{C}}}{m_\xi}}$ according to $\Delta\tilde{x}_k^{\text{C}} = \sqrt{\frac{m_{\text{C}}}{m_\xi}}\Delta x_k^{\text{C}}$, and the Cartesian displacement coordinates associated with the hydrogen atoms are weighted by the factor $\sqrt{\frac{m_{\text{H}}}{m_\xi}}$ according to $\Delta\tilde{x}_k^{\text{H}} = \sqrt{\frac{m_{\text{H}}}{m_\xi}}\Delta x_k^{\text{H}}$. In this way, the mass associated with the reaction coordinate ξ is still given by $m_\xi = (m_C + m_{\text{H}})/4$ and the displacement is calculated as

$$\Delta\xi = \frac{1}{2}\sqrt{\sum_k^{3M/2}\left[\left(\Delta\tilde{x}_k^{\text{C}}\right)^2 + \left(\Delta\tilde{x}_k^{\text{H}}\right)^2\right]}. \tag{2.270}$$

In practice, the molecular structures along the reaction coordinate ξ are obtained by linear interpolation between the potential minima as

$$\mathbf{X}_{\text{R}} + \lambda_1\mathbf{X}_{\text{R}\to\text{P}}, \tag{2.271}$$

where $\mathbf{X}_{\text{R}\to\text{P}} = \mathbf{X}_{\text{P}} - \mathbf{X}_{\text{R}}$ is the direction from R to P with $\mathbf{X}_{\text{R}}$ and $\mathbf{X}_{\text{P}}$ being $3M$-dimensional vectors of the Cartesian coordinates corresponding to the reactant and product, respectively. Hence, the parameter $\lambda_1 = 0$ yields the reactant structure, $\lambda_1 = 1$ yields the product structure and $\lambda_1 = 1/2$ yields the center structure $\mathbf{X}_{B_{\text{d}}}$ corresponding to the potential barrier B_{d} in this one-dimensional model. For the succeeding quantum dynamical simulations with associated

Table 2.3: Displacement of Jabobi/Mobile coordinates for the degenerate Cope rearrangement of semibullvalene in Å from the potential barrier B_d associated with the one-dimensional reaction coordinate ξ to the transition state. Structures refer to B3LYP/cc-pVTZ calculations.

	Jabobi/Mobile coordinate	ΔX	ΔY	ΔZ
$\mathbf{Q}_1$:	$\mathrm{C_2H_{12}}$	0.025	0.000	0.018
$\mathbf{Q}_2$:	$\mathrm{C_8H_{18}}$	-0.020	-0.127	-0.108
$\mathbf{Q}_3$:	$\mathrm{C_4H_{14}}$	0.000	-0.011	-0.009
$\mathbf{Q}_4$:	$\mathrm{C_6H_{16}}$	0.020	-0.127	-0.108
$\mathbf{Q}_5$:	$\mathrm{C_3H_{13}}$	-0.025	0.000	0.018
$\mathbf{Q}_6$:	$\mathrm{C_7H_{17}}$	0.020	0.127	-0.108
$\mathbf{Q}_7$:	$\mathrm{C_5H_{15}}$	0.000	0.011	-0.009
$\mathbf{Q}_8$:	$\mathrm{C_1H_{11}}$	-0.020	0.127	-0.108
$\mathbf{Q}_9$:	$\mathrm{C_2H_{12}, C_8H_{18}}$	0.000	0.118	0.000
$\mathbf{Q}_{10}$:	$\mathrm{C_4H_{14}, C_6H_{16}}$	0.000	0.118	0.000
$\mathbf{Q}_{11}$:	$\mathrm{C_3H_{13}, C_7H_{17}}$	0.000	0.092	0.000
$\mathbf{Q}_{12}$:	$\mathrm{C_1H_{11}, C_5H_{15}}$	0.010	0.000	0.000
$\mathbf{Q}_{13}$:	$\mathrm{C_2H_{12}C_8H_{18}, C_4H_{14}C_6H_{16}}$	-0.017	0.000	0.000
$\mathbf{Q}_{14}$:	$\mathrm{C_3H_{13}C_7H_{17}, C_6H_{16}C_4H_{14}C_8H_{18}C_2H_{12}}$	0.000	0.000	-0.005
$\mathbf{Q}_{15}$:	$\mathrm{C_1H_{11}C_5H_{15}, C_2H_{12}C_8H_{18}C_4H_{14}C_6H_{16}C_3H_{13}C_7H_{17}}$	0.000	0.000	-0.047
$\mathbf{Q}_\mathrm{com}$:		0.000	0.000	0.000

mass $m_\xi = (m_\mathrm{C} + m_\mathrm{H})/4$, the ξ-axis is scaled such that the displacement from R to B_d amounts to $\Delta\xi = 0.958\,\text{Å}$, eqn. (2.268). Specifically, we set $\xi_R = -0.958\,\text{Å}$, $\xi_{B_\mathrm{d}} = 0\,\text{Å}$ and $\xi_P = 0.958\,\text{Å}$, c.f. Figure 4.2(b) in Chapter 4.

2.4.2.2 Extension of the model

A straightforward extension of this one-dimensional model, motivated by previous work on the Cartesian reaction plane Hamiltonian with applications to hydrogen-atom transfer reactions [245–248], is the incorporation of the transition state (TS). Accordingly, a second direction corresponding to the direct path from the geometric center $\mathbf{X}_{B_\mathrm{d}}$ to the transition state is introduced as

$$\mathbf{X}_{B_\mathrm{d}\to\mathrm{TS}} = \mathbf{X}_\mathrm{TS} - \mathbf{X}_{B_\mathrm{d}}, \tag{2.272}$$

where $\mathbf{X}_\mathrm{TS}$ denotes the $3M$-dimensional vector of the Cartesian coordinates corresponding to the transition state. In analogy to Table 2.2, the displacements from B_d to TS in terms of Jabobi/Mobile coordinates are shown in Table 2.3. They are both more evenly distributed among the coordinates and overall smaller compared to the displacements from R to P shown in Table 2.2. The two thus defined directions are orthogonal

$$\mathbf{X}_{\mathrm{R}\to\mathrm{P}} \cdot \mathbf{X}_{B_\mathrm{d}\to\mathrm{TS}} = 0. \tag{2.273}$$

The corresponding displacement from B_{d} to TS is given by

$$\Delta\xi' = \sum_{k}^{3M} \left(\Delta\tilde{Q}_{k,B_{\mathrm{d}}\to\mathrm{TS}}\right)^2 = \sum_{k}^{3M/2} \left[\left(\Delta\tilde{x}^{\mathrm{C}}_{k,B_{\mathrm{d}}\to\mathrm{TS}}\right)^2 + \left(\Delta\tilde{x}^{\mathrm{H}}_{k,B_{\mathrm{d}}\to\mathrm{TS}}\right)^2\right], \tag{2.274}$$

where $\Delta\tilde{Q}_{k,B_{\mathrm{d}}\to\mathrm{TS}}$ as well as $\Delta\tilde{x}^{\mathrm{C}}_{k,B_{\mathrm{d}}\to\mathrm{TS}}$ and $\Delta\tilde{x}^{\mathrm{H}}_{k,B_{\mathrm{d}}\to\mathrm{TS}}$ denote weighted Jabobi/Mobile and Cartesian displacement coordinates from B_{d} to TS, respectively. Taking for convenience the arbitrary reduced mass for coordinate ξ' equal to ξ, i.e. $m_{\xi'} = m_{\xi} = (m_{\mathrm{C}} + m_{\mathrm{H}})/4$, yields

$$\Delta\xi' = 0.172\,\text{Å}. \tag{2.275}$$

The corresponding potential energy surface for the electronic ground and first excited state is shown in Chapter 5, Figure 5.1. It is calculated according to

$$\mathbf{X}_{\mathrm{TS}} + \lambda_1\left(\mathbf{X}_{\mathrm{P}} - \mathbf{X}_{\mathrm{R}}\right) + \lambda_2\left(\mathbf{X}_{\mathrm{TS}} - \mathbf{X}_{B_{\mathrm{d}}}\right), \tag{2.276}$$

c.f. eqn. (2.272), with corresponding scaling of the ξ- and ξ'-axis to yield the displacements according to eqns. (2.268) and (2.275), respectively.

3 Results

3.1 First Part: Electron-Nuclear Quantum Fluxes in Pericyclic Reactions, Exemplified for the Cope Rearrangement of Semibullvalene

3.1.1 D. Andrae, I. Barth, T. Bredtmann*, H.-C. Hege, J. Manz*, F. Marquardt, B. Paulus,

Electronic Quantum Fluxes during Pericyclic Reactions Exemplified for the Cope Rearrangement of Semibullvalene,
J. Phys. Chem. B, 115, 5476-5483 (2011)

D. Andrae, I. Barth, T. Bredtmann*, H.-C. Hege, J. Manz*, F. Marquardt, B. Paulus,
Electronic Quantum Fluxes during Pericyclic Reactions Exemplified for the Cope Rearrangement of Semibullvalene,
J. Phys. Chem. B, **115**, 5476-5483 (2011).

DOI: 10.1021/jp110365g
URL: http://dx.doi.org/10.1021/jp110365g

D. Andrae, I. Barth, T. Bredtmann*, H.-C. Hege, J. Manz*, F. Marquardt, B. Paulus,
Electronic Quantum Fluxes during Pericyclic Reactions Exemplified for the Cope Rearrangement of Semibullvalene,
J. Phys. Chem. B, **115**, 5476-5483 (2011).

DOI: 10.1021/jp110365g
URL: http://dx.doi.org/10.1021/jp110365g

D. Andrae, I. Barth, T. Bredtmann*, H.-C. Hege, J. Manz*, F. Marquardt, B. Paulus,
Electronic Quantum Fluxes during Pericyclic Reactions Exemplified for the Cope Rearrangement of Semibullvalene,
J. Phys. Chem. B, **115**, 5476-5483 (2011).

DOI: 10.1021/jp110365g
URL: http://dx.doi.org/10.1021/jp110365g

D. Andrae, I. Barth, T. Bredtmann*, H.-C. Hege, J. Manz*, F. Marquardt, B. Paulus,
Electronic Quantum Fluxes during Pericyclic Reactions Exemplified for the Cope Rearrangement of Semibullvalene,
J. Phys. Chem. B, **115**, 5476-5483 (2011).

DOI: 10.1021/jp110365g
URL: http://dx.doi.org/10.1021/jp110365g

D. Andrae, I. Barth, T. Bredtmann*, H.-C. Hege, J. Manz*, F. Marquardt, B. Paulus,
Electronic Quantum Fluxes during Pericyclic Reactions Exemplified for the Cope Rearrangement of Semibullvalene,
J. Phys. Chem. B, **115**, 5476-5483 (2011).

DOI: 10.1021/jp110365g
URL: http://dx.doi.org/10.1021/jp110365g

D. Andrae, I. Barth, T. Bredtmann*, H.-C. Hege, J. Manz*, F. Marquardt, B. Paulus,
Electronic Quantum Fluxes during Pericyclic Reactions Exemplified for the Cope Rearrangement of Semibullvalene,
J. Phys. Chem. B, **115**, 5476-5483 (2011).

DOI: 10.1021/jp110365g
URL: http://dx.doi.org/10.1021/jp110365g

D. Andrae, I. Barth, T. Bredtmann*, H.-C. Hege, J. Manz*, F. Marquardt, B. Paulus,
Electronic Quantum Fluxes during Pericyclic Reactions Exemplified for the Cope Rearrangement of Semibullvalene,
J. Phys. Chem. B, **115**, 5476-5483 (2011).

DOI: 10.1021/jp110365g
URL: http://dx.doi.org/10.1021/jp110365g

D. Andrae, I. Barth, T. Bredtmann*, H.-C. Hege, J. Manz*, F. Marquardt, B. Paulus,
Electronic Quantum Fluxes during Pericyclic Reactions Exemplified for the Cope Rearrangement of Semibullvalene,
J. Phys. Chem. B, **115**, 5476-5483 (2011).

DOI: 10.1021/jp110365g
URL: http://dx.doi.org/10.1021/jp110365g

3.1.2 T. Bredtmann*, J. Manz*, Quantum Control of the Initiation of a Pericyclic Reaction in the Electronic Ground State, J. Chem. Sci., 124, 121-129 (2012)

J. Chem. Sci. Vol. 124, No. 1, January 2012, pp. 121–129.

Optimal control of the initiation of a pericyclic reaction in the electronic ground state[#]

TIMM BREDTMANN* and JÖRN MANZ*
Institut für Chemie und Biochemie, Freie Universität Berlin, Takustr. 3, 14195 Berlin, Germany
e-mail: bredt@chemie.fu-berlin.de; jmanz@chemie.fu-berlin.de

Abstract. Pericyclic reactions in the electronic ground state may be initiated by down-chirped pump-dump sub-pulses of an optimal laser pulse, in the ultraviolet (UV) frequency and sub-10 femtosecond (fs) time domain. This is demonstrated by means of a quantum dynamics model simulation of the Cope rearrangement of Semibullvalene. The laser pulse is designed by means of optimal control theory, with detailed analysis of the mechanism. The theoretical results support the recent experimental initiation of a pericyclic reaction. The present approach provides an important step towards monitoring asynchronous electronic fluxes during synchronous nuclear pericyclic reaction dynamics, with femto-to-attosecond time resolution, as motivated by the recent prediction of our group.

Keywords. Quantum dynamics; optimal control; pericyclic reaction; semibullvalene.

1. Introduction

Laser control of pericyclic reactions in their electronic ground states is a challenge in chemical reaction dynamics. Schwebel *et al.* in 1984[1] demonstrated an important mechanism, initiation by means of high overtone excitations of various mode selective vibrations, in the infrared (IR) frequency domain. This experimental success has served, in part, as motivation for our previous design of IR pump-dump laser pulse control of pericyclic reactions.[2–4] The approach relies, however, on a prerequisite which is difficult to satisfy, i.e., strong changes of the dipole along the reaction path. Recently, Iwakura, Yabushita and Kobayashi could demonstrate an alternative approach, i.e., initiation of a pericyclic reaction in the electronic ground state, by means of an ultrashort laser pulse in the ultraviolet (UV) frequency domain, within less than ten femtoseconds (fs).[5] Detailed analysis yields the mechanism, essentially intrapulse UV pump-dump control of the initiation. This stimulating experiment serves as the first, general motivation for the present work. Accordingly, we shall apply optimal control theory (OCT)[6–10] in order to design an ultrashort laser pulse which initiates a pericyclic reaction in the electronic ground state. The goal is to investigate whether the UV pump-dump type mechanism will indeed turn out as the most efficient way to start the reaction.

As specific system, we shall consider the degenerate 3,3-sigmatropic shift, or Cope rearrangement[11] of semibullvalene[2–4,12–34] (C_8H_8, SBV) in the electronic ground state, see figure 1. The reactant (R) has a chain of six carbon atoms C6=C7-C8-C2-C3=C4 (clockwise notation) which is transformed into another chain C2=C3-C4-C6-C7=C8 (same clockwise notation, keeping the labels of the carbon atoms) for the products (P); here R and P may be distinguished by isotopic labelling. Apparently, the carbon-carbon bond C8-C2 (clockwise notation) is broken during the pericyclic reaction, while the C4-C6 bond is formed. Moreover, the double bonds C3=C4 and C6=C7 are shifted to C2=C3 and C7=C8, respectively (double bond shifting, DBS). This pericyclic reaction is similar to the Cope rearrangement of 1,5-hexadiene, except that most of the large amplitude motions of 1,5-hexadiene are essentially frozen by the additional 'bridge' of carbon atoms C1-C5 in SBV. This constraint supports the simple one-dimensioal (1D) model for the Cope rearrangement of SBV which has been introduced in Reference 34, see also Reference 15.

Cope rearrangements of SBV and several derivatives have already served as touchstones for various properties that are related to pericyclic reactivity, from synthesis[12,16,21,22,29] via spectroscopy[13,15,20,24,27] and kinetics[13,14,19] to electronic structure[17,18,21–26,28–31,35] and the related thermochromicity,[3,21,22,24,29] *ab initio* molecular dynamics[32], the role of tunnelling[33], and the above-mentioned quantum dynamics simulations of IR pump-dump laser control.[2–4] In particular, quantum chemistry first principal calculations show that the Cope rearrangement of SBV in the electronic ground state

[#]Dedicated to Prof. N Sathyamurthy on his 60th birthday
*For correspondence

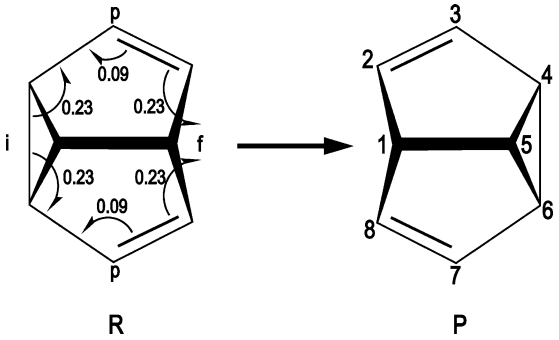

Figure 1. Cope rearrangement of semibullvalene, with pincer-motion-type directionality of electronic fluxes indicated by curved arrows in Lewis structures (adapted from Reference 34.) The numbers in the reactant structure R specify the amounts of pericyclic electrons which flow between neighbouring bonds. Symbols i and f indicate dominant initial and final fluxes of electrons, out of the bond to be broken and into the bond to be formed, respectively. Symbol p indicates perpetual weak electronic flux during double bond shifting. The labels for the carbon atoms (see product structure P) are the same for R and P.

proceeds in a symmetric double well potential energy surface (PES), with two equivalent minima representing R and P which are separated by a rather shallow barrier.[18,21,22,24,26,28–31,33] In contrast, in the first excited electronic state, SBV has a rather steep and deep symmetric single well PES with large energy gap to the potential barrier in the electronic ground state ($\Delta E \gg 2$ eV[18,20,24]).

Recently, we could determine the coupled electronic and nuclear fluxes during the Cope rearrangement of SBV.[34] The results of Reference 34 are quite surprising, in view of the traditional rules for the outcome and the associated net electron transfer during pericyclic reactions, which is symbolized by curved arrows in Lewis structures of the reactant[36], see e.g., the text books of organic[37–41], inorganic[42,43], and biochemistry.[44,45] The corresponding valence electrons which describe the changes of the Lewis structures, from R to P, are called 'pericyclic'. These electrons are complementary to other valence electrons (e.g., those representing CH bonds) or core electrons. Specifically, we were able to identify the directionality of the fluxes of 'pericyclic' electrons: It is well described by the pincer-motion-type (as opposed to clockwise or anticlockwise) pattern of the curved arrows, as illustrated in figure 1. Also, we discovered that the number of pericyclic electrons which is transferred per curved arrow, is typically between 0.09 and 0.23 i.e., much smaller than the traditional assumption of 1 or even 2. Furthermore, we detected significant opposite fluxes of other valence electrons. For the scenario of Reference 34, the time scale of the Cope rearrangement of SBV was determined to be less than 30 fs. Moreover, we could discover that various individual processes of the pericyclic reaction such as C8-C2 bond breaking, DBS from C3=C4 to C2-C3 as well as from C6=C7 to C7=C8, and C4-C6 bond formation, are associated with asynchronous electronic fluxes during synchronous nuclear motions. This is a significant extension of previous investigations which have centred attention on the simpler question of synchronicity or concertedness versus sequentiality, just for the nuclear motions during chemical reactions, while ignoring electronic motions, see e.g., References 35, 46 and 47. Some important results of Reference 34 are summarized in figure 1.

Certainly, it is a challenge to investigate the predictions of Reference 34 experimentally, using e.g., modern techniques of femto- to attosecond spectroscopy which allow to monitor the time evolutions of valence electrons[48–51], see also References 52–60 and the review 61. For this purpose, it will be necessary to initiate the Cope rearrangement of SBV in the electronic ground state. This request provides the second, specific motivation of this paper, that means we shall explore the efficiency of the intrapulse UV pump-dump mechanism of Iwakura, Yabushita and Kobayashi[5], for initiation of the specific pericyclic reaction, Cope rearrangement of SBV in the electronic ground state. For this purpose, we shall adapt the same 1D model for the nuclear wavepacket dynamics which has been employed in Reference 34, with extensions based on Reference 2. The results for this idealized scenario should serve as a reference for accurate quantum simulations of more demanding realistic models.

This paper presents the model and techniques, the results and discussion followed by conclusions in sections 2, 3 and 4, respectively.

2. Model and techniques

The subsequent quantum simulations of the nuclear wave packet dynamics representing the laser driven pericyclic reaction of SBV employ the simple model of Reference 34. It is illustrated in figure 2. The model is motivated by the constrained mobility of SBV, as outlined in section 1, and also by the fact that for the scenario of Reference 34, the transformation from R to P takes less than 30 fs. This suggests that the reaction should be induced by exciting a distinguished 'reactive' nuclear degree of freedom (dof), called ξ, such

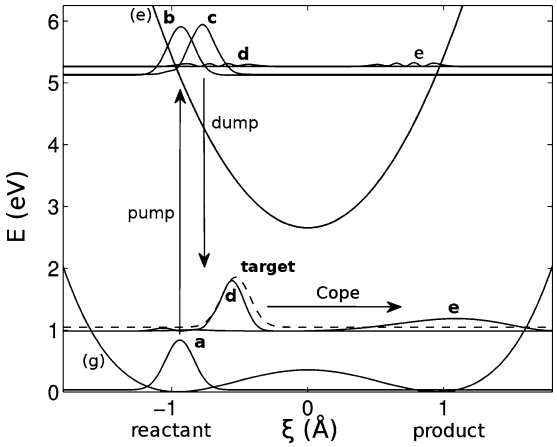

Figure 2. Optimal control of the initiation of the Cope rearrangement of semibullvalene (SBV) in the electronic ground state. The time evolution of the laser driven wavepacket dynamics from the reactant (R) along the nuclear coordinate ξ to the product (P), is illustrated by the series of snapshots 'a,b,c,d,e' of the nuclear densities, at times $t =$ 0.0 fs, 3.1 fs, 7.1 fs, 10.0 fs (the end of the laser pulse) and $t = 33.5$ fs, respectively. They are embedded in the potential energy surfaces of SBV in the electronic ground and excited states, $V_g(\xi)$ and $V_e(\xi)$, adapted from References 34 and 2, respectively. The asymptotic base lines of the densities correspond to their mean energies. Also shown is the density of the target state, eqn. (5), adapted from Reference 34 which runs from R to P, with total energy E well above the barrier of $V_g(\xi)$ (dashed line). Snapshot 'a' shows the density of the initial ground state $\Psi_{g,v=0}(\xi)$ of R, with energy $E_{g,v=0}$. Snapshots 'b,c,d' illustrate the evolution in the electronic excited state, $V_e(\xi)$, mediated by the pump and dump sub-pulses of the optimal control pulse, which are indicated by the vertical arrows. Snapshot 'd' embedded in $V_g(\xi)$ shows the density of the wavepacket at the end of the laser pulse, $t = \tau$, close to the 'target' state. Subsequently, it evolves to snapshot 'e' representing the product P in the electronic ground state. A small fraction of the total density is left in the excited electronic state, and runs simultaneously from snapshot 'd' to 'e' embedded in $V_e(\xi)$.

that motion along ξ is much faster than any competing process such as intramolecular vibrational redistribution (IVR) of the available energy from ξ to the other $3\times16-6-1 = 41$ 'passive' vibrational dofs. The single dof ξ that we consider leads straight from the minimum of the symmetric double well PES representing R to the other one representing P. It accounts for synchronous motions of all the nuclei during the pericyclic reaction. As dominant large amplitude motion, it describes the difference of the lengths of the two carbon-carbon bonds C8-C2 and C4-C6 (clockwise notation, cf. figure 1) which are broken and formed, respectively, during the Cope rearrangement, see also Reference 15, confirmed by Reference 32. Accordingly, the values ξ_R and ξ_P of ξ at the potential minima representing R and P have the same absolute values, but opposite signs, see figure 2. The associated reduced mass is $\mu = (M_C + M_H)/4$.[15] The 1D curve of the PES $V_g(\xi)$ of SBV in the electronic ground (g) state which is shown in figure 2 is adapted from Reference 34. It was evaluated by means of quantum chemical first principles calculations based on Kohn-Sham density functional theory. The calculations are performed with the MOLPRO[62] program package, using the B3LYP functional[63,64] together with the cc-pVTZ[65] basis sets. The reliability of this method concerning structures and energies along the coordinate ξ is ensured by comparison to high-level *ab initio* methods (CASPT2/cc-pVTZ and MRCI/cc-pVTZ, CCSD(T)/cc-pVTZ, respectively). In addition, the PES of SBV in the excited (e) state is modelled as harmonic potential with empirical parameters, as derived in Reference 2.

The initial (t = 0) state of the system representing R is the vibrational ground state ($v = 0$) which is localized in the potential well of the electronic ground state (g) representing R, $\Psi_g(t = 0) = \Psi_{g,v=0}$, without any component in the excited electronic state (e), $\Psi_e(t = 0) = 0$. The density $\rho_{g,v=0}(\xi) = |\Psi_{g,v=0}(\xi)|^2$ is shown as wavepacket labelled 'a' in figure 2. The time evolution of the laser driven wavepackets, $\Psi_g(t > 0)$ and $\Psi_e(t > 0)$, is obtained as solution of the time-dependent Schrödinger equation (TDSE), in semiclassical dipole approximation,

$$i\hbar\frac{\partial}{\partial t}\begin{pmatrix}\Psi_e(t)\\ \Psi_g(t)\end{pmatrix} = \left[\begin{pmatrix}T+V_e & 0\\ 0 & T+V_g\end{pmatrix} - \mathcal{E}(t)\begin{pmatrix}d_{ee} & d_{eg}\\ d_{ge} & d_{gg}\end{pmatrix}\right]\begin{pmatrix}\Psi_e(t)\\ \Psi_g(t)\end{pmatrix}. \quad (1)$$

The rather simple form of the TDSE (1) applies to the scenario of a pre-oriented, non-rotating molecule interacting with a linearly polarized laser pulse. Pre-orientation may be achieved e.g., by the methods of References 66–69. The laser pulse with electric field component $\mathcal{E}(t)$ should then be polarized parallel to the transition dipole between the ground (g) and excited (e) electronic state. The relevant component is modelled as $d_{eg} = d_{ge} = 0.3934\,ea_0 = 1$ debye in Condon approximation. Furthermore, we neglect the dipole functions, $d_{gg} = d_{ee} = 0$. The experiment of Reference 5 suggests a rather short duration τ of the laser pulse; we set $\tau = 10$ fs. Molecular rotations are negligible, indeed, on this time scale. As a consequence, the model describes nuclear motions exclusively along ξ, with kinetic energy operator $T = -\hbar^2/(2\mu) \times \partial^2/\partial\xi^2$. Kinetic

couplings are also neglected, in Born-Oppenheimer approximation.

The wavefunctions $\Psi_g(\xi, t)$ and $\Psi_e(\xi, t)$ allow to calculate all the properties which are important for the subsequent analysis, including the densities

$$\begin{aligned} \rho_g(t) &= |\Psi_g(\xi, t)|^2 \\ \rho_e(t) &= |\Psi_e(\xi, t)|^2, \end{aligned} \tag{2}$$

the populations

$$\begin{aligned} P_g(t) &= \langle \Psi_g(t) | \Psi_g(t) \rangle \\ P_e(t) &= \langle \Psi_e(t) | \Psi_e(t) \rangle \end{aligned} \tag{3}$$

where $\langle \ldots | \ldots \rangle$ denotes integration over the nuclear coordinate ξ, and the energies

$$\begin{aligned} E_g(t) &= \langle \Psi_g(t) | T + V_g | \Psi_g(t) \rangle / P_g(t), \\ E_e(t) &= \langle \Psi_e(t) | T + V_e | \Psi_e(t) \rangle / P_e(t). \end{aligned} \tag{4}$$

The double-motivated, specific goal of the present investigation is to design a laser pulse $\mathcal{E}(t)$ which initiates the Cope rearrangement of SBV in the electronic ground state, starting from the ground state $\Psi_g(\xi, t = 0) = \Psi_{g,v=0}(\xi)$ and yielding essentially the same wavepacket dynamics as in Reference 34. For this purpose, we request that at the end ($t = \tau$) of the laser pulse, the laser driven wavepacket $\Psi_g(\xi, t = \tau)$ should agree with the reactant wavefunction of Reference 34, soon after the start of the Cope rearrangement – this wave function will be called the 'target wave function $\Psi_{g,\text{target}}(\xi)$'. For convenience, we employ

$$\Psi_{g,\text{target}}(\xi) \approx \Psi_{g,v=0}(\xi - \Delta\xi) \times e^{ik\xi}. \tag{5}$$

The density of $\Psi_{g,\text{target}}(\xi)$ is illustrated in figure 2 by the dashed line. Apparently, the first factor in eqn. (5) describes the shift of the initial wavefunction from its centre at ξ_R to $\xi_{\text{target}} = \xi_R + \Delta\xi$, soon after the start of the reaction, but before the onset of wavepacket dispersion. For the present application, we use $\Delta\xi = 0.41$ Å. The second factor $e^{ik\xi}$ describes nuclear motions directed from R to P, with momentum $\hbar k$. The corresponding kinetic and total energies are $E_{\text{kin}} = \hbar k^2/(2\mu)$ and

$$E_g = E_{\text{kin}} + V_g(\xi_{\text{target}}), \tag{6}$$

respectively. The target value $E_g = 1.04$ eV is adapted from Reference 34, so that perfect generation of the target wavepacket, eqn. (5), launches the same wavepacket dynamics of SBV, from R to P, as in Reference 34.

The design of the laser pulse $\mathcal{E}(t)$ which drives the initial wavefunction $\Psi_g(\xi, t = 0) = \Psi_{g,v=0}(\xi)$ to the target wavefunction, eqn. (5), is achieved by means of OCT.[6–10] It maximizes the cost functional, that means the absolute value of the overlap, $|\langle \Psi_{g,\text{target}} | \Psi_g(t = \tau) \rangle|$ at the end ($t = \tau$) of the laser pulse, subject to the ubiquitious 'penalty' for all-too-strong electric field strengths.[6–10] In practice, we employ the version of OCT as implemented in the Multi Configuration Time Dependent Hartree (MCTDH) package for propagation of (laser driven) nuclear wavepackets, as documented in References 70–72. The perfect laser pulse should yield the ideal value $|\langle \Psi_{g,\text{target}} | \Psi_g(t = \tau) \rangle| = 1$ – this would guarantee that the subsequent ($t > \tau$) free evolution of $\Psi_g(\xi, t)$ is the same as in Reference 34.

3. Results and discussion

The optimal laser pulse $\mathcal{E}(t)$ and the resulting population dynamics, $P_g(t)$, $P_e(t)$, are documented in the middle and bottom panels of figure 3, respectively. The interpretation is obvious: the optimal laser pulse consists of two sub-pulses which 'pump' and 'dump' populations, first from the electronic ground to the excited state, and then back to the ground state. Subsequently, we shall analyse these sub-pulses in order to discover their cooperative mechanisms, which allow them to reach the present goal of laser control, that is initiation of the Cope rearrangement of the model SBV, from R to P, in the electronic ground state, equivalent to the reaction dynamics in Reference 34, *cum grano salis*. We shall also discuss some remaining drawbacks.

The first and second sub-pulse are well separated from each other — apparently, they have different tasks which need to be carried out at special times with selective time delay t_d. Specifically, they are centered at $t_{\text{pump}} = 2.4$ fs and at $t_{\text{dump}} = 7.7$ fs , respectively, thus $t_d = 5.3$ fs, and they last from approximately $t = 1.7$ fs till $t = 3.1$ fs and from $t = 7.1$ fs till $t = 8.3$ fs, respectively, i.e., they have similar durations of 1.4 fs and 1.2 fs, respectively. They consist of a little less than four and about three half-cycles, respectively, implying an overall down chirp, that means larger frequency of the pump sub-pulse than for the dump sub-pulse (see figure 2, top panel). The corresponding photon energies are resonant or near-resonant to the energy gaps of the PES,

$$\begin{aligned} \hbar\omega_{\text{pump}} &\approx V_e(\xi_{\text{pump}}) - V_g(\xi_{\text{pump}}) \approx 5.1\,\text{eV} \\ \hbar\omega_{\text{dump}} &\approx V_e(\xi_{\text{dump}}) - V_g(\xi_{\text{dump}}) \approx 4.1\,\text{eV} \end{aligned} \tag{7}$$

at the positions $\xi_{\text{pump}} = \xi_R = -0.94$ Å and $\xi_{\text{dump}} = -0.74$ Å. This supports resonant population transfer by vertical Franck-Condon (FC) type pump and dump transitions at ξ_{pump} and ξ_{dump}, respectively. These positions and the transitions are indicated by the vertical arrows in figure 2. Note that the resonant position ξ_{dump}

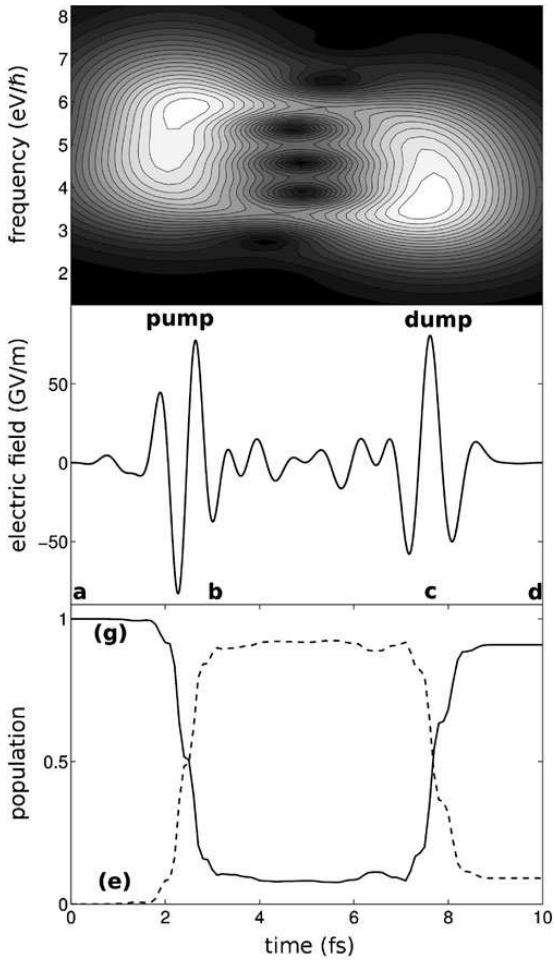

Figure 3. Optimal laser pulse $\mathcal{E}(t)$ for control of the initiation of the Cope rearrangement of semibullvalene SBV (middle panel), and the resulting population dynamics $P_g(t)$ and $P_e(t)$ in the electronic ground (g) and excited (e) states, respectively (bottom panel). The events labelled 'a,b,c,d' correspond to the snapshots of the laser-driven wavepacket dynamics shown in figure 2. Obviously, the optimal control pulse consists of two sub-pulses which induce the 'pump' and 'dump' transitions, as indicated in figure 2. The laser pulse and the resulting population dynamics are switched off at $\tau = 10$ fs. The top pannel shows the time-frequency profile of the optimal pulse, obtained by a Gabor transform using a Gaussian time-window (see e.g., References 73,74).

of the dump sub-pulse is located slightly before the centre ξ_{target} of the target wavepacket $\Psi_{g,\text{target}}(\xi)$, cf. figure 2. This allows to generate $\Psi_g(\xi, t)$ with proper kinetic and total energies (see below) at $t = t_{\text{dump}} = 7.7$ fs, readily before the final time $\tau = 10$ fs when the laser pulse is switched off, after driving the wavepacket $\Psi_g(\xi, t = \tau)$ as close to the target $\Psi_{g,\text{target}}(\xi)$ as possible. The criterion for the decisive value, $\xi_{\text{dump}} = -0.74$ Å, will be quantified below.

The half cycles of the pump and dump sub-pulses have rather strong field amplitudes, with maximum absolute value $\mathcal{E}_{\max} \approx 80\,\text{GV/m}$ corresponding to maximum transient intensity, $I_{\max} = c\epsilon_0\mathcal{E}^2_{\max} = 1.7 \times 10^{15}\,\text{W/cm}^2$. The value of the integral $\int \mathcal{E}(t)dt = 0.23\,\frac{\text{GV}}{\text{m}}\text{fs}$ is much smaller than $\mathcal{E}_{\max}\tau = 800\,\frac{\text{GV}}{\text{m}}\text{fs}$, in accord with References 75,76. Close inspection of figure 3 shows that most of the populations are transferred at times close to the maxima or minima of the half cycles of the pump and dump sub-pulses. In contrast, rather small amounts of population are transferred whenever the electric field is close to zero, switching sign. As a consequence, the population transfers proceed in a stepwise manner, as documented in figure 3.

The laser driven wavepacket dynamics is illustrated in figure 2 by the snapshots of the corresponding densities, eqn. (2), labelled 'a,b,c,d,e', which are embedded in the respective PESs of the electronic ground and excited states. The choice of these snapshots has been made in order to explain the mechanism of the optimal laser pulse. Apparently, its pump sub-pulse transfers the original wavefunction $\Psi_{g,v=0}(\xi)$ (snapshot 'a') to $\Psi_e(\xi, t)$ in the excited electronic state (snapshot 'b'). The resonance condition, eqn. (7), of the FC-type vertical transition at $\xi = \xi_{\text{pump}} = \xi_R$ implies that $\Psi_e(\xi, t)$ is generated with energy

$$E_e(t) \approx E_e = V_g(\xi_R) + \hbar\omega_{\text{pump}} = V_e(\xi_R), \qquad (8)$$

which remains approximately constant during the time window between the pump and dump sub-pulses. The strong force of the steep repulsive wall of $V_e(\xi)$ close to $\xi = \xi_{\text{pump}} = \xi_R$ drives the wavepacket $\Psi_e(\xi, t)$ from R toward P. This is illustrated by the shift of the snapshot 'b' to 'c'. At the same time, the wavefunction $\Psi_e(\xi, t)$ gains momentum directed from R to P, and corresponding kinetic energy. Approximate conservation of energy during the time window between the pump and dump laser pulses implies that the kinetic energy of $\Psi_e(\xi, t)$ is approximately equal to

$$E_e(t) - V_e(\xi) \approx V_e(\xi_R) - V_e(\xi), \qquad (9)$$

where ξ denotes the centre (mean value) of $\Psi_e(\xi, t)$.

Next, the second sub-pulse dumps $\Psi_e(\xi, t)$ back to $\Psi_g(\xi, t)$ in the ground state, again in a vertical FC-type manner, located at ξ_{dump} and applied at t_{dump}. The time delay $t_d = t_{\text{dump}} - t_{\text{pump}}$ between the pump and dump sub-pulses corresponds to the time that $\Psi_e(\xi, t)$ needs to run from $\xi_{\text{pump}} = \xi_R$ to ξ_{dump}. Also, the value of ξ_{dump}

determines the optimal transition frequency or photon energy $\hbar\omega_{\mathrm{dump}}$, according to eqn. (7). Finally, the time from t_{dump} to τ is essentially the time $\Psi_{\mathrm{g}}(\xi, t)$ needs to run from ξ_{dump} till ξ_{target}. The resulting wavepacket $\Psi_{\mathrm{g}}(\xi, t = \tau)$ is illustrated by the snapshot labelled 'd' embedded in $V_{\mathrm{g}}(\xi)$.

The preceding analysis thus leaves us with the task to determine the parameter ξ_{dump} of the dump sub-pulse, for comprehensive understanding of the entire optimal laser pulse. The solution is as follows: By its FC nature, the dump sub-pulse is not only vertical, conserving the nuclear position at ξ_{dump}, but it also conserves nuclear momentum and, therefore, kinetic energy, thus

$$\begin{aligned} V_{\mathrm{e}}(\xi_{\mathrm{R}}) - V_{\mathrm{e}}(\xi_{\mathrm{dump}}) &= E_{\mathrm{g}}(t_{\mathrm{dump}}) - V_{\mathrm{g}}(\xi_{\mathrm{dump}}) \\ &\approx E_{\mathrm{g}} - V_{\mathrm{g}}(\xi_{\mathrm{dump}}). \end{aligned} \tag{10}$$

For the given PES $V_{\mathrm{g}}(\xi)$ and $V_{\mathrm{e}}(\xi)$ of the model SBV, for the given initial and target wavefunctions, and for the given duration τ of the optimal laser pulse, the equation (10), combined with the previous ones (6) – (9), imposes the total energy (6) of the target wavefunction (5) as decisive contraint, which determines all the frequencies and the timing of the two pump and dump sub-pulses of the optimal laser pulse. The second equation (10) is based on approximate conservation of the total energy, during the time window from the dump sub-pulse till the end ($t = \tau$) of the optimal laser pulse.

Comparison of the laser driven wavefunction $\Psi_{\mathrm{g}}(\xi, \tau)$ and the target wave function $\Psi_{\mathrm{g,target}}(\xi)$ shows good but not perfect agreement; for the energies, locations, and shapes, see figure 2. As a consequence, the subsequent free evolution of $\Psi_{\mathrm{g}}(\xi, t)$ for $t > \tau$ is also similar to the free evolution of the target wavefunction, which has been adapted from, and which is documented in Reference 34. Snapshot 'e' shows the density of $\Psi_{\mathrm{g}}(t = t_{\mathrm{P}})$ on arrival at the product configuration P, i.e., when it is centred at ξ_{P}. As expected, it agrees almost perfectly with the corresponding snapshot of the product wavefunction which is shown in figure 1 of Reference 34.

As a summary, the optimal laser pulse $\mathcal{E}(t)$ shown in figure 3 fulfils its task, i.e., it initiates the Cope rearrangement of the model SBV in the electronic ground state so that the resulting wavepacket dynamics from R to P is similar to that of Reference 34. Close analysis reveals, however, that $\mathcal{E}(t)$ is not perfect. First of all, its pump sub-pulse does not achieve perfect population transfer from the electronic ground to the excited state. Figure 3 shows that the population which remains in $V_{\mathrm{g}}(\xi)$ is about $P_{\mathrm{g}}(t) \approx 0.08$, from $t \approx 3$ fs till 7 fs. As a consequence, $\Psi_{\mathrm{g}}(\xi, t)$ keeps a small partial wave which remains trapped in the reactant well of $V_{\mathrm{g}}(\xi)$. This partial wave is not an eigenstate, hence it exhibits non-stationary dynamics. This is visible in the time evolution of the small lobes of the densities $\rho_{\mathrm{g}}(\xi, t)$ labelled 'd' and 'e', close to $\xi = \xi_{\mathrm{R}}$. Similar effects of a pump pulse, called 'hole carving' in the ground state wavepacket, have been discovered first by Kosloff and coworkers.[77,78] Likewise, the dump sub-pulse does not achieve perfect population transfer from the excited electronic state back to the ground state. This is documented by the rather small but clearly non-vanishing densities $\rho_{\mathrm{e}}(\xi, t)$ labelled 'd' and 'e', embedded in $V_{\mathrm{e}}(\xi)$, see figure 2. These deficiencies could possibly be eliminated by even larger field strength, but in practice, this is prohibitive due to competing effects such as excitations of higher electronic states, or ionization.

4. Conclusions

The present model investigation confirms the general experimental result of Reference 5, which has served as first, general motivation, i.e., pericyclic reactions in the electronic ground state may be induced by laser pulses in the visible to UV frequency and sub-10-fs time domains. OCT yields a down-chirped intra-pulse pump-dump mechanism as the most efficient approach towards this goal. The two pump and dump sub-pulses induce resonant FC-type transitions, from the ground to the electronic excited state, and back, with optimal time delay. In contrast, Reference 5 employs non-resonant sub-pulses. The present results suggest that the efficiency of the experiment may be enhanced by means of properly chirped resonant ones. In any case, the sub-pulses of Reference 5 and the present one are few (one to two) cycle pulses, with corresponding broad spectral ranges (approximately 1 eV). This supports the rather flexible generation of suitable time-dependent nuclear wavepackets, which may consist of several vibrational eigenstates, first in the excited electronic state and subsequently in the electronic ground state, as documented in figure 2.

The intrapulse pump–dump mechanism of the present optimal laser pulse is somewhat analogous to the original pump-dump mechanism of Tannor and Rice[6,9,10], but there are important differences: Their motivation has been laser control of photodissociations towards competing product channels; they were able to achieve this goal by means of OCT in the weak field limit, at the expense of rather low product yields.[6] In contrast, we aim at a new task of laser control (compare e.g., with References 79, 80) that is initiation of a unimolecular reaction, exclusively in the electronic ground state, and with perfect product yield. For this

purpose, we have to employ OCT in the strong field limit.[7,8] The analysis of the mechanism in section 3 suggests to design analytical laser pulses e.g., with Gaussian envelopes and similar frequencies, durations and time delay, lending themselves more easily to experimental applications than those obtained by means of OCT. In any case, the present laser pulse is complementary to previous down-chirped intra-pulse pump-dump laser pulses which serve different purposes, e.g., to induce large amplitude vibrations in the electronic ground state[81,82], or control of branching ratios and photodesorption yields.[83]

The present results are encouraging also concerning the second, specific motivation, that means to pave the way towards experimental monitoring the electronic fluxes during the Cope rearrangement of SBV in the electronic ground state, as predicted in Reference 34, cf. figure 1. At the same time, it calls for several extensions, e.g., the present empirical potential $V_e(\xi)$ of the electronic excited state should be replaced by quantum chemical *ab initio* calculations, and the simple 1D model should be replaced by a multi-dimensional one. For example, the forces of the PES in the electronic excited state V_e, and subsequently also in the ground state V_g, may possibly (but not neccessarily, depending on the system) drive the wavepackets $\Psi_e(t)$ and subsequently also $\Psi_g(t)$ away from the ideal 'short-cut' along ξ – this may cause excitations of several vibrational modes in the product P, as observed in Reference 5; for an early, illuminating discussion of the relations of potential energy surfaces and molecular reaction dynamics, see e.g., Reference 84. In order to suppress these competing channels, one may employ the tools of Reference 85, compare with Reference 86.

Another challenge is perfect suppression of any partial wave $\Psi_e(t)$ which 'survives' in the electronic excited state, after the optimal laser pulse. This task is motivated by the work of the group of Takatsuka *et al.*[87–89], which implies that the interplay of the ground state wave function $\Psi_g(t)$ with even just a small component of $\Psi_e(t)$ might have a rather strong effect on the results for the net electronic fluxes from R to P in the electronic ground state. This task may be supported by model systems with shallower PES V_e in the electronic excited case, supporting perfect generation and subsequent annihilation of slower wavepackets $\Psi_e(t)$ by means of longer and less intense pump and dump sub-pulses. Alternatively, following a suggestion of Prof. W Jakubetz (Universität Wien), one might employ another laser pulse which eliminates any remaining components of $\Psi_e(t)$, by means of state-(e)-selective photoionization.

Work along these lines is in progress.

Acknowledgements

We would like to thank Professor W Jakubetz (Universität Wien) for stimulating discusssions of the present OCT results, and to Professor B Paulus (Freie Universität Berlin) for helpful advice on the underlying applications of the quantum chemistry, and to Dr. M Schröder (Universität Heidelberg) for advice on the OCT implementation in the MCTDH program package. Generous financial support by the Deutsche Forschungsgemeinschaft DFG, project Ma515/25-1, and by the Fonds der Chemischen Industrie FCI are also gratefully acknowledged.

References

1. Schwebel A, Brestel M and Yogev A 1984 *Chem. Phys. Lett*. **107** 579
2. Dohle M, Manz J and Paramonov G K 1995 *Ber. Bunsenges. Phys. Chem*. **99** 478
3. Dohle M, Manz J, Paramonov G K and Quast H 1995 *Chem. Phys*. **197** 91
4. Korolkov M V, Manz J and Paramonov G K 1996 *J. Chem. Phys*. **105** 10874
5. Iwakura I, Yabushita A and Kobayashi T 2010 *Chem. Lett*. **39** 374
6. Tannor D J and Rice S A 1985 *J. Chem. Phys*. **83** 5013
7. Peirce A P, Dahleh M A and Rabitz H 1988 *Phys. Rev. A* **37** 4950
8. Jakubetz W, Manz J and Schreier H-J 1990 *Chem. Phys. Lett*. **165** 100
9. Rice S A and Zhao M 2000 *Optical Control of Molecular Dynamics* (John Wiley & Sons, New York)
10. Shapiro M and Brumer P 2003 *Principles of the quantum control of molecular processes* (Wiley, New Jersey)
11. Cope A C and Hardy E M 1940 *J. Am. Chem. Soc*. **62** 441
12. Zimmerman H E and Grunewald G L 1966 *J. Am. Chem. Soc*. **88** 183
13. Cheng A K, Anet F A L, Mioduski J and Meinwald J 1974 *J. Am. Chem. Soc*. **96** 2887
14. Martin H-D and Urbanek T 1985 *J. Am. Chem. Soc*. **107** 5532
15. Bergmann K, Görtler S, Manz J and Quast H 1993 *J. Am. Chem. Soc*. **115** 1490
16. Quast H, Herkert T, Witzel A, Peters E M, Peters K and von Schnering H G 1994 *Chem. Ber*. **127** 921
17. Williams R V and Kurtz H A 1994 *J. Chem. Soc. Perkin Trans. 2* **2** 147
18. Jiao H, Nagelkerke R, Kurtz H A, Williams R V, Borden W T and von Ragué Schleyer P 1997 *J. Am. Chem. Soc*. **119** 5921
19. Jackman L M, Fernandes E, Heubes M and Quast H 1998 *Eur. J. Org. Chem*. 2209
20. Quast H and Seefelder M 1999 *Angew. Chem. Int. Ed*. **38** 1064
21. Williams R V 2001 *Eur. J. Org. Chem*. 227
22. Williams R V 2001 *Chem. Rev*. **101** 1185
23. Staroverov V N and Davidson E R 2001 *J. Mol. Struct*. **573** 81

24. Goren A C, Hrovat D A, Seefelder M, Quast H and Borden W T 2002 *J. Am. Chem. Soc*. **124** 3469
25. Garavelli M, Bernardi F, Cembran A, Castaño O, Frutos L M, Merchán M and Olivucci M 2002 *J. Am. Chem. Soc*. **124** 13770
26. Brown E C, Henze D K, and Borden W T 2002 *J. Am. Chem. Soc*. **124** 14977
27. Seefelder M, Heubes M, Quast H, Edwards W D, Armantrout J R, Williams R V, Cramer C J, Goren A C, Hrovat D A, and Borden W T 2005 *J. Org. Chem*. **70** 3437
28. Shaik S S and Hiberty P C 2008 *A chemist's guide to valence bond theory* (Wiley, Hoboken)
29. Williams R V 2009 *Strained hydrocarbons* (Wiley, Weinheim) pp. 399–424
30. Brown E C, Bader R F W and Werstiuk N H 2009 *J. Phys. Chem. A* **113** 5254
31. Greve D R 2010 *J. Phys. Org. Chem*. **24** 222
32. Rozgonyi T, Bartók-Pártay A and Stirling A 2010 *J. Phys. Chem. A* **114** 1207
33. Zhang X, Hrovat D A and Borden W T 2010 *Org. Lett*. **12** 2798
34. Andrae D, Barth I, Bredtmann T, Hege H-C, Manz J, Marquardt F and Paulus B 2011 *J. Phys. Chem. B* **115** 5476
35. Dewar M J S 1984 *J. Am. Chem. Soc*. **106** 209
36. Desimoni G, Tacconi G, Barco A and Pollini G P 2007 *Natural products synthesis through pericyclic reactions* (American Chemical Society, Washington, DC)
37. Berson J A 1980 *Rearrangements in ground and excited states, Vol. 1* (Academic Press, New York) p. 311
38. Lowry T H and Richardson K S 1987 *Mechanism and theory in organic Chemistry* (Harper and Row, New York)
39. Anslyn E V and Dougherty D A 2006 *Modern physical organic chemistry* (University Science Books, Sausalito)
40. Smith M B and March J 2007 *Advanced organic chemistry reactions, mechanisms, and structure* (Wiley, Hoboken)
41. Vollhardt K P C and Schore N E 2007 *Organic chemistry – structure and function* (Freeman, New York)
42. Wilkins R G 1991 *Kinetics and mechanism of reactions of transition metal complexes* (Verlag Chemie, Weinheim)
43. Jordan R B 2007 *Reaction mechanisms of inorganic and organometallic systems* (Oxford University Press, Oxford)
44. Mathews C K, van Holde K E and Ahern K G 1999 *Biochemistry* (Prentice Hall, Upper Saddle River)
45. Nelson D L and Cox M M 2009 *Lehninger principles of biochemistry* (Freeman, New York)
46. Borden W T, Loncharich R J, and Houk K N 1988 *Ann. Rev. Phys. Chem*. **39** 213
47. Xu L, Doubleday C E and Houk K N 2010 *J. Am. Chem. Soc*. **132** 3029
48. McFarland B K, Farrell J P, Bucksbaum P H and Gühr M 2008 *Science* **322** 1232
49. Bisgaard C Z, Clarkin O J, Wu G, Lee A M D, Geßner O, Hayden C C and Stolow A 2009 *Science* **323** 1464
50. Wörner H J, Bertrand J B, Kartashov D V, Corkum P B and Villeneuve D M 2010 *Nature* **466** 604
51. Goulielmakis E, Loh Z-H, Wirth A, Santra R, Rohringer N, Yakovlev V S, Zherebtsov S, Pfeifer T, Azzeer A M, Kling M F, Leone S R and Krausz F 2010 *Nature* **466** 739
52. Ben-Nun M, Martínez T J, Weber P M and Wilson K R 1996 *Chem. Phys. Lett*. **262** 405
53. Niikura H, Villeneuve D M and Corkum P B 2005 *Phys. Rev. Lett*. **94** 083003
54. Chelkowski S, Yudin G L and Bandrauk A D 2006 *J. Phys. B* **39** S409
55. Debnarova A, Techert S, and Schmatz S 2006 *J. Chem. Phys*. **125** 224101
56. Schweigert I V and Mukamel S 2007 *Phys. Rev. A* **76** 012504
57. Mukamel S, Abramavicius D, Yang L, Zhuang W, Schweigert I V and Voronine D V 2009 *Acc. Chem. Res*. **42** 553
58. Smirnova O, Mairesse Y, Patchkovskii S, Dudovich N, Villeneuve D, Corkum P and Ivanov M Y 2009 *Nature* **460** 972
59. Baum P and Zewail A H 2009 *Chem. Phys*. **366** 2
60. Debnarova A, Techert S and Schmatz S 2010 *J. Chem. Phys*. **133** 124309
61. Krausz F and Ivanov M 2009 *Rev. Mod. Phys*. **81** 163
62. Werner H-J, Knowles P J, Manby F R, Schütz M, Celani P, Knizia G, Korona T, Lindh R, Mitrushenkov A, Rauhut G, Adler T B, Amos R D, Bernhardsson A, Berning A, Cooper D L, Deegan M J O, Dobbyn A J, Eckert F, Goll E, Hampel C, Hesselmann A, Hetzer G, Hrenar T, Jansen G, Köppl C, Liu Y, Lloyd A W, Mata R A, May A J, McNicholas S J, Meyer W, Mura M E, Nicklass A, Palmieri P, Pflüger K, Pitzer R, Reiher M, Shiozaki T, Stoll H, Stone A J, Tarroni R, Thorsteinsson T, Wang M and Wolf A 2010 *Molpro, version 2010.1, a package of ab initio programs*, see http://www.molpro.net
63. Becke A. D 1993 *J. Chem. Phys*. **98** 5648
64. Lee C, Yang W and Parr R G 1998 *Phys. Rev. B* **37** 785
65. Dunning T H 1989 *J. Chem. Phys*. **90** 1007
66. Stapelfeldt H and Seideman T 2003 *Rev. Mod. Phys*. **75** 543
67. Leibscher M, Averbukh I S and Rabitz H 2003 *Phys. Rev. Lett*. **90** 213001
68. Leibscher M, Averbukh I S and Rabitz H 2004 *Phys. Rev. A*. **69** 013402
69. Seideman T and Hamilton E 2006 *Adv. At. Mol. Opt. Phys*. **52** 289
70. Worth G A, Beck M H, Jäckle A and Meyer H-D 2007 The MCTDH Package, Version 8.2, (2000). H-D Meyer, Version 8.3 (2002), Version 8.4. See http://mctdh.uni-hd.de
71. Wang L, Meyer H-D and May V 2006 *J. Chem. Phys*. **125** 014102
72. Schröder M, Carreón-Macedo J L, and Brown A 2008 *Phys. Chem. Chem. Phys*. **10** 850
73. Combes J M, Grossmann A and Tchamitchian P 1989 *Wavelets* (Springer-Verlag, Berlin)
74. Chandre C, Wiggins S and Uzer T 2003 *Physica D* **181** 171
75. Milošević D B, Paulus G G, Bauer D and Becker W 2006 *J. Phys. B.: At. Mol. Opt. Phys*. **39** R203
76. Bandrauk A D, Chelkowski S and Shon N. H 2002 *Phys. Rev. Lett*. **89** 283903

77. Hartke B, Kosloff R and Ruhman S 1989 *Chem. Phys. Lett*. **158** 238
78. Banin U, Bartana A, Ruhman S and Kosloff R 1994 *J. Chem. Phys*. **101** 8461
79. Sathyamurthy N 1992 *Lasers in chemical and biological sciences* (Wiley Eastern, New Delhi) pp. 19–29
80. Kühn O and Wöste L (eds) *Analysis and control of ultrafast photoinduced reactions*, (Springer-Verlag Berlin)
81. Ruhman S and Kosloff R 1990 *J. Opt. Soc. Am. B* **7**, 1748
82. Cerullo G, Bardeen C J, Wang Q and Shank C V 1996 *Chem. Phys. Lett*. **262** 1362
83. Mishima K and Yamashita K 1999 *J. Chem. Phys*. **110** 7756
84. Sathyamurthy N and Joseph T 1984 *J. Chem. Edu*. **61** 968
85. Belz S, Grohmann T and Leibscher M 2009 *J. Chem. Phys*. **131** 034305
86. Deeb O, Leibscher M, Manz J, von Muellern W and Seideman T 2007 *ChemPhysChem* **8** 322
87. Nagashima K and Takatsuka K 2009 *J. Phys. Chem. A* **113** 15240
88. Yonehara T and Takatsuka K 2009 *Chem. Phys*. **366** 115
89. Okuyama M and Takatsuka K 2009 *Chem. Phys. Lett*. **476** 109

3.1.3 T. Bredtmann*, J. Manz*, Electronic Bond-to-Bond Fluxes in Pericyclic Reactions: Synchronous or Asynchronous? Angew. Chem. Int. Ed., 50, 12652-12654 (2011)

T. Bredtmann*, J. Manz*,
Electronic Bond-to-Bond Fluxes in Pericyclic Reactions: Synchronous or Asynchronous?
Angew. Chem. Int. Ed., **50**, 12652-12654 (2011).

DOI: 10.1002/anie.201104465
URL: http://dx.doi.org/DOI: 10.1002/anie.201104465

T. Bredtmann*, J. Manz*,
Electronic Bond-to-Bond Fluxes in Pericyclic Reactions: Synchronous or Asynchronous?
Angew. Chem. Int. Ed., **50**, 12652-12654 (2011).

DOI: 10.1002/anie.201104465
URL: http://dx.doi.org/DOI: 10.1002/anie.201104465

T. Bredtmann*, J. Manz*,
Electronic Bond-to-Bond Fluxes in Pericyclic Reactions: Synchronous or Asynchronous?
Angew. Chem. Int. Ed., **50**, 12652-12654 (2011).

DOI: 10.1002/anie.201104465
URL: http://dx.doi.org/DOI: 10.1002/anie.201104465

3.1.4 T. Bredtmann*, H. Kono, J. Manz*, K. Nakamura*, C. Stemmle, Nuclear Flux Densities during a Model Pericyclic Reaction with Energies Well Above and Below the Potential Barrier, ChemPhysChem, 14, 1397-1404 (2013)

T. Bredtmann*, H. Kono, J. Manz*, K. Nakamura*, C. Stemmle,
Nuclear Flux Densities during a Model Pericyclic Reaction with Energies Well Above and Below the Potential Barrier,
ChemPhysChem, **14**, 1397-1404 (2013).

DOI: 10.1002/cphc.201200943
URL: http://dx.doi.org/10.1002/cphc.201200943

T. Bredtmann*, H. Kono, J. Manz*, K. Nakamura*, C. Stemmle,
Nuclear Flux Densities during a Model Pericyclic Reaction with Energies Well Above and Below the Potential Barrier,
ChemPhysChem, **14**, 1397-1404 (2013).

DOI: 10.1002/cphc.201200943
URL: http://dx.doi.org/10.1002/cphc.201200943

T. Bredtmann*, H. Kono, J. Manz*, K. Nakamura*, C. Stemmle,
Nuclear Flux Densities during a Model Pericyclic Reaction with Energies Well Above and Below the Potential Barrier,
ChemPhysChem, **14**, 1397-1404 (2013).

DOI: 10.1002/cphc.201200943
URL: http://dx.doi.org/10.1002/cphc.201200943

T. Bredtmann*, H. Kono, J. Manz*, K. Nakamura*, C. Stemmle,
Nuclear Flux Densities during a Model Pericyclic Reaction with Energies Well Above and Below the Potential Barrier,
ChemPhysChem, **14**, 1397-1404 (2013).

DOI: 10.1002/cphc.201200943
URL: http://dx.doi.org/10.1002/cphc.201200943

T. Bredtmann*, H. Kono, J. Manz*, K. Nakamura*, C. Stemmle,
Nuclear Flux Densities during a Model Pericyclic Reaction with Energies Well Above and Below the Potential Barrier,
ChemPhysChem, **14**, 1397-1404 (2013).

DOI: 10.1002/cphc.201200943
URL: http://dx.doi.org/10.1002/cphc.201200943

T. Bredtmann*, H. Kono, J. Manz*, K. Nakamura*, C. Stemmle,
Nuclear Flux Densities during a Model Pericyclic Reaction with Energies Well Above and Below the Potential Barrier,
ChemPhysChem, **14**, 1397-1404 (2013).

DOI: 10.1002/cphc.201200943
URL: http://dx.doi.org/10.1002/cphc.201200943

T. Bredtmann*, H. Kono, J. Manz*, K. Nakamura*, C. Stemmle,
Nuclear Flux Densities during a Model Pericyclic Reaction with Energies Well Above and Below the Potential Barrier,
ChemPhysChem, **14**, 1397-1404 (2013).

DOI: 10.1002/cphc.201200943
URL: http://dx.doi.org/10.1002/cphc.201200943

T. Bredtmann*, H. Kono, J. Manz*, K. Nakamura*, C. Stemmle,
Nuclear Flux Densities during a Model Pericyclic Reaction with Energies Well Above and Below the Potential Barrier,
ChemPhysChem, **14**, 1397-1404 (2013).

DOI: 10.1002/cphc.201200943
URL: http://dx.doi.org/10.1002/cphc.201200943

3.1.5 T. Bredtmann*, B. Paulus, Electron-Nuclear Motion in the Cope Rearrangement of Semibullvalene: Ever Synchronous? J. Chem. Theor. Comp., 9, 3026–3034 (2013)

T. Bredtmann*, B. Paulus,
Electron-Nuclear Motion in the Cope Rearrangement of Semibullvalene: Ever Synchronous?
J. Chem. Theor. Comp., **9**, 3026–3034 (2013).

DOI: 10.1021/ct400318z
URL: http://dx.doi.org/10.1021/ct400318z

T. Bredtmann*, B. Paulus,
Electron-Nuclear Motion in the Cope Rearrangement of Semibullvalene: Ever Synchronous?
J. Chem. Theor. Comp., **9**, 3026–3034 (2013).

DOI: 10.1021/ct400318z
URL: http://dx.doi.org/10.1021/ct400318z

T. Bredtmann*, B. Paulus,
Electron-Nuclear Motion in the Cope Rearrangement of Semibullvalene: Ever Synchronous?
J. Chem. Theor. Comp., **9**, 3026–3034 (2013).

DOI: 10.1021/ct400318z
URL: http://dx.doi.org/10.1021/ct400318z

T. Bredtmann*, B. Paulus,
Electron-Nuclear Motion in the Cope Rearrangement of Semibullvalene: Ever Synchronous?
J. Chem. Theor. Comp., **9**, 3026–3034 (2013).

DOI: 10.1021/ct400318z
URL: http://dx.doi.org/10.1021/ct400318z

T. Bredtmann*, B. Paulus,
Electron-Nuclear Motion in the Cope Rearrangement of Semibullvalene: Ever Synchronous?
J. Chem. Theor. Comp., **9**, 3026–3034 (2013).

DOI: 10.1021/ct400318z
URL: http://dx.doi.org/10.1021/ct400318z

T. Bredtmann*, B. Paulus,
Electron-Nuclear Motion in the Cope Rearrangement of Semibullvalene: Ever Synchronous?
J. Chem. Theor. Comp., **9**, 3026–3034 (2013).

DOI: 10.1021/ct400318z
URL: http://dx.doi.org/10.1021/ct400318z

T. Bredtmann*, B. Paulus,
Electron-Nuclear Motion in the Cope Rearrangement of Semibullvalene: Ever Synchronous?
J. Chem. Theor. Comp., **9**, 3026–3034 (2013).

DOI: 10.1021/ct400318z
URL: http://dx.doi.org/10.1021/ct400318z

T. Bredtmann*, B. Paulus,
Electron-Nuclear Motion in the Cope Rearrangement of Semibullvalene: Ever Synchronous?
J. Chem. Theor. Comp., **9**, 3026–3034 (2013).

DOI: 10.1021/ct400318z
URL: http://dx.doi.org/10.1021/ct400318z

T. Bredtmann*, B. Paulus,
Electron-Nuclear Motion in the Cope Rearrangement of Semibullvalene: Ever Synchronous?
J. Chem. Theor. Comp., **9**, 3026–3034 (2013).

DOI: 10.1021/ct400318z
URL: http://dx.doi.org/10.1021/ct400318z

3.1.5.1 Supporting Information

T. Bredtmann*, B. Paulus,
Electron-Nuclear Motion in the Cope Rearrangement of Semibullvalene: Ever Synchronous?
J. Chem. Theor. Comp., **9**, 3026–3034 (2013).

DOI: 10.1021/ct400318z
URL: http://dx.doi.org/10.1021/ct400318z

T. Bredtmann*, B. Paulus,
Electron-Nuclear Motion in the Cope Rearrangement of Semibullvalene: Ever Synchronous?
J. Chem. Theor. Comp., **9**, 3026–3034 (2013).

DOI: 10.1021/ct400318z
URL: http://dx.doi.org/10.1021/ct400318z

T. Bredtmann*, B. Paulus,
Electron-Nuclear Motion in the Cope Rearrangement of Semibullvalene: Ever Synchronous?
J. Chem. Theor. Comp., **9**, 3026–3034 (2013).

DOI: 10.1021/ct400318z
URL: http://dx.doi.org/10.1021/ct400318z

T. Bredtmann*, B. Paulus,
Electron-Nuclear Motion in the Cope Rearrangement of Semibullvalene: Ever Synchronous?
J. Chem. Theor. Comp., **9**, 3026–3034 (2013).

DOI: 10.1021/ct400318z
URL: http://dx.doi.org/10.1021/ct400318z

3.2 Second Part: Analysis of Electronic Fluxes and Nuclear Flux Densities in Experimentally Readily Accessible Molecular Systems

3.2.1 T. Bredtmann*, E. Hupf, B. Paulus, Electronic Fluxes during Large Amplitude Vibrations of Single, Double and Triple Bonds, Phys. Chem. Chem. Phys., 14, 15494-15501 (2012)

Time-Dependent Analysis of Single, Double and Triple Bonds Performing Large Amplitude Vibrations in Terms of Electronic Fluxes

Timm Bredtmann,* Emanuel Hupf,† and Beate Paulus

Physikalisch und Theoretische Chemie,

Institut für Chemie und Biochemie, Freie Universität Berlin,

Takustr. 3, 14195 Berlin, Germany

Abstract

We present a time-dependent quantum mechanical analysis of ethane, ethene and ethine performing large amplitude vibrations in the electronic ground state in terms of electronic fluxes. We find that in general most electrons participate in the concerted electron-nuclear vibrations in the case of ethane followed by ethene and ethine. This counter-intuitive result is due to similar electron distributions of single, double and triple bonds along the carbon-carbon (CC)-axis at equal CC-distances. Different initial conditions and different sets of "observer planes" which monitor the electronic rearrangement are tested to demonstrate the robustness of the results. These predictions should stimulate emerging experiments using techniques of femto- to attosecond time-resolved spectroscopy.

*bredt@chemie.fu-berlin.de

†Institut für Anorganische und Physikalische Chemie, Universität Bremen, Leobener Str. NW2, 28359 Bremen, Germany

INTRODUCTION

Chemical reactions and molecular vibrations involve the correlated motion of both nuclei and electrons. The real-time observation and control of the nuclear dynamics using ultrashort laser sources with pulse durations on the order of 10-100 femtoseconds (fs, $1\text{fs} = 10^{-15}\text{s}$) constitutes the established field of *Femtochemistry*, pioneered by A. H. Zewail and co-workers [1], see also [2, 3]. More recently, new ultrashort pulse technologies, e.g. time-resolved photoelectron spectroscopy [4], time-resolved X-ray spectroscopy [5], high harmonic spectroscopy [6–9], also enabled monitoring changes of the electronic structure in real-time. These changes might roughly be divided into two regimes: On the one hand, multi-state electron dynamics, i.e. preparation of the atomic or molecular systems at sufficiently high energies allowing electronic transitions, leads to electronic motion on the attosecond (as, $1\text{as} = 10^{-18}\,\text{s}$) timescale which has recently been studied both experimentally and theoretically, see e.g. Refs. [8, 10, 11] and [10, 12–18], respectively. On the other hand, single-state electron dynamics, i.e. the collective rearrangement of both electrons and nuclei involving non-degenerate electronic quantum states proceeds on the femtosecond time scale of nuclear motion, see e.g. Refs. [19–21] and Refs. therein, which is the regime investigated in this study. More specifically, we analyze and compare the time-dependent rearrangement of the electronic structure of a single, double and triple bond performing large amplitude vibrations in the electronic ground state, exemplified by vibrating ethane, ethene and ethine. The present study is partly motivated by recent experiments on one of the compounds investigated here (ethane), which involved measurements of the multi-state electron dynamics on attosecond time scale using High Harmonic Generation [8], and should stimulate corresponding experimental investigations in the regime of single-state ground state electron dynamics.

For several decades, calculations of nuclear quantum fluxes through a dividing surface which separates the domains associated with reactants and products are used for ab-initio calculations of chemical reaction rates [22–26]. Only recently, two complementary methods for the calculation of electron-nuclear fluxes have been proposed: Takatsuka and co-workers focus on multi-state electron dynamics using semiclassical Ehrenfest dynamics for the nuclear motion coupled to quantum electronic fluxes [15–17, 27]. In our group, Manz and co-workers, including two of the authors (T.B. and B.P), investigated electron-nuclear fluxes in the non-

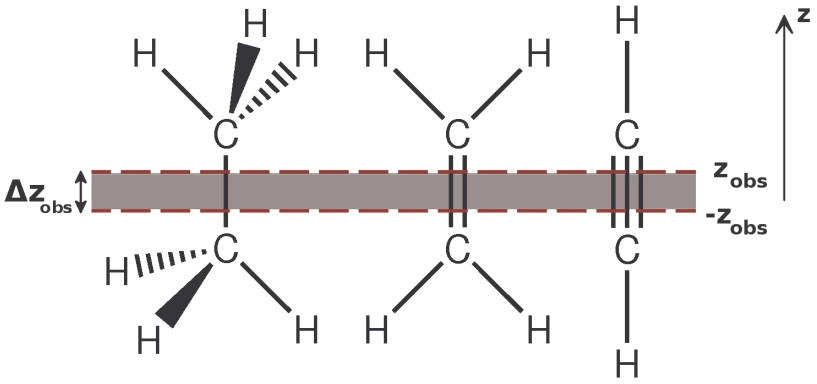

Figure 1. Lewis structures of ethane, ethene and ethine with sketches of observer planes for electronic movement shown by red dashed lines, oriented perpendicular to the carbon-carbon (CC)-axis at symmetric positions $\pm z_{\mathrm{obs}}$ above and below the respective center of mass (COM). The origin of the coordinate system is chosen as the COM and the molecules are assumed to be oriented along the z-axis which coincides with the CC-axis.

degenerate electronic ground state using the quantum method developed in Ref. [19] which is also the method used in this study, for recent applications to molecular vibrations and chemical reactions see e.g. Refs. [19, 20] and [21, 28], respectively. Here, we extend the former investigations on molecular vibrations which focused on the one and two electron systems H_2^+ and H_2 and their heavier isotopes to larger molecular systems presenting different kinds of chemical bonding. We calculate the number of electrons which cross certain planes situated within the molecules (electronic observer planes) per time (electronic fluxes) and the corresponding overall number of electrons that cross these observers within a certain time range, e.g. one vibrational period (time-integrated electronic fluxes or electronic yields). Figure 1 shows the three compounds under investigation with the corresponding electronic observer planes shown as red dashed horizontal lines. Based on the respective Lewis structures, one expects the largest electron localization between the carbon-atoms and hence the largest electronic flux and electronic yield in the case of the triple bond. These predictions, based on chemical intuition, will be compared to the quantum results and the robustness of the results will be tested by systematic variation of the electronic observer planes and the initial conditions.

THEORY AND METHODS

We describe the coupled electronic and nuclear movement of vibrating ethane, ethene and ethine in the electronic ground state quantum mechanically within the framework of the Born-Oppenheimer (BO) Approximation [29–31]. Consequently, the molecular wavefunction is approximated as

$$\Psi_n(\mathbf{q}, \mathbf{Q}, t) = \chi_n(\mathbf{Q}, t)\Phi_n(\mathbf{q}; \mathbf{Q}), \tag{1}$$

where $n = 1, 2, 3$ denotes the wavefunction for ethine, ethene and ethane, respectively. The coordinates $\mathbf{q}$ and $\mathbf{Q}$ collectively denote the spatial and spin coordinates of the N electrons, $\mathbf{q}_i = \{\mathbf{r}_i, \sigma_i\}$ $(i = 1, \ldots, N)$ and the M nuclei, $\mathbf{Q}_A = \{\mathbf{R}_A, \Sigma_A\}$ $(A = 1, \ldots, M)$. In this adiabatic approximation, the nuclear wavefunction, $\chi_n(\mathbf{Q}, t)$, depends explicitly on time and the electronic wavefunction, $\Phi_n(\mathbf{q}; \mathbf{Q})$, depends parametrically on the nuclear coordinates, which allows the separate treatment of the electronic and nuclear degrees of freedom.

The electronic wavefunction, $\Phi_n(\mathbf{q}; \mathbf{Q})$, is calculated as approximate solution of the time independent electronic Schrödinger equation

$$\hat{H}_{\mathrm{el},n}(\mathbf{r}; \mathbf{R})\Phi_n(\mathbf{q}; \mathbf{Q}) = V_n(\mathbf{R})\Phi_n(\mathbf{q}; \mathbf{Q}) \tag{2}$$

using the MRCISD method [32, 33] with a CASSCF [34, 35] reference function. The calculations are performed with the MOLPRO [36] program package using the cc-pVTZ [37] basis-sets. The chosen active space in the CASSCF calculations allows a description of the homolytic dissociation of the respective bonds. Hence, for ethane two active electrons are placed in overall two active σ and σ^* orbitals (CAS[2,2]), for ethene two electrons and two orbitals (π and π^*) are added (CAS[4,4]) and for ethine another two electrons and two orbitals (π and π^*) are added (CAS[6,6]). The computed carbon-carbon (CC)-distances agree within an accuracy of 10^{-2} Å with the experimental results, for a comparison see Table I.

In this study, we treat the nuclear dynamics in reduced dimensionality, with the distance of the respective CH_n fragments being the only nuclear degree of freedom considered, which will be denoted as ξ in the following. Hence, the time evolution of the respective nuclear wavefunctions is given as solution of the time-dependent nuclear Schrödinger equation

$$i\hbar\frac{\partial}{\partial t}\chi_n(\xi, t) = -\frac{\hbar^2}{2\mu_n}\frac{\partial^2}{\partial\xi^2}\chi_n(\xi, t) + V_n(\xi)\chi_n(\xi, t), \tag{3}$$

	Scenario I					Scenario II				
ξ_0^n	$\langle\xi\rangle^n(t=0)$	$\langle\xi\rangle^n(t=t_{\rm tp}^n)$	A^n	$T_{\rm vib}^n$	$\bar{E}^n$	$\langle\xi\rangle^n(t=0)$	$\langle\xi\rangle^n(t=t_{\rm tp}^n)$	A^n	$T_{\rm vib}^n$	$\bar{E}^n$
Ethane 1.53 (1.53)	2.38	1.26	1.12	49.4	3.06	1.86	1.34	0.52	36.4	0.95
Ethene 1.34 (1.34)	1.83	1.11	0.72	27.8	3.09	1.67	1.15	0.52	12.6	1.85
Ethine 1.19 (1.19)	1.54	1.02	0.52	18.8	3.13	1.54	1.02	0.52	18.8	3.13

Table I. Equilibrium positions ξ_0^n (in Å, experimental values from Ref. [38] given in brackets) and details of the nuclear quantum dynamics for scenario I and II, cf. Figure 2(a): mean Carbon-Carbon distance at the starting point $\langle\xi\rangle^n(t=0)$ and at the first turning point $\langle\xi\rangle^n(t=t_{\rm tp})^n$ with associated amplitude of vibration A^n (in Å), vibrational period $T_{\rm vib}^n$ of the first vibration (in fs) and mean total energies $\bar{E}^n$ (in eV).

where the dependence on nuclear spin was dropped since it does not influence the dynamics in this study. Figure 2(a) shows the individual potential energy curves (PEC) as a function of the CC-distance. The reduced masses are given by $\mu_n = \frac{(M_C+nM_H)^2}{2(M_C+nM_H)}$, where M_C and M_H denote the nuclear mass of a carbon and a hydrogen atom, respectively. The calculations are carried out by means of the WavePacket [39] program on a set of 512 spatial grid points ranging from $\xi_{\rm min} = 0.794\,$Å to $\xi_{\rm max} = 3.502\,$Å with step size $\Delta\xi = 0.0053\,$Å and time steps of $\Delta t = 0.01\,$fs. Two different sets of initial conditions are used in this work to analyze the electron dynamics of the three molecular systems in terms of electronic fluxes, henceforth referred to as scenario I and II and illustrated in Figure 2: In scenario I, all systems are excited by the same amount of energy, i.e. the initial nuclear wave packet, $\chi_n(\xi, t=0)$, is the ground state of the respective PEC, whose center, defined by $\langle\xi\rangle^n(t) = \int \chi_n^*(\xi,t)\xi\chi_n(\xi,t)d\xi$, is displaced in the same PEC to $\langle\xi\rangle^n(t=0)$ in the direction of increasing bond distances such that the mean total energy is given by $\bar{E}^n = E_{\rm GS}^n + E_{\rm ex}$, where $E_{\rm GS}^n$ is the mean energy of the respective ground state (including the zero point energy) and $E_{\rm ex} = 3\,$eV is the common excitation energy for ethane, ethene and ethine. The initial nuclear wave packets at time $t=0$ and at times $t = t_{\rm tp}^n$ when the center of the respective wave packet reaches the inner turning point for the first time, is illustrated in the left panel of Figure 2(a), see also Table I for a list of the respective parameters.

In scenario II, the displacements and corresponding excitation energies are chosen such that all systems exhibit equal amplitudes of vibration, $A^n = \langle\xi\rangle^n(t=0) - \langle\xi\rangle^n(t=t_{\rm tp}^n)$,

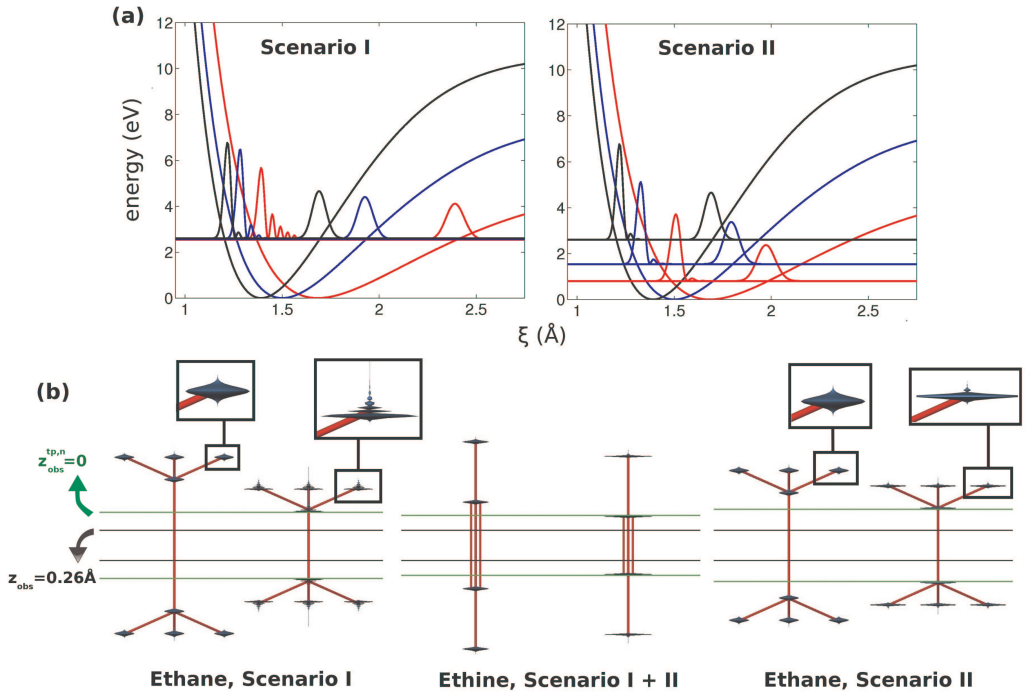

Figure 2. (a) Potential energy curves of ethane (red), ethene (blue) and ethine (black) calculated at the MRCISD/cc-pVTZ level and shown as a function of the internuclear carbon - carbon distance including snapshots of the respective nuclear wave packets at the outer starting point and at the first inner turning point, with baseline at the respective mean total energies, $\bar{E}^n$. Two sets of initial conditions are used in this study: In scenario I (left panel), the same amount of energy, $E_{\rm ex} = 3\,{\rm eV}$, added to the respective zero point energies, is used to excite each of the systems. In scenario II (right panel), the excitation energy of ethane and ethene are decreased such that all molecules show the same amplitude of vibration, see Table I for a summary of the nuclear dynamics. (b) Snapshots of the nuclear quantum dynamics including Lewis structures at the starting and first turning point for ethane with initial conditions corresponding to scenario I (left panel) and to scenario II (right panel) and for ethine (middle panel, scenario I + II). The magnitude of the respective nuclear densities, shown in Figure 2(a), is proportional to the rotationally symmetric shape, also shown as blow-ups for ethane, centered in the respective nuclei and oriented along the z-axis. Also shown is one example of "laboratory fixed" observers for electronic motion, which are characterized by their distance to the COM $z_{\rm obs}$, as black horizontal lines for $z_{\rm obs} = 0.26\,$Å, and one set of "molecular fixed" observers, characterized by their distance $z_{\rm obs}^{{\rm tp},n}$ to the respective turning points, shown as green horizontal lines with position $z_{\rm obs}^{{\rm tp},n} = 0$. The program Amira [40] is used for data visualization.

chosen as the amplitude of ethine in scenario I and illustrated in the right panel of Figure 2(a). For theoretical and experimental work on the initialization of small and large amplitude vibrations, see Refs. [41, 42] and [43, 44], respectively.

Following the method developed in Ref. [19], we calculate the electronic flux, $F_{\mathrm{obs},n}(t)$, out of or into a domain S_{obs} with volume V_{obs} through its boundary surface A_{obs} in terms of the time-dependent BO one-electron density

$$\rho_{\mathrm{el},n}(\mathbf{r},t) = \int d\xi |\chi_n(\xi,t)|^2 \tilde{\rho}_{\mathrm{el},n}(\mathbf{r};\xi) \tag{4}$$

with

$$\tilde{\rho}_{\mathrm{el},n}(\mathbf{r};\xi) = N \int \cdots \int |\Phi_n(\mathbf{q};\xi)|^2 d\sigma_1 d\mathbf{q}_2 \cdots d\mathbf{q}_N \tag{5}$$

as

$$F_{\mathrm{obs},n}(t) = \frac{d}{dt} \int_{V_{\mathrm{obs}}} \rho_{\mathrm{el},n}(\mathbf{r},t) dV = \frac{d}{dt} \bar{N}_{\mathrm{obs},n}(t), \tag{6}$$

where N denotes the total number of electrons in the molecular system and $\bar{N}_{\mathrm{obs},n}(t)$ the mean number of electrons in the volume V_{obs} at time t. A suitable observer domain for this study with associated boundaries A_{obs} (referred to as observer planes in the following) oriented perpendicular to the CC-axis at symmetric positions above and below the respective center of mass (COM) is shown in Figure 1 by the shaded area. Due to this symmetry, the electronic flux through either of the shown observer planes is of course the same and equals half the electronic flux out of the corresponding domain S_{obs}. The time integration of the electronic flux, eq. 6, gives the electronic yield

$$Y_{\mathrm{obs},n}(t) = \int_{V_{\mathrm{obs}}} dV \rho_{\mathrm{el},n}(\mathbf{r},t) - \int_{V_{\mathrm{obs}}} dV \rho_{\mathrm{el},n}(\mathbf{r},0), \tag{7}$$

which quantifies the number of electrons that flow out of or into the domain S_{obs} within a certain period of time, $[0,t]$. This method yields excellent agreement with exact, numerical solutions of the time-dependent Schrödinger equation without invoking the BO approximation for processes occurring in the electronic ground state as shown in Ref. [19].

For the subsequent discussion it is illuminating to express the electronic yield, eq. 7, in terms of time-dependent reduced electron densities along the CC-axis which is chosen to be the z-axis with the origin at the COM, cf. Figure 1, and are defined by

$$\rho_{\mathrm{el},n}(z,t) = \int \int \rho_{\mathrm{el},n}(\mathbf{r},t) dx dy. \tag{8}$$

Hence, the number of electrons that flow out of or into the domain S_{obs} with associated width Δz_{obs} along the CC-axis, cf. Figure 1, in terms of reduced densities is given by

$$\begin{aligned} Y_{\mathrm{obs},n}(t) &= \int_{-z_{obs}}^{z_{\mathrm{obs}}} \rho_{\mathrm{el},n}(z,t) - \int_{-z_{obs}}^{z_{\mathrm{obs}}} \rho_{\mathrm{el},n}(z,0) \\ &= \bar{N}_{\mathrm{obs},n}(t) - \bar{N}_{\mathrm{obs},n}(0), \end{aligned} \tag{9}$$

where $z_{\mathrm{obs}} = \frac{1}{2}\Delta z_{\mathrm{obs}}$ is the distance of the observer planes from the COM.

The time-independent one-electron densities, $\rho_{\mathrm{el}}(\mathbf{r};\xi)$, are evaluated by the same quantum chemistry first principle calculations described above on a spatial grid ($301\times301\times301$ points) centered at the respective COM with axis oriented along the respective CC-bond (z-axis) and orthogonal to it, cf. Figure 1. The equidistant step size is chosen as $\Delta x = \Delta y = \Delta z = 0.026\,\text{Å}$. The reduced electron densities along the CC-bond used to calculate the electronic yields, cf. eqs. (8) and (9), are interpolated using cubic splines.

RESULTS AND DISCUSSION

The aim of this study is the time-dependent quantum mechanical investigation of ethane, ethene and ethine performing large amplitude vibrations in terms of electronic fluxes. Such an analysis depends both on the initial conditions and on the position of the observer planes used to monitor the electron dynamics. Hence in order to analyze the robustness of the results, we use two different sets of initial conditions and two different sets of observer planes: Concerning the former, in scenario I, all systems are excited by the same amount of energy and in scenario II the excitation energy is chosen such that all molecular systems show the same amplitude of vibration. For the subsequent analysis of the electronic fluxes a comparison of the electronic structure at times when the systems show equal CC-distances will turn out to be useful. Hence, in scenario I the chosen excitation energy corresponds to the energy needed to stretch the ethine molecule from its equilibrium bond length to the equilibrium bond length of ethane. In scenario II, the excitation energy for ethine is kept constant, and the excitation energies for ethane and ethene are adapted such that all systems show identical amplitudes of vibration (right panel in Figure 2(a) and Table I). The nuclear dynamics for these two scenarios is illustrated in Figure 2(a) by snapshots of the wave packets at the outer starting point and at the first inner turning point, embedded in the

respective PEC as a function of the CC-distance with baselines at the corresponding mean total energies. We observe well known characteristics of nuclear wave packet dynamics such as increasing vibrational periods and increasing dispersion manifested in more pronounced quantum interferences at the inner turning point in the order ethane > ethene > ethine, see Table I for details.

To monitor the electronic motion, we use observer planes which are oriented perpendicular to the CC-axis, cf. Figure 1. In general, electronic fluxes are largest close to the nuclei since electron densities increase enormously in the vicinity of the nuclei. Hence, using the same "laboratory fixed" observers for all molecules, characterized by their distance z_{obs} from the COM, as illustrated by the black horizontal lines for $z_{\mathrm{obs}} = 0.26\,\text{Å}$ in Figure 2(b), is not well suited for a comparison of the electronic fluxes of different molecular systems, especially when the respective turning points of the nuclei are located at different distances from the COM, cf. Table I. Hence, for a proper comparison we introduce "molecular fixed" sets of observer planes which are characterized by their distance to the turning points of the respective carbon atoms, $z_{\mathrm{obs}}^{\mathrm{tp},n}$, as exemplified in Figure 2(b) by the horizontal green lines for $z_{\mathrm{obs}}^{\mathrm{tp},n} = 0$. Note that negative signs denoting the position of the "molecular fixed" observers ($z_{\mathrm{obs}}^{\mathrm{tp},n} < 0$) correspond to displacements in the direction of the COM. In the following, the results will be presented for both kinds of observer planes for various positions $z_{\mathrm{obs}}^{\mathrm{tp},n}$ and z_{obs}, with the results of the "laboratory fixed" observers meant to complement the comparison given by the "molecular fixed" observer planes. Finally note that the same wave packets shown in Figure 2(a) are also shown in Figures 2(b) by the rotationally symmetric shapes around the lines parallel to the respective CC-axis and centered at the carbon and hydrogen atoms.

We begin our discussion of the electronic fluxes with scenario I and the molecular fixed set of observer planes. The results are illustrated in the left panels of Figure 3. The top panel shows the electronic fluxes for $z_{\mathrm{obs}}^{\mathrm{tp},n} = 0$ for ethane (red), ethene (blue) and ethine (black) for the total electron density (solid lines) and the valence electron density (dashed lines), defined as $\rho_{\mathrm{val},n}(\mathbf{r},t) = \rho_{\mathrm{el},n}(\mathbf{r},t) - \rho_{\mathrm{core},n}(\mathbf{r},t)$, where $\rho_{\mathrm{core},n}(\mathbf{r},t)$ accounts for the 4 core electrons of the carbon atoms. Positive values of the electronic fluxes characterize electronic movement through the observers in the direction of the COM. In general, electronic and nuclear movement in the electronic ground state occurs synchronously and unidirectionally, possibly with minor deviations on the attosecond time scale, which are however insignificant

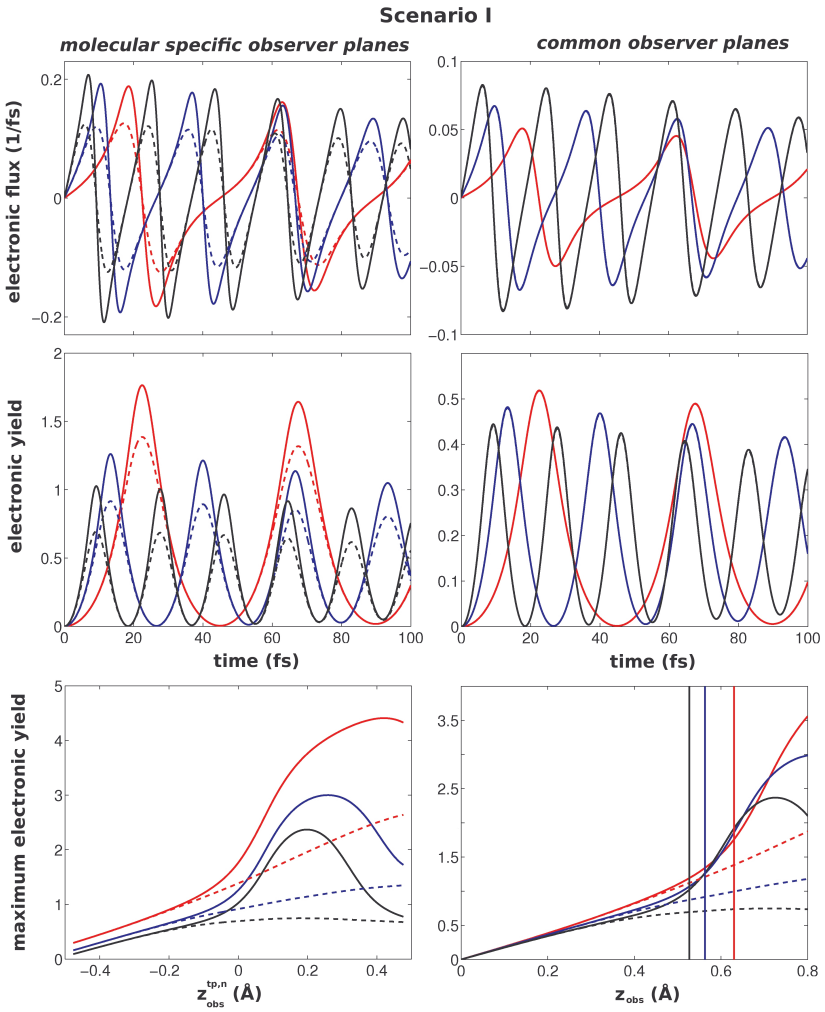

Figure 3. Electronic fluxes (top) and time-integrated electronic fluxes (electronic yields) (middle) as function of time for "molecular fixed" observer planes (left panels) located at $z_{\mathrm{obs}} = 0.26$ Å, see black horizontal lines in Figure 2(b) and for "laboratory fixed" observers (right panels) located at the respective turning points of the molecular systems at $z_{\mathrm{obs}}^{\mathrm{tp},n} = 0$, see green horizontal lines in Figure 2(b). The results are shown for scenario I, i.e. all molecules (ethane (red), ethene (blue) and ethine (black)) are excited by the same amount of energy with fluxes for the total and valence electron density shown as solid and dashed lines, respectively. The bottom panels show all maximal electronic yields as function of the position of the respective observer planes with the mean positions of the respective carbon atoms indicated by vertical lines for the "laboratory fixed" observers.

for the present study, for details see e.g. Ref. [19]. Hence, various characteristics of the PEC and the associated nuclear dynamics are mapped on the electronic fluxes, e.g. the zero-crossings of the electronic fluxes correlate with the turning points of the nuclear wave packets, cf. Table I and hence with the vibrational periods. Furthermore, the different gradients of the respective potentials, resulting in different velocities acquired by the associated wave packets, are reflected in the maximum values of the corresponding electronic fluxes with the maximum value corresponding to ethine. These maxima of the electronic fluxes are reached shortly after the nuclear wave packets pass their equilibrium positions with maximal velocity and the different slopes of the electronic fluxes left and right of these maxima reflect the different slopes of the PEC left and right of the equilibrium positions.

More insight into the actual electronic structure of the molecular systems is gained by an analysis of the time-integrated electronic fluxes (electronic yields), cf. eq. (7), i.e. the number of electrons that cross the respective observer planes in a given time interval shown in the left middle panel of Figure 3 for $z_{\mathrm{obs}}^{\mathrm{tp},n} = 0$. The maximum yields, Y_{max}^{n}, reached at the first zero-crossing of the electronic fluxes, are largest in the case of ethane followed by ethene and then by ethine for both the total electron densities (solid lines) and the valence densities (dashed lines). This counter-intuitive result is observed for all molecular fixed observer planes, see left bottom panel of Figure 3 which shows the maximal electronic yields as function of the position of the observer planes, $z_{\mathrm{obs}}^{\mathrm{tp},n}$.

The corresponding results for the "laboratory fixed" observers are shown for the special case $z_{\mathrm{obs}} = 0.26\,\text{Å}$, cf. Figure 2(b), in the top and middle right panels of Figure 3. Here, the difference between the maximal electronic yields is smaller but most electrons still cross the observers in the case of ethane. This is confirmed by the right bottom panel of Figure 3 which shows the maximal electronic yields as a function of the position of the laboratory fixed observers, z_{obs}, with the mean position of the nuclei at the turning points illustrated as vertical lines. Note that $Y_{\mathrm{obs,max}}^{n}$ is largest in the case of ethane except for special positions of the observer planes for which the rather localized core density $\rho_{\mathrm{core},n}(\mathbf{r},t)$ of ethine or ethene already penetrate the observers with the core density of ethane still being quite far away. This is confirmed by an analysis of the associated valence densities (dashed lines) which show dominant maximal electronic yields for ethane for the whole range of electronic observer planes.

The result that most electrons cross the respective observer planes in the case of ethane

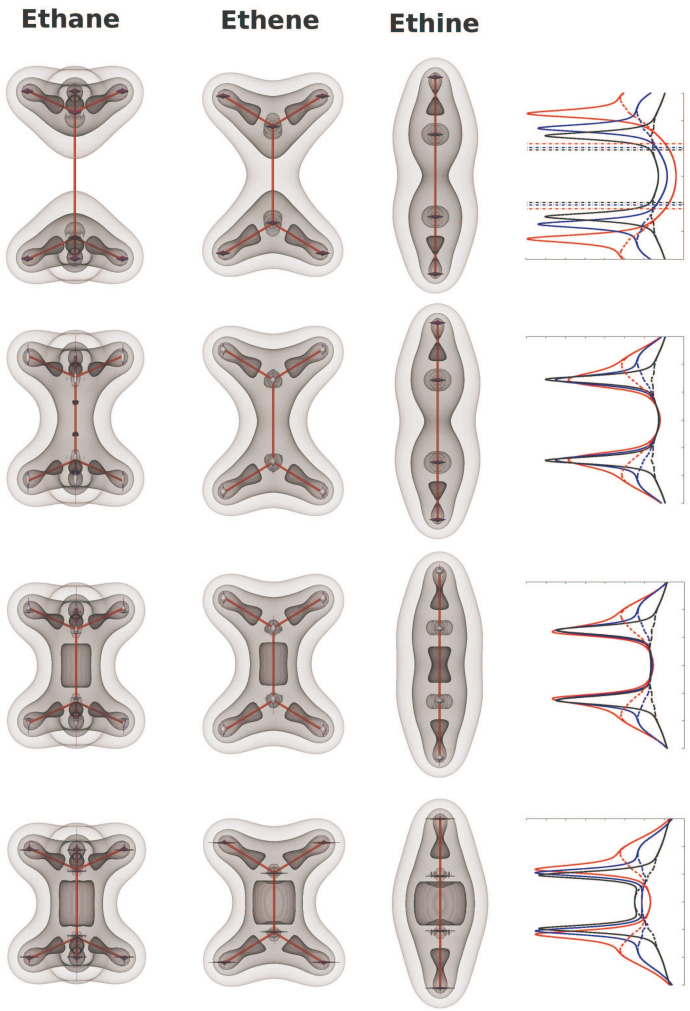

Figure 4. Illustration of the rearrangement of the valence electronic structure in vibrating ethane (left), ethene (middle) and ethine (right) within the first half period of vibration. The dynamics is shown for initial conditions corresponding to scenario I, cf. left panel in Figure 2(a) and Table I, as three nested equidensity contours with values $0.34\,\text{Å}^{-3}$ (light gray), $0.51\,\text{Å}^{-3}$ (gray) and $1.01\,\text{Å}^{-3}$ (dark gray). The snapshots are taken at $t = 0$ (top), at times when the mean values of the respective nuclear wave packets reach the equilibrium distance of ethane (second from top), the equilibrium distance of ethene (third from top), and the respective turning points (bottom), cf. Table I. Also shown are the corresponding reduced total electron densities (solid lines) and reduced valence densities (dashed lines) along the carbon-carbon axis, cf. eq. (8), for ethane (red), ethene (blue) and ethine (black). The program Amira [40] is used for data visualization.

when all systems are excited by the same amount of energy is rationalized by a comparison and analysis of the respective time-dependent electron densities shown in Figure 4 by three nested equidensity contours of the one-electron valence density at the starting point ($t = 0$) (top panel), at times when the center of the respective nuclear wave packets reaches the equilibrium distance of ethane (second panel from top), the equilibrium distance of ethene (third panel) and the respective turning points at $t^n_{\rm tp}$ (bottom panel), see also Table I. First of all, this comparison shows striking similarities between the electron densities associated with single, double and triple bonds at equal CC-distances. Figure 4 also shows complementary to the equidensity plots the time-dependent reduced densities along the CC-axis (z-axis, cf. Figure 1), eqs. (8) and (9), for ethane (red), ethene (blue) and ethine (black) for the reduced total density (solid lines) and the reduced valence density (dashed lines). The narrow spikes of the total reduced densities coincide with the mean values of the respective CC-distance monitoring the core densities of the C-atoms and the shoulders indicate the positions of the respective H-atoms as emphasized by the maxima of the reduced valence density. Note that the different height and width of these spikes at $t = 0$ is due to the different electronic structures of ethane, ethene and ethine and that the different heights at the successive times are due to more or less pronounced dispersion of the associated nuclear wave packets, see above and Figure 2. Additionally, the mean positions of the C-atoms at the respective turning points are shown in the top right panel by horizontal dashed-dotted lines which coincide with the position of the "molecular fixed" observers for $z^{{\rm tp},n}_{\rm obs} = 0$.

The reduced time-dependent densities both confirm the previous observation, i.e. very similar electron densities of ethane, ethene and ethine between the C-atoms at equal CC-distance, and explain the fact that most electrons cross the respective observer planes in the case of ethane by a comparison of the mean number of electrons in the corridors of width $\Delta z_{\rm obs}$ at times $t = 0$ and at the respective turning points $t = t^n_{\rm tp}$ which are shown in Figure 5 at the same points of time as in Figure 4 for ethane (red), ethene (blue) and ethine (black), again as solid lines for the total density and as dashed lines for the valence density. Additionally indicated are the respective mean CC-distances by the vertical dashed dotted lines. Note that these vertical lines at the respective turning points (bottom panel) coincide with the observer planes for $z^{{\rm tp},n}_{\rm obs} = 0$. Concentrating on the number of electrons at time $t = 0$ in the corridor bounded by the "laboratory fixed" observers at $z_{\rm obs} = 0.26$ Å, cf. right middle panel in Figure 3, marked by the green lines in the insets in Figure 5, we note that

due to the larger CC-distance, much less electrons are found in the associated corridor in the case of ethane ($\bar{N}^{\text{ethane}}(t=0)=0.41$) compared to ethene ($\bar{N}^{\text{ethane}}(t=0)=0.87$) and ethine ($\bar{N}^{\text{ethine}}(t=0)=1.31$). This overcompensates the fact that at the turning point, due to the different internuclear CC-distances marked by the vertical dashed-dotted lines, slightly less electrons are situated in this corridor in ethane ($\bar{N}^{\text{ethane}}(t=t^n_{\text{tp}})=1.77$) than in ethene ($\bar{N}^{\text{ethene}}(t=t^n_{\text{tp}})=2.14$) and ethine ($\bar{N}^{\text{ethane}}(t=t^n_{\text{tp}})=2.46$) and consequently the largest electronic yield is observed for ethane ($Y^{\text{max}}_{\text{obs},n}=0.68$) followed by ethene ($Y^{\text{max}}_{\text{obs},n}=0.63$) and ethine ($Y^{\text{max}}_{\text{obs},n}=0.58$), cf. eq. (8). This situation is even more pronounced when "molecular fixed" observers are used, since the different locations of the respective turning points are compensated. Hence, the larger amplitude of vibration for ethane, cf. Table I, in conjunction with the fact that practically equal numbers of electrons are found between the carbon nuclei at equal CC-distances, explains the fact that most electrons cross the different electronic observers in the case of ethane in the course of the respective large amplitude vibrations.

Motivated by this analysis, we change the excitation energies of ethane and ethene in scenario II such that all systems now show the same amplitude of vibration around their respective equilibrium position, which coincides with the amplitude of vibration of ethine in scenario I, see right panel in Figure 2(a) and Table I. Figure 6 shows, in an analogous manner as Figure 3, the electronic fluxes (top) and yields (middle) as well as the maximal electronic yields as a function of the respective position of the observer planes (bottom) both for the "molecular fixed" (left) and "laboratory fixed" (right) electronic observers for scenario II. While the electronic fluxes show the same characteristics discussed above for scenario I, we observe surprisingly that, despite the decrease of its amplitude of vibration, ethane still shows slightly larger electronic yields for all "molecular fixed" observer planes compared to ethene and ethine. This is a manifestation of the overall higher number of electrons in ethane, also reflected in the higher and broader peaks of the reduced densities along the CC-axis discussed above and shown in the rightmost panels of Figure 4. In case of the "laboratory fixed" observer planes, ethine shows the largest electronic yields which is due to its much shorter mean CC-distance at the turning point.

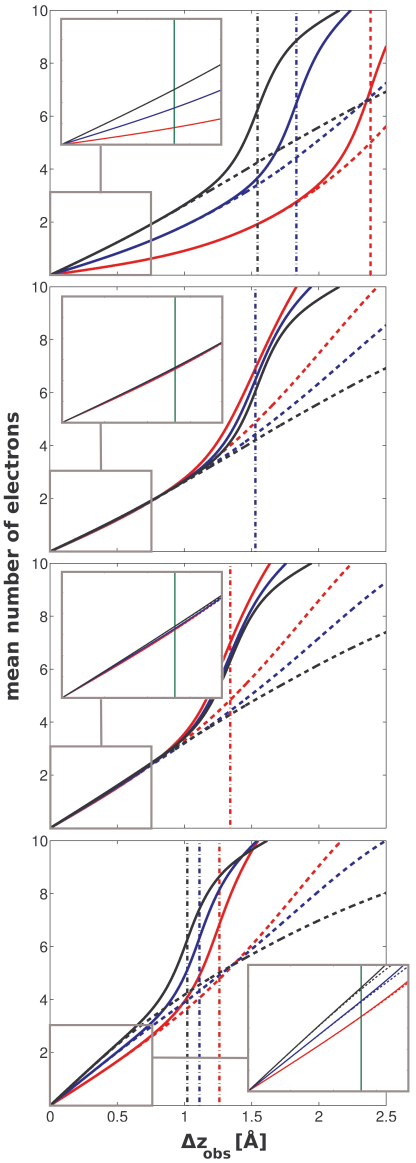

Figure 5. Mean number of electrons, $\bar{N}_{\mathrm{obs},n}(t)$, cf. eqs. (6) and (7), as function of the corridor width along the carbon-carbon axis, Δz_{obs}, cf. Figure 1, for total (solid lines) and valence (dashed lines) electron densities of ethane (red), ethene (blue) and ethine (black) at same times as shown in Figure 4. Vertical dashed-dotted lines show the mean positions of the carbon atoms. The inlets show blow-ups in the range $0 < \Delta z_{\mathrm{obs}} < 0.75\,\text{Å}$ with vertical green lines indicating the position of the "laboratory fixed" observer plane at $z_{\mathrm{obs}} = 0.26\,\text{Å}$, for details see text.

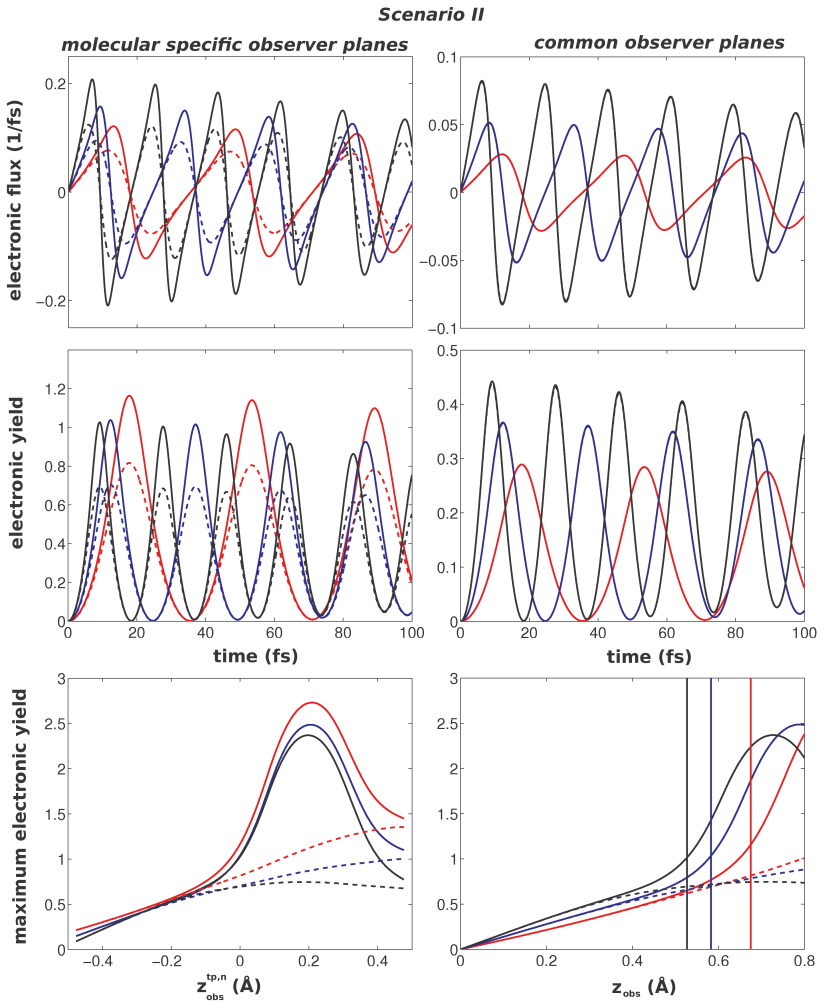

Figure 6. Same as Figure 3 for initial conditions corresponding to scenario II, cf. right panel in Figure 2(a) and Table I.

SUMMARY

The time-dependent quantum mechanical analysis of vibrating ethane, ethene and ethine presented in this study reveals in general that more electrons participate in the concerted electron-nuclear vibrations in case of ethane compared to ethene and ethine. This surprising result is counter-intuitive to the qualitative model based on the respective Lewis-structures which predict higher electron localization between the carbon atoms in the case of the triple bond of ethine and hence more pronounced electronic rearrangement during nuclear vibrations in the reverse order as found by our quantum results. In particular, we calculated the number of electrons (time-integrated electronic fluxes) that cross various observer planes which are all aligned perpendicular to the respective CC-axis (Figures 1 and 2(b)) in the course of the molecular vibration. To check the robustness of the results, we used two different sets of initial conditions (scenario I and II) and two different sets of electronic observer planes with the "molecular fixed" observers, defined relative to the respective turning points, allowing a proper comparison of the time-integrated electronic fluxes and the "laboratory fixed" observers, defined relative to the COM, meant to complement the analysis, cf. Figure 2(b). In scenario I, all molecules were assumed to be excited by the same amount of energy and for both sets of observer planes, we found $Y^{\max}_{\text{obs,ethane}} > Y^{\max}_{\text{obs,ethene}} > Y^{\max}_{\text{obs,ethine}}$, where $Y^{\max}_{\text{obs},n}$ is the maximum number of electrons that cross the respective observer planes. This counter-intuitive result is due to similar reduced electron densities of ethane, ethene and ethine along the respective CC-axis at equal CC-distances (Figures 4 and 5), so that the molecule with the largest amplitude of vibration (ethane, Figure 2 and Table I) also shows the largest maximum electronic yield. This dominant electronic rearrangement in case of ethane still persisted in scenario II, where the excitation energy was chosen such that all molecules show the same amplitude of vibration.

Our quantum investigation provides insight into the time-dependent rearrangement of the electronic density in concerted electron-nuclear vibrations in the electronic ground state and should stimulate both further experimental [5, 6, 8] and theoretical investigations involving e.g. electronic rearrangements during concerted electron-nuclear vibrations of asymmetric molecules and electronic fluxes accompanying molecular dissociation.

[1] A. H. Zewail, *Angew. Chem. Int. Ed.*, 2000, **39**, 2586.

[2] *Femtosecond Chemistry*, ed. J. Manz and L. Wöste, VCH, New York, 1995.

[3] *Femtochemistry*, ed. F. De Schryver, S. De Feyter and G. Schweitzer, Wiley-VCH, 2001.

[4] A. Stolow, *Ann. Rev. Phys. Chem.*, 2003, **54**, 89.

[5] P. Wernet, *Phys. Chem. Chem. Phys.*, 2011, **13**, 16941.

[6] F. Krausz and M. Y. Ivanov, *Rev. Mod. Phys.*, 2009, **81**, 163.

[7] *Quantum Dynamics Imaging*, ed. A. D. Bandrauk and M. Y. Ivanov, Springer, 2011.

[8] H. Niikura, H. J. Wörner, D. M. Villeneuve and P. B. Corkum, *Phys. Rev. Lett.*, 2011, **107**, 093004.

[9] J. P. Marangos, S. Baker, N. Kajumba, J. S. Robinson, J. W. G. Tisch and R. Torres, *Phys. Chem. Chem. Phys.*, 2007, **10**, 35.

[10] G. Sansone, F. Kelkensberg, J. F. Pérez-Torres, F. Morales, M. Kling, W. Siu, O. Ghafur, P. Johnsson, M. Swoboda, E. Benedetti, F. Ferrari, F. Lépine, J. L. Sanz-Vicario, S. Zherebtsov, I. Znakovskaya, A. L´Huillier, M. Y. Ivanov, M. Nisoli, F. Martín and M. J. J. Vrakking, *Nature*, 2010, **465**, 763.

[11] E. Goulielmakis, Z. Loh, A. Wirth, R. Santra, N. Rohringer, V. Yakovlev, S. Zherebtsov, T. Pfeifer, A. Azzeer, M. Kling, S. Leone and F. Krausz, *Nature*, 2010, **466**, 739.

[12] A. Dutoi and L. S. Cederbaum, *J. Phys. Chem. Lett.*, 2011, **2**, 2300.

[13] M. Łabuda, J. González-Vázquez and L. González, *Phys. Chem. Chem. Phys.*, 2010, **12**, 5439.

[14] S. Klinkusch, T. Klamroth and P. Saalfrank, *Phys. Chem. Chem. Phys.*, 2009, **11**, 3875.

[15] M. Okuyama and K. Takatsuka, *Chem. Phys. Lett.*, 2009, **476**, 109.

[16] T. Yonehara and K. Takatsuka, *Chem. Phys.*, 2009, **366**, 115.

[17] K. Nagashima and K. Takatsuka, *J. Phys. Chem. A*, 2009, **113**, 15240.

[18] T. Bredtmann, S. Chelkowski and A. D. Bandrauk, *Phys. Rev. A*, 2011, **84**, 021401.

[19] I. Barth, H.-C. Hege, H. Ikeda, A. Kenfack, M. Koppitz, J. Manz, F. Marquardt and G. Paramonov, *Chem. Phys. Lett.*, 2009, **481**, 118.

[20] A. Kenfack, F. Marquardt, G. K. Paramonov, I. Barth, C. Lasser and B. Paulus, *Phys. Rev. A*, 2010, **81**, 052502.

[21] T. Bredtmann and J. Manz, *Angew. Chem. Int. Ed.*, 2011, **50**, 12652.

[22] W. H. Miller, *Acc. Chem. Res.*, 1993, **26**, 174.

[23] W. H. Miller, *J. Phys. Chem. A*, 1998, **102**, 793.

[24] W. H. Miller, *J. Chem. Phys.*, 1974, **61**, 1823.

[25] U. Manthe, T. Seideman and W. H. Miller, *J. Chem. Phys.*, 1994, **101**, 4759.

[26] T. Wu, H.-J. Werner and U. Manthe, *Science*, 2004, **306**, 2227.

[27] T. Yonehara, K. Hanasaki and K. Takatsuka, *Chem. Rev.*, 2011, **112**, 499.

[28] D. Andrae, I. Barth, T. Bredtmann, H.-C. Hege, J. Manz, F. Marquardt and B. Paulus, *J. Phys. Chem. B*, 2011, **115**, 5476.

[29] M. Born and R. Oppenheimer, *Ann. Phys.*, 1927, **389**, 457.

[30] M. Born and K. Huang, *Dynamical Theory of Crystal Lattices*, Oxford University Press, Oxford, UK, 1954.

[31] M. Born, *Nachr. Akad. Wiss. Göttingen, Math.-Phys. Kl., 2A: Math.-Phys.-Chem. Abt.*, 1951, **6**, 1.

[32] H.-J. Werner and P. J. Knowles, *J. Chem. Phys.*, 1988, **89**, 5803.

[33] P. J. Knowles and H.-J. Werner, *Chem. Phys. Lett.*, 1988, **145**, 514.

[34] H.-J. Werner and P. J. Knowles, *J. Chem. Phys.*, 1985, **82**, 5053.

[35] P. J. Knowles and H.-J. Werner, *Chem. Phys. Lett.*, 1985, **115**, 259.

[36] H.-J. Werner, P. J. Knowles, G. Knizia, F. R. Manby, M. Schütz, P. Celani, T. Korona, R. Lindh, A. Mitrushenkov, G. Rauhut, K. R. Shamasundar, T. B. Adler, R. D. Amos, A. Bernhardsson, A. Berning, D. L. Cooper, M. J. O. Deegan, A. J. Dobbyn, F. Eckert, E. Goll, C. Hampel, A. Hesselmann, G. Hetzer, T. Hrenar, G. Jansen, C. Köppl, Y. Liu, A. W. Lloyd, R. A. Mata, A. J. May, S. J. McNicholas, W. Meyer, M. E. Mura, A. Nicklass, D. P. O'Neill, P. Palmieri, K. Pflüger, R. Pitzer, M. Reiher, T. Shiozaki, H. Stoll, A. J. Stone, R. Tarroni, T. Thorsteinsson, M. Wang and A. Wolf, *MOLPRO, version 2010.1, a package of ab initio programs, see http://www.molpro.net*, 2010.

[37] T. H. Dunning, *J. Chem. Phys.*, 1989, **90**, 1007.

[38] *Structure of Free Molecules in the Gas-Phase*, CRC Handbook of Chemistry and Physics, 92nd edn., 2011.

[39] B. Schmidt and U. Lorenz, *WavePacket (version 4.7), a program package for quantum mechanical wavepacket propagation and time-dependent spectroscopy, see http://wavepacket.sourceforge.net (Freie Universität Berlin, 2009).*

[40] D. Stalling, M. Westerhoff and H.-C. Hege, *The Visualization Handbook*, Elsevier, Amsterdam, 2005, p. 749.

[41] B. Hartke, R. Kosloff and S. Ruhman, *Chem. Phys. Lett.*, 1989, **158**, 238.

[42] E. Goll, G. Wunner and A. Saenz, *Phys. Rev. Lett.*, 2006, **97**, 103003.

[43] W. Li, X. Zhou, R. Lock, S. Patchkovskii, A. Stolow, H. C. Kapteyn and M. M. Murnane, *Science*, 2008, **322**, 1207.

[44] T. Ergler, B. Feuerstein, A. Rudenko, K. Zrost, C. D. Schröter, R. Moshammer and J. Ullrich, *Phys. Rev. Lett.*, 2006, **97**, 103004.

ACKNOWLEDGEMENT

We thank Prof. J. Manz (Freie Universität Berlin) for valuable and stimulating discussions. T.B. and B. Paulus thank Deutsche Forschungsgemeinschaft (DFG, project Ma 515/25-1) for financial support.

3.2.2 T. Bredtmann, H. Katsuki, J. Manz*, K. Ohmori, C. Stemmle*, Wavepacket Interferometry for Nuclear Densities and Flux Densities, Mol. Phys., 111, 1691-1696 (2013)

T. Bredtmann, H. Katsuki, J. Manz*, K. Ohmori, C. Stemmle*,
Wavepacket Interferometry for Nuclear Densities and Flux Densities,
Mol. Phys., **111**, 1691-1696 (2013).

DOI: 10.1080/00268976.2013.780103
URL: http://dx.doi.org/10.1080/00268976.2013.780103

T. Bredtmann, H. Katsuki, J. Manz*, K. Ohmori, C. Stemmle*,
Wavepacket Interferometry for Nuclear Densities and Flux Densities,
Mol. Phys., **111**, 1691-1696 (2013).

DOI: 10.1080/00268976.2013.780103
URL: http://dx.doi.org/10.1080/00268976.2013.780103

T. Bredtmann, H. Katsuki, J. Manz*, K. Ohmori, C. Stemmle*,
Wavepacket Interferometry for Nuclear Densities and Flux Densities,
Mol. Phys., **111**, 1691-1696 (2013).

DOI: 10.1080/00268976.2013.780103
URL: http://dx.doi.org/10.1080/00268976.2013.780103

T. Bredtmann, H. Katsuki, J. Manz*, K. Ohmori, C. Stemmle*,
Wavepacket Interferometry for Nuclear Densities and Flux Densities,
Mol. Phys., **111**, 1691-1696 (2013).

DOI: 10.1080/00268976.2013.780103
URL: http://dx.doi.org/10.1080/00268976.2013.780103

T. Bredtmann, H. Katsuki, J. Manz*, K. Ohmori, C. Stemmle*,
Wavepacket Interferometry for Nuclear Densities and Flux Densities,
Mol. Phys., **111**, 1691-1696 (2013).

DOI: 10.1080/00268976.2013.780103
URL: http://dx.doi.org/10.1080/00268976.2013.780103

T. Bredtmann, H. Katsuki, J. Manz*, K. Ohmori, C. Stemmle*,
Wavepacket Interferometry for Nuclear Densities and Flux Densities,
Mol. Phys., **111**, 1691-1696 (2013).

DOI: 10.1080/00268976.2013.780103
URL: http://dx.doi.org/10.1080/00268976.2013.780103

4 Summary and Conclusions

In this thesis, it was shown that the quantum dynamical evaluation and analysis of electron-nuclear quantum fluxes provides quantitative insight into adiabatic chemical processes occurring in specific non-degenerate electronic quantum states [T1,T3-T7]. Special emphasis was laid on pericyclic reactions in the electronic ground state, exemplified for the degenerate Cope rearrangement (DCR) of semibullvalene (SBV) [T1-T5], c.f. Figure 1.1, which constitutes part one of the results of this thesis. One of the main objectives was the quantification of the qualitative rules traditionally used in organic, inorganic and biochemistry [29–31, 34, 35] to indicate the net outcome of chemical reactions by curved arrows embedded in the reactant, c.f. top left panel in Figure 4.1. The latter figure, which presents a graphical summary of some of the results obtained in part one, shows "top" or "bird's eye views" of the DCR of SBV, while Figure 1.1 shows "side views" of this pericyclic reaction.

At first, the reaction from the reactant R over the potential barrier B_{d} to the product P, at energies E well above the potential barrier B_{d} ($E > B_{\mathrm{d}}$), involving synchronous nuclear quantum motion along the one-dimensional reaction coordinate ξ, was investigated [T1]. The reader is referred to section 2.4 for a detailed description of the underlying model, see also Ref. [72]. Hence, according to section 2.4, the barrier associated with this direct path from R to P is denoted by B_{d} and the actual transition state by TS, whereas barriers without explicit specification will be denoted by B in the following. The underlying potential energy surface along the one-dimensional reaction coordinate ξ was calculated at the B3LYP/cc-pVTZ level of theory, sections 2.2.2 and 2.2.4, which is a very reasonable approximation [T5]. Visual data analysis in cooperation with the *Zuse-Institut für Visualisierung und Datenanalyse Berlin* showed that exclusively pincer-shaped patterns of the electronic fluxes, topmost depiction in the top left panel in Figure 4.1, are observed for the DCR of SBV. Such flux patterns are a general feature of unimolecular pericyclic reactions in the non-degenerate electronic ground state, as successively shown in Ref. [161]. In the latter study, exploiting the fact that for such reactions the mean electronic angular momentum is equal to zero, a selection rule for the corresponding directionality of electronic fluxes was derived. Accordingly, such electronic fluxes must change directions, forbidding counter-clockwise or clockwise ring-current like electronic fluxes, c.f. middle and bottommost depiction, respectively, in the top left panel in Figure 4.1. These selection rules are in analogy to spectroscopic selection rules for "symmetry forbidden" and "symmetry allowed" transitions [145], with the determination of the "true" directionality of the fluxes and their quantitative values relying on specific quantum dynamical evaluations [161]. Note that clockwise or counter-clockwise electronic fluxes occur in chemical processes involving degenerate or quasi-degenerate excited electronic states, see Refs. [14, 15] and [16, 21, 25], respectively, as well as in processes involving multiple excited non-degenerate electronic quantum states, involving complex electronic flux patterns [18, 23].

Furthermore, Ref. [T1] showed that series of time-integrated electronic fluxes can be as-

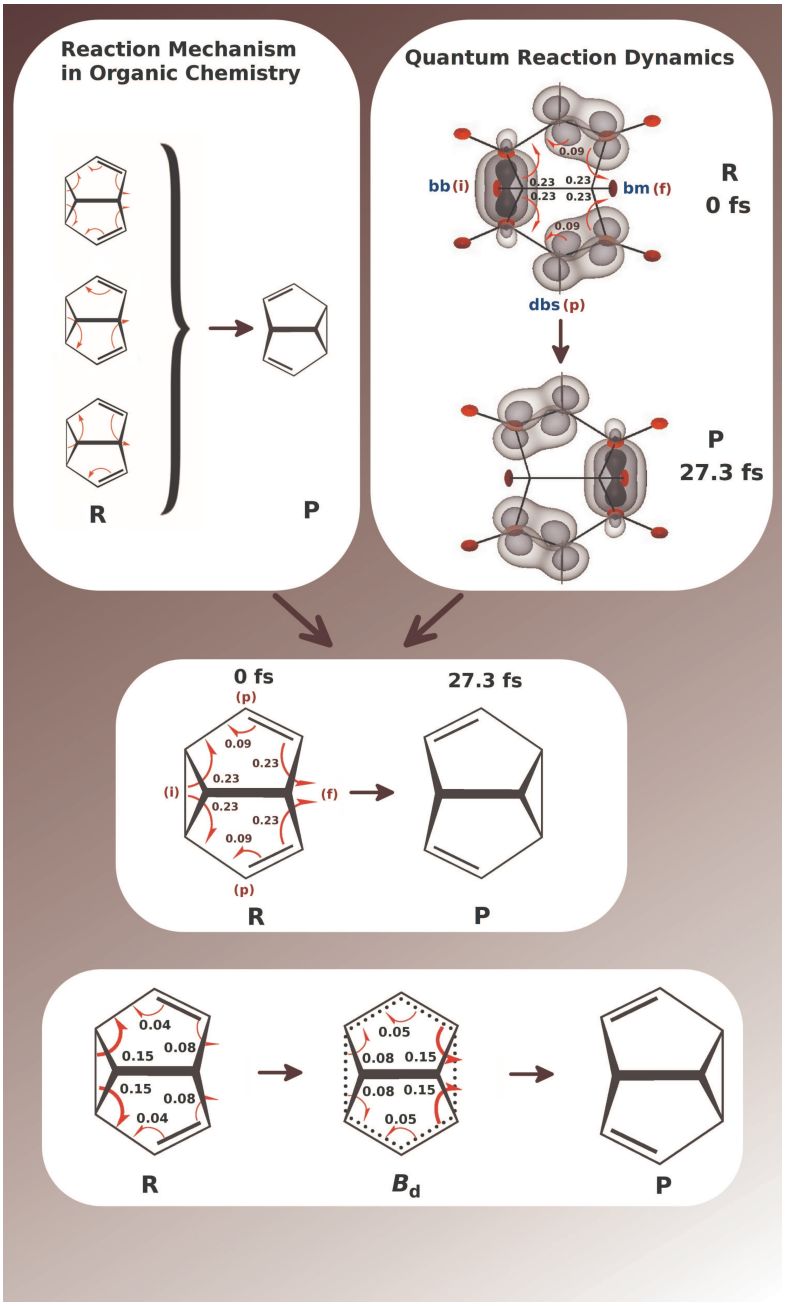

Figure 4.1: Quantum dynamical results (top right panel) may be combined with traditional depictions of reaction mechanisms in organic chemistry (top left panel) in order to yield new insight into pericyclic reactions (middle panel). The actual directionality of the electronic bond-to-bond fluxes is indicated by pincer-shaped curved arrows. These arrows may be complemented both by the number of electrons transferred from bond to bond from the reactant (R) to the product (P) and by labels indicating the time-sequences of the electronic bond-to-bond fluxes: (i) for initial dominant flux associated with bond breaking (bb) from R to the barrier B_{d} corresponding to the direct path from R to P, see text and section 2.4.2.1, (f) for final dominant flux associated with bond making (bm) from B_{d} to P, and (p) for perpetual fluxes associated with double-bond-shifting (dbs). The bottommost depiction shows an alternative quantitative depiction emphasizing this asynchronous electronic rearrangement, that is the dominant flux out of the breaking bond from R to B_{d}, by the scale of the associated pincer-shaped arrows together with the numbers of the transferred electrons. From B_{d} to P, these electronic flux patterns are of course inversed due to the underlying symmetry of the reaction. The program Amira [158] was used for data visualization.

signed to the pincer-shaped curved arrows in the Lewis structures corresponding to the number of electrons participating in the electronic bond-to-bond fluxes. For this analysis, the time-dependent one-electron density $\rho_{\mathrm{el}}^{\mathrm{BO}}(\mathbf{r},t)$, eqn. (2.41), had to be partitioned, by means of localized molecular-orbitals, see Ref. [201] and section 2.2.3, in order to filter out spurious contributions mainly due to rearranging CH groups, see also Refs. [T5] and [253]. Hence, the total density was partitioned into a core density, $\rho_{\mathrm{el,core}}^{\mathrm{BO}}(\mathbf{r},t)$, accounting for the sixteen core electrons associated with the eight carbon 1s-shells, into a pericyclic density, $\rho_{\mathrm{el,peri}}^{\mathrm{BO}}(\mathbf{r},t)$, accounting for the mutation of the Lewis structure for the reactant into that for the product, and into a density accounting for the other, remaining, valence electrons, $\rho_{\mathrm{el,oval}}^{\mathrm{BO}}(\mathbf{r},t)$, such that $\rho_{\mathrm{el}}^{\mathrm{BO}}(\mathbf{r},t) = \rho_{\mathrm{el,core}}^{\mathrm{BO}}(\mathbf{r},t) + \rho_{\mathrm{el,peri}}^{\mathrm{BO}}(\mathbf{r},t) + \rho_{\mathrm{el,oval}}^{\mathrm{BO}}(\mathbf{r},t)$. The number of electrons participating in the bond-to-bond fluxes was then evaluated in terms of the pericyclic density, $\rho_{\mathrm{el,peri}}^{\mathrm{BO}}(\mathbf{r},t)$, see section 2.2.3 for further details. This pericyclic density for R and P, including the transferred numbers of electrons, is shown in the top right panel of Figure 4.1, as isosurface plots using three nested equidensity contours.

Concerning the synchronicity of the electronic bond-to-bond fluxes associated with bond breaking (bb), bond making (bm) and double-bond-shifting (dbs), it was found [T1] that initially (i), from R to B_{d}, the electrons dominantly flow out of the breaking bond and finally (f), from B_{d} to P, they dominantly flow into the new bond, i.e. asynchronous electronic fluxes associated with bond breaking and bond making during synchronous nuclear rearrangement were observed. Meanwhile, perpetual (p) electronic flux associated with double-bond-shifting was observed. At the mean total energy considered in Ref. [T1], $E = 1.04\,\mathrm{eV}$, the reaction time τ from R to P was determined as $\tau = 27.3\,\mathrm{fs}$, c.f. Figure 4.1. The latter graphical summary shows how these quantum dynamical results yield new insight into reaction mechanisms in organic chemistry. Specific sets of curved arrows may be used to indicate the actual directionality of electronic bond-to-bond fluxes during pericyclic reactions, complemented by the number of electrons that are transferred from bond-to-bond, as well as by labels of the time sequences, going beyond mere qualitative depictions for the net outcome of such reactions (middle panel). The bottom panel of Figure 4.1 shows an alternative depiction, emphasizing the dominant flux out of the breaking bond from R to B_{d} by the scale of the associated pincer-shaped curved arrows together with the numbers of the transferred electrons. This asynchronicity may be quantized by the parameter α as the difference between the number of electrons that have, from R to B_{d}, flown out of the old and into the new bond, $\alpha = 0.15 - 0.08$. From B_{d} to P, these patterns are of course inversed due to the underlying symmetry of the reaction. The reader is also referred to Ref. [82] for a recent theoretical study based on topological analysis of the electron density along the intrinsic reaction path [200] of the DCR of SBV, which was motivated by Ref. [T1], and confirmed our results.

Pericyclic reactions occurring in the electronic ground state with energies well above the potential barrier may be initialized by ultrashort laserpulses in the ultraviolett frequency domain with pulse durations shorter than 10 fs as shown experimentally for the Claison rearrangement of allyl vinyl ether [89] and allyl phenyl ether [90] involving successive excitation and deexcitation of an excited electronic state. Motivated by these experimental studies on the Claison rearrangement and in order to motivate, on our part, experimental studies aiming to monitor the rich electronic flux phenomena in the DCR of SBV using emerging experimental techniques

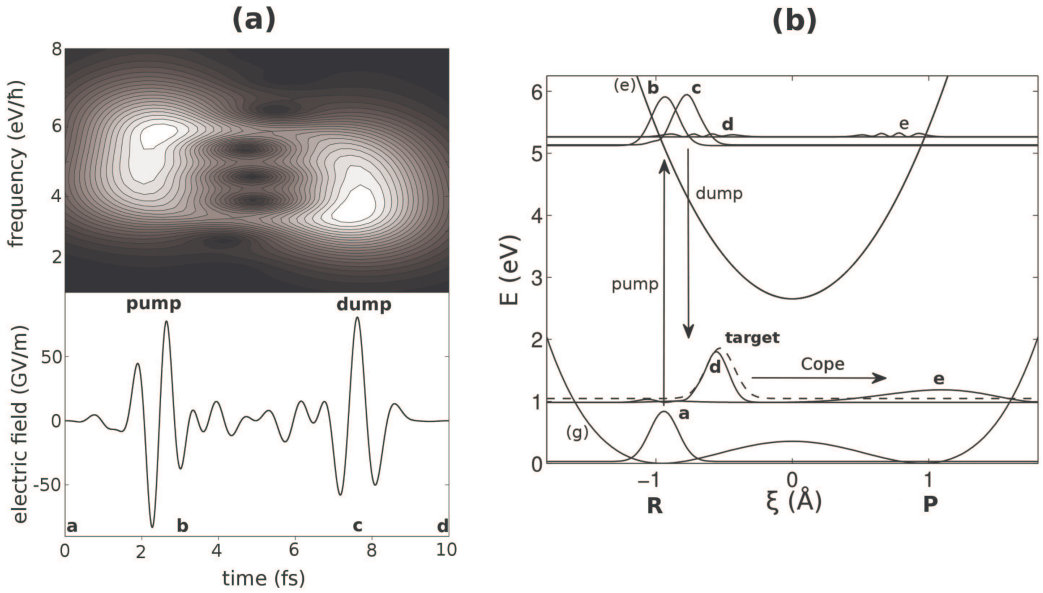

Figure 4.2: Optimal control of the initiation of the Cope rearrangement of semibullvalene in the electronic ground state, adapted from [T2]. (a) Time-frequency profile (top panel) and electric field (bottom panel) of the optimal laser pulse. The time-frequency profile was obtained by a Gabor transform using a Gaussian time-window, see eqn. (2.228). The events labeled "a,b,c,d" correspond to the snapshots of the laser-driven wave packet dynamics shown in (b). (b) The time evolution of the laser driven wave packet dynamics, from the reactant (R) along the nuclear coordinate ξ to the product (P), is illustrated by the series of snapshots "a,b,c,d,e" of the nuclear densities, at times $t = 0\,\mathrm{fs}$, $3.1\,\mathrm{fs}$, $7.1\,\mathrm{fs}$, $10\,\mathrm{fs}$ (the end of the laser pulse) and $t = 33.5\,\mathrm{fs}$, the time when the product structure is reached. The snapshots are embedded in the electronic ground (g) and excited (e) state potential energy surfaces with base lines of the densities corresponding to their mean total energies. Also shown is the density of the target state adapted from Ref. [T1], which runs from R to P, with total energy E well above the barrier B_d (dashed line). After the laser pulse, a small fraction of the total density is left in the excited electronic state, and runs simultaneously in both electronic states from snapshot "d" to "e".

of femto-to-attosecond spectroscopy [4–9, 254], Optimal Control Theory (OCT) [91–99], see also section 2.3.4, was applied in this thesis in order to design an ultra-short laser-pulse that initiates the DCR of SBV in the electronic ground state. Using the model for the electronic ground state from Ref. [T1] and an empirical potential [73] for the first excited electronic state, it was shown in Ref. [T2] that OCT yields a Raman-type pump-dump mechanism as the most efficient initiation. Figure 4.2(a) shows the time-frequency profile (top panel) and the electric field (bottom panel), see section 2.3.3, of the optimal laser pulse. Figure 4.2(b) shows the corresponding time evolution of the laser driven wave packet dynamics from R along the nuclear coordinate ξ to P, illustrated by the series of snapshots "a,b,c,d" of the nuclear densities corresponding to the points of time marked in the depiction of the electric field, bottom panel of Figure 4.2(a). Additionally depicted is the time when the product structure is reached at $t = 33.5\,\mathrm{fs}$ marked by snapshot "e" as well as the predefined target state as dashed line. It may be interesting to note that the initial guess for the optimized laser pulse was a resonant pulse with a $\sin^2$-envelope function of time duration $t_\mathrm{p} = 10\,\mathrm{fs}$, c.f. Figure 2.4(a).

Specifically, the pump sub-pulse of the optimized laser field first induces a resonant Franck-Condon type transition from the electronic ground state (snapshot "a" in Figure 4.2(b)) to the electronic excited state (snapshot "b"), where the nuclear wave packet evolves freely and gains momentum in the direction of the product ("c"). After an optimal time-delay, the dump-sub-pulse transfers the system resonantly back to the electronic ground state ("d"). In this dump-process, the momentum originally gained in the excited electronic state is preserved and the reaction proceeds in the electronic ground state towards the product ("e"). Since the dump-pulse has a lower central laser frequency compared to the pump-pulse (top panel in Figure 4.2(a)), the process may be described as a down-chirped intra-pulse pump-dump mechanism with both sub-pulses being few (one to two) cycle pulses [T2]. This mechanism agrees with the previously suggested pump-dump mechanism [89, 90]. It shall be noted that in the latter experimental studies, non-resonant pulses were used, such that these experiments might be improved using properly chirped resonant laser pulses [T2]. Furthermore, the analysis of both the OCT-pulse and the mechanism of the initiation suggests to design experimentally more accessible analytical pulses with Gaussian- or $\sin^2$-envelope functions, with similar central frequencies, time-durations and time-delays as the OCT-pulse. This study was carried out in Ref. [255] yielding results close to those obtained in Ref. [T2].

The elimination of the complete excited state population after the dump-pulse is essential in the context of monitoring electronic fluxes in the electronic ground state, since the interference between the associated wave function in the excited electronic state with the ground state wave function might induce contributions to electronic fluxes which are much larger then those for the adiabatic reactions from R to P in the electronic ground state [18, 19, 23]+[B1-B4], see also Chapter 5. This might be achieved by employing another laser-pulse for selective photo-ionization from the excited electronic state [256]. In this context, also note that pump-dump laser pulse control involving solely the electronic ground state using infrared laser pulses [73–75] rely on strong changes of the dipole along the reaction coordinate, a prerequisite which is difficult to fulfill, making pump-dump laser pulse-control involving successive excitation and deexcitation of an excited electronic state a promising scheme.

In Refs. [T3] and [T4], the investigations on the DCR of SBV for the reaction above the potential barrier were extended and compared to the tunneling regime occurring at cryogenic

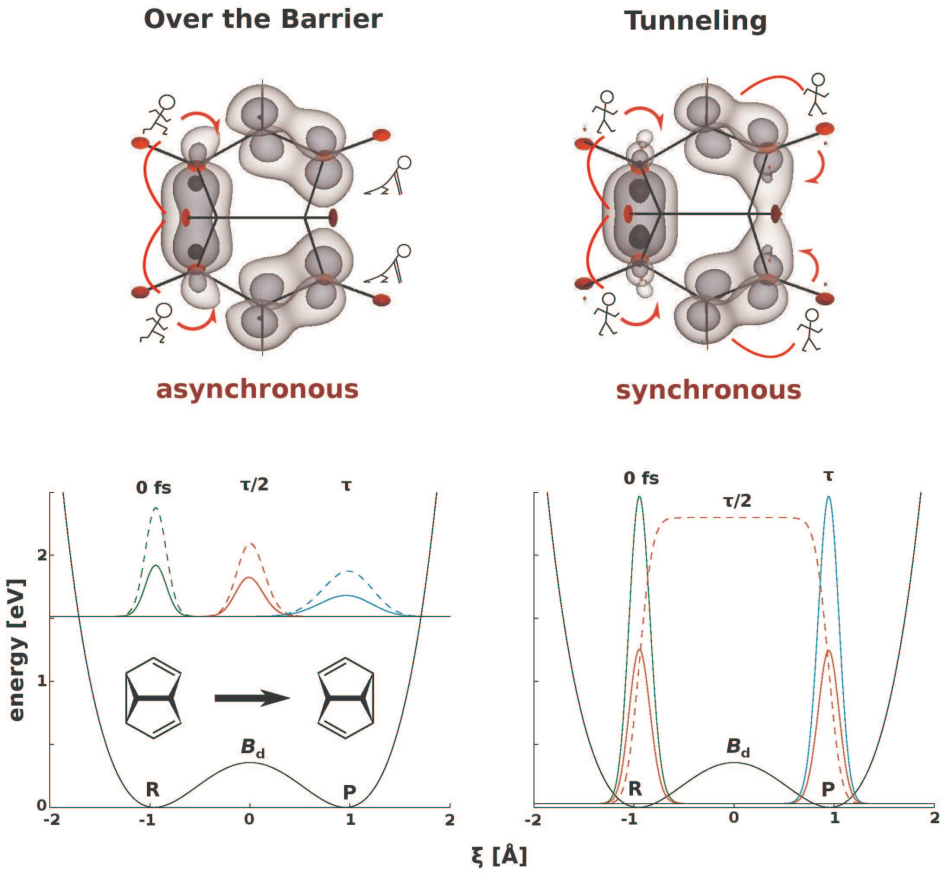

Figure 4.3: (a) Electronic fluxes associated with bond making and bond breaking are asynchronous in the degenerate Cope rearrangement of semibullvalene when the reactants are prepared with energies well above the potential barrier (left), c.f. Figure 4.1, and synchronous in the case of coherent tunneling with energies well below the potential barrier [T3]. The pericyclic density, accounting for the mutation of the Lewis structure for the reactant into that for the product, is shown as isosurface plots using three nested equidensity contours at time $t = \tau/4$, with reaction time $\tau = 27.3\,\mathrm{fs}$ for the over the barrier case [T3] and $\tau = 970\,\mathrm{s}$ in the case of coherent tunneling [80]. The nuclear wave packet dynamics is shown in red, adapted from Ref. [T3]. The program Amira was used for data visualization [158]. (b) Corresponding nuclear flux densities (dashed lines) and nuclear densities (solid lines) embedded in the potential energy surface with baseline at the mean total energies, shown at the characteristic times $t = 0\,\mathrm{fs}$, $t = \tau/2$ and $t = \tau$. For the over the barrier scenario (left), the nuclear flux density is essentially proportional to the nuclear density, whereas in the case of coherent tunneling (right panel) the nuclear flux density increases with decreasing nuclear density, adapted from Ref. [T4].

temperatures T with energies well below the potential barrier ($E < B_\mathrm{d}$). In this scenario, the nuclear dynamics is determined by the two lowest nuclear stationary eigenstates, c.f. section 2.3.1, that is the lowest doublet of the delocalized gerade and ungerade eigenfunctions, as well as the energy gap between these two states, the so-called tunneling splitting $\Delta\tilde{E}$, c.f. eqn. (2.187). In Ref. [80], it was shown that for temperatures $T < 50\,\mathrm{K}$, the DCR of SBV proceeds from R to P within $\tau = 970\,\mathrm{s}$, such that $\Delta\tilde{E} = \hbar\pi/\tau = 2.1318^{-18}\,\mathrm{eV}$. Analysis of the corresponding electronic bond-to-bond fluxes showed synchronous bond making and bond breaking [T3]. Hence, the synchronicity of the electronic bond-to-bond fluxes in the DCR of SBV depends on the preparation of the reactant, i.e. synchronous at cryogenic temperatures ($E < B_\mathrm{d}$) but asynchronous when initiated by ultrashort laser pulses ($E > B_\mathrm{d}$) [T3]. This is illustrated in Figure 4.3(a), which shows snapshots of the respective pericyclic densities, $\rho^{\mathrm{BO}}_{\mathrm{peri}}(\mathbf{r}, t)$, at times $t = \tau/4$, where the reaction time from R to P amounts to $\tau = 26.4\,\mathrm{fs}$ for $E > B_\mathrm{d}$ [T3] and $\tau = 970\,\mathrm{s}$ for $E < B_\mathrm{d}$ [80]. Note that in Ref. [T3] the mean total energy was set to $E = 1.58\,\mathrm{eV}$, whereas previously in Ref. [T1], it was set to $E = 1.04\,\mathrm{eV}$ with $\tau = 27.3\,\mathrm{fs}$. This variation of the mean total energy E and hence the reaction time τ showed that the asynchronicity of the electronic fluxes from R to P is insensitive with respect to the energy for $E > B_\mathrm{d}$, that is, virtually identical asynchronicity parameters α are obtained for different mean total energies E and associated reaction times τ, as long as (partial) reflections of the nuclear wave packet at the barrier is prevented.

The related nuclear flux densities, $\langle j_{\mathrm{nuc}}(\xi, t)\rangle$, were analyzed in Ref. [T4] and are shown for both cases, together with the nuclear densities, $\rho_{\mathrm{nuc}}(\xi, t)$, in Figure 4.3(b). Both densities are embedded in the potential energy surface with baselines at the mean total energies, and are shown at the characteristic times $t = 0\,\mathrm{fs}$, $t = \tau/2$ and $t = \tau$. For the reaction over the barrier (left panel), the nuclear flux density (dashed lines) is essentially proportional to the nuclear density (solid lines), $\langle j_{\mathrm{nuc}}(\xi, t)\rangle \approx \langle v_{\mathrm{nuc}}(t)\rangle \times \rho_{\mathrm{nuc}}(\xi, t)$, where $\langle v_{\mathrm{nuc}}(t)\rangle$ is the mean velocity of the nuclear wave packet. This corresponds to the expected result based on classical trajectories. In the case of coherent tunneling (right panel), on the other hand, the nuclear flux density increases with decreasing nuclear density, such that $\langle j_{\mathrm{nuc}}(\xi, t)\rangle$ has its maximum at the potential barrier B_d, where $\rho_{\mathrm{nuc}}(\xi, t)$ is close to zero [T4]. This counter-intuitive result calls for experimental demonstration, just as the asynchronous electronic bond-to-bond fluxes for $E > B_\mathrm{d}$.

In the last study of the first part of the results of this thesis [T5], the over the barrier scenario, Ref. [T1], was investigated in more detail. In particular, the effect of nuclear motion on the synchronicity of the pincer-shaped electronic rearrangement associated with bond breaking and bond making and vice versa was studied using a time-independent quantum chemical approach. Hence, various paths along the potential energy surface from R to P involving different potential barriers B, including the transition state, were investigated. This traditional approach may be considered as an approximation to the explicitly time-dependent treatment given in Refs. [T1,T3] neglecting effects of nuclear quantum dispersion, which has been shown to be a very reasonable approximation [T1]. Furthermore, the quantum chemical method employed in Refs. [T1-T4] (B3LYP/cc-pVTZ) was tested against high level multireference methods, to assess its ability to describe the underlying potential energy surface, thereby extending previous quantum chemical data for the DCR of SBV.

Specifically, the quantum chemical method needs to provide a balanced description of the

minima of the potential energy surface associated with the reactant and the product (C_s-symmetry) and of the transition state region (C_{2v}-symmetry). The quantum chemical description of the latter region is much more involved. It contains a continuum between radical and bishomoaromatic structures, which are distinguished by the interallylic distance d (distance between carbon atoms C_2 and C_8, or equivalently, atoms C_4 and C_6, in the C_{2v}-structure, see Figure 4.4(a)). Note that more pronounced σ-bond elongation associated with carbon atoms C_2 and C_8 compared to σ-bond contraction associated with carbon atoms C_4 and C_6 from R to B leads to bis-allyl-like structures with corresponding large interallylic distance d, while more pronounced σ-bond contraction compared to σ-bond elongation leads to 3,7-diyl-like structures with associated short d values. Finally, synchronous σ-bond elongation and contraction leads to bishomoaromatic structures with intermediate values of the interallylic distance d.

Comparison to multireference calculations at the RS2/cc-pVTZ level of theory, section 2.2.1.3, including full structure optimizations yielded excellent agreement with the previously reported B3LYP/cc-pVTZ results along the reaction coordinate ξ [T1,T3], that is the asynchronicity of bond breaking and bond making during synchronous nuclear rearrangement was shown to be stable, irrespective of the quantum chemical method used. Similar excellent agreement was observed for the optimized C_{2v}-structure associated with the transition state. The reaction from the reactant to the transition state involves more pronounced σ-bond elongation associated with bond breaking compared to σ-bond contraction associated with bond making [T5]. Consequently, the interallylic distance d associated with the transition state is slightly larger than the one associated with synchronous σ-bond making and breaking, Figure 4.4(a). Hence, this asynchronicity of the nuclear rearrangement involving the transition state enhances the asynchronicity of the electronic rearrangement with respect to the previously reported asynchronicity during synchronous nuclear rearrangement. Furthermore, Ref. [T5] showed that the asynchronicity of the electronic rearrangement is already apparent in the total electron density when appropriate observer planes monitoring the electronic rearrangement are chosen. The partitioning of the electron density using localized molecular-orbitals and the analysis in terms of the resulting pericyclic density is nevertheless recommended. In this way, spurious contributions, mostly due to rearranging core electrons and CH groups, are diminished, simplifying the analysis of the results and yielding straightforward chemical insight. Furthermore, illustrations of this pericyclic density allow the connection to the traditional chemical picture of the underlying reaction, Figures 4.4(a)+(b). In this context, the analysis in terms of the pericyclic density showed that synchronous electronic rearrangement is observed when the reaction proceeds from the reactant over 3,7-diyl-like-structures associated with short interallylic distances d, Figures 4.4(a)+(b), involving more pronounced σ-bond contraction compared to σ-bond elongation, that is asynchronous nuclear rearrangement.

Although both the RS2/cc-pVTZ and B3LYP/cc-pVTZ methods give excellent optimized structures of the stationary points on the potential energy surface, the barrier heights are significantly underestimated for the DCR of SBV by RS2/cc-pVTZ, while B3LYP/cc-pVTZ additionally underestimates the relative stability of the radical structures with respect to the transition state. Hence, for an accurate description of the extended transition state region including accurate barrier heights, a high degree of static and dynamic electron correlation needs to be included. Benchmark results for the DCR of SBV were obtained by refining the corresponding optimized RS2/cc-pVTZ structures at the RS3/cc-pVTZ and the MRCISD+Dav/cc-pVTZ level of theory, sec-

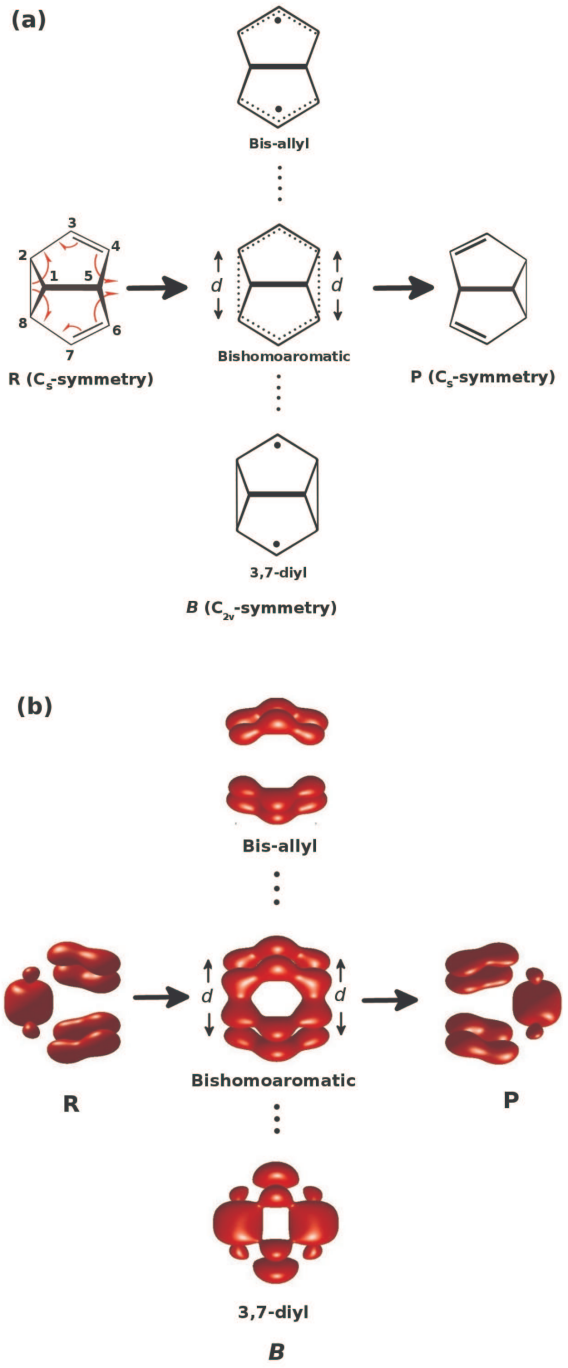

Figure 4.4: Illustration of the degenerate Cope rearrangement of semibullvalene from the reactant (C_s-symmetry) through distinct structures with C_{2v}-symmetry associated with different potential barriers B to the product (C_s-symmetry). The different C_{2v}-structures may be distinguished by the interallylic distance d. The top panel (a) shows traditional depictions of this pericyclic reaction in terms of the associated Lewis structures, while the bottom panel (b) shows the corresponding quantum chemical results in terms of isosurface plots of the pericyclic density, adapted from Ref. [T5].

tions 2.2.1.3 and 2.2.1.4, yielding virtually identical results [T5]. These high level potential energy surfaces are important for further studies on the DCR of SBV involving for example the coherent control of the asynchronicity of the electron-nuclear rearrangement using Optimal Control Theory, see also Chapter 5.

These rich electron-nuclear flux phenomena motivated two further studies on experimentally easier accessible systems [T6,T7], presented in the second part of the results of this thesis. The first study dealt with electronic fluxes during large amplitude vibrations of single, double and triple bonds, occurring in the non-degenerate electronic ground state, exemplified for vibrating ethane, ethene and ethyne [T6]. This time-dependent analysis showed that in general, the number of electrons participating in the concerted electron-nuclear vibrations decrease from ethane via ethene to ethyne. This surprising result is counter-intuitive to the qualitative model based on the respective Lewis-structures, which predicts increasing electron density between the carbon atoms from ethane via ethene to ethyne, such that more pronounced electronic rearrangement during nuclear vibrations is predicted in the reverse order from that found in the quantum dynamical analysis (Figure 4.5(a)). This counter-intuitive result is due to very similar electron distributions of single, double and triple bonds along the carbon-carbon axis at equal carbon-carbon distances (Figure 4.5(b)). Hence, most electrons participate in the electron-nuclear vibrations in the case of the molecule with the largest amplitude of vibrations, that is ethane when all molecules are excited by the same amount of energy. Surprisingly, this dominant electronic rearrangement for ethane also persists when all molecules show the same amplitude of vibration, as shown by a detailed analysis using different sets of observer planes monitoring the electronic rearrangement [T6]. These results should stimulate the transfer of experiments from the regime of multi-state attosecond electron dynamics, already carried out for ethane [13], to the regime of adiabatic single-state electron dynamics, ubiquitous in (thermal) chemistry.

Finally, the detailed analysis of the nuclear flux density in the degenerate Cope rearrangement of semibullvalene proceeding with energies well above the potential barrier, Refs. [131] and [T4], lead to the discovery of interference phenomena in the nuclear flux density close to the classical turning points. These observations gave raise to the extension of wave packet interferometry, see Refs. [106–130] and Chapter 1, from nuclear densities to nuclear flux densities in Ref. [T7]. Since, due to intramolecular vibrational redistribution, the accuracy of the one-dimensional model employed for the DCR of SBV (section 2.4.2.1) becomes less accurate in the vicinity of the classical turning points, these interference phenomena were analyzed in more detail for a diatomic molecular system, for which the one-dimensional model is of course exact when rotational dof are neglected. Motivated by recent experiments on the diatomic molecule I_2, which showed that spatio-temporal images of the associated quantum interferences in the nuclear densities on the excited electronic B-state can be controlled with picometer spatial and femtosecond temporal resolution [130], I_2 was chosen as the molecular system studied theoretically in Ref. [T7].

In particular, it was found that the interferences in the nuclear densities, manifested as a chain of lobe-shaped structures of these densities corresponding to a finite set of bond lengths of the molecule in the excited electronic state (Figure 4.6(a)) also appear in the nuclear flux densities (Figure 4.6(b)) with chains of lobes corresponding to alternating bond stretches and bond compressions. Interestingly, quite often, positive and negative values of the nuclear flux

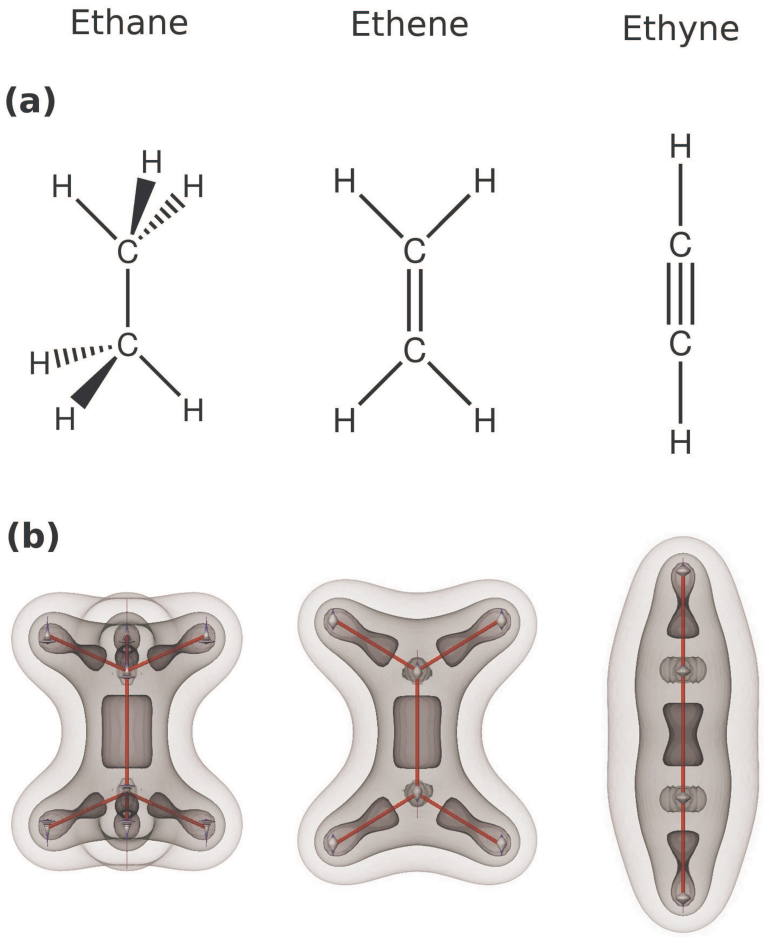

Figure 4.5: (a) Lewis structures of ethane, ethene and ethyne. (b) Corresponding snapshots of the valence electron density, shown as isosurface plots using three nested equidensity contours, at equal carbon-carbon (CC) distances, corresponding to the equilibrium distance of ethyne, CC = 1.21 Å [T6]. The program Amira was used for data visualization [158], adapted from Ref. [T6].

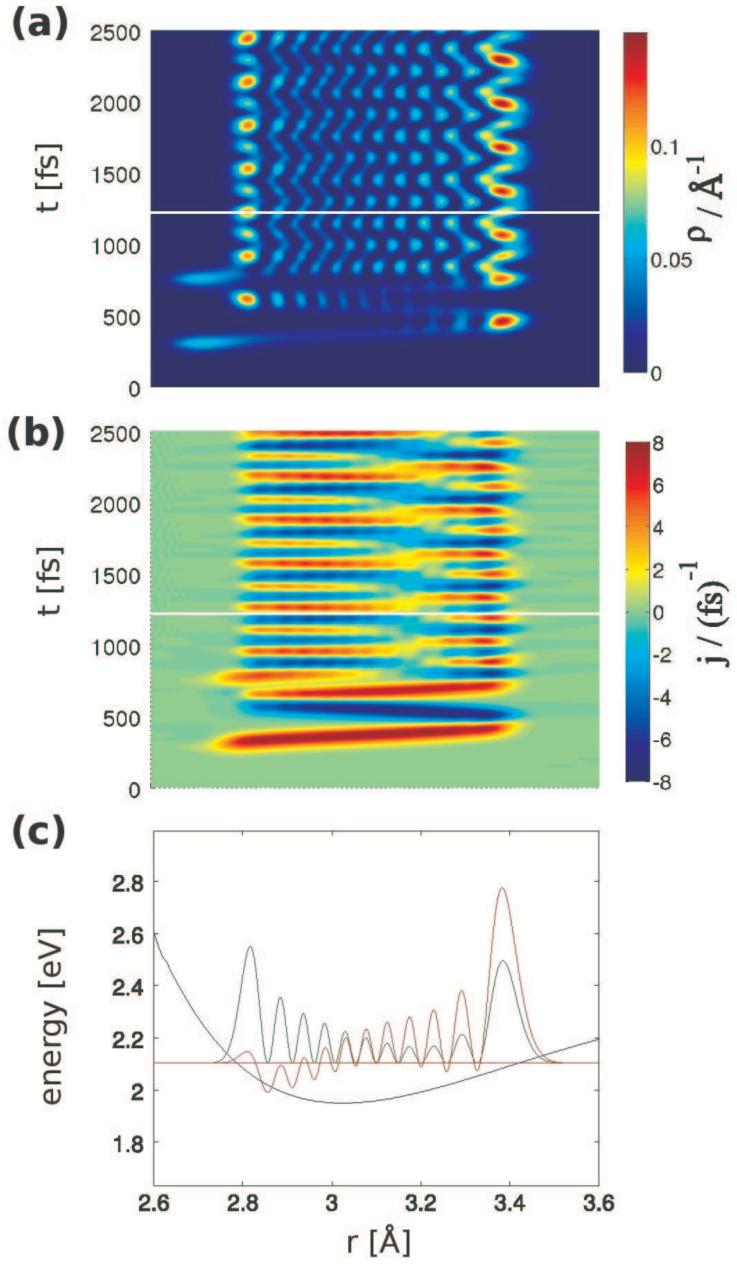

Figure 4.6: Extension of wave packet interferometry [106–130] from nuclear densities to nuclear flux densities, adapted from Ref. [T7]. The panels (a) and (b) show the time evolutions of the nuclear density and nuclear flux density, respectively, after excitation of the vibrational ground state associated with the electronic ground state to the excited electronic B-state in the diatomic I_2, using two time-delayed laser pulses. For both laser pulses, Gaussian shape functions with identical associated durations $\tau_p = 60\,\mathrm{fs}$ and central laser frequencies, $\omega_{0,1} = \omega_{0,2} = 2.087\,\mathrm{eV}/\hbar$ were used, see eqn. (2.226) in section 2.3.3. The corresponding temporal centers were chosen as $\tau_{d,1} = 300\,\mathrm{fs}$ and $\tau_{d,2} = 752\,\mathrm{fs}$ and the respective carrier envelope phases as $\eta_1 = \eta_2 = 0$. The equal amplitudes of the electric fields of the two sub-pulses and the transition dipole moments, eqn. (2.231), were chosen to yield 0.011 population transfer from the ground to the excited B-state per sub-pulse. (c) Snapshots of the nuclear density (green) and of the nuclear flux density (red) embedded in the potential energy surface of the electronic B-state (blue) at times specified by the horizontal lines in (a) and (b).

density correlate with maxima and minima of the nuclear density, respectively, as illustrated in Figure 4.6(c). This latter figure shows horizontal cuts through Figures 4.6(a) and (b) as indicated by the horizontal lines, with the nuclear density shown in green and nuclear flux density shown in red. Additionally, the variation of the laser parameters associated with the two time-delayed laser pulses allows the shaping and hence the control of these lobe-shaped structures [T7].

5 Outlook

In this outlook, from the many ideas for possible extensions of the investigations presented in this thesis, only projects, for which basic preliminary results have already been obtained, are presented. The preliminary results presented in Figure 5.2 are adapted from Refs. [257, 258].

An interesting extension of the investigations on the degenerate Cope rearrangement of semibullvalene presented in the first part of this thesis is the incorporation of the transition state in the quantum dynamical model as well as the ab-initio calculation of the corresponding first excited electronic state. Figure 5.1(a) shows a contour plot of the corresponding two-dimensional potential energy surface of the electronic ground state, calculated at the MRCISD+Dav[6,6]/cc-pVTZ level of theory using a reference CASSCF wave function with six active electrons in six active orbitals, see sections 2.2.1.3 and 2.2.1.5, as well as Ref. [T5] for details. The previously considered direct path [T1-T5] leading straight from the minimum of the symmetric double well potential energy surface representing the reactant over the associated barrier B_{d} to the other potential minimum representing the product, accounting for synchronous motion of all the nuclei, is represented by the grey horizontal line. This model is extended by introducing a second, orthogonal direction, leading straight, from the barrier B_{d} to the transition state. These two direction span the so-called reaction plane [245–248], for further details see section 2.4.2.2. Figure 5.1(b) shows the corresponding potential energy surface of the first excited electronic state (right panel) and again the ground state potential energy surface (left panel), with adapted range of the ξ'-axis. The respective MRCISD+Dav[6,6]/cc-pVTZ calculations used a state averaged CASSCF reference wave function, section 2.2.1.5, with equal weights of the ground and the first excited electronic states. The corresponding vertical excitation energies associated with the reactant (and product) and the transition state are 6.58 eV and 4.34 eV, respectively. These large energy gaps between the ground and first excited electronic state give further justification for employing the Born-Oppenheimer approximation in Refs. [T1-T5].

These two-dimensional potential energy surfaces and the associated transition dipole moments evaluated at the same level of theory (not shown) constitute the basis of quantum dynamical simulations for the laser control of the synchronicity of the electronic and nuclear rearrangement in the degenerate Cope rearrangement of semibullvalene by means of Optimal Control Theory. Specifically, based on the intra pulse pump-dump mechanism described above, c.f. Figure 4.2 and Refs. [T2] and [89, 90], target states situated close to the potential minimum associated with the reactant, with different mean momentum components along the ξ- and ξ'-axis, $\langle p \rangle_{\xi}$ and $\langle p \rangle_{\xi'}$, respectively, are expected to entail different synchronicities of the electron-nuclear rearrangement. Hence, as working hypothesis, nuclear wave packets that cross the potential barrier close to the transition state ($\xi = 0\,\text{Å}$, $\xi' = 0\,\text{Å}$) are expected to entail both asynchronous nuclear and asynchronous electronic rearrangement. On the other hand, nuclear wave packets that cross the C_{2v}-region close to B_{d}, that is the barrier considered in Refs. [T1-T5] ($\xi = 0\,\text{Å}$, $\xi' = 0.172\,\text{Å}$) are expected to entail synchronous nuclear and asynchronous electronic

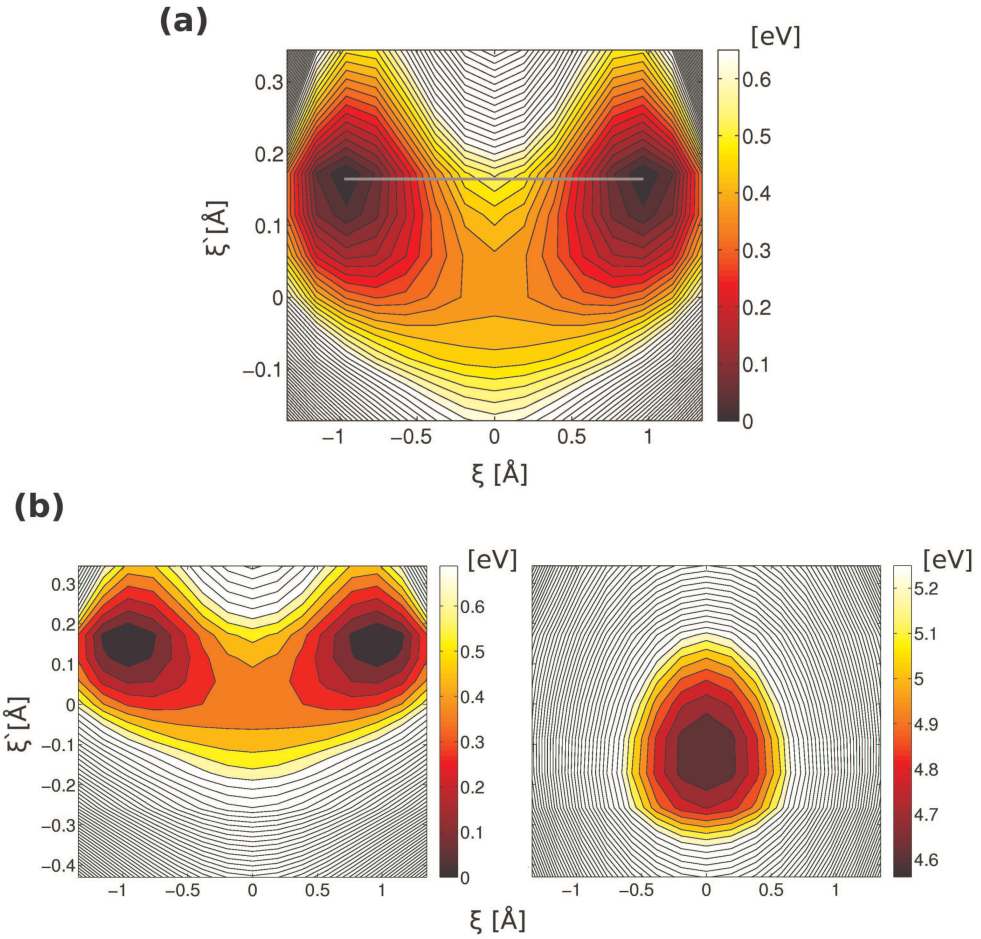

Figure 5.1: (a) Contour plot of a two-dimensional potential energy surface for the degenerate Cope rearrangement of semibullvalene. This so-called reaction plane [245–248] contains the reactant ($\xi = -0.960\,\text{Å}$, $\xi' = 0.172\,\text{Å}$), the product ($\xi = 0.960\,\text{Å}$, $\xi' = 0.172\,\text{Å}$) as well as the transition state ($\xi = \xi' = 0\,\text{Å}$). The previously considered direct path from the reactant to the product, involving synchronous rearrangement of all the nuclei and leading over the associated barrier B_d ($\xi = 0\,\text{Å}$, $\xi' = 0.172\,\text{Å}$) [T1-T5], is shown as grey horizontal line. The potential energy surface was calculated at the MRCISD+Dav/cc-pVTZ level of theory based on fully optimized structures of the reactant (or equivalently of the product) and the transition state obtained at the RS2/cc-pVTZ level of theory. In all cases, a CASSCF reference wave function with six active electrons in six active orbitals was used, see Ref. [T5] for further details of the ground state potential energy surface (b) Corresponding potential energy surface of the excited electronic state (right panel) and, for comparison, the ground state potential energy surface (left panel) with adapted range of the ξ'-axis. The same quantum chemical methods as in (a) were used except that a state averaged CASSCF reference wave function with equal weights for the ground and excited electronic state was used. In all illustrations, the contour line spacing is 0.09 eV and the ranges of the color coding are given in the respective colorbars.

electronic rearrangement. Finally, nuclear wave packets associated with 3,7-diyl-like structures, Figure 4.4, associated with $\xi = 0\,\text{Å}$ and $\xi' > 0.172\,\text{Å}$, are expected to entail asynchronous nuclear and quasi synchronous electronic rearrangement.

Further straightforward extensions are for example the inclusion of additional nuclear degrees of freedom into the quantum mechanical model and the comparison to classical trajectory calculations, as well as the investigation of the reaction occurring with energies close to the potential barrier ($E \approx B$) involving branching of the nuclear wave packet. All of these scenarios might of course be transferred to other pericyclic reactions, involving possibly asymmetric potential energy surfaces, to underline the ubiquity of the discovered results.

Another more fundamental extension of the analysis of electron-nuclear fluxes in adiabatic processes presented in this thesis is the incorporation of excited electronic states including effects of decoherence [259] due to nuclear quantum motion. Such investigations are partly motivated by recent theoretical studies on mapping attosecond electronic motion by molecular high-order-harmonic pump-probe spectroscopy [B1-B4], exemplified for the molecular ion H_2^+, see also Refs. [260–263]: Consider a molecular system prepared in a coherent superposition of two electronic states a and b which may be expressed as the superposition of two Born-Oppenheimer electronic states for the present purpose:

$$\Psi(\mathbf{r},\mathbf{R},t) = |\chi_a(\mathbf{R},t)|\Phi_a(\mathbf{q};\mathbf{R})e^{-iE_a(\mathbf{R})t} + |\chi_b(\mathbf{R},t)|\Phi_b(\mathbf{q};\mathbf{R})e^{-iE_b(\mathbf{R})t}, \tag{5.1}$$

where $\chi_i(\mathbf{R},t)$ and $\Phi_i(\mathbf{q};\mathbf{R})$ denote the nuclear and electronic wave functions, respectively, depending on the set of nuclear and electronic coordinates, $\mathbf{R}$ and $\mathbf{q}$, respectively, with corresponding probability density

$$\begin{aligned}|\Psi(\mathbf{r},\mathbf{R},t)|^2 =& |\chi_a(\mathbf{R},t)|^2|\Phi_a(\mathbf{q};\mathbf{R})|^2 + |\chi_b(\mathbf{R},t)|^2|\Phi_b(\mathbf{q};\mathbf{R})|^2 \\ &+ 2\text{Re}\left(|\chi_a(\mathbf{R},t)||\chi_b(\mathbf{R},t)|\Phi_a(\mathbf{q};\mathbf{R})\Phi_b(\mathbf{q};\mathbf{R})e^{-i(E_a(\mathbf{R})-E_b(\mathbf{R})t)}\right).\end{aligned} \tag{5.2}$$

Eqns. (5.1) and (5.2) are the extension from nuclear wave packets, eqns. (2.186) and (2.187), to electron-nuclear wave packets [B1-B4]. Hence, the coupled electron-nuclear dynamics and consequently the electron-nuclear quantum fluxes in a superposition of two electronic states are governed by three terms: the first two terms describe the collective rearrangement of both electrons and nuclei, occurring typically on the femtosecond time-scale [T1,T3,T6], involving the single electronic quantum states a and b. The third *interference term* describes mainly electronic motion with oscillation period

$$\tilde{T}_{\text{el}}(\mathbf{R}) = 2\pi/(E_a(\mathbf{R}) - E_b(\mathbf{R})), \tag{5.3}$$

depending both on the electronic energies $E_a(\mathbf{R})$ and $E_b(\mathbf{R})$, and hence on the nuclear coordinates, and on the overlap of the nuclear wave packets $\chi_a^*(\mathbf{R},t)\chi_b(\mathbf{R},t)$. As long as this overlap of the nuclear wave packets is sufficient, the electronic fluxes are expected to be governed by the interference term [B1-B4], eqn. (5.2), with time-scales being inversely proportional to the energy gap between the associated electronic states, eqn. (5.3). Thus in the case of energy gaps of several electron volts, see for example Figure 5.1(b), considerably faster timescales than reported in this thesis are expected. However, as soon as the overlap of the nuclear wave

packets in the two electronic states is lost, the interference term in eqn. (5.2) decays to zero and the electron-dynamics is anticipated to slow down considerably being governed by the first two terms in eqn. (5.2). This decoherence as well as recurrences associated with transiently recovered overlap between the corresponding nuclear wave packets is expected to be nicely visualized by the corresponding electron-nuclear fluxes.

Further related extensions are the incorporation of conical intersections or avoided crossings [147, 154, 155, 167], in the vicinity of which the associated electronic states are coupled by the non-adiabatic coupling terms given in eqn. (2.12), see also eqn. (2.14), leading to radiationless transitions between the electronic states. Figure 5.2, adapted from Refs. [257, 258], shows snapshots of the nuclear wave packet dynamics, occurring on the two lowest electronic states of NaCl having the same symmetry after impulsive excitation of the vibrational nuclear ground state associated with the electronic ground state to the first excited electronic state. This system is particularly interesting to study in terms of electron-nuclear fluxes since it exhibits, besides an avoided crossing, different characters (ionic vs. covalent) of the corresponding electronic states, giving raise to charge transfer [167], see also Refs. [46, 264–266]. The potential energy surfaces have been calculated at the MRCISD/aug-cc-pVTZ level of theory with a state averaged CASSCF reference wave function containing six active electrons in four active orbitals [257, 258]. The non-adiabatic vectorial coupling terms, eqn. (2.12), have been calculated at the same level of theory and the propagation was carried out in the diabatic representation, for details see Ref. [257, 258] and also Refs. [267, 268]. Analysis in terms of eqn. (5.2) predicts that at first (Figure 5.2(a)) the electronic fluxes will occur on the femtosecond time-scale describing the collective electron-nuclear rearrangement in the excited covalent electronic state. When the avoided crossing is reached radiationless decay is observed (Figure 5.2(b)) and the electronic fluxes might be dominated by the interference term, eqn. (5.2), giving rise to a deceleration of the electronic fluxes due to the small energy gap between the electronic states. At later times, the overlap between the nuclear wave packets is lost (Figure 5.2(c)) and recovered again (Figure 5.2(d)+(e)) in certain coordinate regions, involving non-trivial structures of the nuclear wave packets, leading possibly to an acceleration of the electronic-fluxes associated with charge transfer. This analysis is, of course, speculative and quantitative evaluations of the corresponding electron-nuclear fluxes are presently being carried out [257, 258].

Finally, the experimental verification of the discovered electron-nuclear flux phenomena in adiabatic processes presented in this thesis provides a major challenge. Although in recent years, considerable theoretical and experimental progress in monitoring changes of the electronic structure in real-time has been achieved, most of these studies focus on measuring non-adiabatic attosecond electron-dynamics involving multiple electronic states, see for instance Refs. [4, 6–13, 24, 27]. The reader is also referred to Refs. [B1-B4] for recent theoretical progress on measuring electronic-fluxes involving attosecond electronic wave packets. Nevertheless, there is also promising experimental progress in measuring adiabatic single state electron dynamics, see for example Refs. [5, 254].

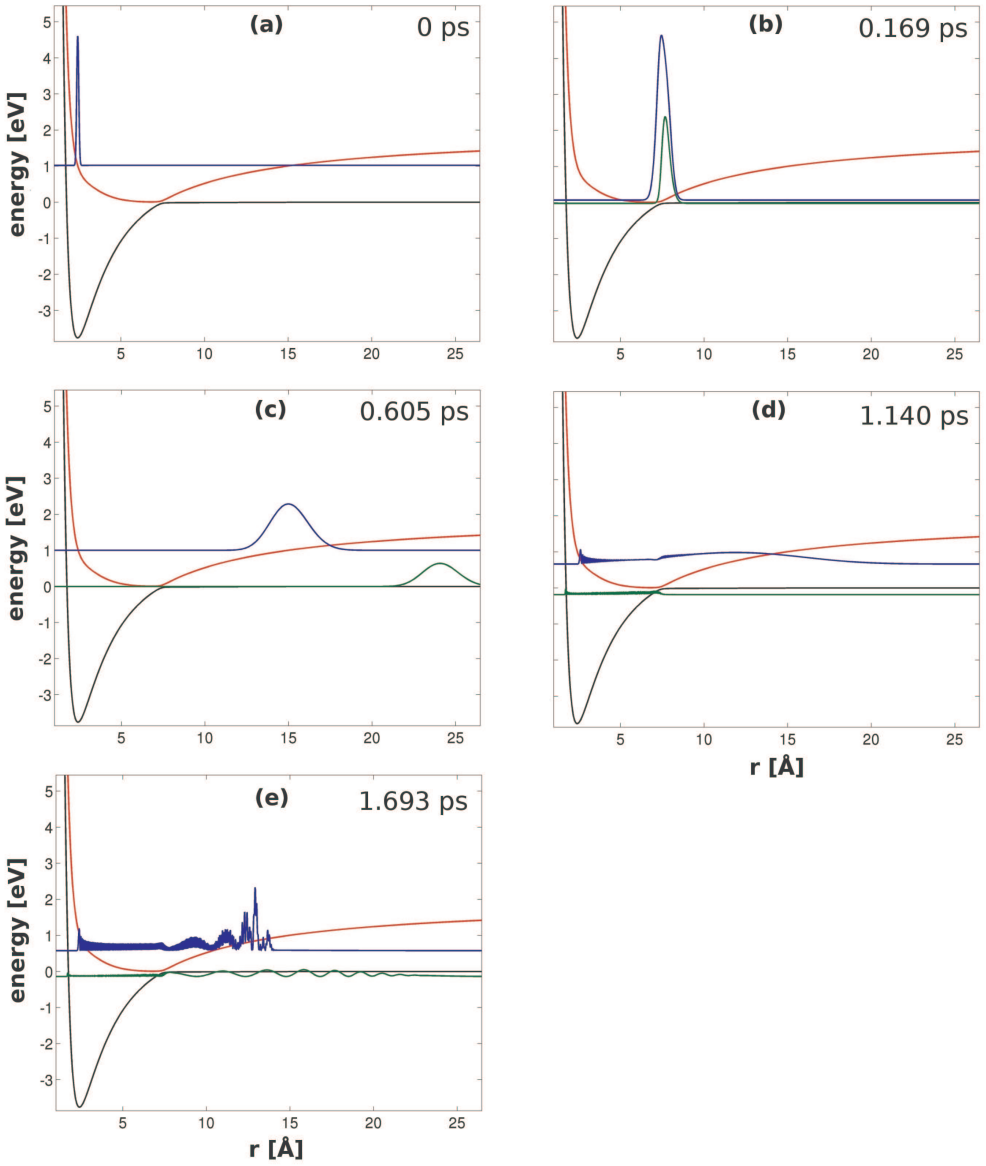

Figure 5.2: Snapshots of the nuclear wave packet dynamics in NaCl occurring in the electronic ground state (black) and the first excited state of the same symmetry (red) after impulsive excitation of the vibrational nuclear ground state associated with the electronic ground state to the excited state. The nuclear wave packets associated with the electronic ground state are shown in green and those associated with the excited electronic state in blue, both with baselines at the respective mean total energies, embedded in the respective potential energy surfaces shown as function of the internuclear distance r. In panel (a) the nuclear wave packet was scaled by a factor of 0.1 with respect to the remaining panels. The potential energy surfaces and nonadiabatic couplings were obtained at the MRCISD/aug-cc-pVTZ level of theory using a state averaged CASSCF wave function containing six active electrons in four active orbitals, adapted from Refs. [257, 258].

6 Appendix

6.1 Functional Derivatives

A function is a mapping from a variable x to a number $f(x)$. A functional is a mapping from a function $f(x)$ to a number $G[f(x)]$. Hence, in a manner of speaking, a functional is a function of which the variable is a function [162]. The search for the minimum of a functional, i.e. the determination of the function $f(x)$ for which the functional $G[f(x)]$ becomes stationary, $\delta G[f(x)] = 0$, is a branch of the calculus of functionals, which is usually called calculus of variation [162, 269]. Functionals and functional derivatives are encountered in this thesis e.g. in the derivation of the Hartree-Fock equations, section 2.2.1.3, eqn. (2.87), in Density Functional Theory involving the minimization of the energy functional $E[\rho_{\mathrm{el}}^{\mathrm{BO}}(\mathbf{r})]$ with respect to the electron density $\rho_{\mathrm{el}}^{\mathrm{BO}}(\mathbf{r})$, see for example eqn. (2.145) in section 2.2.2, or in the framework of Optimal Control Theory involving the maximization of the control functional $J[t_{\mathrm{tar}}; \mathcal{E}_z(t)]$, eqn. (2.236).

First consider the total differential of a function f depending on n-variables

$$\mathrm{d}f(x_1, x_2, \ldots, x_n) = \sum_j \left(\frac{\partial f}{\partial x_i}\right) \mathrm{d}x_i. \tag{6.1}$$

The differential of a functional, $\delta F[f(x)]$, is the extension of eqn. (6.1) to continuous variables. Hence, $\delta G[f(x)]$ is the part of the difference $G[f(x) + \delta f(x)] - G[f(x)]$ that depends on $\delta f(x)$ linearly according to [162]

$$\delta G[f(x)] = \int \frac{\delta G[f(x)]}{\delta f(x)} \delta f(x) \mathrm{d}x, \tag{6.2}$$

where $\frac{\delta G[f(x)]}{\delta f(x)}$ is the functional derivative of $G[f(x)]$. Since the displacement $\delta f(x)$ is arbitrary, the stationary points of the functional $G[f(x)]$ are found by setting the functional derivative equal to zero, $\frac{\delta G[f(x)]}{\delta f(x)} = 0$.

For the calculation of functional derivatives, consider the functional

$$G[f(x)] = \int g(x, f(x), f^{(1)}(x), f^{(2)}(x), \ldots, f^{(n)}(x)) \mathrm{d}x, \tag{6.3}$$

where $f^{(n)}(x) = \frac{\mathrm{d}^n f(x)}{\mathrm{d}x^n}$ and the function $f(x)$ vanishes at the boundary of x. Then, the functional derivative is given by [162, 269]

$$\frac{\delta G[f(x)]}{\delta f(x)} = \frac{\partial g}{\partial f} - \frac{\mathrm{d}}{\mathrm{d}x}\left(\frac{\partial g}{\partial f^{(1)}}\right) + \frac{\mathrm{d}^2}{\mathrm{d}x^2}\left(\frac{\partial g}{\partial f^{(2)}}\right) - \ldots + (-1)^n \frac{\mathrm{d}^n}{\mathrm{d}x^n}\left(\frac{\partial g}{\partial f^{(n)}}\right), \tag{6.4}$$

where $\frac{\partial g}{\partial f^{(p)}}$ are partial derivative, that is $\frac{\partial g}{\partial f^{(p)}}$ is taken holding $f^{(m)}$ with $m \neq p$ constant.

6.2 Details and comparison of Hartree-Fock and Density Functional Theory

In this Appendix, the solution of the Hartree-Fock and the Kohn-Sham equations, eqns. (2.88) and (2.160), respectively, in terms of an auxiliary set of one-electron basis functions, c.f. eqn. (2.53) and section 2.2.4, is discussed in more detail. The resulting equations are usually referred to as the Roothaan [136] or the Roothaan-Hall [148] equations in the case of Hartree-Fock theory. Special emphasize is laid on the similarities between Hartree-Fock and Densitiy Functional Theory.

At first, details of the derivation of the Hartree-Fock equations are presented and the specific expression of the average Hartree-Fock potential $\vartheta^{\mathrm{HF}}(\mathbf{q}_i)$, c.f. eqn. (2.88), is given. Considering again only closed-shell systems, the auxiliary functional $G\left[\{\phi_m(\mathbf{q}_i)\}\right]$, c.f. eqn. (2.87), contains the energy expectation value of the trial Slater determinant $\Phi^{\mathrm{SD}}(\mathbf{q})$ and the set of Lagrange multipliers ϵ_{ab} accounting for the constraint of orthonormal spin-orbitals and is given by

$$G\left[\{\phi_m(\mathbf{q}_i)\}\right] = \langle\Phi^{\mathrm{SD}}(\mathbf{q})|\hat{H}_{\mathrm{el}}|\Phi^{\mathrm{SD}}(\mathbf{q})\rangle - \sum_{ab}\epsilon_{ab}\left[\langle\phi_a(\mathbf{q}_i)|\phi_b(\mathbf{q}_i)\rangle - \delta_{ab}\right]. \tag{6.5}$$

Using the Condon-Slater rules [136,148], the energy expectation value is expressed in terms of the spin-orbitals according to

$$\begin{aligned} G^{\mathrm{HF}}\left[\{\phi_m(\mathbf{q}_i)\}\right] = \sum_a^N \int \phi_a(\mathbf{q}_i) \Bigg(\underbrace{-\frac{1}{2}\boldsymbol{\nabla}^2_{\mathbf{r}_i} - \sum_A \frac{Z_A}{|\mathbf{r}_i - \mathbf{R}_A|}}_{\hat{h}} \Bigg) \phi_a(\mathbf{q}_i)\mathrm{d}\mathbf{q}_i \\ + \sum_{ab}^N \frac{1}{2} \underbrace{\int\int \mathrm{d}\mathbf{q}_i\mathrm{d}\mathbf{q}_j \phi_a(\mathbf{q}_i)\phi_a(\mathbf{q}_i)\frac{1}{|\mathbf{r}_i - \mathbf{r}_j|}\phi_b(\mathbf{q}_j)\phi_b(\mathbf{q}_j)}_{g_{aabb}} \\ - \sum_{ab}^N \frac{1}{2} \underbrace{\int\int \mathrm{d}\mathbf{q}_i\mathrm{d}\mathbf{q}_j \phi_a(\mathbf{q}_i)\phi_b(\mathbf{q}_i)\frac{1}{|\mathbf{r}_i - \mathbf{r}_j|}\phi_b(\mathbf{q}_j)\phi_a(\mathbf{q}_j)}_{g_{abba}} \\ - \sum_{ab}^N \epsilon_{ab}\left[\langle\phi_a(\mathbf{q}_i)|\phi_b(\mathbf{q}_i)\rangle - \delta_{ab}\right]. \end{aligned} \tag{6.6}$$

Here, the one-electron operator $\hat{h}$, and the two-electron Coulomb and exchange integrals, g_{aabb} and g_{abba}, respectively, were introduced [136,148]. Taking the functional derivative of eqn. (6.6) with respect to $\phi^*_m(\mathbf{q}_i)$ leads to

$$\frac{\delta G^{\mathrm{HF}}\left[\{\phi_m(\mathbf{q}_i)\}\right]}{\delta \phi_m^*(\mathbf{q}_i)} = \hat{h}\phi_m(\mathbf{q}_i) + \sum_b^N \left[\underbrace{\int \mathrm{d}\mathbf{q}_j \phi_b^*(\mathbf{q}_j) \frac{1}{|\mathbf{r}_i - \mathbf{r}_j|} \phi_b(\mathbf{q}_j)}_{\hat{J}_b} \phi_m(\mathbf{q}_i) - \int \mathrm{d}\mathbf{q}_j \phi_b(\mathbf{q}_j) \frac{1}{|\mathbf{r}_i - \mathbf{r}_j|} \phi_m(\mathbf{q}_j) \phi_b(\mathbf{q}_i) \right] - \sum_b^N \epsilon_{mb} \phi_b(\mathbf{q}_i), \tag{6.7}$$

where the Coulomb operator $\hat{J}_b$ was defined. To proceed, the exchange operator $\hat{K}_b$ defined by its effect when operating on a spin-orbital $\phi_m(\mathbf{q}_i)$ according to

$$\hat{K}_b \phi_m(\mathbf{q}_i) = \left[\int \mathrm{d}\mathbf{q}_j \phi_b^*(\mathbf{q}_j) \frac{1}{|\mathbf{r}_i - \mathbf{r}_j|} \phi_m(\mathbf{q}_j) \right] \phi_b(\mathbf{q}_i) \tag{6.8}$$

is introduced. Since the result of operating with $\hat{K}_b$ on $\phi_m(\mathbf{q}_i)$ depends on the value of $\phi_m(\mathbf{q}_i)$ throughout all space, it is termed a non-local operator, whereas the Coulomb operator $\hat{J}_b$, eqn. (6.7), is a local operator. Hence, the Hartree-Fock equations, yielding a set of spin-orbitals $\left\{\tilde{\phi}_m^{\mathrm{HF}}(\mathbf{q}_i)\right\}$ for which the auxiliary functional, eqn. (6.7), becomes stationary, may be written in the form

$$[\hat{h} + \underbrace{\sum_b^N \hat{\tilde{J}}_b - \hat{\tilde{K}}_b}_{\tilde{\vartheta}^{\mathrm{HF}}(\mathbf{q}_i)}] \tilde{\phi}_m^{\mathrm{HF}}(\mathbf{q}_i) = \sum_b \tilde{\epsilon}_{bm}^{\mathrm{HF}} \tilde{\phi}_b^{\mathrm{HF}}(\mathbf{q}_i). \tag{6.9}$$

Next, the fact that both the HF wave function, $\Phi^{\mathrm{HF}}(\mathbf{q})$, being a single SD for closed-shell systems, and the Fock operator, $\hat{\tilde{f}}^{\mathrm{HF}}(\mathbf{q}_i) = \hat{h} + \tilde{\vartheta}^{\mathrm{HF}}(\mathbf{q}_i)$, are invariant with respect to a unitarily transformation among the spin-orbitals [136], is used to transform eqn. (6.9) into the form of an eigenvalue equation. Such unitary transformations among the spin-orbitals were already encountered in this thesis in section 2.2.3 for the calculation of localized molecular-orbitals, c.f. eqn. (2.170). In particular, a set of unitary transformed spin-orbitals $\left\{\phi_m^{\mathrm{HF}}(\mathbf{q}_i)\right\}$ that diagonalize the matrix of Lagrange multipliers $\tilde{\boldsymbol{\epsilon}}^{\mathrm{HF}}$ with elements $\tilde{\epsilon}_{ab}^{\mathrm{HF}} = \langle \tilde{\phi}_a^{\mathrm{HF}}(\mathbf{q}_i) | \hat{\tilde{f}}^{\mathrm{HF}}(\mathbf{q}_i) | \tilde{\phi}_b^{\mathrm{HF}}(\mathbf{q}_i) \rangle$ are sought. Since $\tilde{\boldsymbol{\epsilon}}^{\mathrm{HF}}$ is a Hermitian matrix, such a unitary transformation exists such that eqn. (6.9) may be written in the form

$$[\hat{h} + \underbrace{\sum_b^N \left(\hat{J}_b - \hat{K}_b \right)}_{\vartheta^{\mathrm{HF}}(\mathbf{q}_i)}] \phi_m^{\mathrm{HF}}(\mathbf{q}_i) = \epsilon_m^{\mathrm{HF}} \phi_m^{\mathrm{HF}}(\mathbf{q}_i). \tag{6.10}$$

These are the canonical Hartree-Fock equations yielding a set of canonical Hartree-Fock spin-orbitals $\left\{\phi_m^{\mathrm{HF}}(\mathbf{q}_i)\right\}$, c.f. eqn. (2.88).

In the restricted Hartree-Fock method, the set of spin-orbitals $\left\{\phi_m^{\mathrm{HF}}(\mathbf{q}_i)\right\}$ is expressed according to eqn. (2.48), and the spin-orbital HF equations (6.10) are converted to spatial eigenvalue

equations for a set of $N/2$ molecular-orbitals $\{\psi_m^{\mathrm{HF}}(\mathbf{r}_i)\}$, each of which is occupied with two electrons with opposite spin [136]. These spatial eigenvalue equations are obtained by integrating eqn. (6.10) over the spin-functions yielding

$$\underbrace{[\hat{h} + \underbrace{\sum_{b}^{N/2}\left(2\hat{J}_b - \hat{K}_b\right)}_{\vartheta^{\mathrm{HF}}(\mathbf{r}_i)}]}_{\hat{f}^{\mathrm{HF}}(\mathbf{r}_i)}\psi_m^{\mathrm{HF}}(\mathbf{r}_i) = \epsilon_m^{\mathrm{HF}}\psi_m^{\mathrm{HF}}(\mathbf{r}_i), \tag{6.11}$$

where in the expressions for the Coulomb and exchange operators, eqns. (6.7) and (6.8), respectively, the spin-orbitals were replaced by the respective spatial MOs and the sum runs over the $N/2$ occupied MOs. In the Roothaan [136] or Roothaan-Hall [148] scheme, the MOs in eqn. (6.11) are expanded in a set of real-valued one-electron basis-functions (AOs), section 2.2.4, according to

$$\psi_m^{\mathrm{HF}}(\mathbf{r}_i) = \sum_{\mu}^{K} c_{m\mu}^{\mathrm{HF}}\lambda_\mu(\mathbf{r}_i), \tag{6.12}$$

c.f. eqn. (2.53). Inserting eqn. (6.12) into eqn. (6.11), multiplying from the left by $\lambda_\nu(\mathbf{r}_i)$ and integrating over the electronic coordinates yields

$$\sum_{\mu} c_{\mu m}^{\mathrm{HF}} \underbrace{\int \mathrm{d}\mathbf{r}_i \lambda_\nu(\mathbf{r}_i)\hat{f}^{\mathrm{HF}}(\mathbf{r}_i)\lambda_\mu(\mathbf{r}_i)}_{f_{\nu\mu}^{\mathrm{HF}}} = \epsilon_m^{\mathrm{HF}} \sum_{\mu} c_{\mu m}^{\mathrm{HF}} \underbrace{\int \mathrm{d}\mathbf{r}_i \lambda_\nu(\mathbf{r}_i)\lambda_\mu(\mathbf{r}_i)}_{S_{\nu\mu}}, \tag{6.13}$$

where the elements of the Fock matrix $\mathbf{f}^{\mathrm{HF}}$ and of the overlap matrix $\mathbf{S}$, $f_{\nu\mu}^{\mathrm{HF}}$ and $S_{\nu\mu}$, respectively, were defined. These equations may be expressed in matrix form as

$$\mathbf{f}^{\mathrm{HF}}\mathbf{c}^{\mathrm{HF}} = \mathbf{S}\mathbf{c}^{\mathrm{HF}}\boldsymbol{\epsilon}^{\mathrm{HF}}, \tag{6.14}$$

where $\mathbf{c}^{\mathrm{HF}}$ is a $K \times K$ matrix of the AO expansion coefficients $c_{\mu m}^{\mathrm{HF}}$, and $\boldsymbol{\epsilon}^{\mathrm{HF}}$ is a diagonal matrix of the Lagrange multipliers ϵ_m^{HF}, which are also referred to as the molecular orbital energies. The Fock matrix $\mathbf{f}^{\mathrm{HF}}$ may be completely expressed in the AO basis by expanding the respective MOs in the expressions for the coulomb and exchange operators, c.f. eqn. (6.11), in terms of the AOs resulting in

$$f_{\nu\mu}^{\mathrm{HF,AO}}(\mathbf{c}) = \int \mathrm{d}\mathbf{r}_i \lambda_\nu(\mathbf{r}_i)\hat{h}\lambda_\mu(\mathbf{r}_i) + \sum_{\rho\sigma}\underbrace{\sum_{m} c_{\rho m}c_{\sigma m}}_{D_{\rho\sigma}^{\mathrm{AO}}}\left(2g_{\nu\mu\rho\sigma} - g_{\nu\sigma\rho\mu}\right), \tag{6.15}$$

where $D_{\rho\sigma}^{\mathrm{AO}}$ are the elements of the AO representation of the density matrix [136,148].

Applying the same scheme to the Kohn-Sham equations, eqn. (2.160), leads to the analogous matrix equations

$$\mathbf{f}^{\mathrm{KS}}\mathbf{c}^{\mathrm{KS}} = \mathbf{S}\mathbf{c}^{\mathrm{KS}}\boldsymbol{\epsilon}^{\mathrm{KS}}. \tag{6.16}$$

Apart from the expression for the exchange integrals, eqns. (6.6) and (6.15), the expressions for the Kohn-Sham matrix $\mathbf{f}^{\mathrm{KS}}$ in eqn. (6.16) are exactly equal to the expressions for the Fock matrix $\mathbf{f}^{\mathrm{HF}}$ in eqn. (6.14). In the Kohn-Sham matrix, the Hartree-Fock exchange integrals are replaced by the matrix representation of the exchange-correlation potential, eqn. (2.158), in the AO basis according to

$$v_{\nu\mu}^{\mathrm{XC}} = \int \mathrm{d}\mathbf{r}_i \lambda_\nu(\mathbf{r}_i) v_{\mathrm{XC}}(\mathbf{r}_i) \lambda_\mu(\mathbf{r}_i). \tag{6.17}$$

Hence, except for the exchange correlation part, eqn. (2.158), any numerical implementation of the Hartree-Fock equations, involving the analytical evaluation of the respective integrals in terms of the AOs, c.f. section 2.2.4, may be straightforwardly adapted to Kohn-Sham density functional theory. The exchange correlation part, on the other hand, involving the complicated expressions for the exchange correlation energy $E_{\mathrm{XC}}[\rho_{\mathrm{el}}^{\mathrm{BO}}(\mathbf{r})]$, c.f. section 2.2.2.3, need to be evaluated numerically. The reader is referred to Ref. [163] and Refs. therein for further details including the acceleration of the evaluations of the two-electron Coulomb integrals in the case of KS Density Functional Theory. Furthermore, the Roothaan matrix equations, eqn. (6.14), and the analogous KS matrix equations, eqn. (6.16), are usually transformed into a new set of equations resulting from the diagonalization of the overlap matrix $\mathbf{S}$. In this way, eqns. (6.14) and (6.16) can be solved by diagonalization of the transformed Fock and KS matrices, for further details see e.g. Ref. [136].

Since the Fock and Kohn-Sham matrices depend on the AO expansion coefficients, $\mathbf{f}^{\mathrm{HF}}(\mathbf{c}^{\mathrm{HF}})$, $\mathbf{f}^{\mathrm{KS}}(\mathbf{c}^{\mathrm{KS}})$, see e.g. eqn. (6.15), the non-linear eqns. (6.14) and (6.16) need to be solved iteratively. A straightforward implementation of the corresponding iterative procedure, usually referred to as SCF procedure, goes as follows:

- Calculate the Fock/KS matrix using an initial guess for the AO density matrix $D_{\rho\sigma}^{\mathrm{AO}}$, c.f. eqn. (6.15), generated e.g. by an extended Hückel calculation [137].
- Repeatedly update the Fock/KS matrix using the coefficients $\mathbf{c}^{\mathrm{HF}}/\mathbf{c}^{\mathrm{KS}}$ obtained in the previous iteration and generate an improved set of coefficients $\mathbf{c}^{\mathrm{HF}}/\mathbf{c}^{\mathrm{KS}}$ using eqn. (6.14)/(6.16) until convergence is achieved, i.e. until for instance the change in the density matrix from one iteration to the next is below a predefined threshold [136].

This iterative procedure, however, may converge slowly or diverge [148]. Consequently, in modern Quantum Chemistry Program Packages, e.g. Gaussian [135] or Molpro [134], SCF convergence accelerations, usually based on Pulay's method of *direct inversion in the iterative subspace* [270, 271] are used. Basically, these methods use the information from the preceding iterations to generate an averaged effective Hamiltonian by calculating the Fock/KS matrix of the current iteration as a linear combination of the Fock/KS matrix obtained in the previous iterations, see e.g. Ref. [148] for details and analysis of the respective convergence behaviors.

Bibliography

[1] A. H. Zewail, Femtochemistry: Atomic-Scale Dynamics of the Chemical Bond Using Ultrafast Lasers (Nobel Lecture), Angew. Chem. Int. Ed. **39**, 2586 (2000).

[2] J. Manz and L. Wöste, editors, *Femtosecond Chemistry*, VCH, Weinheim, 1995.

[3] F. C. De Schryver, S. De Feyter, and G. Schweitzer, editors, *Femtochemistry*, Wiley-VCH, Weinheim, 2001.

[4] A. Stolow, Femtosecond Time-Resolved Photoelectron Spectroscopy of Polyatomic Molecules, Ann. Rev. Phys. Chem. **54**, 89 (2003).

[5] P. Wernet, Electronic structure in real time: mapping valence electron rearrangements during chemical reactions, Phys. Chem. Chem. Phys. **13**, 16941 (2011).

[6] J. P. Marangos, S. Baker, N. Kajumba, J. S. Robinson, J. W. G. Tisch, and R. Torres, Dynamic imaging of molecules using high order harmonic generation, Phys. Chem. Chem. Phys. **10**, 35 (2007).

[7] M. Lein, Molecular imaging using recolliding electrons, J. Phys. B: At. Mol. Opt. Phys. **40**, R135 (2007).

[8] F. Krausz and M. Y. Ivanov, Attosecond physics, Rev. Mod. Phys. **81**, 163 (2009).

[9] A. Bandrauk and M. Ivanov, editors, *Quantum Dynamics Imaging*, CRM Series in Mathematical Physics, Springer, New York, 2011.

[10] S. Haessler, J. Caillat, and P. Salières, Self-probing of molecules with high harmonic generation, J. Phys. B: At. Mol. Opt. Phys. **44**, 203001 (2011).

[11] G. Sansone, F. Kelkensberg, J. F. Pérez-Torres, F. Morales, M. Kling, W. Siu, O. Ghafur, P. Johnsson, M. Swoboda, E. Benedetti, F. Ferrari, F. Lépine, J. L. Sanz-Vicario, S. Zherebtsov, I. Znakovskaya, A. L'Huillier, M. Y. Ivanov, M. Nisoli, F. Martín, and M. J. J. Vrakking, Electron localization following attosecond molecular photoionization, Nature **465**, 763 (2010).

[12] E. Goulielmakis, Z.-H. Loh, A. Wirth, R. Santra, N. Rohringer, V. S. Yakovlev, S. Zherebtsov, T. Pfeifer, A. M. Azzeer, M. F. Kling, S. R. Leone, and F. Krausz, Real-time observation of valence electron motion, Nature **466**, 739 (2010).

[13] H. Niikura, H. J. Wörner, D. M. Villeneuve, and P. B. Corkum, Probing the Spatial Structure of a Molecular Attosecond Electron Wave Packet Using Shaped Recollision Trajectories, Phys. Rev. Lett. **107**, 093004 (2011).

[14] I. Barth, J. Manz, Y. Shigeta, and K. Yagi, Unidirectional Electronic Ring Current Driven by a Few Cycle Circularly Polarized Laser Pulse: Quantum Model Simulations for Mg-Porphyrin, J. Am. Chem. Soc. **128**, 7043 (2006).

[15] I. Barth and J. Manz, Periodic Electron Circulation Induced by Circularly Polarized Laser Pulses: Quantum Model Simulations for Mg Porphyrin, Angew. Chem. Int. Ed. **45**, 2962 (2006).

[16] M. Kanno, H. Kono, and Y. Fujimura, Control of π-Electron Rotation in Chiral Aromatic Molecules by Nonhelical Laser Pulses, Angew. Chem. Int. Ed. **45**, 7995 (2006).

[17] S. Klinkusch, T. Klamroth, and P. Saalfrank, Long-range intermolecular charge transfer induced by laser pulses: an explicitly time-dependent configuration interaction approach, Phys. Chem. Chem. Phys. **11**, 3875 (2009).

[18] K. Nagashima and K. Takatsuka, Electron-Wavepacket Reaction Dynamics in Proton Transfer of Formamide, J. Phys. Chem. A **113**, 15240 (2009).

[19] T. Yonehara and K. Takatsuka, Characterization of electron-deficient chemical bonding of diborane with attosecond electron wavepacket dynamics and laser response, Chem. Phys. **366**, 115 (2009).

[20] M. Łabuda, J. González-Vázquez, and L. González, A wavepacket study of the low-energy charge transfer process in the S_3^+ + H reaction using time-resolved electronic densities, Phys. Chem. Chem. Phys. **12**, 5439 (2010).

[21] M. Kanno, H. Kono, Y. Fujimura, and S. H. Lin, Nonadiabatic Response Model of Laser-Induced Ultrafast π-Electron Rotations in Chiral Aromatic Molecules, Phys. Rev. Lett. **104**, 108302 (2010).

[22] A. Dutoi and L. S. Cederbaum, An Excited Electron Avoiding a Positive Charge, J. Phys. Chem. Lett. **2**, 2300 (2011).

[23] T. Yonehara, K. Hanasaki, and K. Takatsuka, Fundamental Approaches to Nonadiabaticity: Toward a Chemical Theory beyond the Born–Oppenheimer Paradigm, Chem. Rev. **112**, 499 (2012).

[24] G. Dixit, O. Vendrell, and R. Santra, Imaging electronic quantum motion with light, Proc. Natl. Acad. Sci. **109**, 11636 (2012).

[25] M. Kanno, Y. Ono, H. Kono, and Y. Fujimura, Laser-Polarization Effects on Coherent Vibronic Excitation of Molecules with Quasi-Degenerate Electronic States, J. Phys. Chem. A **116**, 11260 (2012).

[26] R. Borrelli, M. Thoss, H. Wang, and W. Domcke, Quantum dynamics of electron-transfer reactions: photoinduced intermolecular electron transfer in a porphyrin–quinone complex, Mol. Phys. **110**, 751 (2012).

[27] G. Dixit, J. M. Slowik, and R. Santra, Proposed Imaging of the Ultrafast Electronic Motion in Samples using X-Ray Phase Contrast, Phys. Rev. Lett. **110**, 137403 (2013).

[28] H. Wang and M. Thoss, Numerically exact, time-dependent study of correlated electron transport in model molecular junctions, J. Chem. Phys. **138**, 134704 (2013).

[29] R. Brückner, *Reaktionsmechanismen*, Elsevier, München, 3rd edition, 2004.

[30] F. Carey and R. Sundberg, *Advanced Organic Chemistry*, Springer, New York, 5th edition, 2007.

[31] K. P. C. Vollhardt and N. E. Schore, *Organic Chemistry*, W. H. Freeman and Company, New York, 5th edition, 2007.

[32] R. B. Jordan, *Reaction Mechanisms of Inorganic and Organometallic Systems*, Oxford University Press, New York, 3rd edition, 2007.

[33] E. Riedel and C. Janiak, *Anorganische Chemie*, De Gruyter, Berlin New York, 8th edition, 2011.

[34] J. M. Berg, J. L. Tymoczko, and L. Stryer, *Biochemistry*, W H Freeman, New York, 5th edition, 2002.

[35] D. L. Nelson and M. M. Cox, *Lehninger Principles of Biochemistry*, W. H. Freeman and Company, New York, 5th edition, 2008.

[36] W. H. Miller, Quantum mechanical transition state theory and a new semiclassical model for reaction rate constants, J. Chem. Phys. **61**, 1823 (1974).

[37] W. H. Miller, Beyond transition-state theory: a rigorous quantum theory of chemical reaction rates, Acc. Chem. Res. **26**, 174 (1993).

[38] U. Manthe, T. Seideman, and W. H. Miller, Quantum mechanical calculations of the rate constant for the $H_2 + OH \rightarrow H + H_2O$ reaction: Full-dimensional results and comparison to reduced dimensionality models, J. Chem. Phys. **101**, 4759 (1994).

[39] W. Miller, "Direct" and "Correct" Calculation of Canonical and Microcanonical Rate Constants for Chemical Reactions, J. Phys. Chem. A **102**, 793 (1998).

[40] T. Wu, H.-J. Werner, and U. Manthe, First-Principles Theory for the $H + CH_4 \rightarrow H_2 + CH_3$ Reaction, Science **306**, 2227 (2004).

[41] A. Accardi, I. Barth, O. Kühn, and J. Manz, From Synchronous to Sequential Double Proton Transfer: Quantum Dynamics Simulations for the Model Porphine, J. Phys. Chem. A **114**, 11252 (2010).

[42] M. Born and R. Oppenheimer, Zur Quantentheorie der Molekeln, Ann. Phys. **389**, 457 (1927).

[43] M. Born, Nachr. Akad. Wiss. Göttingen, Math.-Phys. Kl., 2A: Math.-Phys.-Chem. Abt. **6**, 1 (1951).

[44] M. Born and K. Huang, *Dynamical Theory of Crystal Lattices*, Oxford University Press, Oxford, UK, 1954.

[45] L. A. Nafie, Adiabatic molecular properties beyond the Born–Oppenheimer approximation. Complete adiabatic wave functions and vibrationally induced electronic current density, J. Chem. Phys. **79**, 4950 (1983).

[46] M. Okuyama and K. Takatsuka, Electron flux in molecules induced by nuclear motion, Chem. Phys. Lett. **476**, 109 (2009).

[47] D. J. Diestler, Coupled-Channels Quantum Theory of Electronic Flux Density in Electronically Adiabatic Processes: Fundamentals, J. Phys. Chem. A **116**, 2728 (2012).

[48] D. J. Diestler, A. Kenfack, J. Manz, and B. Paulus, Coupled-Channels Quantum Theory of Electronic Flux Density in Electronically Adiabatic Processes: Application to the Hydrogen Molecule Ion, J. Phys. Chem. A **116**, 2736 (2012).

[49] D. J. Diestler, Quasi-Classical Theory of Electronic Flux Density in Electronically Adiabatic Molecular Processes, J. Phys. Chem. A **116**, 11161 (2012).

[50] S. Patchkovskii, Electronic currents and Born-Oppenheimer molecular dynamics, J. Chem. Phys. **137**, 084109 (2012).

[51] D. J. Diestler, A. Kenfack, J. Manz, B. Paulus, J. F. Pérez-Torres, and V. Pohl, Computation of the Electronic Flux Density in the Born–Oppenheimer Approximation, DOI: 10.1021/jp4002302, J. Phys. Chem. A (2013).

[52] D. J. Diestler, Beyond the Born–Oppenheimer Approximation: A Treatment of Electronic Flux Density in Electronically Adiabatic Molecular Processes, J. Phys. Chem. A **117**, 4698 (2013).

[53] I. Barth, H.-C. Hege, H. Ikeda, A. Kenfack, M. Koppitz, J. Manz, F. Marquardt, and G. Paramonov, Concerted quantum effects of electronic and nuclear fluxes in molecules, Chem. Phys. Lett. **481**, 118 (2009).

[54] A. Kenfack, F. Marquardt, G. K. Paramonov, I. Barth, C. Lasser, and B. Paulus, Initial-state dependence of coupled electronic and nuclear fluxes in molecules, Phys. Rev. A **81**, 052502 (2010).

[55] A. Kenfack, I. Barth, F. Marquardt, and B. Paulus, Molecular isotopic effects on coupled electronic and nuclear fluxes, Phys. Rev. A **82**, 062502 (2010).

[56] A. Kenfack, S. Banerjee, and B. Paulus, Probing electron correlation in molecules via quantum fluxes, Phys. Rev. A **85**, 032501 (2012).

[57] H.-C. Hege, J. Manz, F. Marquardt, B. Paulus, and A. Schild, Electron flux during pericyclic reactions in the tunneling limit: Quantum simulation for cyclooctatetraene, Chem. Phys. **376**, 46 (2012).

[58] A. Schild, D. Choudhary, V. D. Sambre, and B. Paulus, Electron Density Dynamics in the Electronic Ground State: Motion Along the Kekulé Mode of Benzene, J. Chem. Phys. A **116**, 11355 (2012).

[59] H. E. Zimmerman and G. L. Grunewald, The Chemistry of Barrelene. III. A Unique Photoisomerization to Semibullvalene, J. Am. Chem. Soc. **88**, 183 (1966).

[60] H. E. Zimmerman, R. W. Binkley, R. S. Givens, G. L. Grunewald, and M. A. Sherwin, Mechanistic and exploratory organic photochemistry. XLIV. The barrelene to semibullvalene transformation. Correlation of excited-state potential energy surfaces with reactivity, J. Am. Chem. Soc. **91**, 3316 (1969).

[61] Y. C. Wang and S. H. Bauer, Structure of semibullvalene in the gas phase, J. Am. Chem. Soc. **94**, 5651 (1972).

[62] A. K. Cheng, F. A. L. Anet, J. Mioduski, and J. Meinwald, Determination of the fluxional barrier in semibullvalene by proton and carbon-13 nuclear magnetic resonance spectroscopy, J. Am. Chem. Soc. **96**, 2887 (1974).

[63] G. G. Christoph and M. A. Beno, Strained small ring compounds. Structure of a substituted semibullvalene, 1-cyanotricyclo[3.3.0.02,8]octa-3,6-diene. Geometric evidence for homoaromaticity in the molecular ground state, J. Am. Chem. Soc. **100**, 3156 (1978).

[64] H. Quast and J. Christ, Temperature Dependence of the UV Spectrum of 1,5-Dimethyl-2,6-semibullvalenedicarbonitrile; Evidence for an Equilibrium with a Delocalized, Homoaromatic Isomer, Angew. Chem. Int. Ed. **23**, 631 (1984).

[65] D. Moskau, R. Aydin, W. Leber, H. Günther, H. Quast, H.-D. Martin, K. Hassenrück, L. S. Miller, and K. Grohmann, Die Aktivierungsparameter der Cope-Umlagerung von Semibullvalen, 1,5-Dimethylsemibullvalen und 2,6-Dibrom-1,5-dimethylsemibullvalen, Chem. Ber. **122**, 925 (1989).

[66] H. Quast and M. Seefelder, The Equilibrium between Localized and Delocalized States of Thermochromic Semibullvalenes and Barbaralanes—Direct Observation of Transition States of Degenerate Cope Rearrangements, Angew. Chem. Int. Ed. **38**, 1064 (1999).

[67] M. Seefelder and H. Quast, Solvent Effects on the Equilibrium between Localized and Delocalized States of Thermochromic Semibullvalenes and Barbaralanes, Angew. Chem. Int. Ed. **38**, 1068 (1999).

[68] R. V. Williams, Homoaromaticity, Chem. Rev. **101**, 1185 (2001).

[69] A. C. Goren, D. A. Hrovat, M. Seefelder, H. Quast, and W. T. Borden, The Search for Bishomoaromatic Semibullvalenes and Barbaralanes: Computational Evidence of Their

Identification by UV/Vis and IR Spectroscopy and Prediction of the Existence of a Blue Bishomoaromatic Semibullvalene, J. Am. Chem. Soc. **124**, 3469 (2002).

[70] M. Seefelder, M. Heubes, H. Quast, W. D. Edwards, J. R. Armantrout, R. V. Williams, C. J. Cramer, A. C. Goren, D. A. Hrovat, and W. T. Borden, Experimental and Theoretical Study of Stabilization of Delocalized Forms of Semibullvalenes and Barbaralanes by Dipolar and Polarizable Solvents. Observation of a Delocalized Structure that Is Lower in Free Energy than the Localized Form, J. Org. Chem. **70**, 3437 (2005).

[71] P. R. Griffiths, D. E. Pivonka, and R. V. Williams, The Experimental Realization of a Neutral Homoaromatic Carbocycle, Chem. Eur. J. **17**, 9193 (2011).

[72] K. Bergmann, S. Goertler, J. Manz, and H. Quast, Fundamental frequencies increasing with reduced masses: an inverse quantum isotope effect in molecules with shallow double-well potentials, E.g. semibullvalenes, J. Am. Chem. Soc. **115**, 1490 (1993).

[73] M. Dohle, J. Manz, and G. K. Paramonov, A Pump & Dump & Probe Strategy for the Spectroscopy of the Transition State During a Laser-Controlled Isomerization: Model Simulation for the Cope Rearrangement of 2,6-Dicyanoethylmethylsemibullvalene, Ber. Bunsen-Ges. Phys. Chem. **99**, 478 (1995).

[74] M. Dohle, J. Manz, G. K. Paramonov, and H. Quast, Design of substituted semibullvalenes suitable for control of the Cope rearrangement by two ps IR laser pulses, Chem. Phys. **197**, 91 (1995).

[75] M. V. Korolkov, J. Manz, and G. K. Paramonov, Theory of ultrafast laser control of isomerization reactions in an environment: Picosecond Cope rearrangement of substituted semibullvalenes, J. Chem. Phys. **105**, 10874 (1996).

[76] H. Jiao, R. Nagelkerke, H. A. Kurtz, R. V. Williams, W. T. Borden, and P. von Ragué Schleyer, Annelated Semibullvalenes: A Theoretical Study of How They "Cope" with Strain, J. Am. Chem. Soc. **119**, 5921 (1997).

[77] S. Zilberg, Y. Haas, D. Danovich, and S. Shaik, The Twin-Excited State as a Probe for the Transition State in Concerted Unimolecular Reactions: The Semibullvalene Rearrangement, Angew. Chem. Int. Ed. **37**, 1394 (1998).

[78] E. C. Brown, D. K. Henze, and W. T. Borden, Are 1,5-Disubstituted Semibullvalenes that Have C_{2v} Equilibrium Geometries Necessarily Bishomoaromatic?, J. Am. Chem. Soc. **124**, 14977 (2002).

[79] E. C. Brown, R. F. W. Bader, and N. H. Werstiuk, QTAIM Study on the Degenerate Cope Rearrangements of 1,5-Hexadiene and Semibullvalene, J. Phys. Chem. A **113**, 3254 (2009).

[80] X. Zhang, D. A. Hrovat, and W. T. Borden, Calculations Predict That Carbon Tunneling Allows the Degenerate Cope Rearrangement of Semibullvalene to Occur Rapidly at Cryogenic Temperatures, Org. Lett. **12**, 2798 (2010).

[81] D. R. Greve, Homoaromaticity in aza- and phosphasemibullvalenes. A computational study, J. Phys. Org. Chem. **24**, 222 (2011).

[82] P. González-Navarrete, J. Andrés, and S. Berski, How a Quantum Chemical Topology Analysis Enables Prediction of Electron Density Transfers in Chemical Reactions. The Degenerated Cope Rearrangement of Semibullvalene, J. Phys. Chem. Lett. **3**, 2500 (2012).

[83] Y. Ichikawa and S. Sakai, Theoretical study on the Cope rearrangement mechanisms and the homoaromaticity of semibullvalene, barbaralane, and 1,5-methanosemibullvalene, J. Phys. Org. Chem. **25**, 409 (2012).

[84] M. J. S. Dewar, Multibond reactions cannot normally be synchronous, J. Am. Chem. Soc. **106**, 209 (1984).

[85] W. T. Borden, R. J. Loncharich, and K. N. Houk, Synchronicity in Multibond Reactions, Ann. Rev. Phys. Chem. **39**, 213 (1988).

[86] K. N. Houk, Y. Li, and J. D. Evanseck, Transition Structures of Hydrocarbon Pericyclic Reactions, Angew. Chem. Int. Ed. **31**, 682 (1992).

[87] L. Xu, C. E. Doubleday, and K. N. Houk, Dynamics of 1,3-Dipolar Cycloadditions: Energy Partitioning of Reactants and Quantitation of Synchronicity, J. Am. Chem. Soc. **132**, 3029 (2010).

[88] K. Black, P. Liu, L. Xu, C. Doubleday, and K. N. Houk, Dynamics, transition states, and timing of bond formation in Diels–Alder reactions, Inaugural Article, Proc. Natl. Acad. Sci. (2012).

[89] I. Iwakura, A. Yabushita, and T. Kobayashi, Direct Observation of the Molecular Structural Changes during the Claisen Rearrangement Including the Transition State, Chem. Lett. **39**, 374 (2010).

[90] I. Iwakura, A. Yabushita, J. Liu, K. Okamura, and T. Kobayashi, Photo-impulsive reactions in the electronic ground state without electronic excitation: non-photo, non-thermal chemical reactions, Phys. Chem. Chem. Phys. **14**, 9696 (2012).

[91] D. J. Tannor and S. A. Rice, Control of selectivity of chemical reaction via control of wave packet evolution, J. Chem. Phys. **83**, 5013 (1985).

[92] A. P. Peirce, M. A. Dahleh, and H. Rabitz, Optimal control of quantum-mechanical systems: Existence, numerical approximation, and applications, Phys. Rev. A **37**, 4950 (1988).

[93] W. Jakubetz, J. Manz, and H.-J. Schreier, Theory of optimal laser pulses for selective transitions between molecular eigenstates, Chem. Phys. Lett. **165**, 100 (1990).

[94] S. A. Rice and M. Zhao, *Optical Control of Molecular Dynamics*, John Wiley & Sons, New York, 2000.

[95] M. Shapiro and P. Brumer, *Quantum Control of Molecular Processes*, Wiley-VCH, Weinheim, 2nd edition, 2012.

[96] W. Zhu, J. Botina, and H. Rabitz, Rapidly convergent iteration methods for quantum optimal control of population, J. Chem. Phys. **108**, 1953 (1998).

[97] W. Zhu and H. Rabitz, A rapid monotonically convergent iteration algorithm for quantum optimal control over the expectation value of a positive definite operator, J. Chem. Phys. **109**, 385 (1998).

[98] M. Schröder, J.-L. Carreón-Macedo, and A. Brown, Implementation of an iterative algorithm for optimal control of molecular dynamics into MCTDH, Phys. Chem. Chem. Phys. **10**, 850 (2008).

[99] M. Schröder and A. Brown, Realization of the CNOT quantum gate operation in six-dimensional ammonia using the OCT-MCTDH approach, J. Chem. Phys. **131**, 034101 (2009).

[100] A. D. Becke and K. E. Edgecombe, A simple measure of electron localization in atomic and molecular systems, J. Chem. Phys. **92**, 5397 (1990).

[101] R. F. W. Bader, *Atoms in Molecules: A Quantum Theory*, Oxford University Press, New York, 1994.

[102] B. Silvi and A. Savin, Classification of chemical bonds based on topological analysis of electron localization functions, Nature **371**, 683 (1994).

[103] A. Savin, R. Nesper, S. Wengert, and T. F. Fässler, ELF: The Electron Localization Function, Angew. Chem. Int. Ed. **36**, 1808 (1997).

[104] T. Burnus, M. A. L. Marques, and E. K. U. Gross, Time-dependent electron localization function, Phys. Rev. A **71**, 010501 (2005).

[105] A. Castro, T. Burnus, M. A. L. Marques, and E. K. U. Gross, Time-dependent electron localization function: A tool to visualize and analyze ultrafast processes, in *Analysis and Control of Ultrafast Photoinduced Reactions*, edited by O. Kühn and L. Wöste, Springer Series in Chemical Physics, pages 553–574, Springer, Wiesbaden, 2007.

[106] J. J. Gerdy, M. Dantus, R. M. Bowman, and A. H. Zewail, Femtosecond selective control of wave packet population, Chem. Phys. Lett. **171**, 1 (1990).

[107] N. F. Scherer, J. C. Carlson, A. Matro, M. Du, A. J. Ruggiero, V. Romero-Rochin, J. A. Cina, G. R. Fleming, and S. A. Rice, Fluorescence-detected wave packet interferometry: Time resolved molecular spectroscopy with sequences of femtosecond phase-locked pulses, J. Chem. Phys. **95**, 1487 (1991).

[108] E. D. Potter, J. L. Herek, S. Pedersen, Q. Liu, and A. H. Zewail, Femtosecond laser control of a chemical reaction, Nature **355**, 66 (1992).

[109] R. R. Jones, C. S. Raman, D. W. Schumacher, and P. H. Bucksbaum, Ramsey interference in strongly driven Rydberg systems, Phys. Rev. Lett. **71**, 2575 (1993).

[110] T. J. Dunn, I. A. Walmsley, and S. Mukamel, Experimental Determination of the Quantum-Mechanical State of a Molecular Vibrational Mode Using Fluorescence Tomography, Phys. Rev. Lett. **74**, 884 (1995).

[111] A. P. Heberle and J. J. Baumberg, Ultrafast Coherent Control and Destruction of Excitons in Quantum Wells, Phys. Rev. Lett. **75**, 2598 (1995).

[112] R. R. Jones, Multiphoton Ionization Enhancement Using Two Phase-Coherent Laser Pulses, Phys. Rev. Lett. **75**, 1491 (1995).

[113] V. Blanchet, M. A. Bouchene, and B. Girard, Temporal coherent control in the photoionization of Cs_2: Theory and experiment, J. Chem. Phys. **108**, 4862 (1998).

[114] D. Meshulach and Y. Silberberg, Coherent quantum control of two-photon transitions by a femtosecond laser pulse, Nature **396**, 239 (1998).

[115] T. C. Weinacht, J. Ahn, and P. H. Bucksbaum, Measurement of the Amplitude and Phase of a Sculpted Rydberg Wave Packet, Phys. Rev. Lett. **80**, 5508 (1998).

[116] T. C. Weinacht, J. Ahn, and P. H. Bucksbaum, Controlling the shape of a quantum wavefunction, Nature **397**, 233 (1999).

[117] C. Warmuth, A. Tortschanoff, F. Milota, M. Shapiro, Y. Prior, I. S. Averbukh, W. Schleich, W. Jakubetz, and H. F. Kauffmann, Studying vibrational wavepacket dynamics by measuring fluorescence interference fluctuations, J. Chem. Phys. **112**, 5060 (2000).

[118] C. Warmuth, A. Tortschanoff, F. Milota, M. Leibscher, M. Shapiro, Y. Prior, I. S. Averbukh, W. Schleich, W. Jakubetz, and H. F. Kauffmann, Molecular quantum dynamics in a thermal system: Fractional wave packet revivals probed by random-phase fluorescence interferometry, J. Chem. Phys. **114**, 9901 (2001).

[119] M. Wollenhaupt, A. Assion, D. Liese, C. Sarpe-Tudoran, and T. Baumert, Interferences of Ultrashort Free Electron Wave Packets, Phys. Rev. Lett. **89**, 173001 (2002).

[120] T. S. Humble and J. A. Cina, Molecular State Reconstruction by Nonlinear Wave Packet Interferometry, Phys. Rev. Lett. **93**, 060402 (2004).

[121] C. Petersen, E. Péronne, J. Thøogersen, and H. Stapelfeldt, Control and imaging of interfering wave packets in dissociating I_2 molecules, Phys. Rev. A. **70**, 033404 (2004).

[122] A. Präkelt, M. Wollenhaupt, C. Sarpe-Tudoran, and T. Baumert, Phase control of a two-photon transition with shaped femtosecond laser-pulse sequences, Phys. Rev. A **70**, 063407 (2004).

[123] R. E. Carley, E. D. Boleat, R. S. Minns, R. Patel, and H. H. Fielding, Interfering Rydberg wave packets in Na, J. Phys. B: At. Mol. Opt. Phys. **38**, 1907 (2005).

[124] M. Fushitani, M. Bargheer, M. Gühr, and N. Schwentner, Pump-probe spectroscopy with phase-locked pulses in the condensed phase: decoherence and control of vibrational wavepackets, Phys. Chem. Chem. Phys. **7**, 3143 (2005).

[125] E. Lerch, X. Dai, S. Gilb, E. A. Torres, and S. R. Leone, Control of Li_2 wave packet dynamics by modification of the quantum mechanical amplitude of a single state, J. Chem. Phys. **124**, 044306 (2006).

[126] A. Monmayrant, C. B., and B. Girard, Quantum State Measurement Using Coherent Transients, Phys. Rev. Lett. **96**, 103002 (2006).

[127] K. Ohmori, H. Katsuki, H. Chiba, M. Honda, Y. Hagihara, K. Fujiwara, Y. Sato, and K. Ueda, Real-Time Observation of Phase-Controlled Molecular Wave-Packet Interference, Phys. Rev. Lett. **96**, 093002 (2006).

[128] H. Katsuki, H. Chiba, B. Girard, C. Meier, and K. Ohmori, Visualizing Picometric Quantum Ripples of Ultrafast Wave-Packet Interference, Science **311**, 1589 (2006).

[129] H. Katsuki, K. Hosaka, H. Chiba, and K. Ohmori, Read and write amplitude and phase information by using high-precision molecular wave-packet interferometry, Phys. Rev. A **76**, 013403 (2007).

[130] H. Katsuki, H. Chiba, C. Meier, B. Girard, and K. Ohmori, Actively Tailored Spatiotemporal Images of Quantum Interference on the Picometer and Femtosecond Scales, Phys. Rev. Lett. **102**, 103602 (2009).

[131] C. Stemmle, *Kernflussdichten bei der Cope-Umlagerung von Semibullvalene*, Bachelor-Arbeit, Freie Universität Berlin, 2012.

[132] M. Berry, I. Marzoli, and W. P. Schleich, Quantum carpets, carpets of light, Physics World **14**, 39 (2001).

[133] O. M. Friesch, I. Marzoli, and W. P. Schleich, Quantum carpets woven by Wigner functions, New J. Phys. **2**, 4 (2000).

[134] H.-J. Werner, P. J. Knowles, G. Knizia, F. R. Manby, M. Schütz, P. Celani, T. Korona, R. Lindh, A. Mitrushenkov, G. Rauhut, K. R. Shamasundar, T. B. Adler, R. D. Amos, A. Bernhardsson, A. Berning, D. L. Cooper, M. J. O. Deegan, A. J. Dobbyn, F. Eckert, E. Goll, C. Hampel, A. Hesselmann, G. Hetzer, T. Hrenar, G. Jansen, C. Köppl, Y. Liu, A. W. Lloyd, R. A. Mata, A. J. May, S. J. McNicholas, W. Meyer, M. E. Mura, A. Nicklass, D. P. O'Neill, P. Palmieri, K. Pflüger, R. Pitzer, M. Reiher, T. Shiozaki, H. Stoll, A. J. Stone, R. Tarroni, T. Thorsteinsson, M. Wang, and A. Wolf, MOLPRO, version 2010.1, a package of ab initio programs, 2010.

[135] M. J. Frisch, G. W. Trucks, H. B. Schlegel, G. E. Scuseria, M. A. Robb, J. R. Cheeseman, G. Scalmani, V. Barone, B. Mennucci, G. A. Petersson, H. Nakatsuji, M. Caricato, X. Li, H. P. Hratchian, A. F. Izmaylov, J. Bloino, G. Zheng, J. L. Sonnenberg, M. Hada, M. Ehara, K. Toyota, R. Fukuda, J. Hasegawa, M. Ishida, T. Nakajima, Y. Honda, O. Kitao, H. Nakai, T. Vreven, J. A. Montgomery, Jr., J. E. Peralta, F. Ogliaro, M. Bearpark, J. J. Heyd, E. Brothers,

K. N. Kudin, V. N. Staroverov, R. Kobayashi, J. Normand, K. Raghavachari, A. Rendell, J. C. Burant, S. S. Iyengar, J. Tomasi, M. Cossi, N. Rega, J. M. Millam, M. Klene, J. E. Knox, J. B. Cross, V. Bakken, C. Adamo, J. Jaramillo, R. Gomperts, R. E. Stratmann, O. Yazyev, A. J. Austin, R. Cammi, C. Pomelli, J. W. Ochterski, R. L. Martin, K. Morokuma, V. G. Zakrzewski, G. A. Voth, P. Salvador, J. J. Dannenberg, S. Dapprich, A. D. Daniels, Ö. Farkas, J. B. Foresman, J. V. Ortiz, J. Cioslowski, and D. J. Fox, Gaussian 09 Revision A.1, Gaussian Inc. Wallingford CT 2009.

[136] A. Szabo and N. S. Ostlund, *Modern Quantum Chemistry*, Dover Publications, Mineola, 1996.

[137] I. N. Levine, *Quantum Chemistry*, Prentice Hall, New Jersey, 5th edition, 1999.

[138] E. Schrödinger, Quantisierung als Eigenwertproblem I, Ann. Phys. **384**, 361 (1926).

[139] E. Schrödinger, Quantisierung als Eigenwertproblem II, Ann. Phys. **384**, 489 (1926).

[140] E. Schrödinger, Quantisierung als Eigenwertproblem III, Ann. Phys. **385**, 437 (1926).

[141] E. Schrödinger, Quantisierung als Eigenwertproblem IV, Ann. Phys. **386**, 109 (1926).

[142] C. Cohen-Tannoudji, B. Diu, and F. Laloë, *Quantum Mechanics*, Wiley-VCH, Weinheim, 2006.

[143] W. Pauli, Über den Zusammenhang des Abschlusses der Elektronengruppen im Atom mit der Komplexstruktur der Spektren, Zeitschrift für Physik **31**, 765 (1925).

[144] W. Pauli, The Connection Between Spin and Statistics, Phys. Rev. **58**, 716 (1940).

[145] P. R. Bunker and P. Jensen, *Molecular Symmetry and Spectroscopy*, National Reasearch Council of Canada, Ottawa, 2nd edition, 2006.

[146] L. Cederbaum, Born-Oppenheimer Approximation and Beyond, in *Conical Intersections*, edited by W. Domcke, D. Yarkony, and H. Köppel, World Scientific Publishing Co. Pte. Ltd., Singapore, 2nd edition, 2004.

[147] G. A. Worth and L. S. Cederbaum, BEYOND BORN-OPPENHEIMER: Molecular Dynamics Through a Conical Intersection, Annu. Rev. Phys. Chem. **55**, 127 (2004).

[148] T. Helgaker, P. Jorgensen, and J. Olsen, *Molecular Electronic-Structure Theory*, John Wiley & Sons Ltd., West Sussex, 2000.

[149] T. H. Dunning Jr., K. A. Peterson, D. E. Woon, P. v. R. Schleyer, N. L. Allinger, T. Clark, J. Gasteiger, P. A. Kollman, H. F. Schaefer III, and P. R. Schreiner, editors, *Encyclopedia of Computational Chemistry*, John Wiley & Sons, Chichester, 1998.

[150] P. W. Atkins and R. S. Friedman, *Molecular Quantum Mechanics*, Oxford University Press, New York, 5th edition, 2010.

[151] R. McWeeny, *Methods of Molecular Quantum Mechanics*, Academic Press, London, 2nd edition, 1992.

[152] O. Deeb, M. Leibscher, J. Manz, W. von Muellern, and T. Seideman, Toward Separation of Nuclear Spin Isomers with Coherent Light, ChemPhysChem **8**, 322 (2007).

[153] K. Bonhoeffer and P. Harteck, Z. Phys. Chem. Abt. B4 **4**, 113 (1929).

[154] W. Domcke, D. R. Yarkony, and H. Koppel, *Conical Intersections*, World Scientific Publishing Co. Pte. Ltd., Singapore, 2nd edition, 2004.

[155] M. Baer, *Beyond Born-Oppenheimer*, John Wiley & Sons, New Jersey, 2006.

[156] C. J. Ballhausen and A. E. Hansen, Electronic Spectra, Ann. Rev. Phys. Chem. **23**, 15 (1972).

[157] W. Kutzelnigg, Which masses are vibrating or rotating in a molecule?, Mol. Phys. **105**, 2627 (2007).

[158] D. Stalling, M. Westerhoff, and H.-C. Hege, in *The Visualization Handbook*, edited by C. D. Hansen and C. R. Johnson, page 749, Elsevier, Amsterdam, 2005.

[159] D. J. Tozer, Density Functional Theory, in *European Summerschool in Quantum Chemistry*, edited by P. O. Widmark, Lund University, 7th edition, 2011.

[160] W. Nolting, *Grundkurs Theoretische Physik 3: Elektrodynamik*, Springer-Verlag, Berlin Heidelberg, 8th edition, 2004.

[161] J. Manz and K. Yamamoto, A selection rule for the directions of electronic fluxes during unimolecular pericyclic reactions in the electronic ground state, Mol. Phys. **110**, 517 (2012).

[162] R. G. Parr and W. Yang, *Density-Functional Theory of Atoms and Molecules*, Oxford University Press, New York, 1989.

[163] W. Koch and M. C. Holthausen, *A Chemist's Guide to Density Functional Theory*, Wiley-VCH, Weinheim, 2000.

[164] W. Klopper and W. Kutzelnigg, Møller-Plesset calculations taking care of the correlation CUSP, Chem. Phys. Lett. **134**, 17 (1987).

[165] W. Klopper, R. Röhse, and W. Kutzelnigg, CID and CEPA calculations with linear r_{12} terms, Chem. Phys. Lett. **178**, 455 (1991).

[166] J. Noga, W. Kutzelnigg, and W. Klopper, CC-R12, a correlation cusp corrected coupled-cluster method with a pilot application to the Be_2 potential curve, Chem. Phys. Lett. **199**, 497 (1992).

[167] L. Piela, *Ideas of Quantum Chemistry*, Elsevier, Amsterdam, 2006.

[168] W. Nolting, *Grundkurs Theoretische Physik 5/2: Quantenmechanik*, Springer, Berlin Heidelberg, 6th edition, 2012.

[169] S. Wilson, *Electron correlation in molecules*, Dover Publications, Mineola, 2007.

[170] R. J. Bartlett and G. D. Purvis, Many-body perturbation theory, coupled-pair many-electron theory, and the importance of quadruple excitations for the correlation problem, Int. J. Quantum Chem. **14**, 561 (1978).

[171] P. R. Taylor, Coupled-Cluster Methods in Quantum Chemistry, in *European Summerschool in Quantum Chemistry*, edited by P. O. Widmark, Lund University, 7th edition, 2011.

[172] B. O. Roos, Multiconfigurational (MC) Self-Consistent (SCF) Theory, in *European Summerschool in Quantum Chemistry*, edited by P. O. Widmark, Lund University, 7th edition, 2011.

[173] H.-J. Werner and P. J. Knowles, A second order multiconfiguration SCF procedure with optimum convergence, J. Chem. Phys. **82**, 5053 (1985).

[174] P. J. Knowles and H.-J. Werner, An efficient second-order MC SCF method for long configuration expansions, Chem. Phys. Lett. **115**, 259 (1985).

[175] H.-J. Werner and P. J. Knowles, An efficient internally contracted multiconfiguration–reference configuration interaction method, J. Chem. Phys. **89**, 5803 (1988).

[176] P. J. Knowles and H.-J. Werner, An efficient method for the evaluation of coupling coefficients in configuration interaction calculations, Chem. Phys. Lett. **145**, 514 (1988).

[177] P. Celani and H.-J. Werner, Analytical energy gradients for internally contracted second-order multireference perturbation theory, J. Chem. Phys. **119**, 5044 (2003).

[178] H.-J. Werner, Third-order multireference perturbation theory: The CASPT3 method, Mol. Phys. **89**, 645 (1996).

[179] J. A. Pople, J. S. Binkley, and R. Seeger, Theoretical models incorporating electron correlation, Int. J. Quantum Chem. **10**, 1 (1976).

[180] S. R. Langhoff and E. R. Davidson, Configuration interaction calculations on the nitrogen molecule, Int. J. Quantum Chem. **8**, 61 (1974).

[181] E. R. Davidson and D. W. Silver, Size consistency in the dilute helium gas electronic structure, Chem. Phys. Lett. **52**, 403 (1977).

[182] H.-J. Werner and W. Meyer, A quadratically convergent MCSCF method for the simultaneous optimization of several states, J. Chem. Phys. **74**, 5794 (1981).

[183] P.-Å. Malmqvist and B. O. Roos, The CASSCF state interaction method, Chem. Phys. Lett. **155**, 189 (1989).

[184] P. Hohenberg and W. Kohn, Inhomogeneous Electron Gas, Phys. Rev. **136**, B864 (1964).

[185] W. Kohn and L. J. Sham, Self-Consistent Equations Including Exchange and Correlation Effects, Phys. Rev. **140**, A1133 (1965).

[186] M. Levy, Universal Variational Functionals of Electron Densities, First Order Density Matrices, and Natural Spin Orbitals and Solution of the v-Representability Problem, Proc. Natl. Acad. Sci. **76**, 6062 (1979).

[187] M. A. L. Marques, C. A. Ullrich, F. Nogueira, A. Rubio, K. Burke, and E. K. U. Gross, editors, *Fundamentals of time-dependent density functional theory*, Springer, Heidelberg New York, 2012.

[188] D. M. Ceperley and B. J. Alder, Ground State of the Electron Gas by a Stochastic Method, Phys. Rev. Lett. **45**, 566 (1980).

[189] S. H. Vosko, L. Wilk, and M. Nusair, Accurate spin-dependent electron liquid correlation energies for local spin density calculations: a critical analysis, Can. J. Phys. **58**, 1200 (1980).

[190] A. D. Becke, Density-functional exchange-energy approximation with correct asymptotic behavior, Phys. Rev. A **38**, 3098 (1988).

[191] J. P. Perdew, Density-functional approximation for the correlation energy of the inhomogeneous electron gas, Phys. Rev. B **33**, 8822 (1986).

[192] J. P. Perdew, K. Burke, and M. Ernzerhof, Generalized Gradient Approximation Made Simple, Phys. Rev. Lett. **77**, 3865 (1996).

[193] J. P. Perdew and Y. Wang, Accurate and simple analytic representation of the electron-gas correlation energy, Phys. Rev. B **45**, 13244 (1992).

[194] C. Lee, W. Yang, and R. G. Parr, Development of the Colle-Salvetti correlation-energy formula into a functional of the electron density, Phys. Rev. B **37**, 785 (1988).

[195] R. Colle and O. Salvetti, Approximate Calculation of the Correlation Energy for the Closed Shells, Theoret. Chim. Acta **37**, 329 (1975).

[196] A. D. Becke, Density-functional thermochemistry. III. The role of exact exchange, J. Chem. Phys. **98**, 5648 (1993).

[197] L. A. Curtiss, K. Raghavachari, G. W. Trucks, and J. A. Pople, Gaussian-2 theory for molecular energies of first- and second-row compounds, J. Chem. Phys. **94**, 7221 (1991).

[198] P. J. Stephens, F. J. Devlin, C. F. Chabalowski, and M. J. Frisch, Ab Initio Calculation of Vibrational Absorption and Circular Dichroism Spectra Using Density Functional Force Fields, J. Phys. Chem. **98**, 11623 (1994).

[199] S. F. Boys, Construction of Some Molecular Orbitals to Be Approximately Invariant for Changes from One Molecule to Another, Rev. Mod. Phys. **32**, 296 (1960).

[200] F. Jensen, *Introduction to computational chemistry*, John Wiley & Sons, Chichester, 2007.

[201] J. Pipek and P. G. Mezey, A fast intrinsic localization procedure applicable for ab initio and semiempirical linear combination of atomic orbital wave functions, J. Chem. Phys. **90**, 4916 (1989).

[202] R. S. Mulliken, Criteria for the Construction of Good Self-Consistent-Field Molecular Orbital Wave Functions, and the Significance of LCAO-MO Population Analysis, J. Chem. Phys. **36**, 3428 (1962).

[203] C. Edmiston and K. Ruedenberg, Localized Atomic and Molecular Orbitals. II, J. Chem. Phys. **43**, S97 (1965).

[204] J. Almlöf and P. R. Taylor, Atomic Natural Orbital (ANO) Basis Sets for Quantum Chemical Calculations, Adv. Quantum Chem. **22**, 301 (1991).

[205] J. Almlöf and P. R. Taylor, General contraction of Gaussian basis sets. I. Atomic natural orbitals for first- and second-row atoms, J. Chem. Phys. **86**, 4070 (1987).

[206] T. H. Dunning, Gaussian basis sets for use in correlated molecular calculations. I. The atoms boron through neon and hydrogen, J. Chem. Phys. **90**, 1007 (1989).

[207] J. S. Binkley, J. A. Pople, and W. J. Hehre, Self-consistent molecular orbital methods. 21. Small split-valence basis sets for first-row elements, J. Am. Chem. Soc. **102**, 939 (1980).

[208] W. J. Hehre, R. Ditchfield, and J. A. Pople, Self—Consistent Molecular Orbital Methods. XII. Further Extensions of Gaussian—Type Basis Sets for Use in Molecular Orbital Studies of Organic Molecules, J. Chem. Phys. **56**, 2257 (1972).

[209] D. J. Tannor, *Introduction to quantum mechanics: A time-dependent perspective*, University Science Books, Sausalito, 2007.

[210] C. C. Marston and G. Balint-Kurti, The Fourier grid Hamiltonian method for bound state eigenvalues and eigenfunctions, J. Chem. Phys. **91**, 3571 (1989).

[211] M. D. Feit, J. A. Fleck Jr., and A. Steiger, Solution of the Schrödinger equation by a spectral method, J. Comp. Phys. **47**, 412 (1982).

[212] C. Cohen-Tannoudji, J. Dupont-Roc, and G. Grynberg, *Photons and Atoms: Introduction to Quantum Electrodynamics*, Wiley-VCH, Weinheim, 2004.

[213] E. Cormier and P. Lambropoulos, Optimal gauge and gauge invariance in non-perturbative time-dependent calculation of above-threshold ionization, J. Phys. B: At. Mol. Opt. Phys. **29**, 1667 (1996).

[214] M. Göppert-Mayer, Über Elementarakte mit zwei Quantensprüngen, Ann. Phys. **401**, 273 (1931).

[215] Y.-C. Han and L. B. Madsen, Comparison between length and velocity gauges in quantum simulations of high-order harmonic generation, Phys. Rev. A **81**, 063430 (2010).

[216] J. G. G. Gerber, M. Bergt, Femto-Welt: Eine spielerische Einführung in die Welt der ultrakurzen Laserpulse, http://www.physik.uni-wuerzburg.de/femto-welt.

[217] J. Rauch and G. Mourou, The time integrated far field for Maxwell's and D'Alembert's equations, Proc. Amer. Math. Soc. **134**, 851 (2006).

[218] I. Barth and C. Lasser, Trigonometric pulse envelopes for laser-induced quantum dynamics, J. Phys. B: At. Mol. Opt. Phys. **42**, 235101 (2009).

[219] N. Došlić, Generalization of the Rabi population inversion dynamics in the sub-one-cycle pulse limit, Phys. Rev. A **74**, 013402 (2006).

[220] S. Chelkowski and A. D. Bandrauk, Asymmetries in strong-field photoionization by few-cycle laser pulses: Kinetic-energy spectra and semiclassical explanation of the asymmetries of fast and slow electrons, Phys. Rev. A **71**, 053815 (2005).

[221] A. D. Bandrauk and N. H. Shon, Attosecond control of ionization and high-order harmonic generation in molecules, Phys. Rev. A **66**, 031401 (2002).

[222] G. K. Paramonov and V. A. Savva, Resonance effects in molecule vibrational excitation by picosecond laser pulses, Phys. Lett. A **97**, 340 (1983).

[223] G. K. Paramonov, V. A. Savva, and A. M. Samson, Ultrafast inversion of population in the molecule vibrational mode pumped by a highpower picosecond IR laser pulse, Infrared Phys. **25**, 201 (1985).

[224] C. Chandre, S. Wiggins, and T. Uzer, Time–frequency analysis of chaotic systems, Physica D **181**, 171 (2003).

[225] P. Schwendner, F. Seyl, and R. Schinke, Photodissociation of Ar_2^+ in strong laser fields, Chem. Phys. **217**, 233 (1997).

[226] G. A. Worth, M. H. Beck, A. Jäckle, and H.-D. Meyer, The MCTDH Package, Version 8.2, (2000). H.-D. Meyer, Version 8.3 (2002), Version 8.4 (2007). See http://mctdh.uni-hd.de.

[227] L. Wang, H.-D. Meyer, and V. May, Femtosecond laser pulse control of multidimensional vibrational dynamics: Computational studies on the pyrazine molecule, J. Chem. Phys. **125**(1), 014102 (2006).

[228] C. Daniel, J. Full, L. González, C. Lupulescu, J. Manz, A. Merli, S. Vajda, and L. Wöste, Deciphering the Reaction Dynamics Underlying Optimal Control Laser Fields, Science **299**, 536 (2003).

[229] K. Sundermann and R. de Vivie-Riedle, Extensions to quantum optimal control algorithms and applications to special problems in state selective molecular dynamics, J. Chem. Phys. **110**, 1896 (1999).

[230] H.-D. Meyer, U. Manthe, and L. S. Cederbaum, The Multi-Configurational Time-Dependent Hartree Approach, Chem. Phys. Lett. **165**, 73–78 (1990).

[231] J. M. Bowman, D. Wang, X. Huang, F. Huarte-Larrañaga, and U. Manthe, The importance of an accurate CH_4 vibrational partition function in full dimensionality calculations of the $H + CH_4 \rightarrow H_2 + CH_3$ reaction, J. Chem. Phys. **114**, 9683 (2001).

[232] G. A. Worth, H.-D. Meyer, and L. S. Cederbaum, The effect of a model environment on the S_2 absorption spectrum of pyrazine: A wave packet study treating all 24 vibrational modes, J. Chem. Phys. **105**, 4412 (1996).

[233] H. Wang and M. Thoss, Multilayer formulation of the multiconfiguration time-dependent Hartree theory, J. Chem. Phys. **119**, 1289 (2003).

[234] H. Wang and M. Thoss, Quantum Dynamical Simulation of Electron-Transfer Reactions in an Anharmonic Environment, J. Phys. Chem. A **111**, 10369 (2007).

[235] O. Vendrell and H.-D. Meyer, Multilayer multiconfiguration time-dependent Hartree method: Implementation and applications to a Henon–Heiles Hamiltonian and to pyrazine, J. Chem. Phys. **134**, 044135 (2011).

[236] U. Manthe, A multilayer multiconfigurational time-dependent Hartree approach for quantum dynamics on general potential energy surfaces, J. Chem. Phys. **128**, 164116 (2008).

[237] H. Wang and M. Thoss, Numerically exact quantum dynamics for indistinguishable particles: The multilayer multiconfiguration time-dependent Hartree theory in second quantization representation, J. Chem. Phys. **131**, 024114 (2009).

[238] R. Welsch and U. Manthe, Reaction dynamics with the multi-layer multi-configurational time-dependent Hartree approach: $H + CH_4 \rightarrow H_2 + CH_3$ rate constants for different potentials, J. Chem. Phys. **137**, 244106 (2012).

[239] Q. Meng and H.-D. Meyer, A multilayer MCTDH study on the full dimensional vibronic dynamics of naphthalene and anthracene cations, J. Chem. Phys. **138**, 014313 (2013).

[240] D. Marx and J. Hutter, *Ab Initio Molecular Dynamics: Basic Theory and Advanced Methods*, Cambridge University Press, Cambridge, 2009.

[241] E. B. Wilson, J. C. Decius, and P. C. Cross, *Molecular Vibrations: The Theory of Infrared and Raman Vibrational Spectra*, Dover Publications, Mineola, 2003.

[242] J. O. Hirschfelder and J. S. Dahler, The Kinetic Energy of Relative Motion, Proc. Natl. Acad. Sci. **42**, 363 (1956).

[243] D. W. Jepsen and J. O. Hirschfelder, Set of Co-Ordinate Systems Which Diagonalize the Kinetic Energy of Relative Motion, Proc. Natl. Acad. Sci. **45**, 249 (1959).

[244] I. Matanović, N. Došlić, and B. R. Johnson, Generalized approximation to the reaction path: The formic acid dimer case, J. Chem. Phys. **128**, 084103 (2008).

[245] K. Giese and O. Kühn, The all-Cartesian reaction plane Hamiltonian: Formulation and application to the H-atom transfer in tropolone, J. Chem. Phys. **123**, 054315 (2005).

[246] K. Giese, M. Petkovic, H. Naundorf, and O. Kühn, Multidimensional quantum dynamics and infrared spectroscopy of hydrogen bonds, Phys. Rep. **430**, 211 (2006).

[247] S. Takada and H. Nakamura, Effects of vibrational excitation on multidimensional tunneling: General study and proton tunneling in tropolone, J. Chem. Phys. **102**, 3977 (1995).

[248] K. Yagi, T. Taketsugu, and K. Hirao, Generation of full-dimensional potential energy surface of intramolecular hydrogen atom transfer in malonaldehyde and tunneling dynamics, J. Chem. Phys. **115**, 10647 (2001).

[249] N. Rosen, Lifetimes of Unstable Molecules, J. Chem. Phys. **1**, 319 (1933).

[250] E. Thiele and D. J. Wilson, Anharmonicity in Unimolecular Reactions, J. Chem. Phys. **35**, 1256 (1961).

[251] T. Joseph, T.-M. Kruel, J. Manz, and I. Rexrodt, Model calculation of local versus hyperspherical mode selective dissociation of H_2O, Chem. Phys. **113**, 223 (1987).

[252] H. Kono, Tohoku University, Sendai, private communication, 2012.

[253] M. Berg, T. Bredtmann, and B. Paulus, Time-dependent analysis of polar chemical bonds in terms of electronic quantum fluxes, in preparation (2013).

[254] H. J. Wörner, J. B. Bertrand, D. V. Kartashov, P. B. Corkum, and D. M. Villeneuve, Following a chemical reaction using high-harmonic interferometry, Nature **466**, 604 (2010).

[255] V. Pohl, *Pump-Dump-Laserpuls-Design zur Initiierung einer perizyklischen Modellreaktion*, Bachelor-Arbeit, Freie Universität Berlin, 2011.

[256] W. Jakubetz, Universität Wien, private communication, 2012.

[257] V. Pohl, Electronic Quantum Fluxes in Diatomic Molecules Involving Avoided Crossings, Master Thesis, 2013.

[258] V. Pohl, T. Bredtmann, J. F. Pérez-Torres, and B. Paulus, Visualization of the harpoon effect in terms of electron-nuclear fluxes, in preparation (2013).

[259] J. P. Paz, S. Habib, and W. H. Zurek, Reduction of the wave packet: Preferred observable and decoherence time scale, Phys. Rev. D **47**, 488 (1993).

[260] L. A. Nafie, Electron Transition Current Density in Molecules. 1. Non-Born-Oppenheimer Theory of Vibronic and Vibrational Transitions, J. Phys. Chem. A **101**, 7826 (1997).

[261] T. B. Freedman, X. Gao, M.-L. Shih, and L. A. Nafie, Electron Transition Current Density in Molecules. 2. Ab Initio Calculations for Electronic Transitions in Ethylene and Formaldehyde, J. Phys. Chem. A **102**, 3352 (1998).

[262] A. D. Bandrauk, S. Chelkowski, and H. S. Nguyen, Attosecond localization of electrons in molecules, Int. J. Quantum Chem. **100**, 834 (2004).

[263] A. D. Bandrauk, S. Chelkowski, P. B. Corkum, J. Manz, and G. L. Yudin, Attosecond photoionization of a coherent superposition of bound and dissociative molecular states: effect of nuclear motion, J. Phys. B: At. Mol. Opt. Phys. **42**, 134001 (2009).

[264] M. Grønager and N. E. Henriksen, Real-time control of electronic motion: Application to NaI, J. Chem. Phys. **109**, 4335 (1998).

[265] Y. Arasaki, K. Takatsuka, K. Wang, and V. McKoy, Studies of electron transfer in NaI with pump–probe femtosecond photoelectron spectroscopy, J. Chem. Phys. **119**, 7913 (2003).

[266] M. Spanner and P. Brumer, Probing electron transfer within alkali-metal halides via high-order harmonic generation, Phys. Rev. A **78**, 033840 (2008).

[267] M. Barbatti, S. Belz, M. Leibscher, H. Lischka, and J. Manz, Sensitivity of femtosecond quantum dynamics and control with respect to non-adiabatic couplings: Model simulations for the cis–trans isomerization of the dideuterated methaniminium cation, Chem. Phys. **350**, 145 (2008).

[268] A. B. Alekseyev, H.-P. Liebermann, R. J. Buenker, N. Balakrishnan, H. R. Sadeghpour, S. T. Cornett, and M. J. Cavagnero, Spin–orbit effects in photodissociation of sodium iodide, J. Chem. Phys. **113**, 1514 (2000).

[269] F. W. Byron and R. W. Fuller, *Mathematics of classical and quantum physics*, Dover Publications, New York, 1992.

[270] P. Pulay, Convergence acceleration of iterative sequences. the case of scf iteration, Chem. Phys. Lett. **73**, 393 (1980).

[271] P. Pulay, Improved SCF convergence acceleration, J. Comp. Chem. **3**, 556 (1982).

Acknowledgements

This work was completed between June 2009 and July 2013 at the Institut für Chemie und Biochemie of the Freie Universität Berlin. First of all, I would like to express my appreciation to my supervisors, Prof. Jörn Manz and Prof. Beate Paulus (Freie Universität Berlin), for providing me with this great research project at the frontier between Chemistry and Physics; *PANTHA RHEI*, using Prof. Manz's words. I am very grateful for their support, the enthusiasm, the discussions, the academic freedom . . . Thank you very much for Everything!

I would also like to thank Monika Leibscher (Leibniz Universiät Hannover) for her lectures introducing me to the field of Quantum Dynamics, and for her guidance during my Bachelor and Master Theses. Furthermore, I would like to acknowledge our cooperation partners Prof. Hans-Christian Hege, Falko Marquardt and Christopher Mielack (Zuse-Institut Berlin) for introducing me to their sophisticated techniques of data-visualisation and providing me with their software as well as Prof. Hirohiko Kono and Kosuke Nakamura (Tohoku University, Sendai) for supporting our joint project despite the natural catastrophe in Japan in 2011 and the accompanying limitations. I also want to thank the students Emanuel Hupf (Universität Bremen), Matthias Berg, Vincent Pohl, Chrisitian Stemmle (Freie Universität Berlin) for their interest and their contributions.

I am grateful to Prof. Walter Thiel (Max-Planck-Institut für Kohlenforschung, Mülheim) for his continuing support, kindness and advice, starting with my research stay in his group during my studies with special thanks also to Markus Doerr and Marko Schreiber (formerly MPI Mülheim). Moreover, I would like to express my gratitude to Prof. André D. Bandrauk (Université de Sherbrooke) for the past, present and future cooperation, the extensive support and the great time I spent with him and his group in Sherbrooke, Canada. Special thanks also to Szczepan Chelkowski (Université de Sherbrooke) for his advice, his expertise and his kindness.

Further, a thank you to Profs. Hans-Dieter Meyer and Lorenz S. Cederbaum (Universität Heidelberg), to Prof. Peter Saalfrank, PD Tillmann Klamroth and Dominik Kröner (Universität Potsdam), to Prof. Bretislav Friedrich (Fritz-Haber-Institut), to PD Alejandro Saenz (Humboldt-Universität zu Berlin), to Olga Smirnova and Prof. Mikhail Ivanov (Max-Born-Institut Berlin), to Prof. Ilya Sh. Averbukh and Nirit Dudovich (Weizmann Institute of Science) as well as to Prof. Robin Santra and Oriol Vendrell (CFEL Hamburg) for their interest in my research and the opportunity to present it to a broader audience.

I would also like to thank Thomas Grohmann (Freie Universität Berlin), Markus Schröder (Universität Heidelberg), David Sulzer (Université de Strasbourg) as well as the members of the Theory Double-Group Manz/Paulus for the many scientific and non-scientific discussions.

Financial support from the Center for International Cooperation (Freie Universität Berlin) and Deutsche Forschungsgemeinschaft (DFG, project Ma 515/25-1) is gratefully acknowledged.

Last but not least, I would like to thank my parents, Chang-Sook and Klaus Bredtmann, my dear friend Ille Dogan and, of course, Connie, my sun and stars, for their infinite patience, support, comprehension and Anything Else.

Curriculum Vitae

Der Lebenslauf ist in der Online-Version aus Gründen des Datenschutzes nicht enthalten

Der Lebenslauf ist in der Online-Version aus Gründen des Datenschutzes nicht enthalten

Der Lebenslauf ist in der Online-Version aus Gründen des Datenschutzes nicht enthalten